MODELING OF NANOPARTICLE - MEMBRANE INTERACTIONS

by

Gülşah Gül

B.S., Chemical Engineering, Boğaziçi University, 2015

M.S., Chemical Engineering, Boğaziçi University, 2018

Submitted to the Institute for Graduate Studies in
Science and Engineering in partial fulfillment of
the requirements for the degree of
Doctor of Philosophy

Graduate Program in Chemical Engineering

Boğaziçi University

2022

to justice

ACKNOWLEDGEMENTS

I would like to thank to my thesis advisor Assoc. Prof. Nazar İleri for her support and patience, and the independence she gave me during my research. I am very grateful to Prof. Roland Faller for involving me into his group in UC Davis and for his comments that bring scientific awareness on me.

I would like to thank to Prof. Ramazan Yıldırım for his contributions to my research as well as for making me feel valued throughout my teaching assistantship. I would like to thank to my thesis committee member Assoc. Prof. Mehmet Sayar for his valuable comments on my research, and thesis jury members Prof. Seda Keskin and Assoc. Prof. Mesut Kırca for their time and evaluation on my thesis. I would like to thank to Assoc. Prof. Kerem Uğuz and Prof. Türkan Haliloğlu for their kindness and support throughout my student and assistant years in Boğaziçi University.

I would like to present my sincere appreciation to my friends Orhun Başteke li and Mustafa Varol for sharing their computational resources without any hesitation. I'm grateful to Dilek Kırkoç and Yakup Bal for their assistance on official transactions. I'd like to thank to Beyza Yılmaz for her friendship and scientific support during my graduate years in Boğaziçi University. Cordial thanks to Ayşegül Karakuş and all teaching assistants and students that I work with for their friendship and the moments that we have fun.

Heartfelt thanks to my friend Zhikai Liu who opens the doors of his house and guide me in any subject while I was homeless and stranger in Davis. I'd like to thank to my friends Didar Aşık, Merve Demir, Volga Kocasoy, Özge Emeksiz, Emel Akdoğan and Cem Yetişmişoğlu for the time that we spent together in Davis by exploring new tastes, places, and activities with fun. I also want to thank to my lifelong friends Gizem Özkartal and Yekta Yeşilyurt for their wisdom and experience that extend and change my perspective in addition to share best and worst moments of life with enthusiasm.

I would like to express my deep sense of gratitude to my parents İbrahim and Dilşat and brothers Barış and Savaş who make me feel special, smart, and strong in my most desperate moments. Every time I gave up, it was their support and belief that kept me up and moving on. Finally, I would like to thank to my deceased grandmother Gülşah who teach me to believe that there are good people, and you can be good whatever life brings you.

I would like to express my gratitude for the financial support of TUBITAK 2214A International Doctoral Research Fellowship Programme. This thesis is partially supported by the Bogazici University Research Fund Grant Number 21AD3. Computations were performed at TUBITAK ULAKBIM, High Performance and Grid Computing Center (TRUBA resources) and UC Davis HPC Clusters.

ABSTRACT

MODELING OF NANOPARTICLE - MEMBRANE INTERACTIONS

Understanding the toxicity behavior of NPs is of great importance to ensure efficient drug delivery to intracellular targets without causing cytotoxicity, to measure the long-term effects of nanoparticles (NPs), and to predict risks and hazards to humans and the environment. In this context, the current study involves (i) Coarse-grained (CG) Molecular Dynamics modeling of interactions of pristine and half polar (Janus) fullerenes with regular and peroxidized lipid membranes, (ii) cytotoxicity analysis of inorganic, organic and carbon-based NPs by applying Association Rule Mining (ARM), (iii) Atomistic (AA) and CG modeling of pristine and polystyrene (PS) functionalized CNTs and their interactions with lipid bilayers. In the first part, the translocation of pure and semi-polar fullerenes along the DOPC and POPC bilayers was investigated by varying the fullerene concentration and the peroxidation level of the bilayers, and the distribution of fullerenes in the lipid bilayer was mainly explained by the degree of peroxidation and saturation level of the lipid acyl chains. In the second part, a meta-heuristic model was constructed by extracting information from the literature based on NP and cell-derived properties, as well as the conditions tested. It was determined that cytotoxicity in terms of cell viability was primarily related to the core and coating material of NPs, their synthesis pathways, and the cell type to which they were exposed. Finally, the end rings of CNT were modified at atomistic and CG level with PS and carboxyl-terminated PS (PSCOOH), which were found to be an alternative and safe material through ARM. While AA simulation results showed that PSCOOH modification was advantageous in terms of drug release, more comprehensive CG results revealed that PS chain length and grafting density should be investigated further to prevent PS blockade that may pose a threat to drug release. Increasing CNT concentration changed the structural and elastic properties of the bilayers without causing permanent membrane damage and limited the transmembrane movement of cholesterols. The penetration of the developed models to the lipid membrane occurred by non-endocytic routes.

ÖZET

NANOPARTİKÜL – MEMBRAN ETKİLEŞİMLERİNİN MODELLENMESİ

Nanopartiküllerin toksisite davranışını anlamak, sitotoksisiteye neden olmadan hücre içi hedeflere etkili ilaç iletimini sağlamak, uzun vadeli etkilerini ölçmek ve insanlara ve çevreye yönelik riskleri ve tehlikelerini tahmin etmek açısından büyük önem taşımaktadır. Bu bağlamda, mevcut çalışma üç bölümden oluşmaktadır: (i) Saf ve yarı polar fullerenlerin düzenli ve peroksitlenmiş lipid membranlar ile etkileşimlerinin Kaba Taneli (CG) Moleküler Dinamik modellemesi, (ii) Birliktelik Kuralı Madenciliği (ARM) uygulanarak inorganik, organik ve karbon-bazlı nanopartiküllerin sitotoksisite analizi, (iii) Saf ve polistiren (PS) ile fonksiyonelleştirilmiş karbon nanotüplerin atomistik (AA) ve CG düzeyde modellenmesi ve geliştirilen modellerin lipid çift katmanları ile etkileşimleri. İlk bölümde, DOPC ve POPC çift katmanları boyunca saf ve yarı-polar fullerenlerin translokasyonu, fulleren konsantrasyonu ve çift katmanların peroksidasyon seviyesi değiştirilerek araştırılmış ve lipid membran içindeki fullerenlerin dağılımı esas olarak lipid açil zincirlerinin peroksidasyon derecesi ve doygunluk seviyesi ile açıklanmıştır. İkinci bölümde, NP ve hücreden türetilmiş özelliklerin yanı sıra test edilen koşullara dayalı olarak literatürden bilgi çıkarımı yoluyla bir meta-sezgisel model oluşturulmuştur. Hücre canlılığı açısından sitotoksisitenin öncelikle NP'lerin çekirdek ve kaplama malzemesi, sentez yolları ve maruz kaldıkları hücre tipi ile ilişkili olduğu tespit edilmiştir. Son olarak, CNT'nin uç halkaları ARM ile alternatif ve güvenli bir malzeme olduğu tespit edilen PS ve PSCOOH ile AA ve CG düzeyde modifiye edilmiştir. AA simülasyon sonuçları PSCOOH modifikasyonunun ilaç salınımı açısından avantajlı olduğunu gösterirken daha kapsamlı CG sonuçlar, PS zincir uzunluğunun ve aşılama yoğunluğunun ilaç salınımı açısından tehdit oluşturabilecek PS blokajını önlemek için daha fazla araştırılması gerektiğini ortaya koymuştur. Artan CNT konsantrasyonu kalıcı bir membran hasarına neden olmadan çift tabakaların yapısal ve elastik özelliklerini değiştirirken kolesterollerin transmembran hareketini sınırlandırmıştır. Geliştirilen modellerin zardan geçişi endositik olmayan yollarla gerçekleşmiştir.

TABLE OF CONTENTS

LIST OF FIGURES

LIST OF TABLES

LIST OF SYMBOLS

b	Bond
c	Offset
D	Diffusion constant
F	Force
H	Hamiltonian
K	Force constant
m	Mass
n	Number of beads
P	Pressure
q	Partial charge
r	Equilibrium bond length, radial distance
R	Universal gas constant
S	Deuterium order parameter
t	Time
T	Temperature
U	Potential energy
x	Coordinate in x-direction
y	Coordinate in y-direction
z	Coordinate in z-direction
α	Equilibrium angle
β	Equilibrium improper angle
ε	Well depth
ε_r	Permitivity constant
ϵ_0	Dielectric constant
ΔG	Free energy
θ	Bond angle
λ	Coupling parameter
π	Pi constant

σ	Nearest distance between two particles
ϕ	Improper angle
χ	Dihedral angle

LIST OF ACRONYMS/ABBREVIATIONS

A549	Human Lung Alveolar Epithelial Cells
AA	All-atom
AI	Artificial Intelligence
ANN	Artificial Neural Network
ARM	Association Rule Mining
ATP	Adenosine Triphosphate
BEAS-2B	Bronchial Epithelial Cell Line
CAGR	Compound Annual Growth Rate
CC_{50}	Cytotoxic Concentration
CCK-8	Cell Counting Kit-8
CG	Coarse-grained
CHO-K1	Chinese Hamster Ovary Cells
CLIO	Cross Linked Iron Oxide
CNT	Carbon Nanotube
COM	Center of Mass
CTAB	Cetyltrimethylammonium bromide
DLS	Dynamic Light Scattering
DOPC	1,2-dioleoyl-sn-glycero-3-phosphocholine
DT	Decision Tree
EBPVD	Electron Beam Physical Vapor Deposition
EC_{50}	Half Maximal Effective Concentration
ECHA	European Chemicals Agency
E. coli	Escherichia coli
HAP	Hydroxyapatite
HCMEC	Human Cardiac Microvascular Endothelial Cells
HUVEC	Human Umbilical Vein Endothelial Cells
IBU	Ibuprofen
IC_{50}	Half Maximal Inhibitory Concentration
kNN	K-Nearest Neighbor

L929	Murine Fibroblast Cell Line
LC_{50}	Lethal Concentration
LDA	Linear Discriminant Analysis
LDH	Lactate Dehydrogenase
logP	Partition Coefficient
LR	Logistic Regression
MBMC	Mouse Bone-Marrow derived Stem Cells
MC	Monte Carlo
MD	Molecular Dynamics
ML	Machine Learning
MLR	Multiple Linear Regression
MTS	3-(4,5-dimethylthiazol-2-yl)-5-(3-carboxymethoxyphenyl)-2-(4-sulfophenyl)-2H-tetrazolium
MTT	3-(4,5-dimethylthiazol-2-yl)-2,5-diphenyltetrazolium bromide
MWCNT	Multi-Walled Carbon Nanotube
NP	Nanoparticle
NRU	Neutral Red Uptake
PC	Phosphatidylcholine
PC12	Rat Pheochromocytoma Cell Line
PDI	Polydispersity Index
PEG	Polyethylene Glycol
PLGA	Poly (lactic-co-glycolic acid)
POPC	1-palmitoyl-2-oleoyl-sn-glycero-3-phosphocholine
PS	Polystyrene
PSCOOH	Carboxyl-terminated Polystyrene
PVP	Polyvinylpyrrolidone
Ref	Reference
RF	Random Forest
QD	Quantum Dot
QSAR	Quantitative Structure-Activity Relationship
QSTR	Quantitative Structure-Toxicity Relationship
RAW264.7	Murine Macrophage Cell Line
SEM	Scanning Electron Microscopy

SHSY5Y	Human Neuroblastoma Cell Line
SIRC	Statens Seruminstitut Rabbit Cornea Cell Line
SVM	Support Vector Machine
SWCNT	Single-Walled Carbon Nanotube
TC_{50}	Toxic Concentration
TEM	Transmission Electron Microscopy
THP-1	Human Monocytic Cell Line
XTT	2,3-bis-(2-methoxy-4-nitro-5-sulfophenyl)-2H-tetrazolium-5-carboxanilide

1. INTRODUCTION

Recently, nanoparticles used as drug carriers and theranostic agents have been extensively studied to enable the targeted and controlled release of drugs and increase the safety and efficacy of therapeutics. Since nanoparticles are required to pass a selective cellular barrier, i.e., the membrane, and localize within specific compartments of the cell without causing any damage, understanding the interactions between nanoparticles and the membrane is critical to determine their cellular uptake and cytotoxicity mechanism [1].

Many experimental studies have been conducted to analyze the toxic behavior of nanoparticles. In this context, cytotoxicity of nanoparticles has been evaluated through parameters including cell viability, oxidative stress, and lactate dehydrogenase release (LDH). Current studies have revealed that the physicochemical properties of nanoparticles such as material, size, shape, surface potential, and concentration as well as exposure time to cells, the type of cells, and the toxicity assays used play important roles in their toxicity [2,3]. With the increase in experimental findings, Machine Learning (ML) models such as random forest regression [4], decision tree classification [5], and artificial neural network models [6] have been developed to better understand and predict NP toxicity. However, although a great number of investigations, a generalized model could not be obtained due to the heterogeneity of published data, individual sampling, and missing information [4,7].

Association rule mining (ARM), a rule-based ML algorithm, is an alternative method that easily overcomes these limitations and discovers important hidden relationships between two or more attributes or between the attributes and the response, in large data sets. To date, it has only been used to determine the cellular responses of metal and metal oxide NPs [8]. However, NP toxicity, inversely related to cell viability, has not been investigated via ARM until our study. In this regard, we proposed an ARM model to analyze the cytotoxicity behavior of inorganic, organic, and carbon-based NPs by identifying significant associations of descriptors (including physicochemical properties of NPs, as well as cell and test properties) that result in high cell viability [9].

Passage of NPs through the membranes without any membrane damage or disruption is essential in determining safer carrier alternatives. On the other hand, the inability of experimental methods to explain the interactions of nanoparticles with the cell membrane has brought Molecular Dynamics (MD) simulations to the center of attention. Several nanoparticles, i.e., gold, fullerene, carbon nanotube, etc., and membrane models consisting of single/dual lipids have been proposed by MD modeling [10–13]. However, designing a realistic cell membrane has increased the cost of simulations as it requires the use of a wide variety of lipids and water molecules to meet the hydration level. For this reason, replacing atomistic detail with lower resolution, i.e., coarse-graining, has opened the way to simulate large-scale biomolecular systems on time scales inaccessible to atomistic simulations [14,15]. Coarse-grained (CG) modeling has several advantages which include (i) performing simulations of large and complex systems, (ii) allowing the simulations of slow processes at the time scales of micro to millisecond ranges, (iii) showing where molecular details matter, and where they do not, (iv) enabling computationally inexpensive testing for exploring biophysical pathways. In comparison to all-atom (AA) models, coarse-grained models are two to three-fold faster thanks to lower degrees of freedom with higher integration time steps and quick sampling via smoothened energy landscapes [15].

By using CG simulations, various NPs including carbon nanoparticles (CNPs) have been studied in terms of their interactions with lipid bilayers [16]. In addition to having superior thermal, electrical, and mechanical properties [17], CNPs have biocompatibility, high permeability, and antioxidant properties that allow them to be used as suitable drug carrier agents [18]. On the other hand, due to their hydrophobic nature, CNPs form aggregates in an aqueous environment by limiting their usage as drug carriers and threatening the health and environment by accumulating in cells [19]. Although they form large aggregates, experimental findings reveal that CNPs can penetrate cells and cross the blood-brain barrier (BBB) to deliver cargo [20,21]. However, the toxicity of CNPs has been related to their insolubility in water [22,23] and the main toxicity mechanism has been addressed as the oxidative stress triggered by reactive oxygen species (ROS) formation during exposure to cells [24–26]. Contradictorily, fullerenes have also been used as antioxidizing agents against ROS-mediated disruption in membrane integrity [27]. Thus, although their toxicity mechanism is controversial, CNPs functionalized with hydrophilic or

amphiphilic molecules such as proteins, surfactants, lipids, and polymers have been reported to be safer as they overcome the solubility limitation [28–30].

The focus of previous literature has been on polyethylene glycol (PEG) modification of carbon nanotubes (CNTs). Physical or covalent conjugation of PEG onto CNTs has provided low toxicity, long blood circulation lifetime, and more effective clearance [31–33]. On the other hand, polystyrene (PS) functionalization of CNTs has facilitated solubility and dispersion in aqueous and organic solvents [34,35] as well as improving mechanical properties like modulus of elasticity and shear stress [36,37]. However, PS-coated CNTs, despite their superior performance, have not been used in drug delivery systems up to now. The only experimental study where MWCNTs have been coated with PS showed that PS functionalization reduces inflammation and oxidative stress both *in vitro* and *in vivo* [38].

The current thesis aims to develop a meta-analysis model for NP toxicity and MD models for CNP-lipid membrane interactions. First, the translocation of pristine and half-polar (Janus) fullerenes across regular and peroxidized DOPC and POPC bilayers are investigated by changing fullerene concentration, and peroxidation level of bilayers. Then, the cytotoxicity data of various nanoparticles collected from the literature are analyzed with the ARM method and the significant rules that resulted in high cell viability are determined. Finally, PS, and carboxyl-terminated PS (PSCOOH), which is found to be as a safe material through ARM, was used to modify the CNT models at AA and CG levels and the developed functionalized nanotubes are explored through their interactions with pure POPC and POPC with cholesterol by changing PS chain length and grafting density in the end ring of CNTs.

In Chapter 2, a comprehensive literature survey on the prediction and analysis of NP toxicity, as well as NP-membrane interactions are presented. Chapter 3 involves the details of the computational methodology behind this thesis. In Chapter 4, the ML and MD modeling results are presented together with explanations and discussions. Finally, the conclusions of the current study and recommendations for the future are demonstrated in Chapter 5.

2. LITERATURE SURVEY

2.1. Cell Membrane

Cells are the smallest building blocks of living organisms which consist of a cytoplasm bounded by a membrane. Cell membranes, which are also called plasma membranes, are selective barriers separating the inner constituents of a cell from the outer environment. They have three main functions: (i) to protect the cells from toxic substances, (ii) to enable the transfer of nutrients, hormones, and microorganisms through their receptors and channels, (iii) to regulate metabolic activities [39]. In 1972, Singer and Nicolson introduced the fluid mosaic model of the cell membrane as a two-dimensional liquid, which includes lipids, proteins, carbohydrates, and cholesterol (c.f. Figure 2.1). According to this model, the fluidity and elasticity of the membrane are provided by the phospholipid bilayer where protein molecules are embedded [40] and the chain length and saturation level of lipids influence the fluidity of the membrane. Unsaturated lipids form kink and decrease melting temperature which result in an increase in membrane fluidity [41].

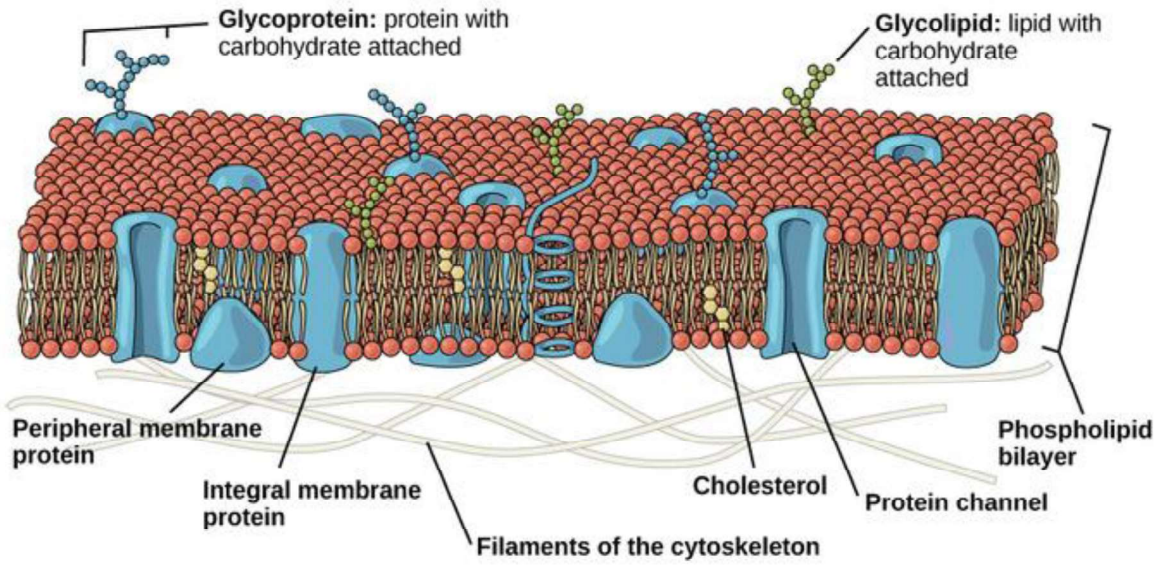

Figure 2.1. The plasma membrane model consisting of the phospholipid bilayer, and proteins [42].

The lipid bilayer forms through the self-assembly process of amphipathic lipids composed of a hydrophilic head group and a hydrophobic tail region (c.f. Figure 2.2). This spontaneous process is driven by the hydrophobic interactions in which fatty acid tails form clusters in an aqueous environment. Lipid bilayers are a few nanometers in length [43] and are generally impermeable to ions and water-soluble (polar) molecules. Therefore, the transport of these molecules occurs via transmembrane proteins, i.e., pores, gates, and channels while hydrophobic molecules, in general, passively diffuse into the membrane.

The amphipathic lipids that form the cell membrane are divided into three classes: phospholipids, glycolipids, and sterols. Although their amount varies according to the cell type, in most cases more than 50 % of all lipids are made up of phospholipids. In eukaryotic cells, plasma membranes are of about half lipid and half protein by weight, and cholesterol and glycolipids constitute about 40 % of total lipid content in the mammalian plasma membrane [41].

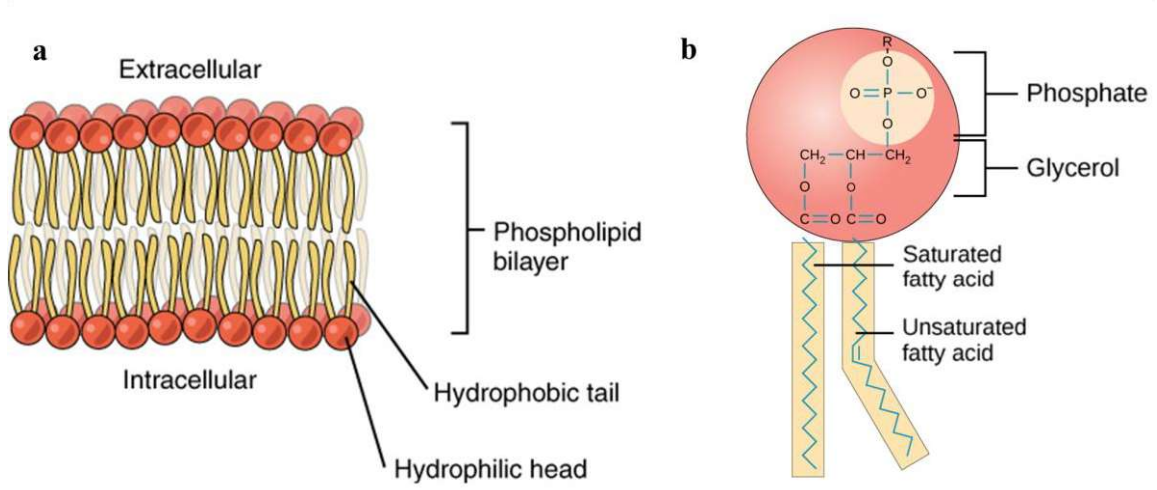

Figure 2.2. The structure of a) lipid bilayer, b) a phospholipid. Here, two chemical groups (choline and serine) may bond to the phosphate at the position labeled as R. Figures are adapted from ref. [44].

2.2. Nanotechnology and Nanotoxicity Overview

Nanotechnology, which was the subject of Richard Feynman's famous 1959 lecture "There's Plenty of Room at the Bottom" [45], was formally defined by Norio Taniguchi in 1974 [46]. In the nearly 50-year history of the nanotechnology field, tremendous advances have been recorded that have contributed to economic growth and public interest. With growing governmental, academic, and industrial initiatives [47], nanotechnology has been involved in major industry sectors, including materials science, electronics and informatics, energy, health, and environment [48,49]. Despite the negative impact of COVID-19 pandemic [50], global nanotechnology market was estimated to be 2.4 USD billion by *Emergen Research* in 2021 and expected to reach ~34 USD billion with a 34 % Compound Annual Growth Rate (CAGR) in 2030 [51]. Over the last decade, scientific publications listed in the Web of Science Core Collection (based on a topic search with the keyword of 'nanotechnology' on July 20, 2022) reached to 218,879 in total with a sharp increase in 2018 with 25,940 publications (c.f. Figure 2.3a). When the publication metrics of 105 countries were classified by cluster analysis, 30% of all scientific publications, including patents, were made up of the 2nd cluster countries with the great contribution of China and the US (c.f. Figure 2.3b) [52]. Among the nanotechnology application areas, nanomaterials have made a great leap forward with their use in medicine (especially as drug delivery agents) and their transformation into commercialized products. In this context, studies on nanomaterials showed an increasing tendency with 339,100 publications recorded between 2002-20 July 2022 (based on WOS search by topic) as demonstrated in Figure 2.3c and about 70% of these publications have been related to 'toxicity' (c.f. Figure 2.3d). This growing tendency agrees with the projected market trends [53,54].

Nanomaterials are generally considered to be materials that are 1-100 nm in size in at least one direction. Owing to their small size and high surface-to-volume ratio, they are capable of passing biological barriers, i.e., skin, intestine, mucosa, or blood-brain barrier, and reaching the targeted cellular site. However, the physicochemical properties which make nanocarriers unique can also lead to toxic effects. Therefore, determining which properties of nanoparticles cause toxic effects has been one of the main concerns of the nanotechnology field. Conventional toxicity assessments have relied on *in vivo* testing but suffered from economical, technical, and ethical challenges regarding the use of animals [55]. To promote

non-animal testing, European Chemicals Agency (ECHA) suggested 3R (replacement, reduction, refinement) legislation which includes *in vitro* and *in silico* approaches as alternative toxicology assessment methods [56]. By integrating these alternative methods with an intelligent design, it is aimed to further reduce the cost and number of animals [57].

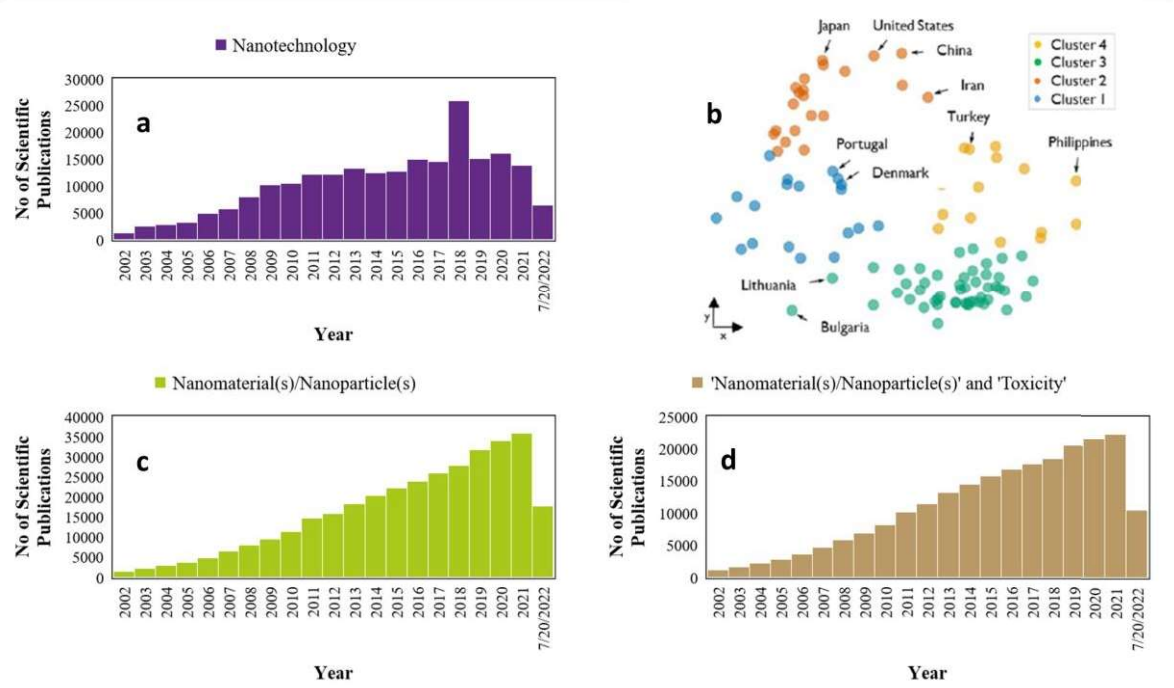

Figure 2.3. Scientific publication trends of the last 10 years based on topic search in Web of Science on 20 July 2022 with keywords (a) “nanotechnology”, (c) “nanomaterial(s)” or “nanoparticle(s)”, (d) “nanomaterial(s)” or “nanoparticle(s)” and “toxicity”. Section (b) shows the cluster analysis results of 105 countries based on their scientific publications and was adapted with permission from ref. [52] Copyright 2021 American Chemical Society.

2.3. Cellular Uptake Mechanisms

There are two major pathways, which are endocytosis and direct permeation, for the transport of NPs across a cell membrane. In endocytosis, extracellular NPs are wrapped by the deformation of a small fragment of the membrane, and a membrane-bounded vesicle (i.e., endosome) forms. Endocytosis which is a kind of active transport route is primarily used for the translocation of NPs, especially for polar and charged NPs. It can be divided into two categories named phagocytosis and pinocytosis. Phagocytosis is the process in

which certain mammalian cells called phagocytes (neutrophils, monocytes, macrophages etc.) ingest or engulf large size particles. Whereas in pinocytosis, small particles suspended in the extracellular fluid are taken into the cell by invagination of the cell membrane. To distinguish between phagocytosis and pinocytosis, the size of their endocytic vesicles is compared: Pinocytosis covers the uptake of the fluid through small vesicles with sizes up to hundreds of nanometers while phagocytosis allows the uptake of larger particles with vesicles around 250 nm [58].

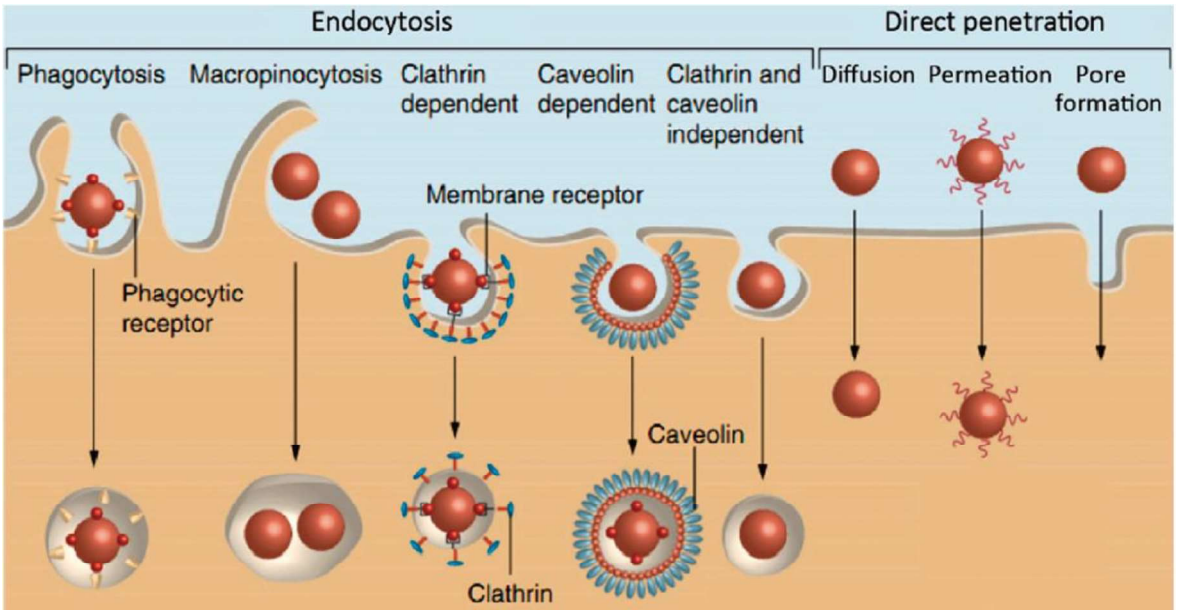

Figure 2.4. Cellular uptake mechanisms. Reprinted with the permission from ref. [59]. Copyright (2013) Future Science Group.

Pinocytosis can be classified into clathrin-mediated endocytosis, caveolae-mediated endocytosis, clathrin- and caveolae-independent endocytosis, and macropinocytosis. In the clathrin-mediated route, specific ligands in an extracellular fluid bind to the receptors on the surface of the cell membrane. The ligand-receptor complex moves to the clathrin-rich portions of the membrane and is internalized by forming clathrin-coated vesicles. In caveolae-mediated endocytosis, the flask-shaped structures, i.e., caveolae, form by invagination of the plasma membrane. They are found in many vertebrate cell types such as endothelial cells and adipocytes and are used for several functions in signal transduction. Clathrin- and caveolae-independent endocytosis does not use clathrin and caveolae coats. It is used by growth hormones, some types of proteins, or hijacked by bacteria and viruses to

gain access to the host cell. Macropinocytosis is a ‘cell-drinking’ type of endocytosis, which involves the uptake of extracellular material, such as nutrients and antigens. The macropinosomes are vesicles that greatly vary in size, with their diameters ranging between 0.5 and 10 micrometers. All lipid-derived NPs use a clathrin-dependent route while micron-sized NPs pass through the membrane by macropinocytosis. In nanomedicine, the caveolae-dependent pathway is preferred since the cargo which is engulfed by the cell does not eventuate in the lysosome in which degradation takes place. On the other hand, the clathrin-mediated pathway causes inefficient drug delivery because of the lysosomal degradation of particles [58,60].

Direct permeation is how NPs passively transport through membranes. In this pathway, NPs permeate across the membrane without being surrounded by endocytic vesicles. The uptake process is driven by the concentration gradient therefore energy is not utilized. NPs diffuse from higher to lower concentration zones enabling direct delivery process across the membrane. Unlike direct permeation, endocytosis occurs against a concentration gradient, and the required energy is provided by adenosine triphosphate (ATP). Therefore, the direct permeation route is also energetically favorable in addition to the fact that NPs cannot function by digestion or trapping by the vesicles [1,58].

2.4. Cytotoxicity Mechanisms

The toxic effects of nanoparticles have been correlated with metabolic activity, membrane integrity, cell viability, mitochondrial damage, mitochondrial integrity, and reactive oxygen species (ROS) formation. Various methods have been utilized to assess the cytotoxicity of nanoparticles such as proliferation, apoptosis, and necrosis assays [2].

Cellular metabolism is measured by proliferation assays in which metabolically active cells are determined. 3-(4,5-Dimethylthiazol-2-yl)-2,5-diphenyltetrazolium bromide (MTT) is the most encountered tetrazolium salt used as an indicator in the toxicity evaluation. However, the measurements are sensitive to the changes in culture media such as pH, temperature and chemical additives. Another assay used is Alamar Blue which measures cellular redox potential, but it is limited due to the lack of biochemical mechanisms behind

the assay. There is also a clonogenic assay in which the proliferating cells are counted by visual observation after imposing the NPs on the cells [2].

Disruption of cell membrane integrity is another important marker of nanotoxicity. Cells may be disrupted through membrane fractionation or adsorption of NPs to the membrane. A significant disruption of cell membrane integrity leads to cell membrane destabilization or lyse, thereby causing cytotoxicity. Necrosis is a form of cell injury which results in the death of cells due to cell lysis. Cells undergoing necrosis do not follow apoptotic signal transduction, instead, various receptors are activated, and the cell membrane integrity is damaged. By the loss of membrane integrity, the cells release their contents to the extracellular environment and initiate an inflammatory response in the surrounding medium. On the other hand, apoptosis is a form of programmed cell death that is sourced by the increase of oxidative stress in cell culture upon the formation of excessive free radicals. Necrosis is identified by the uptake of the dye such as Neutral Red or Trypan Blue while several assays such as Comet or TdT-mediated dUTP-biotin nick end labeling (TUNEL) assay are employed to determine apoptosis. TUNEL assay is widely used to detect DNA fragmentation in both apoptotic and non-apoptotic cells based on the incorporation of an enzyme terminal, deoxynucleotidyl transferase, into free 3′-hydroxyl termini of DNA double-strand breaks [2].

Nanoparticle exposure on cells induces pro-oxidant effects which bring about the production of ROS. When nanoparticles are internalized, phagocytosis can lead to ROS generation. The cytotoxic nature of ROS is a driving force behind apoptosis, but more increase in ROS amount can result in both apoptosis and necrosis, a form of uncontrolled cell death, in cancer cells [2].

2.5. Physicochemical Properties Effecting Cellular Uptake and Toxicity of Nanoparticles

The physical and chemical characteristics of nanoparticles, including the size, shape, surface charge, hydrophilicity/hydrophobicity, and surface functionalization have a major impact on the uptake level and permeation route as well as cytotoxicity of NPs.

The size of NP plays an important role in determining the efficiency of its cellular uptake and toxic potential. The large specific surface area provides effective adsorption of NPs on the cell surface due to the increase in reaction capacity and catalytic activity. Several experimental studies have shown that NPs smaller than 5 nm transport across the cell membrane through translocation whereas larger particles are taken by the cells by phagocytosis or macropinocytosis. NPs with several nanometers in size have been found more toxic than 10 nm or larger ones since small nanoparticles enter the nucleus [3]. For instance, NPs with a size of 1.4 nm have demonstrated 60 times higher toxicity than NPs 15 nm in size [61]. Furthermore, NPs with the size of < 200 nm have been internalized by cells via clathrin-mediated pits. It has been shown that for particles as large as 500 nm, the predominant pathway is caveolae-mediated internalization [62]. Another study has demonstrated that the clathrin-mediated route induces the formation of vesicles that are 120-150 nm in size. NPs in the range of 250 nm to 3 μm have been exhibited in vitro phagocytosis while NPs with an upper limit of 200 nm involve in caveolae or clathrin-dependent paths [63]. In many studies, an optimum size of ∼50 nm has been reported for a high and efficient uptake rate of gold nanoparticles [64,65].

In addition to size, the shape of NPs is an important factor in nanoparticle uptake and toxicity. The characteristic shapes of NPs consist of spheres, cylinders, rods, cubes, and sheets. NPs with spherical shapes have a higher tendency to be taken into the cell by endocytosis compared to nanotubes or nanofibers [3]. In another study, it has been shown that spherical gold nanoparticles had five times higher uptake rate than gold nanorods [66]. Zhao et al. studied the effect of shape on cytotoxicity of hydroxyapatite nanoparticles. They imposed spherical, needle-like, rod-like, and plate-like NPs on cultured BEAS-2B cells and observed that needle-like and plate-like nanoparticles lead to cell death in large portions than rod-like and spherical NPs [67].

The surface charge of NPs is another determinant factor in their interaction with cellular membranes. Since cell membranes are negatively charged, the uptake of positively charged NPs are more favorable than neutral or negatively charged ones considering electrostatics. However, the cellular uptake of positively charged NPs can increase cytotoxicity by disrupting membrane integrity. Liu et al. investigated the effect of the surface charge of polystyrene NPs on cancer HeLa and normal NIH3T3 cells and reported that

positively charged polystyrene is more toxic. This is accounted for not only effective penetration of positively charged NPs through membranes but also setting a strong bound with negatively charged DNA. The latter results in DNA damage, disruption of cell membrane integrity, and prolongation of the G0/G1 phase cycle [68]. Additionally, the mechanisms of uptake are affected by the surface charge of NPs. Positively charged NPs are more prone to macropinocytosis while negatively charged NPs are independent of clathrin or caveolae coats [69].

Another critical factor that affects cellular uptake and cytotoxicity of NPs is surface modification. NPs are prone to surface functionalization or coating process to decrease their toxicity, increase stability, and control cellular uptake level. Surface functionalization of NPs mainly involves polyethylene glycol (PEG), positive amine ($-NH_2$), neutral hydroxyl (-OH), and negative carboxyl (-COOH) groups [58]. Qui et al. showed that surface coating of gold nanorods with cationic poly diallyldimethyl ammonium chloride cause negligible toxicity and high cellular uptake efficiency [70]. Comparison of the interactions of plain polystyrene (PS) and amino-functionalized polystyrene (NPS) NPs with mesenchymal stem cells revealed that amino modification increases uptake rate. The predominant pathway has been identified as clathrin-mediated for NPS while PS NPs are internalized via clathrin-independent endocytosis [71]. In another study, the effect of polydopamine functionalization on aptamer-NP bioconjugates has been investigated for tumor targeting. It has been demonstrated that functionalized NPs achieve higher targeting efficiency and enhanced therapeutic effects [72].

2.6. Carbon Nanoparticles

Fullerenes are allotropes of carbon and form cage-like structures (~1 nm in diameter) via the connection of carbons with single or double bonds. The arrangement of the carbons in cylindrical shape results in the formation of carbon nanotubes (c.f. Figure 2.5). Carbon nanotubes can be open or closed-ended and are generally a few nanometers in diameter and micrometers to millimeters in length. Their unique molecular structure provides advantageous properties including high electrical and thermal conductivity and high tensile strength. There are several types of nanotubes based on their number of walls or chiral vectors. They can be single-walled CNTs or double-walled and multi-walled CNTs

consisting of nested SWCNTs [73,74]. Herein, we focus on the toxicity of fullerenes and CNTs to be used as drug-carrier agents.

In literature, it has been shown that carbon NPs can cross the cellular barriers [20,21] and has high adsorption capacity to host several biological entities like peptides, genes, and drugs [75–78]. However, they still suffer from undesirable toxic effects on biological systems. It has been reported that the toxicity of fullerenes is not only concentration or time-dependent but also affected by the type, functional groups, and administration method [79].

Previously, the insolubility of fullerenes in water and the consequent aggregation has been shown as the major factor contributing to their toxicity [23,26]. However, both pristine and functionalized fullerenes have been observed to accumulate at the cell membrane or reach the intracellular site [80,81]. Fullerenes exhibited no significant toxicity against alveolar macrophages up to a concentration level of 226 $\mu g/cm^2$ [82] and very low toxicity towards human macrophages [83]. One of the most important toxicity mechanisms behind fullerene exposure was associated with ROS formation [84] which leads to oxidative stress, inflammation, and lipid peroxidation [26]. Some studies showed that water-soluble fullerenes are more prone to free radical scavenging than pristine fullerenes [27,85,86]. In particular, hydroxylated fullerenes have been addressed as free radical scavengers to protect the cell against hydrogen peroxide-induced oxidative damage [87]. This antioxidant capability of fullerene derivatives also increased the lifespan of mice by quenching ROS [88].

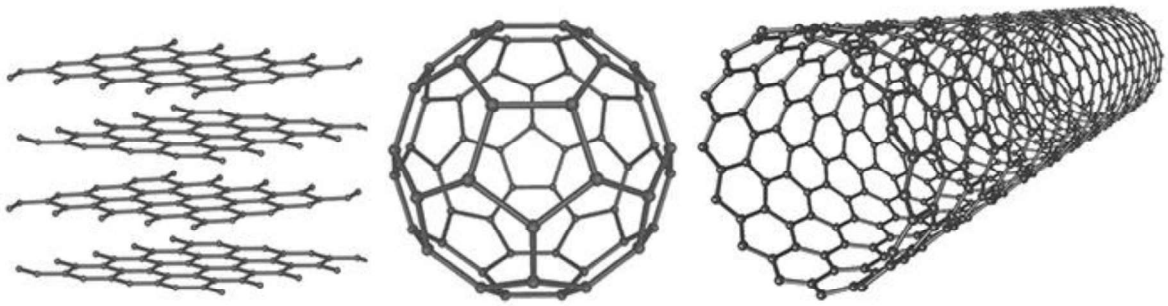

Figure 2.5. Graphene layers, a Buckminsterfullerene, and a single-walled nanotube from left to right [89].

Numerous studies have been recorded on CNT toxicity across different cell lines. The size of CNTs, especially the length, has shown a considerable effect on their toxicity. In vitro toxicity tests in rat alveolar macrophages revealed that relatively thick and long CNTs cause acute lung inflammation directly upon inhalation [90]. Long MWCNTs (20 μm) remarkably decreased cell viability and increased ROS formation in human alveolar macrophages as compared to shorter ones (0.6 μm) [91]. Similarly long (5-15 μm) and thick (20-60 nm) CNTs revealed DNA damage and inflammatory responses in A549 cell line [92]. On the other hand, several studies reported that thin MWCNTs are more toxic than thick ones [93,94] but opposite findings were also obtained depending on the cell types used [95]. To reduce cytotoxicity, CNTs have been functionalized with various groups including PEG and COOH. PEG-functionalized MWCNTs were found to be less toxic than carboxylated MWCNTs on macrophages. This was explained by the lower cellular uptake of PEG-modified MWCNTs which cause less activation of oxidative responses [96]. Greater uptake rates and less toxicity of carboxylated MWCNTs in comparison to unfunctionalized MWCNTs were further confirmed by different groups [97,98].

On the other hand, both covalent bonding of PEG and physical wrapping with PEGylated lipids resulted in improved circulation time in the bloodstream, lower toxicity, and more effective clearance [31–33]. Consequently, it has been noted that coating of SWCNTs with PEGylated branch polymers provided an ultralong blood circulation time of ~22 hr in mice [33]. PEG-modified SWCNTs used for the release of the anticancer drug cisplatin in mice showed lower toxicity with high dispersion [99]. Although the focus of the literature is on PEG modification, other polymers have rarely been used. SWCNTs modified with hexamethylenediamine and poly(diallyldimethylammoni-um)chloride allowed non-covalent binding of negatively charged siRNA and exhibited an efficient intracellular delivery with few cytotoxic effects on rat heart cells up to a concentration level of 10 mg/l [100]. The cytotoxicity of polystyrene (PS) coated MWCNTs were investigated *in vitro* in murine macrophages and *in vivo* in mice lung for 6 months period. Results demonstrated that PS coating decreases oxidative stress and inflammation in both and prevents pulmonary toxicity [38]. Despite their high solubility and dispersion [34,35] as well as improved mechanical properties [36,37], PS coated CNTs haven’t been used in drug delivery systems. To gain insight into the drug-carrier potential of PS functionalized CNTs, we performed atomistic and CG MD simulations within the scope of this thesis.

2.7. Meta-Analysis of Cytotoxicity of Nanoparticles

Exploratory and predictive computational approaches are complementary nanosafety assessment methods but are of great importance to understand the structure-to-function relationship of nanomaterials and how they interact with cells, organisms, and biological molecules. By correlating physicochemical properties of nanomaterials with toxicity endpoints, various Artificial Intelligence (AI) and ML tools have been implemented so far to obtain materials with desired properties [101]. Most of these studies consisted of Quantitative Structure-Activity Relationship (QSAR) models based on toxicity data of metals/metal oxides from *in vitro* studies. Although these models gain rising attention for safe-by-design of nanoparticles, they still face the challenge of material diversity, limited sampling within individual studies, lack of harmonization, and great heterogeneity of published data [7].

ML, which is a sub-category of AI, utilize data, algorithms, and statistical knowledge to develop analytical and predictive models. It can enable systems to learn and make predictions, identify patterns, and derive heuristics from large data sets. In the last two decades, various ML tools have been developed that seek to predict the toxicological properties of NPs. Among the most widely used ML applications in nanotoxicology, QSARs play a leading role. In addition to classical QSAR methods, nano-QSAR, quasi-QSAR, and perturbation-based QSAR techniques have emerged as promising tools [102].

The main characteristics of 64 ML studies conducted on nanomaterial toxicity are listed in Table 2.1. ML algorithms that have been implemented to predict or classify the cytotoxicity of nanomaterials in general consist of multiple linear regression (MLR), logistic regression (LR), tree-based algorithms, i.e., decision trees (DT), random forests (RF) etc., neural networks, linear discriminant analysis (LDA) and Monte Carlo (MC) schemes. Considering the frequency of use of these methods (c.f. Figure 2.6a), it is seen that RF and DT are mostly preferred methods and followed by MLR and MC schemes. Among the investigated nanomaterials, metal oxides (especially ZnO and TiO_2) form the vast majority and 55 of 64 studies cover the toxicity of metal oxides (c.f. Figure 2.6b). The pioneer cell types to which the NPs are exposed include Escherichia coli (E. coli) and the human epidermal keratinocyte cell line (HaCaT). On the other hand, toxicity endpoints of the

models rely on cellular viability, natural and negative logarithmic forms of EC_{50} and LC_{50} values, and lactate dehydrogenase (LDH) release. The details of these studies are explored in the next paragraphs.

From a historical point of view, ML applications in nanotoxicology first emerged in 2009. MLR analysis of a limited number of samples on the toxicity of metal oxides towards E. coli showed that there is a high correlation between the metal cation charge and toxicity. It has been reported that the lower the cation charge, the higher the toxicity of metal oxides [103]. Sayes and Ivanov utilized linear discriminant analysis (LDA) classification and multivariate linear regression to predict cytotoxicity in terms of LDH release which is an indicator of cell membrane disruption. Their dataset consisted of 42 samples of which 24 TiO_2 and 18 ZnO NPs were studied at different concentrations. The TiO_2 NPs were characterized by five feature descriptors which are engineered size, size in water, size in PBS, zeta potential, and concentration. For the ZnO NPs, size in the cell culture medium was also added to the parameters investigated. The LDA analysis of TiO_2 NPs yielded R^2 scores in the range of 0.70-0.77. The multivariate linear regression analysis of both NPs pointed out overfitting by showing the highest performance when all possible descriptors are used. Therefore, it was reported that either the dataset did not have enough data to make accurate predictions or other significant features were not included in the dataset to obtain better prediction models [104].

For classifying the toxicity of metal oxides on transformed bronchial epithelial cells (BEAS-2B), a nano-QSAR study was performed by using LR. Based on the toxicity endpoint of plasma membrane integrity loss, the best model performance was obtained using three (period of metal, atomization energy, and primary size of metal oxide) out of 14 physicochemical descriptors [105]. By measuring the cytotoxicity of several metal oxide and silica NPs in E. coli, Puzyn et al. developed an MLR model in combination with a genetic algorithm. Their model reliably predicted the pEC_{50} of all NPs tested as a function of one descriptor, namely enthalpy of formation of a gaseous cation [106]. The QSAR performance of the same dataset was further explored in a set of articles [107–113]. Toropov et al. tested the applicability of CORAL software [114] which relies on MC sampling to predict the NP toxicity and showed that pEC_{50} in E. coli can be predicted through CORAL with SMILES-based optimal descriptors [108]. Many studies have used CORAL in estimating the toxicity

of metal oxides [107,115–117], MWCNTs [118], nanozeolites [119], and silica [120], and obtained satisfactory results. However, Casano et al. compared the performances of CORAL and RF models on the cytotoxicity of silica NPs based on pseudo-SMILES descriptors and pointed out the failure of CORAL to capture the significance of aspect ratio and zeta potential which is implied by RF model [121].

Horev-Azaria et al. compared the *in vitro* cytotoxicity of cobalt NPs with cobalt ions by using six different cell lines from the lung, liver, intestine, kidney, and immune system. They employed a decision tree model (J48) where training and validation of the model are determined iteratively and found that concentration of cobalt NPs is of the highest importance while the type of cobalt or the cell line used is of the secondary importance on cobalt toxicity. Furthermore, it has been suggested that a larger database is required to make the model more generalizable [122]. For another QSAR study, the cytotoxicity of metal oxides on human BEAS-2B and murine macrophage (RAW264.7) cell lines were assessed through MTS, LDH, and ATP assays. By using tree-based classification and regression models, oxidative stress and acute pulmonary inflammation were related to the particle dissolution and band gap energy levels [123]. The same dataset was also modeled by excluding Fe_3O_4 with impurities that cause ambiguous physicochemical characterization, and NP toxicity class was predicted with SVM and LR with high accuracies of 94% and 90%, respectively [124].

The bioactivity of 44 iron oxide core-based NPs was classified through a Naïve Bayesian classifier depending on four descriptors: Primary size, zeta potential, spin-lattice, and spin-spin relaxivities. The nano-QSAR model produced larger than 78% accuracy with different combinations of the descriptors [125]. Another meta-analysis study that focuses on iron oxide NPs employed Bayesian Neural Networks to investigate smooth muscle apoptosis through different cells including endothelial and smooth muscle cells, hepatocytes, and monocytes [126]. Smooth muscle apoptosis was also used as an endpoint in addition to cell viability and pEC_{50} toxicity endpoints by Singh et al. Their data set consisted of 5 classes of NPs taken from *in vitro* toxicity experiments: 51 metals, 109 surface-modified metals, 17 metal oxides, 80 MWCNTs, and 48 fullerenes. Proposed nano-QSAR models via Decision Tree Forest (DTF) and Decision TreeBoost (DTB) based on gradient boosting and bagging algorithms resulted in high accuracies with rigorous validation [111]. The toxicity of carbon

nanotubes based on *in vivo* [127] and *in vitro* [128] literature has been further discussed in different ML articles. The length of the nanotubes correlated negatively with pulmonary toxicity, while the diameter was significantly positively correlated [127].

Gajewicz et al. carried out experiments to measure the toxicity of 18 metal oxide NPs across human keratinocyte cell line (HaCaT) and described their results by applying MLR with a genetic algorithm based on descriptors of Mulliken's electronegativity and enthalpy of formation of metal oxides [129]. They also developed a read-across model to predict the physicochemical properties and toxicological endpoints of untested metal oxides across E. coli and HaCaT cell lines [112] and showed that unknown properties or toxicities of NPs can be estimated by using known properties of structurally similar NPs [112,130,131]. Sizochenko et al. used an RF algorithm on the same data set by introducing the Liquid Drop Model (LDM) descriptors [132] in addition to electronegativity, van der Waals interactions, and metal-ligand binding characteristics of metal oxides [110]. They claimed that LDM can represent the significant properties of NPs like surface area or surface-to-volume ratio in a size-dependent manner avoiding high-cost quantum-mechanical calculations. Followingly, LDM-based descriptors were applied in other ML studies of the same group by RF [133] and partial least squares (PLS) algorithms on determining metal oxide toxicity [134].

A perturbation-based QSAR model, which overcomes validation requirements and lack of knowledge in the data set, was suggested to predict the toxicity of metals and metal oxides across several mammalian cell lines. A data set of 1681 nanoparticle-nanoparticle pairs was processed in the QSTR-perturbation model and the toxicity endpoint was predicted with larger than 93% accuracy [135]. The same group developed other perturbation models aiming to predict ecotoxicity and cytotoxicity endpoints of assorted NPs under different experimental conditions. For each nanoparticle pair out of 36488 pairs in total, four descriptors were considered: size, molar volume, polarizability, and electronegativity. The proposed model was shown to be very promising for predicting the cytotoxicity of Ag and $NiFe_2O_4$ [136]. In addition to physicochemical descriptors, 2D-topological descriptors were included in the unified perturbation model of Concu et al. via ANN. The QSTR-perturbation model resulted in higher than 97% accuracy when applied to 260 unique NPs [6]. Further, the genotoxicity of metal oxides obtained from different biological entities through *in vitro* Comet assay was investigated by the QSTR-perturbation model using physicochemical,

quantum chemical, and constitutional descriptors, as well as experimental conditions. Across a set of 78 unique NPs, a reliable model with high accuracy (> 96%) were obtained [137].

Oh et al. examined the toxicity of CdSe quantum dots (QDs) by using the meta-analysis of 307 papers involving 1741 cell viability-related data samples. By using the RF regression models, it has been shown that quantum dot toxicity is closely correlated with the size and surface properties of CdSe (including shell, ligand, and surface functionalization), the assay type used, and the exposure time [4]. The same group also developed Bayesian Network model based on their enlarged QD data set (3028 cell viability and 837 IC_{50} data from 517 papers). In addition to their previous findings, cell viability was correlated with QD concentration and their model generated association rules regarding QD toxicity [138].

Ban et al. utilized the RF model to screen the priority factors determining the reproductive toxicity of NPs. By extracting 10 qualitative and quantitative factors from 82 publications, a dataset of 250 samples was obtained. The nanoparticle type and exposure route were found as dominant factors for NP accumulation and reproductive toxicity had a high correlation with NP type and toxicity indicators (testosterone concentration, sperm parameters, and testis index). Moreover, it was observed that NPs involving major elements such as Zn or Fe induce lower toxicity than NPs containing noble metals [139].

ML studies involving the toxicity of organic NPs are very sparse in the literature. A QSAR study was proposed by Liu et al. on the toxicity of various metal, metal oxide, dendrimer, and polymeric NPs in embryonic zebrafish. Under physicochemical descriptors of 82 NPs with 656 *in vivo* experimental results, various algorithms (kNN, Bagging, M5P, KStar) were compared through their performances in predicting 24 hrs post-fertilization (hpf) mortality, and their case study exhibited high prediction accuracy on 24 hpf mortality and 12 hpf heart malformation [140]. Jones et al. investigated the toxicity of PAMAM dendrimers on Caco-2 cell line with various ML algorithms and identified the most important descriptors as size, charge, and concentration [141]. A more comprehensive data set was suggested by Labouta et al. which includes various inorganic, organic, and carbon-based NPs. They applied DT together with a feature selection algorithm on their data set which contains 2896 samples (collected from 93 studies) with 15 features. The primary predictor of nanoparticle toxicity was determined as material type, followed by concentration and size

of NPs, cell type, and toxicity test indicator. Also, it has been stated that the complexity and heterogeneity of previously published data, as well as the interdependency of possible significant attributes, make it difficult to generalize the toxicity behaviors of NPs [5]. Recently, we developed a rule-based ML model using ARM on the toxicity data set of a wide range of inorganic, organic, and carbon-based NPs with 4111 cell viability samples from 152 articles. Encoding the descriptors of material and cell properties, and experimental conditions, we found that toxicity is mainly related to the core and coating material of the NPs as well as their synthesis route. Also, we identified associations of features that result in high cell viability [9].

Most of the datasets of available meta-analysis studies have been generated by performing in vitro or in vivo toxicity tests of NPs or collecting/extracting toxicity data from the literature. Nevertheless, some studies used databases such as the S2NANO database [142] to obtain cell viability data of MWCNTs [118] or metal oxides [116,143–145]. Furthermore, Pravin et al. combined various databases NanoDESK [146], eNanoMapper [147], NANoREG [148] and published literature to form their data set [149].

Table 2.1. Key features of meta-analysis studies developed to predict/classify the cytotoxicity of nanoparticles in chronological order.

ML Algorithm	**Nanoparticle Type**	**Toxicity Endpoint**	**Cell Type**	**Year**	**Ref.**
MLR	Metal oxides	LD_{50}	E. coli	2009	[103]
MLR, LDA	TiO_2 and ZnO	LDH Release	immortalized rat L2 lung epithelial cells and rat lung alveolar macrophages	2010	[104]
LR	Metal oxides	Plasma-Membrane Leakage	Transformed BEAS-2B	2011	[105]
MLR	Metal oxides	$\log(1/EC_{50})$	E. coli	2011	[106]
DT	Cobalt	Cell Viability	Caco-2, MDCK, HepG2, A549, NCIH441, Primary mouse dendritic cells	2011	[122]

Table 2.1. Key features of meta-analysis studies developed to predict/classify the cytotoxicity of nanoparticles in chronological order (cont.).

MC	Metal oxides	log(1/EC_{50})	E. coli	2012	[108]
DT	Metal oxides	Cell Viability, LDH Release, ATP Level	RAW 264.7, BEAS-2B	2012	[123]
kNN, Bagging, DT, K-Star	Metals, metal oxides, dendrimer, and polymeric materials	24 hrs Post Fertilization Mortality	Embryonic zebrafish	2013	[140]
NBC, LR, LDA, kNN	Iron oxide	Bioactivity	aorta endothelial, vascular smooth muscle, hepatocyte, monocyte/macrophage	2013	[125]
NBC, MLR, LDA, LR, SVM	Metal oxides	Cell Viability, LDH Release, ATP Level	RAW 264.7, BEAS-2B	2013	[124]
LDA	Metals and metal oxides	CC_{50}, EC_{50}	RAW264.7, A549	2014	[136]
LDA	Metals and metal oxides	TC_{50}	A549, HepG2	2014	[135]
MLR	Metal oxides	log(1/LC_{50})	E. coli	2014	[113]
ANN	Iron oxides (CLIO)	Smooth Muscle Apoptosis	endothelial and smooth muscle cells, monocytes, hepatocytes	2014	[126]
RF	Metal oxides	log(1/LC_{50}), log(1/EC_{50})	E. coli, HaCaT	2014	[110]
DTF, DTB	Metals, metal oxides, MWCNTs, fullerenes	Smooth Muscle Apoptosis, Cell Viability, log(1/EC_{50})	Mixed	2014	[111]

Table 2.1. Key features of meta-analysis studies developed to predict/classify the cytotoxicity of nanoparticles in chronological order (cont.).

DT, RF	Carbon nanotubes	Neutrophils, Macrophages, LDH, total protein	Mice, rat	2014	[127]
MLR, PLS	Metal oxides	$\log(1/EC_{50})$	E. coli	2014	[109]
MLR, SVM, ANN	TiO_2 and ZnO	LDH Release	immortalized rat L2 lung epithelial cells, rat lung alveolar macrophages	2015	[150]
MLR	Metal oxides	$\log(1/LC_{50})$	HaCaT	2015	[129]
MC	Metal oxides	$\log(1/LC_{50})$	E. coli	2015	[115]
Read-across	Metal oxides	LC_{50}, EC_{50}	E. coli, HaCaT	2015	[112]
NBC, SMO, DT, RF, Bagging, *	PAMAM dendrimers	Cell Viability	Caco-2	2015	[141]
RF	Metal oxides	Cell Viability	RAW 264.7, BEAS-2B	2015	[133]
MLR, ANN	ZnO	Cell Viability, LDH Release, Oxidative Stress	HUVECs, HepG2	2016	[151]
kNN, RF, SVM	Carbon nanotubes	Cell Viability	THP-1 macrophages	2016	[128]
MLR	Metal oxides	$\log(1/EC_{50})$	E. coli	2016	[152]
RF, MC	Silica	$\log(1/EC_{25})$	THP-1, 16HBE, A549, HaCaT, NRK-52E	2016	[121]
MC	Metal oxides	$\log(1/LC_{50})$, $\log(1/EC_{50})$	E. coli, HaCaT	2016	[107]
DT	Metal oxides	Cell Viability, LDH Release, ATP Level	RAW 264.7, BEAS-2B	2016	[153]
MC	Silica	Cell Viability	HEK293	2016	[120]
RF	Quantum dots	Cell Viability, IC_{50}	Mixed	2016	[4]

Table 2.1. Key features of meta-analysis studies developed to predict/classify the cytotoxicity of nanoparticles in chronological order (cont.).

ANN	Metals and metal oxides	CC_{50}, LC_{50}, EC_{50}	RAW 264.7, A549, Danio rerio (embryos), Pseudokirchneriella subcapitata	2017	[6]
ANN	Metal oxides	$\log(1/EC_{50})$	E. coli	2017	[154]
LR	Metals and metal oxides	Toxicity class	RAW 264.7, BEAS-2B	2017	[155]
Read-across	Metal oxides	$\log(1/LC_{50})$, $\log(1/EC_{50})$	E. coli, HaCaT	2017	[130]
Read-across	Metal oxides	$\log(1/LC_{50})$, $\log(1/EC_{50})$	E. coli, HaCaT	2017	[131]
Gaussian	TiO_2-based	EC_{50}	Chinese hamster ovary cells (CHO-K1)	2017	[156]
BN	Metals, metal oxides, cellulose	Cell Viability	Mixed	2017	[157]
RF	Metal oxides	$\log(1/LC_{50})$, $\log(1/EC_{50})$	E. coli, HaCaT	2017	[158]
MLR	TiO_2-based	$\log(1/EC_{50})$	Chinese hamster ovary cells	2018	[159]
MC	Nanozeolites	Cell Viability	HeK293, HeLa	2018	[119]
MC	MWCNTs	Cell Viability	BEAS-2B, 16HBE14o-, WI-38, HBE	2018	[118]
MC	Gold	EC_5, EC_{10}, EC_{50}, HED	hepatocytes, HUVEC, HRPTEC, keratinocytes	2018	[160]
RF	Metal oxides	Cell Viability	Mixed	2018	[143]
RF	Metals, metallic alloys, metal oxides, MWCNTs, graphene oxide	Reproductive toxicity, accumulation	Male rodents	2018	[139]

Table 2.1. Key features of meta-analysis studies developed to predict/classify the cytotoxicity of nanoparticles in chronological order (cont.).

LR, SVM, RF, ANN	ZnO, TiO_2, SiO_2, Fe_3O_4, Al_2O_3, CuO, and Fe_2O_3	Cell Viability	Mixed	2018	[144]
DT	Inorganic, organic and carbon-based	Cell Viability	Mixed	2019	[5]
BN	Quantum dots	Cell Viability, IC50	Mixed	2019	[138]
MC	Metal oxides	Cell Viability	BEAS-2B, HaCaT	2019	[116]
BN	Ag, Au, Polymeric NPs, CuO, ZnO, TiO_2, SiO_2, Fe_2O_3, Polystyrene NPs, $CoFe_2O_4$	Cellular Effects	Mixed	2019	[161]
PLS, DT	SiO_2, TiO_2, CeO_2, AlOOH, ZnO, $Ni(OH)_2$	LDH Release	RAW 264.7	2019	[162]
PLS	Metal oxides	$\log(1/LC_{50})$, $\log(1/EC_{50})$	E. coli, HaCaT	2019	[134]
kNN	Metal oxides	Cell Viability	RAW 264.7, BEAS-2B	2020	[145]
MC	Metal oxides	LC_{50}	A549	2020	[117]
AutoML (LR)	SPIONs	Cell Viability	Stem Cells	2020	[163]
RF	FeO, SiO_2, TiO_2, Ag, CuO, ZnO, GO, MnO, SWCNT	Cell Viability	Brain tissue	2020	[164]

Table 2.1. Key features of meta-analysis studies developed to predict/classify the cytotoxicity of nanoparticles in chronological order (cont.).

DT, SVM, LR	Metal oxides	Fold change in Interleukin-1β ($log_2(FC_{IL-1\beta})$)	THP-1	2020	[165]
LDA, RF	Metal oxides	Cell Viability, DNA in the tail	Mixed	2020	[149]
LDA	Metal oxides	Genotoxicity	Mixed	2020	[137]
LDA, NB, LR, SMO, AdaBoost, DT, RF	Metal oxides	EC_{50}	E. coli	2021	[166]
RF	Graphene	Cell Viability, IC_{50}, LDH Release	Mixed	2021	[167]
DT, RF	Silver	Cell Viability	Mixed	2021	[168]
ARM	Inorganic, organic and carbon-based	Cell Viability	Mixed	2021	[9]
DT	ZnO	Cell Viability	Mixed	2022	[169]

ANN: Artificial Neural Network, ARM: Association Rule Mining, AutoML: Automated Machine Learning, BN: Bayesian Network, DT: Decision Tree, DTB: Decision Treeboost, DTF: Decision Tree Forest, kNN: k-Nearest Neighbor, LDA: Linear Discriminant Analysis, LR: Logistic Regression, MC: Monte Carlo, MLR: Multiple Linear Regression, NBC: Naïve Bayesian Classifier, PLS: Partial Least Squares, RF: Random Forest, SMO: Sequential Minimal Optimization, SVM: Support Vector Machine. *Other ML tools.

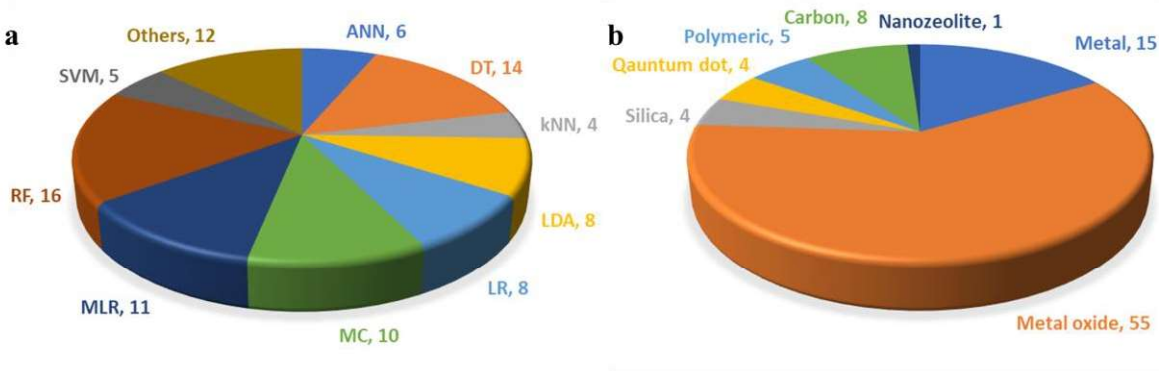

Figure 2.6. Number of (a) machine learning models developed to predict/classify the cytotoxicity of nanomaterials, (b) nanomaterial type used in the developed machine learning models.

2.7.1. Limitations and Challenges

The difficulties faced by the proposed models can be grouped under three general headings: heterogeneity, knowledge gaps, and lack of standardization [4,5,127].

- Diversity, purity, and synthesis methods of NPs, toxicity indicators, measured physicochemical properties, measurement techniques, and parameters differ from study to study and create a great variation. There is still an ongoing effort to deal with the heterogeneity of the published literature.
- Not all of the selected toxicity descriptors can be accessed in the articles or databases. While some models can handle missing data (e.g. QSAR-perturbation, ARM etc.), most ML tools (especially regression-based) fail to work with data gaps. In this regard, (i) various replacement/imputation techniques, e.g., mean/median value imputation, regression-based imputation, similarity-based replacement, are used, (ii) the data set is divided into small sub-sets or (iii) the samples with a data gap are excluded from the model [143].
- There are no standard testing protocols while determining the properties such as size or zeta potential of NPs. Mostly the NP size is classified as core size, primary size, and hydrodynamic size. Core/primary size can be measured by SEM or TEM while the hydrodynamic size and zeta potential can be measured by DLS in different mediums such as distilled water, salt water, or cell medium at different temperatures. Since NPs

interact with the molecules that are present in the medium, their dispersion and aggregation behavior change with respect to the structure of molecules that they interact with or the environmental conditions.

Furthermore, collinearity between descriptors and class imbalance in toxicity endpoints can become a challenge in ML models. In the regression-type analysis, the toxicity features should be independent of each other, therefore, a correlation between variables should be identified to remove the collinearity problem which reduces the reliability of models. If correlated variables are identified, the one with the higher correlation with the endpoint is selected in the development of the model. Then, a feature selection algorithm may be implemented to optimize the performance of the model [170]. In classification-type analysis, class imbalance may arise if the number of samples in one toxicity class is much larger than the samples in another toxicity class. Thus, the major class is predicted with high accuracy while the minor class prediction fails. This may be eliminated with some techniques such as random sampling [144,161].

2.8. Nanoparticle-Membrane Interactions by MD Simulations

How nanoparticles cross and interact with biological membranes and what their toxicity mechanisms are is not yet well understood. In this regard, experimental studies cannot show the required resolution to explain the translocation and distribution of NPs across membranes. Therefore, computational approaches, i.e., MD simulations, have been adopted to determine the energetics and distributions of NPs through cell membrane models. Atomistic simulations have provided important information with high resolution but have not been able to reflect the realistic size and complexity of biological systems due to high simulation costs. To improve the time and length scales of systems by moving beyond the traditional atomistic models, CG molecular modeling has been developed with lower resolution. Thus, large system sizes and simulation timescales have become accessible at the expense of losing some molecular detail [15]. Studies including both methods will be summarized followingly. Since the focus of this study is carbon-based NPs, fullerenes and carbon nanotubes will be investigated under two subheadings after cell membrane models.

2.8.1. Cell Membrane Models

In literature, developed membrane models mainly consist of single DOPC, POPC, or DPPC lipids or their mixture in the presence and absence of cholesterol (CHOL). The most complex cellular membrane model was proposed by Ingolfsson et al. to represent an idealized mammalian plasma membrane. By using CG MD simulations with 63 different lipid types, they obtained a detailed molecular view of lipid organization. Their plasma membrane model did not exhibit phase separation or domain formation but a heterogeneous mixture of lipids. The asymmetrical nature of the membrane was cholesterol-rich in the outer leaflet with nanodomains of gangliosides while phosphoinositides are clustered in the inner leaflet. Characterization of PM lipids in terms of the order parameter, diffusion rates, and local environment gave insight into the functional roles of lipids. With this study, it has been seen that more realistic membrane models can be developed via embedding proteins, which form a large fraction of a real plasma membrane [171].

Later, Ingolfsson et al. extended their average plasma membrane model by developing a complex neuronal plasma membrane model. Although they used remarkably different lipid compositions, the characteristics of the models showed high similarities in terms of average bilayer properties. This was attributed to the increased tail unsaturation in balance with a higher cholesterol content. On the other hand, it was observed that the size and duration of domains change depending on the lipid composition (Brain or Average) and bilayer undulations. Furthermore, it was reported that the lipids in the Brain mixture diffuse and flip-flop slower and the variation of properties is greater in the lower and upper leaflets of the Brain plasma membrane [172].

Koldso et al. proposed mammalian plasma membrane models consisting of asymmetrically organized lipids and transmembrane (TM) proteins. They introduced compartments at various degrees of restraints within the membrane models and showed that compartmentalization caused by cytoskeletal immobilization reduces the mobility of lipids and proteins. Thus, the dimerization of protein within the membrane and hopping of membrane proteins between compartments diminished as well [173].

The effect of cholesterol flip-flop on domain registration has been studied by Thallmair et al. by using ternary and quaternary lipid mixtures in addition to the plasma membrane model developed by Ingolfsson et al. They have found that cholesterol plays an important role in signal transduction across the leaflets by populating the interleaflet space. Moreover, they have pointed out that cholesterol can transfer local density gradients rapidly by the alignment of transient domains [174].

2.8.2. Interactions of Fullerenes with Lipid Membranes

There are several studies carried out on the interactions and energetics of fullerene NPs across lipid bilayers in the literature. The AA fullerene models used are mostly based on the parameters suggested by Girifalco [175], while the CG fullerene models are based on Monticelli et al. [176].

First, Qiao et al. calculated the free energy of a C_{60} and its hydroxyl-derivative ($C_{60}(OH)_{20}$) with respect to the distance from the center of the DPPC bilayer. It was observed that an energetically favorable location is at the interior of the bilayer (~1.1 nm from the center of the bilayer) for C_{60} but the water-lipid interface for $C_{60}(OH)_{20}$. Since the area increased when C60 penetrated the bilayer, the toxicity of fullerene was associated with the membrane leakage caused by microphore formation [177]. However, this interpretation was denied since fullerene molecules are hydrophobic and there is no evidence that water molecules are presented in the hydrophobic core of the membrane [178].

Li et al. investigated the interactions of two C60 molecules inside DMPC bilayer and in tridecane by AA simulations. According to PMF calculations, the preferred position of a single C60 was determined at 0.6-0.7 nm distance from the center of the bilayer. This was explained by the strong dispersion interactions in the denser regions of the membrane. On the other hand, placing fullerene close to the water-membrane interface region created a higher free energy barrier as it causes a large distortion in lipid headgroups. Furthermore, the interaction energy between the fullerene pair as a function of separation distance was found less favorable in DMPC than in tridecane because of the perturbation of the lipid bilayer structure [179]. The same group also reported that the transport of C60 from bulk water to the membrane core is of no free energy barrier and the decrease in free energy as

C60 passes through the headgroups is due to the stronger dispersion interactions between C60 and the bilayer than those between C60 and water molecules. Thus, weakening the strength of the dispersion interactions of fullerenes with the surroundings created a higher free energy barrier to penetrate the lipid headgroups [12].

Using experimental partitioning data of fullerenes in polar and organic phases, Wong-Ekkabut et al. developed a CG model [180]. They represented a 60 carbon fullerene molecule with 16 beads by applying an approximately 4:1 mapping strategy. Thus, the speed of simulations increased by about 800 times that of AA simulations, enabling simulations at the microsecond time scale [178]. In this way, they observed the aggregation behavior of fullerenes and found that fullerenes rapidly form clusters in the water phase and disintegrate in the bilayer at hundreds of nanoseconds. Although insertion of fullerenes causes small distortions, it did not lead to membrane damage even at high fullerene concentrations [180]. Another CG approach based on approximately 4:1 mapping of carbon atoms [181] was adopted by D'Rozario et al. to compare the permeation energetics of fullerene and its hyroxyl- derivatives through a DPPC bilayer. They replaced the apolar carbon beads with 5, 10, 15, or 20 polar-type beads to describe the hydroxylated fullerenes. Predictably, fullerenes with less polarity are partitioned into the bilayer while the ones with high polarity adsorbed on the bilayer surface [182].

Chang et al. studied the clustering of fullerenes across DMPC bilayer by atomistic simulations. Similar to Wong-Ekkabut et al., they observed aggregation of fullerenes in the aqueous phase and dispersion inside the bilayer. This was attributed to the bilayer thickening effect of fullerenes. Once fullerenes are internalized, the thickness of the bilayer increases and generates room for the motion of fullerenes. Consequently, increasing the concentration of fullerenes resulted in faster dynamics inside the bilayer compared to that in the water phase [183]. Zhang et al. identified two mechanisms for the self-assembly of fullerenes: (i) self-assembly of fullerenes is completed before their penetration, (ii) self-assembly of fullerenes overlaps with their penetration through the membrane. Their simulations showed that not only single fullerenes but also small aggregates of fullerenes can be inserted into the DOPC membrane by creating local changes in the membrane structure. The favorable position inside the membrane was found about 1.0 nm from the center plane [184], in parallel to previous studies [177,179]. This work is important in terms of characterizing the stacking

modes of fullerene clusters such as equilateral triangle, tetrahedron, trigonal bipyramid, and octahedron for 3, 4, 5, and 6 clusters of fullerenes [184]. Clustering of fullerenes was further studied by different groups through CG simulations [185–188]. Barnoud et al. observed fullerene aggregation in alkanes and POPC bilayer by both AA and CG simulations. It was reported that aggregation of fullerenes is an entropy-driven process but lipid membranes reduce this tendency of fullerenes because of the enthalpic costs. Thus, similar to Li et al. [179], dimerization of fullerenes was found to be more favorable in alkanes than in lipid bilayer. Membrane density, which depends on the composition of the bilayer, and perturbation of lipid membrane structure were important factors in this enthalpic burden [185].

Xie et al. reported that the initial aggregation states of fullerenes determine their interactions with the bilayer. Small fullerene clusters increased the membrane area and thickness while large fullerene clusters reduced the area due to the protrusion of lipids. They also showed that in the presence of large fullerene clusters transmembrane movement of lipids causes the symmetry of the bilayer to be broken [186]. Nalakarn et al. performed a clustering study through DPPC, DOPC, and POPC membranes and explained the effect of lipid saturation on fullerene aggregation. Due to the enthalpic contributions, fullerenes formed clusters in the saturated membrane, however, in the unsaturated membrane, the dominant effect of entropy caused fullerenes to disperse [188]. A similar study has been conducted on fullerene clustering inside various saturated and unsaturated lipid membranes and the same conclusion were drawn [189].

Functionalized fullerenes have been explored in some studies. Kraszewski et al. investigated the uptake route of amino-functionalized C60 molecules by POPC membrane. They demonstrated that charged amino groups bind to the lipid headgroups while the non-functionalized side of the fullerene interacts with the hydrophobic core of the membrane. Furthermore, they reported that increasing amino functionalization added a hydrophilic character to fullerenes, and therefore, deprotonation of the amino group is required for their full translocation. Nevertheless, fullerenes have been addressed as suitable drug-carrier agents since they facilitated the uptake of cationic groups [190]. Tri-malonyl-functionalized amphiphilic derivatives of fullerenes have been studied by Bozdaganyan et al. through DPPC membrane. The free energy minimum of pristine C60 has been found at 0.7-0.8 nm from the

bilayer center as in line with previous literature. They also confirmed that both single C60 and oligomers of C60 spontaneously diffuse into the membrane core and remain inside during the simulation. On the other hand, amphiphilic derivatives of C60 couldn't penetrate the bilayer but were adsorbed at the surface of the bilayer [191].

The effect of surface modification of fullerenes was further studied by Mohammadyani and Modarress [192]. They determined the favorable location of pristine fullerene as the central region of the bilayer, by confirming previous PMF results [12,179] and suggested the optimal hydroxyl group number as four for the transport of fullerenes across DPPC [192]. Hydroxyl modification of fullerenes was also studied by AA simulations [193] and it was shown that fullerenes with <=2 number of hydroxyl groups penetrate the hydrophobic region of the DMPC membrane while with >=8 number of hydroxyl adhere onto the bilayer surface. Therefore, the optimal number of hydroxyl groups was suggested as 6 to cross the cell membrane and reach the interior of the cell. However, it should be noted that the difference between the two studies can be sourced from the different calculation methods and membrane structures.

Sun and Gu explored the cholesterol effect on the translocation of single pristine fullerene across the DPPC bilayer. At increasing concentrations of cholesterol between 0-50%, equilibrated positions of fullerenes increased in the z-direction and it was shown that the more the cholesterol concentration the less the permeability coefficient of the fullerene due to the condensing effect of cholesterol [194]. Alves et al. further studied the effect of cholesterol on fullerene translocation across DOPC membrane with three different cholesterol concentrations between 10-30%. Similarly, they found that cholesterol increases the rigidity of the membrane and the required force for fullerene insertion. This effect was reported to be more pronounced with a 30% cholesterol concentration [195].

Sridhar et al. observed the effect of temperature in addition to the concentration and polarity of the fullerenes by CG simulations. They reported that pristine fullerene locate close to the DSPC bilayer center but as polarity increases, they tend towards the lipid headgroups. They found that the more the polarity of fullerenes, the longest the residence time passed in aqueous water site. These trends were also reproduced with AA simulations with a larger residence time in the water than those obtained with CG simulations.

Furthermore, the temperature influenced the pristine and half-polar (Janus) fullerene in different ways: the residence time of pristine fullerene in water has a positive correlation with temperature while that of Janus has an opposite correlation. They drew attention to two problems that are frequently encountered: (i) pristine fullerenes cannot come out after entering the membrane and (ii) fullerene with polar groups cannot fully penetrate the membrane. To overcome these challenges, they suggested (half-polar) Janus fullerenes as promising drug delivery agents and showed that complete migration can be achieved by Janus NPs [196]. Recently, we explored the peroxidation degree of DOPC and POPC lipids as well as the polarity and concentration of fullerenes across lipid bilayers. We observed that lipid peroxidation is not the likely mechanism of fullerene toxicity in terms of disruption of membrane integrity. Moreover, we identified the preferred locations of fullerenes and their polar derivatives in pure and peroxidized lipid bilayers. Contrary to Sridhar et al., we couldn't obtain complete migration of Janus NPs across investigated membrane types [197].

It is seen that the membrane models developed in fullerene MD studies are generally composed of single or binary lipids. However, a more realistic membrane model which represents the skin bilayer has been proposed using an equimolar mixture of ceramides, cholesterol, and fatty acids. Their unconstrained MD simulations demonstrated that at low concentrations of fullerenes, penetration occurs within a few microseconds while at high concentrations, large clusters of fullerenes can not disperse in the membrane interior even after 12 μs simulation time. Thus, the permeation process of fullerenes was associated with their concentration level and explained by the thermodynamics and diffusivity of fullerenes. Moreover, lower concentrations of fullerenes did not alter the bilayer properties, such as area per lipid, bilayer thickness, and order parameter, in a significant manner but higher concentrations of fullerenes cause undulations [198].

Sastre et al. investigated the interactions of fullerenes with different membrane models including single, binary and ternary lipids. The change in lipid saturation and fullerene concentration as well as the presence of cholesterol resulted in different behaviors of fullerenes. In unsaturated DUPC lipid, fullerene molecules rapidly penetrated the bilayer while in monounsaturated POPC and saturated DPPC membranes translocation took longer times due to the high internal ordering and compactness of saturated lipids. Since the introduction of cholesterol increases the membrane compactness, adsorption of fullerenes in

cholesterol-including membranes occurred at longer times. Cholesterol flip-flop which is more pronounced in DUPC membrane was blocked by the increasing concentrations of fullerenes as they occupy central regions of the bilayer and reduce the hydroxyl density. Additionally, fullerenes were observed to alter the structural and dynamic properties of membranes and promote phase segregation and alignment of domains by concentrating on the disordered hydrophobic domains of the bilayer [199].

The partitioning of fullerene from water to the lipid bilayer was investigated in various studies. The free energy minimum of a single fullerene in DMPC membrane interior was reported as ~92 kJ/mol [12] and ~35 kJ/mol [177] while in DOPC it was reported as ~110 kJ/mol [180] and ~80-90 kJ/mol [200]. The difference between free energy values can be sourced from the different force fields used in these studies. The free energy minimum in the DPPC membrane was found to be ~198 kJ/mol [182] while in the DSPC membrane as ~115 kJ/mol [196]. The free energy minimum in the POPC bilayer was estimated as ~80 kJ/mol [176] by both AA and CG simulations. We also calculated the free energy minima in DOPC and POPC as ~110 kJ/mol and ~90 kJ/mol [197], respectively in consistent with the literature.

Table 2.2. Free energy of transfer of a single fullerene molecule from bulk water into the lipid bilayer. The equilibrium distance is the distance between the COM of the fullerene and the center of the bilayer at the position where the free energy is minimum.

Lipid Bilayer Type	**Equilibrium Distance (nm)**	**ΔG (kJ/mol)**	**Ref.**
DMPC	1.1	-35	[177]
DMPC	0.6-0.7	-92	[12]
DOPC	1	-110	[180]
DOPC	0.7	-80	[200]
DOPC	1.1	-110	[197]
DPPC	0-1	-198	[182]
DSPC	0	-115	[196]
POPC	AA:0.8, CG:1.1	-80	[176]
POPC	1	-90	[197]

2.8.3. Interaction of Carbon Nanotubes with Lipid Membranes

Lopez et al. showed the insertion mechanism of SWCNTs terminated by hydrophilic groups in two steps: (i) adsorption of the nanotube on membrane surface in parallel alignment with the water-membrane interface, (ii) spontaneous orientation to a transmembrane configuration in which the hydrophilic ends of the nanotube interact with hydrophilic headgroups. The second step was observed to be promoted by the chaperone lipids by coating the hydrophilic terminals of the nanotube with the lipid headgroups. Thus, chaperone lipids are transported to the opposite leaflet of the bilayer by transbilayer movement with the nanotube [201]. It was noted that the transmembrane configuration of the nanotube is suitable for use as channels or nanosyringes in drug delivery systems [202].

Gan and Chen studied the effect of CNT size on the bulk modulus of a POPC lipid bilayer. They found that the bulk modulus does not increase monotonically with the increase in the length of the nanotube. This was explained by the attraction-repulsion forces between the nanotube and the bilayer [203]. The size effect on the penetration of nanotubes into DPPC was investigated by different groups [181,204]. Wallace and Sansom changed the diameters of SWCNTs between 1.4 – 6.1 nm and pulled them through the bilayer at velocities between 0.5 – 50 nm/ns. At higher rates of penetration velocity, fewer lipids blocked the inner surface of the nanotube. However, all CNTs were coated by the lipids from both inner and outer sides, especially from the leaflet on the exit site. Only CNTs with 5 and 6.1 nm in diameter had partially blocked by the lipids but also a column of water. Moreover, they reported that the force required to extract the nanotube from the bilayer is larger in the parallel alignment of the nanotube to the bilayer plane than in oblique (45°) or vertical alignment. This was associated with the higher perturbation i.e., deformation of lipid membrane in the former case [181]. Shi et al. also studied how nanotubes of different sizes enter the bilayer. They used SWCNTs in the 1-1.5 nm diameter range and MWCNTs in the 2-10 nm diameter range at the same length of 6 nm and found that the uptake mechanism of CNTs is size-dependent. While thin nanotubes directly diffuse into the cells, thick nanotubes were observed to be wrapped by the lipids and the transition between two entry routes was explained by a critical radius of ~1.5 nm which is obtained through integrating a theoretical model with MD results [204].

The interactions of CNTs with lipid membranes were investigated in the presence of cholesterol in some studies [205–207]. Steered MD simulations were performed with CNTs, of 1 nm in diameter and 2 nm in length, through POPC and POPC with cholesterol. They calculated the forces and the free energy barrier to puncture the membranes and found that neither forces nor free energies change significantly in POPC with 30% cholesterol compared to that of POPC [205]. Similarly, Raczynski et al. conducted a steered MD study on the nanoindentation process of CNTs through DMPC/CHOL bilayer. Contrary to previous studies, they used open-ended and capped CNTs of 1.34 nm diameter and 6 nm length in the armchair configuration. Their results showed that the insertion of capped nanotubes requires a lower free energy barrier and open-ended CNTs lead to larger deformations on the membrane structure because of the entrainment of lipids. Nevertheless, no permanent damage was identified in the membrane structure for both models [206]. The same group also carried out a steered MD study on nanoindentation and extraction of open-ended CNTs by changing the diameter between 0.7-1.5 nm. Membrane damage was determined to be higher at the high speed of indentation but lower at the high speed of extraction. It was also observed that CNTs have a greater tendency to extract cholesterol than DMPC, however, no matter how many lipids are removed, the system returned to equilibrium at a maximum of 12 ns [207].

The interaction of functionalized CNTs with lipid bilayers has been covered by many studies [208–215]. Kraszewski et al. studied the insertion of pristine and amino-functionalized CNTs into the POPC bilayer [208]. They supported the direct permeation of short CNTs (5 nm in length) through the membrane by confirming previous studies and proposed three steps for CNT insertion: (i) landing on the membrane surface, (ii) penetration to the lipid headgroups, (iii) sliding to the core of the membrane. This nanoneedle-like insertion process was confirmed later with experimental findings [210] and did not change depending on the functionalization or whether CNT is open-ended or closed-ended, but the increasing density of functionalization increased the penetration angle with respect to the bilayer plane [208]. Based on MD simulation results, the same group generated a Monte Carlo model to explore the internalization of CNTs by a lipid bilayer as a function of their length. They demonstrated that the insertion of CNTs is driven by hydrophobic interactions and short CNTs have a stronger affinity to penetrate the bilayer passively [209].

Lee developed functionalized SWCNTs (1.4 nm in diameter and 20 nm in length) by wrapping them either with lipids or PEGylated lipids. It was noted that hydrophobic interactions dominate the insertion of CNTs into bilayers, however, wrapping of CNTs with charged lipids or long hydrophilic PEG chains (M_w =2 kDa) hinders the insertion process despite their electrostatic interactions with lipid headgroups. Moreover, it was shown that although pristine CNTs aggregate, lipid-wrapped CNTs partially aggregate, and CNTs wrapped with PEGylated lipids disperse [212]. The comparison of covalent and non-covalent PEG conjugation of SWCNTs revealed that covalently functionalized CNTs bind to the membrane surface but can not insert into the bilayer while the noncovalently coated CNTs penetrate inside the bilayer since PEGylated lipids separate from the nanotube and blend with membrane lipids. On the other hand, coated CNTs form aggregates that can not be easily excreted through renal paths consistent with the experiments [213]. By using lipid-coated CNTs, a vertical channel was tried to be developed as a function of lipid coating density and CNT length and it was suggested that repulsion forces between coating lipids and membrane lipids can prevent CNTs from being fully inserted into the membrane [214]. Another study on lipid-coated CNTs of 10 nm length showed that the free energy barrier to penetrate the bilayer increases with increasing number and density of lipid-coating [215].

Baoukina et al. investigated the interactions of pristine and functionalized closed-end CNTs of different sizes with lipid bilayers. Short and hydrophobic CNTs oriented parallel to the bilayer plane after they are internalized but cap functionalized CNTs adopted a tilted configuration. As the hydrophobic length of the nanotube increased, the tilt angle between the center-of-mass of the tube and bilayer normal increased. Furthermore, the penetration of CNT aggregates consisting of four and 16 monomers was observed. While the former adopts a parallel alignment with respect to the bilayer plane inside the bilayer, the latter did not enter the bilayer [211]. Gao et al. confirmed that pristine CNTs can spontaneously enter the membrane and stay in the hydrophobic region of the membrane if their length is less than the bilayer thickness. However, contrary to previous studies, they claimed that there is no specific orientation of CNTs inside the bilayer. On the other hand, they observed that hydroxyl-modified CNTs stand perpendicular to the bilayer plane owing to the electrostatic forces between hydroxyl groups of CNTs and lipid headgroups. Thus, functionalized CNTs have been addressed as suitable carriers of small molecules such as CO_2 by connecting the extracellular and intracellular sides of the membrane [216].

Parthasarathi et al. embedded the pristine closed-end CNTs of ~6 nm in length into the DOPC bilayer and observed the effect of embedded single and bundle of CNTs on membrane structure. Their AA simulations showed that the presence of CNTs reduce lipid mobility and perturb the interfacial water structure [217]. The perturbation of membrane was associated to the size and type of the nanotube [218]. Vögele et al. also studied the interactions of embedded pristine CNTs and their polar derivatives using AA and CG simulations. They found that CNT chirality and the degree of polarity of functional groups at the end ring of CNTs has no effect on the interactions with lipid acyl tails, however, the latter significantly influence water permeability and the interactions with lipid headgroups. They also confirmed that longer tubes have higher tilting angles with respect to the normal of the bilayer compared to short CNTs and polar functional groups inhibit the tilting of CNTs [219].

2.8.4. Limitations and Challenges

Although MD simulations provide understanding at the molecular level that experimental studies cannot reach, they have some difficulties and limitations [15]:

- Atomistic simulations present the highest level of molecular detail, however, they are limited by time and length scales of μs and nm due to the high computational cost. Therefore, they can not reflect the complexity of cellular membranes and do not allow us to observe long-lasting biological processes. Consequently, proposed membrane models are limited in terms of lipid diversity and surface area while NP sizes (max. 20 nm) do not cover the ranges tested on the experimental scale.
- Coarse-grained simulations provide the access to tens of μs time and tens of nm length scales by allowing the simulations of large and complex systems. However, losing atomistic detail results in approximate estimations of the interactions of molecules. Strong electrostatic interactions, hydrogen bond interactions, or solvation effects are roughly described.
- In CG simulations, parameterization of molecules is tailored for only the investigated system and may cause problems of transferability to other states or compatibility with other biological molecules.

- Most of the previous studies cover simple membrane models consisting of single or dual lipid types despite there being several entities like proteins in cell membrane structure. Therefore, the influence of receptors is not taken into consideration.

3. COMPUTATIONAL METHODOLOGY

3.1. Toxicity Analysis of Nanoparticles by Machine Learning

3.1.1. Literature Search and Data Curation

Articles published between 2010 and 2020 were filtered by 'nanomaterial/nanoparticle + toxicity/cytotoxicity' keywords via various online resources, especially Google, Web of Knowledge, and Scopus. At least the knowledge of material type and size (core diameter or hydrodynamic size) of the NPs, cell type, exposure duration, and a clear description of cell viability/death were required in the initial selection of articles. By extracting toxicity data of various NPs from 152 articles, a data set was formed consisting of 4111 toxicity samples. WebPlotDigitizer version 4.2 [220] was used to read mean cell viability values from line or bar charts. Physicochemical properties of NPs, cell properties, and test conditions were determined as descriptors against the toxicity endpoint of cell viability. The summary of attributes is presented in Figure 3.1.

It should be noted that the size of NPs in the data set has been measured by different techniques (i.e., SEM, TEM, DLS, etc.). While DLS measurements mostly show the hydrodynamic sizes, microscopy analysis reflected the core/primary size. Hydrodynamic size and zeta potential values were classified based on their environment as 'in water' and 'in culture medium'. The measurements conducted in a salt environment were included in the 'in culture medium' category because of the agglomeration or colloidal instability of salt compounds [221] when compared to pure water. If not explicitly written, the surface charge of NPs was identified as positive, negative, or neutral according to the zeta-potential values. In ARM analysis, core diameter, aspect ratio and polydispersity index (PDI) were used as size indicators while hydrodynamic size in water/medium was excluded to prevent confusion. Similarly, zeta potential values were not used as an independent parameter since they are used in the determination of surface charge.

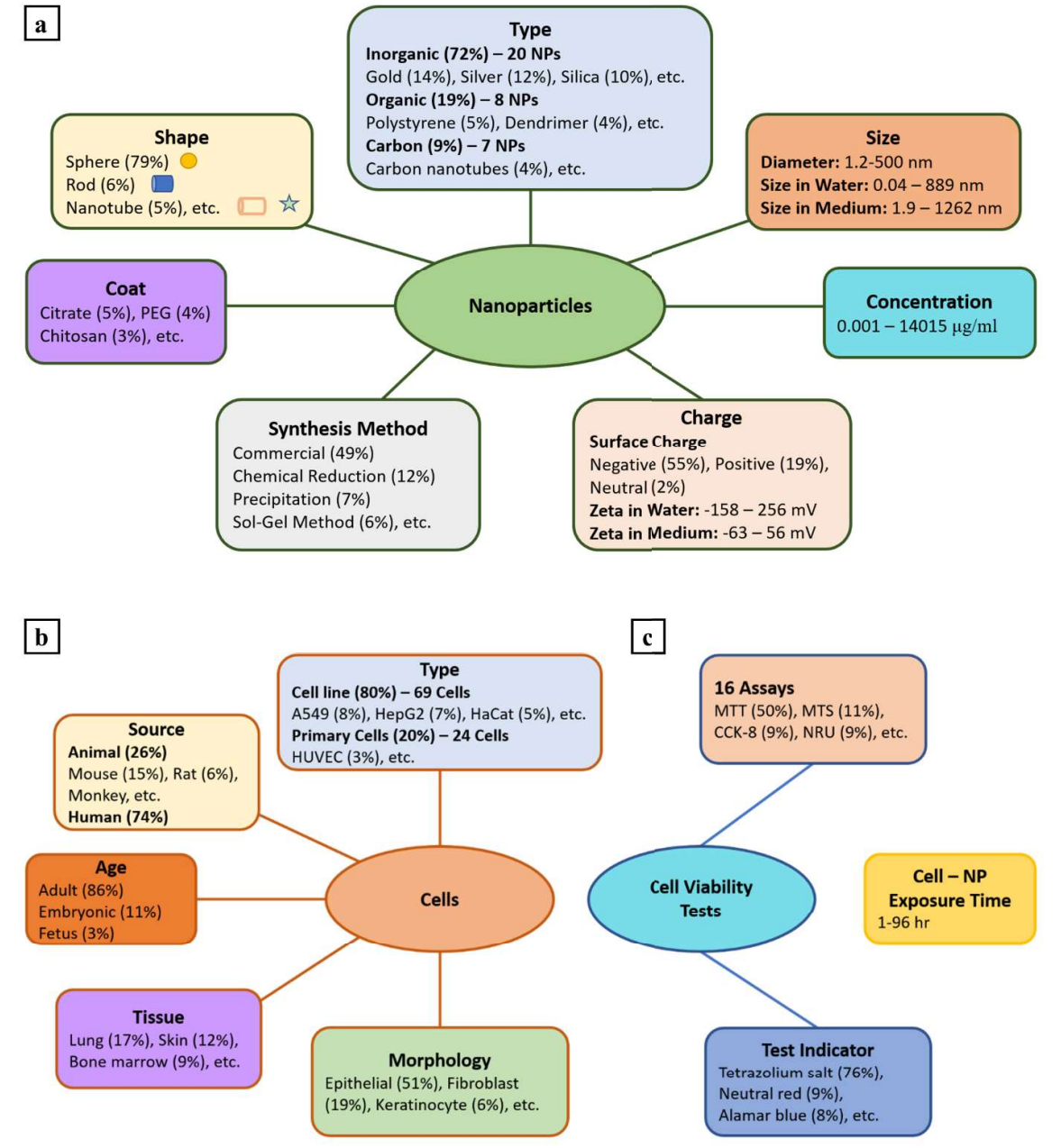

Figure 3.1. Summary of the features involved in the data set in relation to a) nanoparticles, b) cell, c) testing properties. Quantitative descriptors are listed with their min–max ranges in the data set while qualitative descriptors are shown based on the frequency of the classes. Reproduced from Ref. [9] with permission from the Royal Society of Chemistry.

To reduce the heterogeneity of the data set, iron oxide NPs which are unidentified, or described by Fe_2O_3 or Fe_3O_4 formulas were included in the same class. Commercial NPs were assumed as spherical particles unless otherwise stated. In addition, NPs that appear

spherical or sphere-like on microscope images were considered to be spherical. Given synthesis methods relied on the preparation method of core NPs, not functionalization or coating procedures. Unique or transformed synthesis methods were collected under corresponding general headings. For instance, Brust–Schiffrin, modified Brust–Schiffrin methods, or modified Frens methods were considered as the 'chemical reduction' method while the modified sol-gel method was included in the sol-gel method. In vivo literature, metalloids or metallic alloys and NPs loaded with drugs are out of the scope of this work. The whole data set is given in ref. [9] as an Excel table.

3.1.2. Preprocessing

First, the data set was harmonized in terms of units of NP diameter (nm), mass concentration (μg/ml), zeta potential (mV), and exposure duration (h). To handle categorical attributes, one-hot encoding was applied. Continuous attributes were discretized into intervals to prevent huge dimensionality problems and individual sampling in the calculations. Here, we adopted the *equal-width* approach [222] which is based on the generation of a specified number of intervals at the same size for discretization. However, considering the biological knowledge we slightly changed the bin width for diameter and concentration.

The discretization process was performed on diameter, concentration, aspect ratio, and PDI variables. The minimum, maximum and mean values of these variables in the data set are listed in Table 3.1. The PDI values were discretized into five intervals between 0 and 1 which corresponds to the ranges of (0-0.2], (0.2-0.4], (0.4-0.6], (0.6-0.8] and (0.8-1.0]. Since aspect ratio and concentration in the data set cover a wide range, they were discretized based on the logarithmic scale. Aspect ratio was split into four intervals consisting of (0-1), [1-2), [2-3) and above 3. Here, values from 0 to 10 fall into the first range, values from 10 to 100 fall into the second range, and so on. Similarly, concentration was divided into five intervals including (0-1), [1-2), [2-3), [3-4) and above 4. However, based on the sample values in the bins, the upper bound of third class was reduced to 200 μg/ml.

Table 3.1. The statistical descriptors of continuous numerical data.

	Min	**Max**	**Mean**
Diameter (nm)	1.15	500	47.3
Concentration (μg/ml)	0.001	14015.2	152.8
PDI	0.005	1.0	0.33
Aspect Ratio	0.1	3333	155.2

As to diameter, two procedures were followed. First, the range of diameter values was discretized into five bins of 25 nm width. However, these intervals did not differentiate from each other in terms of significance for single factor association including diameter and viability. In literature, nanoparticles smaller than 10 nm have been shown to have more potential to be toxic [3]. Therefore, we changed our discretization technique to present whether this hypothesis is true or not. In our approach, discretization was performed using min-max and mean values based on the reported cellular internalization of nanoparticles. The range of diameter values was divided into five intervals as shown in Table 3.2. It has been reported that NPs having a size <200 nm can be internalized by clathrin- or caveolin-mediated endocytosis [223], while caveolin-mediated endocytosis inhibits the uptake of larger particles (>100 nm) [224]. Moreover, several studies reported an optimal size of 50 nm for NP internalization, while a smaller size (~25 nm) NP internalization has been shown to decrease [58]. Hence, we took this information into account while discretizing our size data (Table 3.2). We obtained similar results with both discretization technique but had a chance to reflect the effect of narrow ranges of 0-10 nm and 10-25 nm in the manuscript.

Table 3.2. Discretization of nanoparticle diameter.

Method	**Diameter Range (nm)**				
Equal width	(0 - 25] nm	(25 - 50] nm	(50 - 75] nm	(75 - 100] nm	100 <
Our approach	(0 - 10] nm	(10, 25] nm	(25-100] nm	(100-200]	200 <

3.1.3. Association Rule Mining

To carry out ARM analysis, cell viability (which is the consequent in our study) was divided into three categories: low (≤ 50%), medium (50–85%) and high (≥ 85%) cell viability. The ARM technique was applied using single variable associations (individual contribution to cell viability) and multiple variable associations (interactive contributions to cell viability) on 24 h data to identify the factors resulting in high viability. The *apriori* [225] algorithm in the *mlxtend* [226] library of Python software [227] was used, and the association rules were determined through three main parameters of support, confidence, and lift.

Support shows how often a specific factor (such as material type, synthesis method, etc.) results in high viability in the entire data set. In our case, the minimum support value has been set to 0.01 which corresponds to at least 24 data points so that sufficiently reliable generalizations can be done. This threshold is used for only the first points in time dependent analysis to allow the decreases in the data points with time to be easily observed. Confidence is the probability of finding the high viability under all samples containing that specific factor. A confidence cutoff of 70% was determined in our study to obtain stronger associations. Lift is the ratio of the probability of a specific factor resulting in high viability to the probability of finding high cell viability in the entire sample space. It is a measure of a statistical significance of a rule: A lift value of one for a factor (or set of factors) demonstrates that the corresponding factor has no positive or negative impact to obtain the desired high viability result. If the lift value is less than one there is a negative correlation between that factor(s) and cell viability. On the other hand, a lift value higher than one indicates that the possibility of obtaining high cellular viability is higher with the use of that factor(s) and increases with increasing lift value.

To further elucidate the effects of single factors on cell viability, the ARM algorithm was also implemented on the data collected after 24 h, 48 h and 72 h. Thus, the change in lift values with respect to time was monitored; since the number of data decreases with time, the lift values of desirable associations were expected to increase. Here, the samples satisfying the rule are taken from the cumulative combination of time data, i.e., the '24 h and more' class contains the samples in 24 h, 48 h, 72 h, and 96 h; '48 h and more' class contains the samples in 48 h, 72 h, and 96 h; ’72 h and more’ class contains the samples in 72 h and

96 h. This analysis is carried out to capture the trends of attributes over time (by observing the change in lift values) and to obtain additional findings to support our results.

3.2. Molecular Dynamics Simulations

As a computer simulation technique, Molecular Dynamics allow to observe the dynamic evolution of systems through physical movements and interactions of molecules. They are used quite often because they can realistically describe the movements and resultant conformational changes of molecules [228]. For a system of interacting particles, the trajectories of atoms or molecules are solved by the numerical integration of Newton's equation of motion given as:

$$\frac{d^2x_i}{dt^2} = \frac{F_i}{m_i} \tag{3.1}$$

where *m* represents the mass, *x* shows the coordinate, *t* is time and *F* is the force acting on species *i*.

The forces between the atoms or molecules are calculated by interatomic potentials or molecular mechanics force fields. The CHARMM is a widely used force field that is first described by Karplus group [229] and it has been integrated with several simulation softwares. The potential energy function of CHARMM rely on the combination of bonded (covalent bonds, valence, and dihedral angles) and non-bonded (van der Waals and electrostatics) interactions as following [230]:

$$U(\vec{R}) = \sum_{bonds} K_b(b - b_0)^2 + \sum_{angles} K_\theta(\theta - \theta_0)^2 + \sum_{UB} K_{UB}(S - S_0)^2 + \sum_{dihedrals} K_\chi(1 + cos(n\chi - \delta)) + \sum_{impropers} K_{imp}(\phi - \phi_0)^2 + \sum_{nonbond, i \neq j} \left(\varepsilon_{ij} \left[\left(\frac{R_{min,ij}}{r_{ij}} \right)^{12} - 2 \left(\frac{R_{min,ij}}{r_{ij}} \right)^{6} \right] + \frac{q_i q_j}{\varepsilon_l r_{ij}} \right) \quad (3.2)$$

where $\vec{R}$ is the vector of coordinates of atoms in a system. Intramolecular terms consist of bonds (b), angles (θ), Urey-Bradley (UB, S), dihedrals (χ), and impropers (ϕ) with corresponding force constants (K) and equilibrium values (subscript '0'). Intermolecular (non-bonded) terms contain van der Waals interactions which are described by Lennard Jones as potential with well depth (ε_{ij}) and the distance of minimum interaction energy ($R_{min,ij}$) and electrostatic interactions which are represented by Coulomb's potential with partial charges (q).

3.2.1. Coarse-Grained Molecular Dynamics

Coarse-grained models have been proposed to decrease the degrees of freedom of atomistic simulations and have been widely used to improve the time and length scales of systems. In these models, molecules are represented not by individual atoms, but by pseudo-atoms approximating groups of atoms. A wide range of coarse-grained models have been developed including solvent-free or more realistic models with explicit but simplified solvent [231,232].

The Martini model developed by Marrink et al. is based on a four-to-one mapping of heavy atoms including hydrogen atoms bound to them [231,232]. It considers 4 types of interaction sites which are polar (P), nonpolar (N), apolar (C), and charged (Q). Each bead type has several subtypes to account for the degree of polarity and hydrogen bonding

capability. The polarity ranges from low (1) to high (5), while hydrogen bonding ability is divided into acceptor (a), donor (d), donor and acceptor (da), and none (0).

Two kinds of nonbonded interactions between beads at a distance r are described in the model. A shifted Lennard-Jones (LJ) 12-6 potential energy is utilized as follows:

$$U_{LJ}(r) = 4\epsilon_{ij}\left[\left(\frac{\sigma_{ij}}{r}\right)^{12} - \left(\frac{\sigma_{ij}}{r}\right)^{6}\right] \tag{3.3}$$

where σ_{ij} is the nearest distance between two particles and ϵ_{ij} is the strong of their interaction. Lennard-Jones interactions are split into 10 levels with Roman numbers from O to IX and corresponding well depths between 5.6 kJ/mol and 2 kJ/mol. Therefore, it is possible to fit experimental data by adjusting a small number of interaction strengths. Additionally, a shifted Coulombic potential energy function is utilized for charged groups:

$$U_{el}(r) = \frac{q_i q_j}{4\pi\epsilon_0\epsilon_r r} \tag{3.4}$$

where q_i and q_j are electric charges, ϵ_0 is the dielectric constant and ϵ_r is the relative dielectric constant for explicit screening.

The bonded interactions between chemically connected sites are included as harmonic potentials for bonds and angles, respectively:

$$V_{bond}(R) = \frac{1}{2}K_{bond}(R - R_{bond})^2 \tag{3.5}$$

$$V_{angle}(\theta) = \frac{1}{2}K_{angle}\{cos\,(\theta) - cos\,(\theta_0)\}^2 \tag{3.6}$$

where R denotes the distances between the bonded interaction sites, K_{bond} is the bond force constant, and R_{bond} is the equilibrium distance while analogously θ denotes the angle between two neighboring bonds, K_{angle} is the angle force constant and θ_0 is the equilibrium bond angle [232].

In comparison to atomistic models, Martini model reduces the degrees of freedom together with the use of short-range potentials and achieves 3 to 4-fold efficiency in terms of computational cost. Furthermore, the simple design of model allows a wide range of applications with accurate predictions as well as speeding up the calculations [231].

3.2.2. Interactions of Fullerenes with Lipid Bilayers by CG Simulations

To investigate the interactions of fullerenes and their polar derivatives with regular and peroxidized lipid bilayers, CG simulations have been performed with Martini force field [231,232] on Gromacs 5.1.1 [233] software. To visualize the systems, the Visual Molecular Dynamics (VMD) tool was used [234].

3.2.2.1. Coarse-Grained Modeling. For CG simulations, 1,2-dioleoyl-sn-glycero-3-phosphocholine (DOPC) and 1-palmitoyl-2-oleoyl-sn-glycero-3-phosphocholine (POPC) phospholipid membranes at four different peroxidation degrees including 0, 30, 70, and 100% were constructed by modifying *insane.py* script [235]. CG models of peroxidized membranes were obtained based on the parameters developed by Guo et al. [236]. On the other hand, the fullerene model was described by 16 beads forming a spherical surface of 0.72 nm diameter with approximately 4:1 atomistic-to-CG mapping as proposed by Monticelli et al. [176]. To obtain the half-polar (Janus) derivative of fullerene, half of the carbon beads (CNP) were replaced with the polar (P5) Martini beads [196]. The structure of lipids and fullerenes used in this study were demonstrated in Figure 3.2.

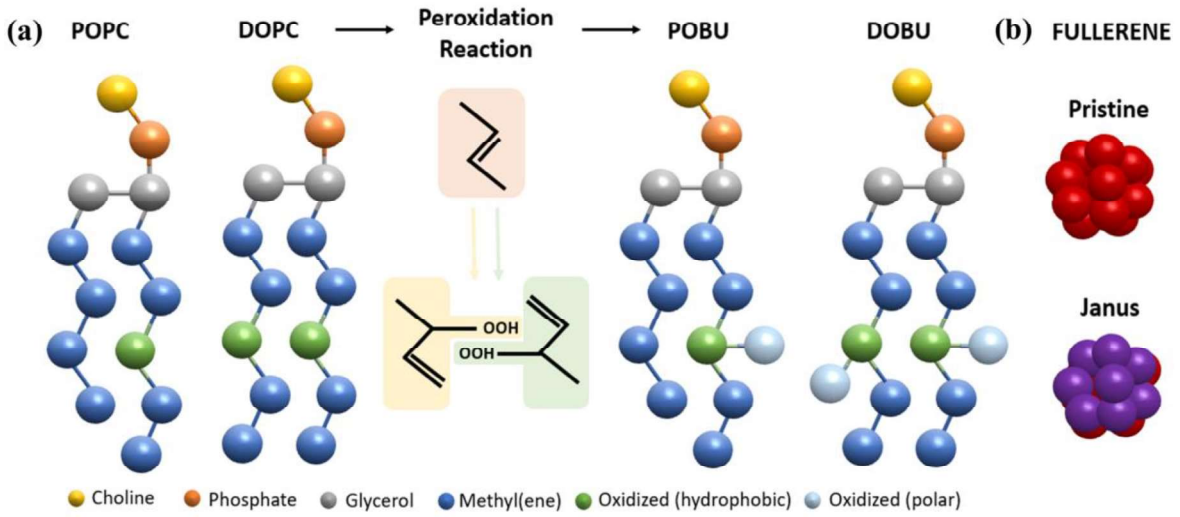

Figure 3.2. Martini CG models of (a) regular (DOPC, POPC) and peroxidized (DOBU, POBU) lipids, (b) fullerene molecules. Reproduced from Ref. [197] with permission from the Royal Society of Chemistry.

The simulated membrane systems consisted of 512 lipids, 12312 CG water molecules with 0.15 M NaCl salt to reflect the biological cell medium. Each of the eight bilayer systems was simulated in the absence and presence of pristine/Janus fullerene molecules and initially, fullerenes were randomly placed in the aqueous medium at a distance of ~1.5 nm in z-direction from the lipid headgroups. Fullerene-to-lipid ratio was varied as 0.002 and 0.02 in accordance with one and 10 fullerene molecules, respectively. The details of the systems were presented in Table B1. For the sake of convenience, peroxidized DOPC and peroxidized POPC were called as DOBU and POBU, respectively. Thus, the simulated system was named as (Lipid Type)(% Peroxidation)-(Number of Fullerene)(Pristine/Janus). For example, DOBU70-10J means that the corresponding system consists of a 70 mol% peroxidized DOPC (DOBU) and 10 Janus fullerene nanoparticles.

3.2.2.2. Coarse-Grained Simulation Parameters. First, the systems were energetically minimized by the steepest descent algorithm. To eliminate bad contacts and overlaps of beads, constant particle number, pressure, and temperature (NPT) equilibration was conducted for 60 ns with a 10 fs time step. During equilibration, the pressure was controlled at 1 bar by using Berendsen barostat [237] with a coupling constant of 5 ps. The production run of each system lasted for 10 μs with a 20 fs time step under the NPT ensemble. The temperature was kept at 310 K using a velocity rescale thermostat [238] with a coupling constant of 1 ps. The pressure was coupled to 1 bar semi-isotropically using Parrinello-Rahman barostat [239] with a compressibility factor of $3x10^{-4}$ bar^{-1}. Non-bonded interactions were cut off at a 1.2 nm distance. Lennard Jones interactions were tuned by cutoff scheme [240] with a Potential-Shift Modifier [241]. Coulomb interactions were treated by Reaction Field [242] algorithm with a permittivity constant of 15. In all three dimensions, periodic boundary conditions were implemented, and the neighbor list was updated every 10 steps. The last 5 μs of trajectories were used for the MD analysis.

3.2.2.3. PMF Simulation Parameters. PMF calculations were carried out by Umbrella Sampling [243] with the Weighted Histogram Analysis Method (WHAM) [244,245] to understand the translocation of a pristine fullerene across regular (DOPC, POPC) and peroxidized (DOBU, POBU) lipid membranes. A single fullerene molecule was placed in bulk water at ~4.5 nm with respect to the membrane center. After energy minimization and equilibration steps (as described in the previous section), the fullerene molecule was pulled through the center of the bilayer in 0.1 nm increments. Each of the resultant 45 umbrella windows was run at 310 K for 600 ns (100 ns extracted for equilibration) under the NPT ensemble. During the simulations, the distance between the COM of fullerene and the bilayer was restrained in the z-direction by applying a harmonic force constant of 1000 kJ mol^{-1}. Integrating separate umbrella windows via WHAM showed the change in penetration free energy of fullerene from water to the lipid bilayer. As a result, the favorable locations of fullerene inside the membranes were determined.

3.2.3. Interactions of Carbon Nanotubes with Lipid Bilayers by AA Simulations

We used AA molecular dynamics simulations to study the interactions between pristine/functionalized CNTs and lipid bilayer systems. MD simulations are performed with

GROMACS 2021.3 version [233]. VMD software was used to visualize the simulated systems [234].

3.2.3.1. Atomistic Modeling. Initial configurations of the SWCNT [246], amide, carboxyl (COOH), ibuprofen (IBU) [247], polystyrene (PS) [248], and lipid bilayers [249–251] were generated via CHARMM-GUI software [252]. SWCNTs were ~1 nm in diameter and ~3 nm C-to-C length with the chirality of (12,0) to represent the zig-zag configuration of the nanotubes. They were functionalized with PS or COOH-terminated PS (PSCOOH) through an amidation reaction as suggested in experimental studies [253–255] (c.f. Figure 3.3). The PS chain length was considered as 29 monomers (~3 kDa) in atactic form. The simulated systems consisted of 180 POPC lipids and 14951 water molecules with 0.15 M NaCl salt to mimic the biological cell environment. CHARMM36 force field [256,257] was used for the lipids [258], CGenFF 4.5 [259] for the linker and functional groups with the TIP3P water model while CHARMM compatible INTERFACE (IFF) force field [260] was used for the nanotube. The partial charges and bonded parameters were obtained from the CGenFF website [261] for the IBU, PS, and PSCOOH functional groups with low penalty scores between 0-5.

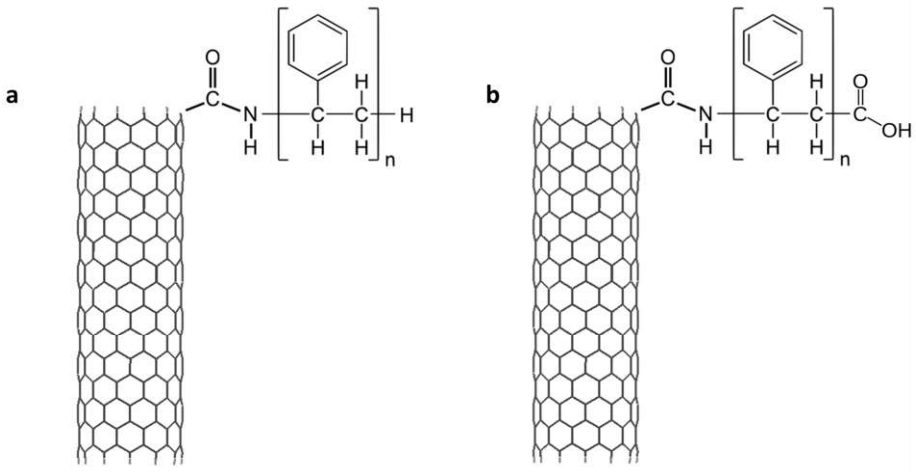

Figure 3.3. Modification of CNT with (a) PS and (b) PSCOOH via amidation reaction. Here n shows the number of monomers of the polystyrene chain.

3.2.3.2. Atomistic Simulation Parameters. First, NPs were equilibrated in water under the NPT ensemble for 50 ns and 100 ns for pristine and functionalized SWCNTs, respectively. Then IBU was loaded to the center of the CNT (12,0) models and equilibrated for an additional 50 ns. The resultant NP configurations were placed 3 nm above the bilayer center with a 45° angle to the bilayer plane in the absence and presence of IBU. After energy minimization by the steepest descent algorithm, the systems were equilibrated for 5 ns with a 1 fs time step in the constant particle number, volume, and temperature (NVT) ensemble. The temperature was kept at 310 K by velocity rescaling thermostat [238] with a time constant of 1.0 ps. Non-bonded interaction cutoff was applied at a 1.2 nm distance and van der Waals interactions were switched off between 1.0 and 1.2 nm by using the force-switch modifier. The long-range electrostatic interactions were calculated by the particle mesh Ewald (PME) algorithm [262]. Depending on the equilibration time of the systems, simulation times varied between 200-710 ns with 2 fs timestep. The pressure of the systems was controlled at 1 bar in a semi-isotropic fashion by the Parrinello–Rahman barostat [239] with a coupling constant of 5 ps and a compressibility factor of 4.5×10^{-5} bar^{-1}. During the simulations, hydrogen bonds were constrained through the LINCS algorithm [263].

3.2.4. CG Modeling of Pristine and Functionalized Carbon Nanotubes

We adapted Martini3 small molecule parameterization strategy as given in Figure 3.4 to develop CG models of pristine and PS or PSCOOH functionalized CNTs. Free energy simulations were performed with GROMACS 2020 while other MD simulations are performed with GROMACS 2021.3 version [233]. VMD software was used to visualize the simulated systems [234].

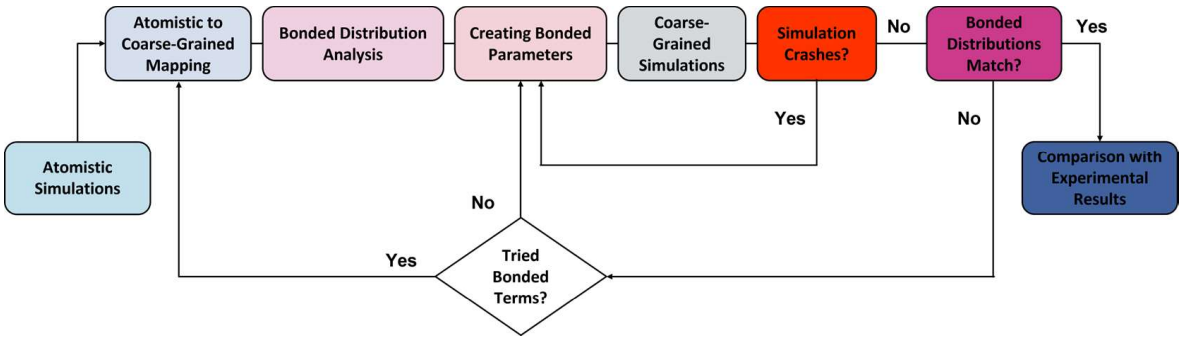

Figure 3.4. Martini3 small molecule parameterization strategy adapted from [264].

3.2.4.1. Atomistic Reference Simulations. SWCNTs with the chirality of (6,0) and (18,0) were constructed by CHARMM-GUI [252]. After functionalization by five and 29 monomers of PS for CNT (6,0) and CNT (18,0), respectively, the nanotube systems were solvated in TIP3P water. The resultant configurations were simulated for 50 ns and 100 ns, respectively, for pristine and functionalized CNTs. The pressure of the systems was controlled at 1 bar in an isotropic fashion and other simulation parameters were given in the 'Atomistic Simulation Parameters' section.

3.2.4.2. CG Modeling of CNT. In CGMD simulations, especially for phospholipid membrane systems, Martini force field parameters have been widely used. Recently a new version of Martini which is called Martini3 has been proposed with significant improvements in bead types and interaction levels which make more versatile and accurate predictions of realistic systems [265]. Therefore, we adopted the Martini3 parameterization procedure for small molecules [264]. By applying the 2-to-1 mapping to consecutive C beads in the same ring of SWCNTs by using the CGBuilder tool [266], end group beads (H-bonded) were represented with TC5 bead type while others are represented with TC5e bead type.

The bonded interactions between neighbor beads were obtained from atomistic reference simulations and force constants were determined by trial-and-error procedure to capture the equilibrium bond lengths, and bond angles which correspond to:

$$\alpha = \pi(1 - \frac{2}{n}) \tag{3.7}$$

Where *n* is the number of beads in one ring [219]. Also, the stiffness of the SWCNTs was provided through improper dihedral angles between two intersecting planes. The mapping scheme is demonstrated in Figure 3.5 with bonded interactions for CNT (18,0). CG model and bonded parameters of CNT (6,0) were given in Figure C.1.

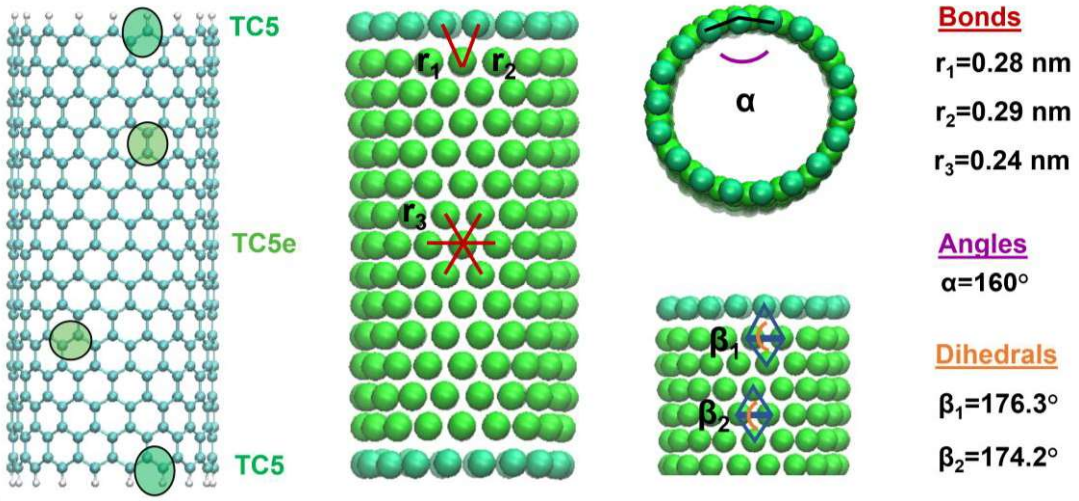

Figure 3.5. CNT (18,0) mapping from all-atom to CG Martini3 model with bond lengths, angles, and improper dihedrals. Force constants of 50000 kJ $mol^{-1}nm^{-2}$, 1500 kJ mol^{-1} $rad^{-2,}$ and 1000 kJ $mol^{-1}rad^{-2}$ were used to capture equilibrium bond lengths, angles, and dihedrals.

3.2.4.3. CG Modeling of PS and PSCOOH functionalized CNT. Martini3 parameters of PS were obtained from the *polyply.py* script [267]. PS chains are covalently linked to the nanotube with an amide linker, which was represented by one bead. Carboxyl modification was applied to the open end of the PS ring. The amide linker and carboxyl group were represented with the polar P3 bead. However, only for the carboxyl bead, the Lennard-Jones interaction parameter (epsilon) was reduced (with a trial-and-error procedure) to 3.0 kJ/mol between P3 and W beads to obtain correct free energy partitioning behavior. Two bonds and three angles were defined between the nanotube-linker-PS beads at the connection point. The bonded parameters reflected the atomistic symmetry, and the mapping scheme is demonstrated in Figure 3.6 The bonded parameters between the PS and carboxyl group, on the other hand, were assumed to be the same as the parameters of a continuing chain of PS [268] as shown in Figure C.2.

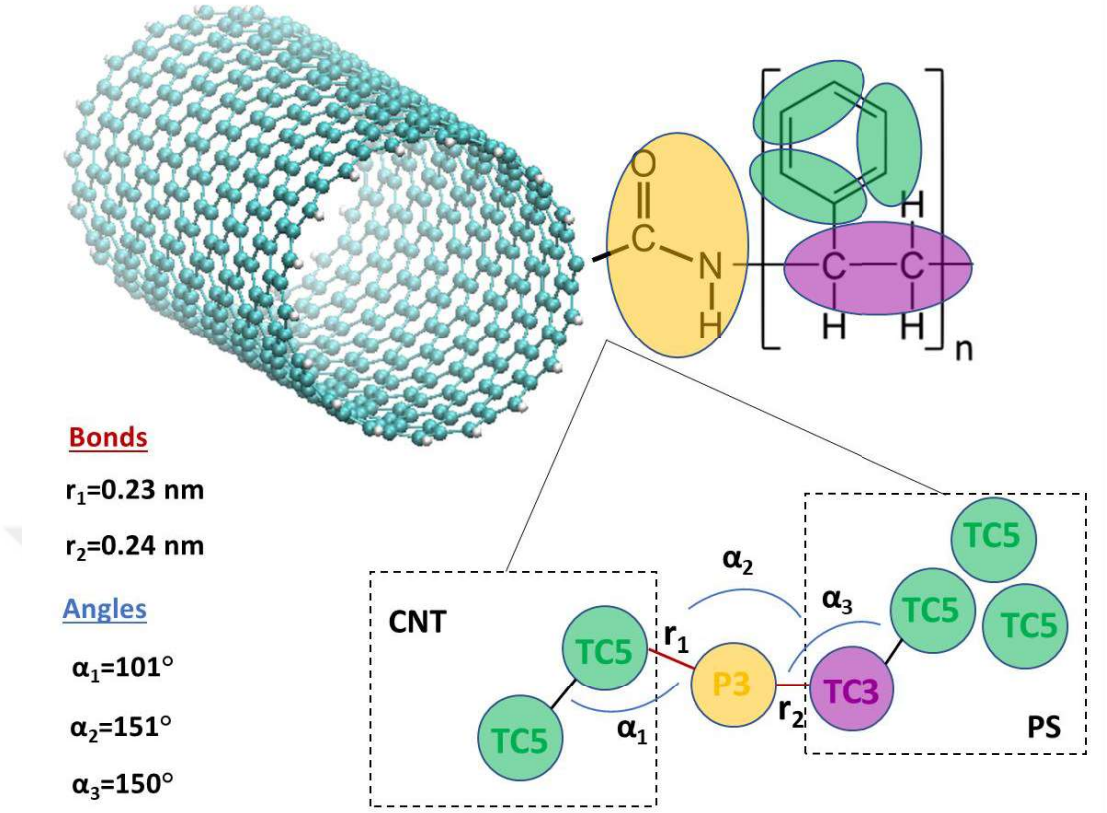

Figure 3.6. CG modeling of PS-functionalized CNT (18,0). The linker is demonstrated by the P3 bead type, and the bonded parameters at the connection point are listed on the left.

3.2.4.4. CG Simulation Parameters. The mapped SWCNT configuration was solvated with SPC water in a box in which the solute to box edge distance is 2 nm for CNT (6,0) and 4 nm for CNT (18,0). After energy minimization by steepest descent, equilibration was done for 30 ns with 10 fs timestep in the NPT ensemble to relax the system. During equilibration, isotropic pressure coupling was applied to keep the pressure at 1 bar with Berendsen barostat [237] with a coupling constant of 5 ps. The temperature was maintained at 310 K by the velocity rescale thermostat [238] with a time constant of 1.0 ps. Non-bonded interactions were cut off at a 1.2 nm distance. The Lennard-Jones interactions were shifted with the Potential-Shift-Verlet modifier while the Coulomb potential was screened on the Reaction Field scheme [242] with a permittivity constant of $\varepsilon_r = 15$. The pressure of the system was set to 1 bar by using Parrinello–Rahman barostat [239] with a coupling constant of 5 ps and a compressibility factor of 3 x 10^{-4} bar^{-1}. NPT production runs took 1 μs and half the simulation time was used for the analysis.

3.2.4.5. Free Energy Simulations. Free energies of solvation were calculated through the thermodynamic integration (TI) method by using Bennett's Acceptance Ratio [269] which is based on the numerical integration of the derivative of Hamiltonian with respect to the coupling parameter λ [270]:

$$\Delta G = \int_{\lambda=0}^{\lambda=1} \left\langle \frac{\partial H(\lambda)}{\partial \lambda} \right\rangle_{\lambda} d\lambda \tag{3.8}$$

Then the free energy of transfer was calculated from the difference in the free energy of solvation values in water and octanol solvents:

$$\Delta G_{transfer} = \Delta G_{octanol} - \Delta G_{water} \tag{3.9}$$

Partition coefficient, which is represented as *logP*, is proportional to the free energy of transfer between two immiscible solvents and found by [271]:

$$logP = \frac{-\Delta G_{transfer}}{RTln(10)} \tag{3.10}$$

where *R* is the gas constant, and *T* is the temperature.

Due to the high simulation cost, CNT (6,0) which is of ~0.5 nm in diameter and ~1.5 nm C-to-C length was used for the calculations. The PS or PSCOOH chain length was considered as five monomers (~0.5 kDa). For pristine SWCNTs, only van der Waals interactions were coupled between λ = 0 (interactions are off) and λ = 1 (interactions are on) since SWCNT has no partial charges. For functionalized SWCNTs, both van der Waals and Coulomb interactions were coupled sequentially. The λ values were equally spaced and identical in each simulation so we obtained 10 and 20 runs for pristine and functionalized SWCNTs, respectively. In each run of all-atom simulations, 1 ns of NVT and 4 ns of NPT equilibration were applied before 50 ns of NPT production run. The stochastic dynamics integrator with 2 fs of timestep was used in all simulations and the temperature was set to 298 K. The pressure was controlled at 1 bar by using Parrinello-Rahman barostat [239] with a time constant of 1 ps. Non-bonded interaction cutoff values were set to 1.2 nm. The PME

algorithm [262] was used for the calculation of long-range electrostatic interactions with a sixth-order spline interpolation and a 0.12 nm grid spacing. To remove the singularity in the potentials, a soft-core potential was used [272] with the soft-core parameter of 0.5 and the soft-core power of 1. For CG simulations, the same parameters in the 'CG Simulation Parameters' section were used, and 1 μs of production run followed 50 ns of equilibration with the stochastic integrator at 298 K.

3.2.4.6. PMF Simulations. PMF calculations were performed to investigate the transfer of a single CNT across the lipid bilayer by the umbrella sampling method [243]. Smaller POPC bilayer consisting of 128 lipids was used with our CNT (6,0) model (D = ~0.5 nm, L= ~1.5 nm). The nanoparticle was placed ~3.75 nm away from the z-coordinate of the bilayer center-of-mass. Once the systems were equilibrated for 5 ns, the nanoparticle was pulled through the center of the bilayer at 0.1 nm intervals. The distance between the center-of-mass of the nanoparticle and the membrane was restrained in the z-direction with a harmonic potential force constant of 1000 kJ mol^{-1}. Each all-atom umbrella window was simulated for 50 ns (10 ns extracted for equilibration) under the NPT ensemble at 310 K with a total simulation time of ~2 μs. Each CG umbrella window was simulated for 1 μs (200 ns extracted for equilibration) under the NPT ensemble at 310 K with a total simulation time of ~40 μs. The analysis of the umbrella simulations was performed using the WHAM [244,245].

3.2.5. Interactions of Carbon Nanotubes with Lipid Bilayers by CG Simulations

CNT (18,0) was covalently linked to PS or PSCOOH, which has 29 (~3 kDa), 48 (~5 kDa), or 96 (~10 kDa) monomers. The grafting density in the end ring of CNT was one, two, four, or six PS or PSCOOH chains with 29 monomers (c.f. Figure 3.7). Two model membranes, POPC only and POPC with 30% CHOL, were constructed by CHARMM-GUI [252]. To reflect the realistic biological environment, 2048 lipids were solvated in 48401 and 49571 CG waters for POPC and POPC/CHOL systems, respectively, in 0.15 M NaCl. Each membrane system was simulated in the absence of nanoparticles, and in the presence of one and five NPs. Initially, the NPs were equilibrated in water for 1 μs under the NPT ensemble, then the resultant configurations were placed vertically about ~2 nm away from the headgroups of the equilibrated bilayer in the z-direction. After a short equilibration, the systems were simulated in the NPT ensemble for 10 μs with a 20 fs timestep using Martini3

parameters which are described elsewhere [265]. Last 2 μs of the trajectories were used for the analysis.

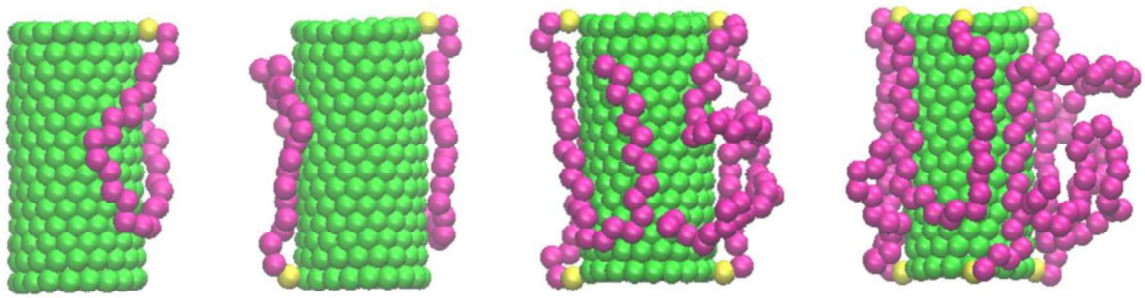

Figure 3.7. Grafting of CNT with one, two, four, and six chains of PS from left to right. Here, CNT is in green, linker is in yellow and aliphatic chain of PS is in purple. Aromatic rings of PS are not shown for clarity.

It should be noted that the pre-released version of Martini3 cholesterol was obtained from Paulo Souza and validated by comparing with the atomistic and Martini2 parameters after changing the cholesterol content between 0-50 % in POPC lipid systems. Results for the area per lipid, bilayer thickness, and order parameter are available in the Figure C.5 and C.6.

3.2.6. Analysis of Molecular Dynamics Simulations

The membrane properties and the interactions of pristine and functionalized CNTs with the membrane were evaluated through the area per lipid (APL), volume per lipid (VPL), lipid bilayer thickness, lipid order parameter, density distribution, and radial distribution functions by using corresponding GROMACS modules. APL was computed by either dividing the box area in -xy direction to half of the total lipid number or by Voronoi tessellation via FATSLIM script [273]. In VPL calculation, the box area in -xy direction was multiplied with the z-dimension of the bilayer which is obtained from the distance between the headgroup peaks in the density profile and divided by the total lipid number. The bilayer thickness was found by calculating the center-of-mass distance of P atoms (AA) or PO4 beads (CG) in the z-direction from the upper leaflet to the lower leaflet. To characterize the orientation of the lipids, the deuterium order parameter of lipid acyl chains was calculated

by modifying the *do-order-gmx5.py* script accessed in Martini website [274] which is based on:

$$S = \frac{3}{2}\langle cos^2\theta \rangle - \frac{1}{2} \tag{3.10}$$

where θ is the angle between the bilayer normal and the vector along a particular bond in a lipid tail. Here, S = 1, −0.5, and 0 indicate perfect alignment with the bilayer surface, an antialignment, and random orientation, respectively [275]. The lateral mean square displacement (MSD) of lipids was extracted for the individual lipids or PO4 and ROH beads of POPC and CHOL, respectively. After removing the system's COM motion, diffusion coefficient values were calculated on MATLAB [276] by fitting the MSD versus time to the linear region of the line:

$$MSD(t) = 4Dt + c \tag{3.11}$$

where the constant c shows the offset at t = 0 [275].

To identify cholesterol flip-flops, the translocation of ROH beads between the leaflets was monitored by the LiPyphilic [277] module of Python [227]. A cholesterol molecule was assigned to a leaflet based on its minimum distance to the leaflet and if the distance is within 1 nm of neither or both leaflets, it was assigned to the midplane. A flip-flop event was defined as successful if the translocation from one leaflet to another follows by residing in the second leaflet for at least 10 ns. To calculate the flip-flop rate of cholesterol, the total number of successful flip-flop events was divided into the number of cholesterol and total simulation time.

4. RESULTS AND DISCUSSION

The results of the current work are presented in five sections. In the first section, results of the CG simulations on fullerene translocation across lipid membranes are reported while the second section includes the data mining results of the NP cytotoxicity. In the third section, atomistic modeling of functionalized CNTs is conducted and their interactions with lipid bilayers are studied. On the other hand, the CG modeling of pristine and functionalized CNTs and their interactions with the bilayers are covered in the fourth and fifth sections, respectively.

4.1. Interactions of Fullerenes with Regular and Peroxidized Lipid Bilayers by Coarse-Grained Simulations

Pristine fullerenes can spontaneously penetrate the membrane due to their hydrophobic nature. The polar derivative of fullerenes, on the other hand, has some hydrophilic character which promotes their interactions with water molecules [177]. Here, we show the interactions of fullerenes and their half-polar derivatives (Janus) with DOPC and POPC bilayers and their peroxidized analogs DOBU and POBU, respectively. In homogeneous bilayers which consist of a single lipid component, the excess area caused by the undulations of the bilayer is negligible. Therefore, the surface area of the bilayer can be assumed the same as the area of the periodic box in the -xy direction. However, the volume of the bilayer significantly differs from the volume of the periodic box because of the presence of water and ion molecules, and to calculate the volume of the bilayer, the volume of the water layer should be subtracted from the total box volume. Based on this information we calculated APL, VPL, and bilayer thickness in addition to the lateral diffusion coefficients of lipids.

In the presence and absence of fullerenes, the change in structural and elastic properties of bilayers are shown in Table 4.1. APL and bilayer thickness values were found in close agreement with the previous experimental and computational studies. For regular DOPC, APL and thickness values are calculated as ~0.66 nm^2 and ~4.4 nm, respectively, whereas the experimental values cover the range of 0.67 – 0.73 nm^2 and 3.5 – 4.6 nm [278–280]. Similarly, the APL and thickness for the POPC bilayer were computed as ~0.63 nm^2 and

~4.3 nm, respectively, comparable to previously reported experimental and computational values between 0.63 – 0.68 nm^2 and 3.7 – 4.3 nm [236,258,281–284]. As increasing peroxidation level, APL values increase whereas bilayer thickness decrease. In parallel to the previous reports [236,285], there is a 20 % and 17 % increase in APL values while a 7 % and 8 % decrease in thickness values in fully peroxidized DOBU and POBU membranes. The addition of single pristine/Janus fullerene to the membrane systems does not change the APL and bilayer thickness. However, the addition of 10 pristine fullerenes slightly increases the thickness and APL values apart from fully peroxidized DOPC: in DOBU the APL stays almost constant. The change in APL values is more pronounced at lower peroxidation levels but the change in thickness is more apparent at higher peroxidation levels. The introduction of 10 Janus fullerenes causes a slight increase in APL values but a decrease in bilayer thickness. Still, these variations are below 1% in all cases, supporting the passive diffusion of fullerene NPs.

In experimental literature, VPL values of DOPC and POPC were reported as 1.30 nm^3 and 1.26 nm^3, respectively, at 303 K [281]. However, computationally, VPL of DOPC and POPC were calculated as 1.49 nm^3 and 1.38 nm^3 [236]. Our results confirm the computational findings by suggesting similar VPL values although higher than in experiments. From Table 4.1 it is also shown that VPL values increase with increasing peroxidation and the highest VPL are observed in DOBU and POBU bilayers. In general, the presence of pristine/Janus fullerenes in bilayer systems has no significant effect on the VPL values except for 70% peroxidized POPC. The introduction of 10 fullerene molecules to 30% peroxidized DOPC and 70% peroxidized POPC results in approximately 8% and 6% increase in VPL values, respectively. Contrary to the increase in VPL in lower peroxidation levels, in fully peroxidized DOPC VPL decreases ~5%.

The diffusion coefficient estimations of CG simulations are 2 to 10 times faster than the experimental measurements depending on the temperature. In our study, the diffusion coefficients of DOPC and POPC at 310 K were calculated as 39.8 and 42 $\mu m^2/s$, respectively, while experimental studies show 16 and 15.3 $\mu m^2/s$ [286]. As expected, the lipid lateral diffusion constants of DOPC and POPC are 2 to 3 times higher than their experimental counterparts. Therefore, it is more appropriate to consider trends of diffusivities rather than numerical values. As is seen in Table 4.1, the mobility of lipids decreases as the peroxidation

level increases. The reduction in lipid mobility is more apparent at 30% peroxidation while similar in 70% and full peroxidation. In DOBU and POBU bilayers, lateral diffusion constants of lipids are 33% and 20% lower than their regular analogs. Similarly, it was reported that there is about 25% reduction in lipid mobility in peroxidized bilayers [236]. This was explained by the strong cohesive forces between peroxidized lipid molecules and increased friction between the membrane surface and bulk water layer.

Lateral diffusion coefficients of pristine and Janus fullerenes are also presented in Table 4.1. It is observed that diffusion of fullerene changes with respect to the saturation and peroxidation level of lipids. In monosaturated POPC lipids, pristine fullerenes move slower than in unsaturated DOPC lipids confirming previous literature [189]. The fullerene mobility in the DOPC bilayer is almost twice that of POPC and its peroxidized forms. Furthermore, Janus NPs have a higher affinity for aggregation than pristine fullerenes in the bilayer, causing Janus to move slower. On the other hand, the aggregation of fullerene molecules considerably rises the standard errors of diffusivities as their mean square displacements do not yield a linear regime. The lateral diffusion coefficients which have high standard errors in Table 4.6 are just given to find additional evidence about the aggregation of fullerenes.

Table 4.1. Area per lipid (APL), volume per lipid (VPL) and bilayer thickness of lipid membranes, and lateral diffusion coefficients of DOPC and POPC lipids and fullerene molecules. Here P/J denotes pristine or Janus fullerene nanoparticle.

Model	**P/J No**	**APL (nm^2)**	**VPL (nm^3)**	**Bilayer Thickness (nm)**	**Lateral Diffusion Coefficient ($\mu m^2/s$)**	
					Lipid	**P/J**
DOPC	-	0.660 ± 0.005	1.49 ± 0.01	4.44 ± 0.03	39.8 ± 2.2	-
	1P	0.661 ± 0.005	1.49 ± 0.01	4.44 ± 0.03	36.5 ± 1.2	-
	1J	0.661 ± 0.005	1.50 ± 0.01	4.44 ± 0.03	36.4 ± 2.3	-
	10P	0.666 ± 0.005	1.50 ± 0.01	4.44 ± 0.03	38.1 ± 3.6	54.8 ± 2.7
	10J	0.664 ± 0.005	1.50 ± 0.01	4.43 ± 0.03	33.3 ± 1.2	14.0 ± 6.1

Table 4.1. Area per lipid (APL), volume per lipid (VPL) and bilayer thickness of lipid membranes, and lateral diffusion coefficients of DOPC and POPC lipids and fullerene molecules. Here P/J denotes pristine or Janus fullerene nanoparticle (cont.).

DOBU30	-	0.717 ± 0.007	1.48 ± 0.01	4.22 ± 0.03	29.5 ± 4.7	-
	1P	0.717 ± 0.007	1.49 ± 0.01	4.22 ± 0.03	30.7 ± 2.1	-
	1J	0.717 ± 0.007	1.51 ± 0.01	4.21 ± 0.03	32.3 ± 2.5	-
	10P	0.719 ± 0.007	1.58 ± 0.02	4.24 ± 0.03	28.2 ± 0.7	27.9 ± 25.7
	10J	0.722 ± 0.007	1.62 ± 0.02	4.21 ± 0.03	27.5 ± 0.3	12.0 ± 2.6
DOBU70	-	0.764 ± 0.008	1.64 ± 0.02	4.14 ± 0.04	26.9 ± 1.8	-
	1P	0.765 ± 0.008	1.64 ± 0.02	4.15 ± 0.04	24.9 ± 2.9	-
	1J	0.765 ± 0.008	1.63 ± 0.02	4.14 ± 0.04	30.6 ± 3.7	-
	10P	0.765 ± 0.008	1.64 ± 0.02	4.18 ± 0.04	26.6 ± 0.4	35.0 ± 9.5
	10J	0.771 ± 0.008	1.64 ± 0.02	4.13 ± 0.04	23.0 ± 2.5	14.4 ± 3.6
DOBU	-	0.795 ± 0.010	1.73 ± 0.02	4.12 ± 0.04	26.6 ± 0.1	-
	1P	0.795 ± 0.009	1.73 ± 0.02	4.12 ± 0.04	28.3 ± 0.5	-
	1J	0.796 ± 0.010	1.73 ± 0.02	4.12 ± 0.04	23.3 ± 2.4	-
	10P	0.794 ± 0.010	1.64 ± 0.02	4.15 ± 0.04	24.2 ± 2.0	35.4 ± 13.0
	10J	0.802 ± 0.010	1.64 ± 0.02	4.10 ± 0.04	24.1 ± 1.5	15.8 ± 2.4
POPC	-	0.631 ± 0.005	1.37 ± 0.01	4.27 ± 0.03	42.0 ± 4.3	-
	1P	0.631 ± 0.005	1.35 ± 0.01	4.27 ± 0.03	40.1 ± 1.6	-
	1J	0.631 ± 0.005	1.37 ± 0.01	4.27 ± 0.03	41.5 ± 0.3	-
	10P	0.637 ± 0.005	1.37 ± 0.01	4.27 ± 0.03	41.4 ± 3.4	21.1 ± 12.5
	10J	0.633 ± 0.005	1.37 ± 0.01	4.26 ± 0.03	39.4 ± 2.8	10.3 ± 19.7
POBU30	-	0.671 ± 0.006	1.39 ± 0.01	4.09 ± 0.03	35.9 ± 1.9	-
	1P	0.671 ± 0.006	1.36 ± 0.01	4.09 ± 0.03	35.8 ± 0.5	-
	1J	0.672 ± 0.006	1.37 ± 0.01	4.09 ± 0.03	34.2 ± 4.5	-
	10P	0.676 ± 0.006	1.38 ± 0.01	4.10 ± 0.03	33.0 ± 2.8	27.3 ± 11.2
	10J	0.676 ± 0.006	1.39 ± 0.01	4.08 ± 0.03	31.4 ± 2.5	12.6 ± 18.3
POBU70	-	0.717 ± 0.007	1.38 ± 0.01	3.95 ± 0.03	33.5 ± 1.0	-
	1P	0.717 ± 0.007	1.46 ± 0.01	3.96 ± 0.03	32.8 ± 1.1	-
	1J	0.718 ± 0.007	1.45 ± 0.01	3.95 ± 0.03	33.1 ± 0.6	-
	10P	0.719 ± 0.007	1.45 ± 0.01	3.98 ± 0.03	28.4 ± 4.2	28.3 ± 12.0
	10J	0.723 ± 0.007	1.48 ± 0.01	3.94 ± 0.03	30.3 ± 2.0	27.4 ± 4.3

Table 4.1. Area per lipid (APL), volume per lipid (VPL) and bilayer thickness of lipid membranes, and lateral diffusion coefficients of DOPC and POPC lipids and fullerene molecules. Here P/J denotes pristine or Janus fullerene nanoparticle (cont.).

POBU	-	0.739 ± 0.008	1.48 ± 0.02	3.92 ± 0.03	33.7 ± 1.3	-
	1P	0.739 ± 0.008	1.46 ± 0.02	3.92 ± 0.03	34.8 ± 3.0	-
	1J	0.740 ± 0.008	1.47 ± 0.02	3.92 ± 0.03	33.8 ± 1.7	-
	10P	0.740 ± 0.008	1.49 ± 0.02	3.95 ± 0.03	31.2 ± 1.9	24.1 ± 7.0
	10J	0.745 ± 0.008	1.48 ± 0.02	3.91 ± 0.03	31.7 ± 2.0	8.4 ± 6.8

The translocation of a single fullerene from water to the lipid bilayer is investigated through PMF calculations, density distributions, residence time plots and radial distributions. The energy profile of a fullerene across the reaction coordinate is shown in Figure 4.1. The preferable location of fullerene with respect to the bilayer center was found at around 1 nm consistent with the literature [176,177,180] for DOPC and POPC bilayers. Wong-Ekkabut et al. calculated the penetration free energy of ~110 kJ/mol in a DOPC membrane with five bead tails [180]. The free energy minima in the POPC bilayer were estimated as 80 kJ/mol through atomistic and CG simulations [176]. Figure 4.1 shows that the free energy minima of pristine fullerene are approximately 90 kJ/mol and 110 kJ/mol within POPC and DOPC bilayers, respectively. To our knowledge, the energy differential of fullerenes in peroxidized bilayers has not been studied so far. On the other hand, the dominant location inside DOBU and POBU bilayers was found around the bilayer center. PMF results show that the free energy minima yield 95 kJ/mol energy for both DOBU and POBU bilayers. Therefore, it can be said that an average 15 kJ/mol energy penalty is added at the expense of peroxidation in DOPC bilayer.

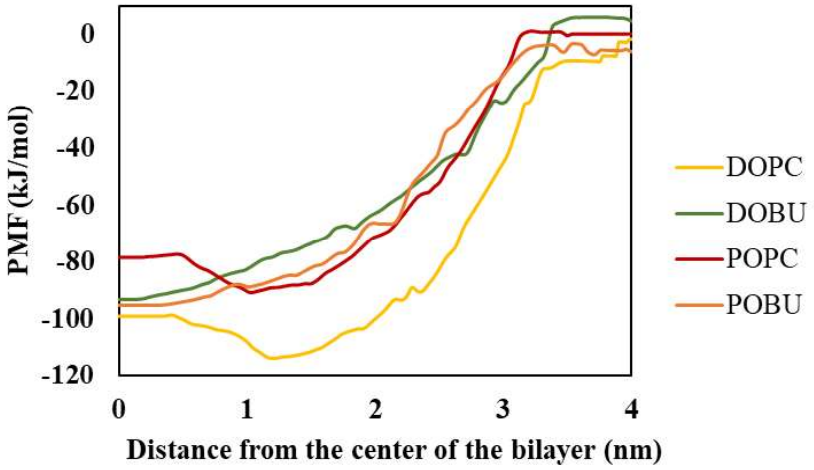

Figure 4.1. PMF profiles of a single pristine fullerene across lipid bilayers with respect to the distance between their center of mass. Reproduced from Ref. [197] with permission from the Royal Society of Chemistry.

As previously mentioned, the hydrophobicity of pristine fullerene NPs promotes their accumulation inside the lipid bilayer. Fullerene molecules land in the water-bilayer interface, traverse the interfacial lipid headgroups and reside in the hydrophobic core of the membrane [199]. As suggested with density distribution profiles in Figure 4.2, pristine fullerenes prefer to locate near glycerol linker groups inside the regular PC bilayers while they reside in the bilayer center within peroxidized bilayers. This difference in their translocation behavior is attributed to the presence of C double bonds in DOPC and POPC bilayers. The accumulation of fullerenes in the center of the bilayer is restricted by an energy penalty due to the unsaturated bonds in regular PC bilayers.

The translocation behavior of fullerenes changes with respect to the peroxidation degree of POPC lipids. In 30% peroxidized POPC, the fullerenes are located near the glycerol groups similar to those in POPC, but in 70% peroxidized POPC they are concentrated in the center as in POBU. On the other hand, fullerenes place in the center of the peroxidized DOPC independent of the peroxidation degree. This may be associated with the saturation levels of lipids which result in different energy penalties. For instance, DOPC lipids are unsaturated because they have double bonds in both chains, but POPC lipids are

monounsaturated because they contain single double bonds. As a result, it may be easier to exceed the energy threshold imposed by a double bond in POPC.

Experimental studies showed that fullerene NPs can cross the cell membrane [20,287]. However, we observed in our simulations that once internalized, they do not return to the aqueous phase throughout the simulation. This raises the question of whether fullerenes can migrate from the extracellular region of the cell membrane to the intracellular region. In this context, Janus fullerenes have been shown to rapidly cross the membrane and settle into the lipid headgroups in the opposite leaflet. Although the desired exit from the membrane headgroups to the aqueous phase is not observed, it has been suggested that the amphiphilic nature of Janus particles will facilitate their use as a drug delivery agent [196]. Contrary to this argument, we found that Janus fullerenes can not transport from one leaflet to another in any of the membrane systems investigated. Instead, they got stuck between the lipid headgroups with which they interact and could not penetrate the interior of the membranes regardless of the peroxidation level (c.f. Figure 4.3). However, it should be noted that we used the most polar Martini bead type while developing Janus fullerenes without making a validation with experiments. Since the balance between the hydrophobic and hydrophilic forces determine the dynamics of NPs, they should be investigated further.

From density distribution analysis, it is also observed that peroxidation of lipids alters the distribution of lipid components. For instance, the density peaks of phosphate groups in peroxidized membranes are lower and broader than that in regular PC bilayers. The more the peroxidation level of lipids, the less the density of PO4 beads. Additionally, the peroxidized lipids allow the diffusion of water molecules along the extremity of the bilayer in contrast to the regular PC lipids (Figure B.1 and B.2). Water penetration inside the membrane is more apparent in the DOBU bilayer since DOPC has twice as many oxidized groups as POPC.

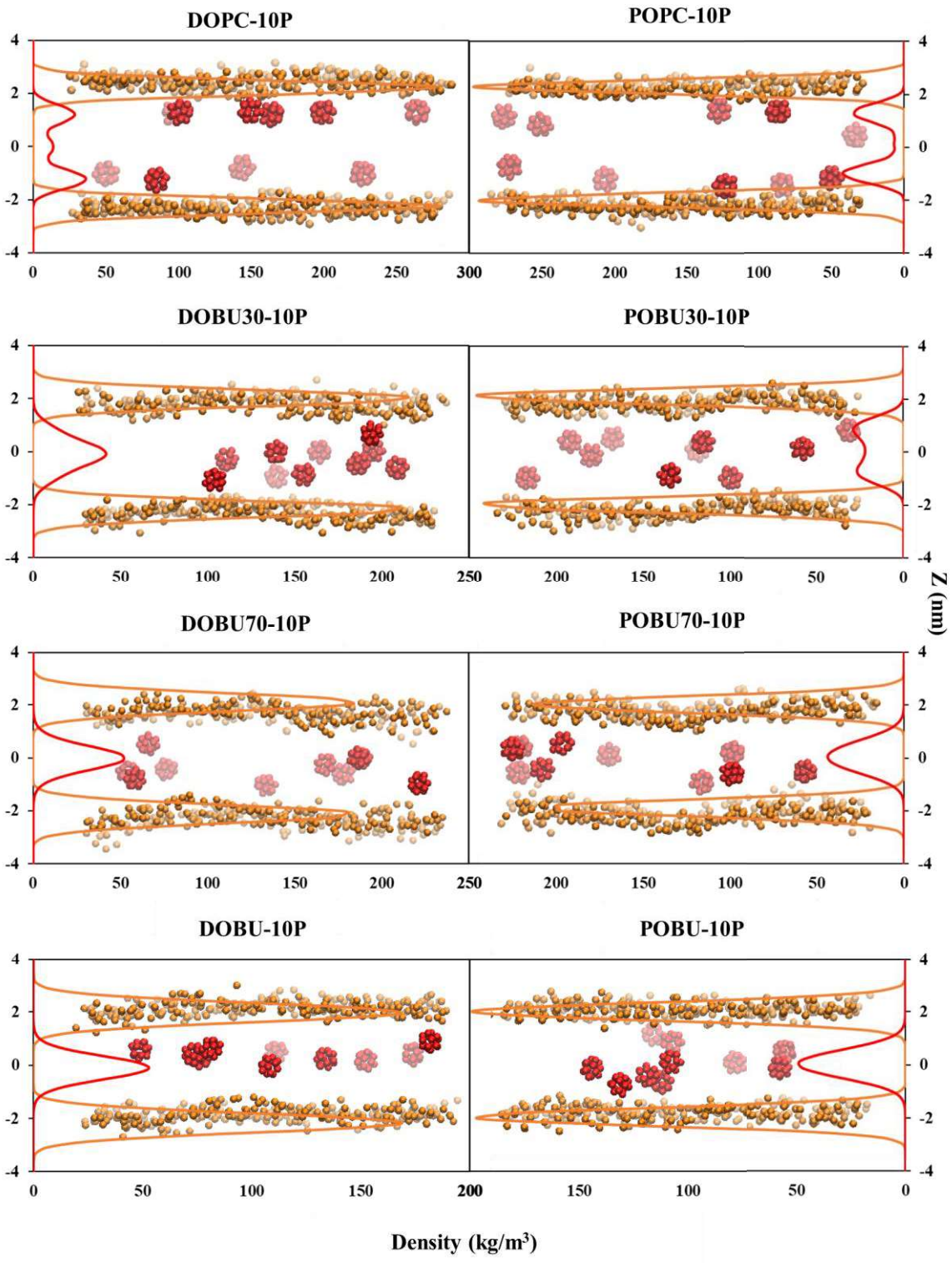

Figure 4.2. Density distribution profiles of lipid phosphate (PO4 beads) groups, and pristine fullerenes at fullerene to lipid ratio of F/L =10/512. Snapshots were taken from the last frame of the 10 μs trajectories.

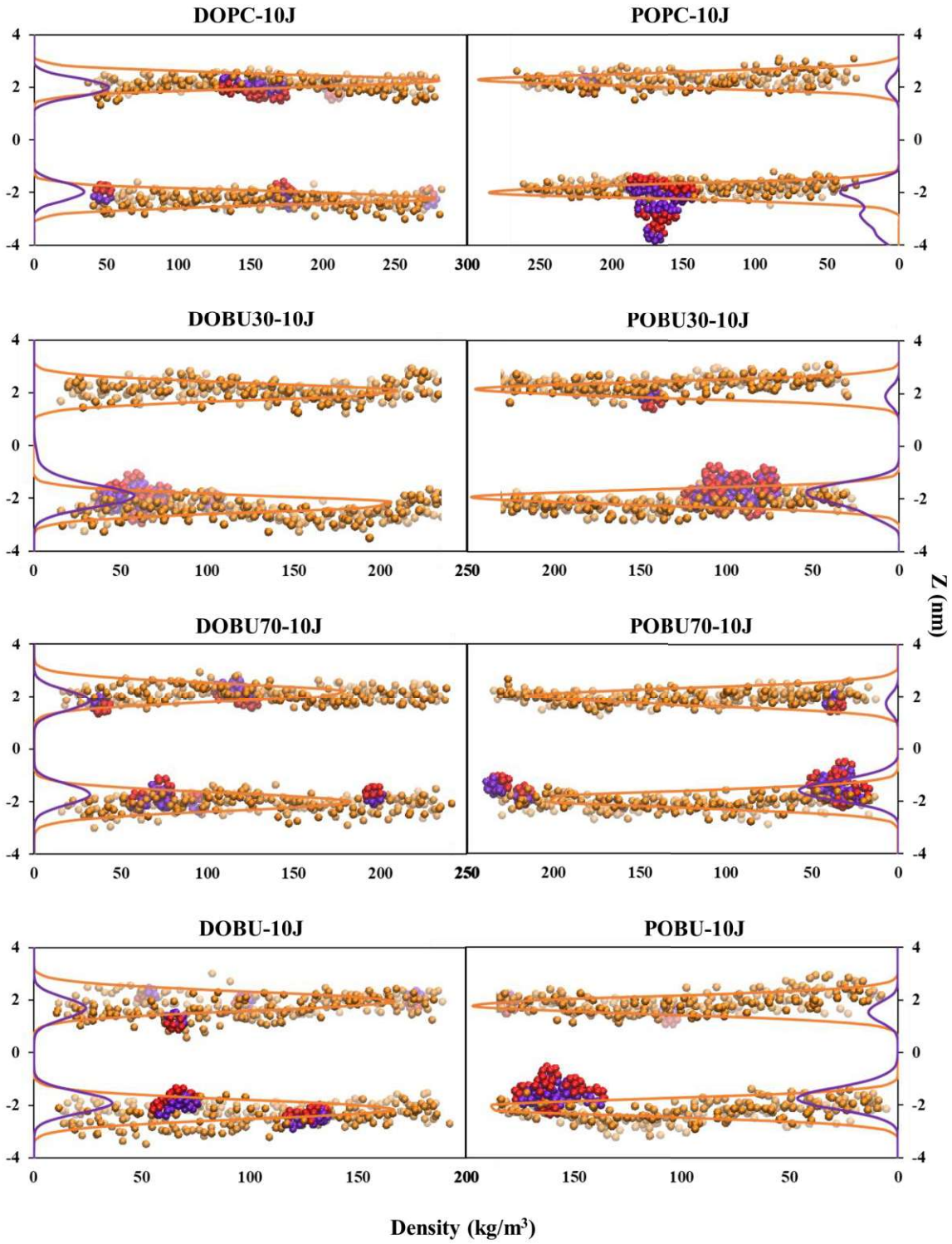

Figure 4.3. Density distribution profiles of lipid phosphate (PO4 beads) groups, and Janus fullerenes at fullerene to lipid ratio of F/L =10/512. Snapshots were taken from the last frame of the 10 μs trajectories.

The residence time of single fullerene NPs in the aqueous phase is demonstrated in Figure 4.4 and 4.5. As previously demonstrated, the residence time of pristine fullerenes in bulk water was found less than its polar derivative Janus. The longer time spent in the water was associated with the hydrophilic character of Janus NPs. As polarity increases, van der Waals interactions between the fullerene and water increase, and the penetration of fullerenes into the bilayer is restricted. Furthermore, it was observed that fullerenes diffuse into the peroxidized bilayers faster than that the regular bilayers due to the higher water permeability of peroxidized bilayers. This result reveals that the penetration of fullerenes is a diffusion limited process. Therefore, as expected, among all the membrane models studied, the longest time spent in the aqueous phase was recorded across the DOPC bilayer with 171 ns and 327 ns for pristine and Janus NPs, respectively. When the regular PC bilayer is compared to its fully peroxidized counterpart, the time difference was found to be more pronounced in DOPC and DOBU than in POPC and POBU. Since DOBU lipids are doubly oxidized, this may be the triggering factor behind the fast penetration of fullerenes. It is worth noting that we did not repeat the simulations by changing the initial configuration or the velocity of the fullerene molecules to draw a conclusion. However, our simulations including 10 fullerene NPs confirm the trends obtained by single fullerenes.

The interactions of fullerenes and their polar derivatives with the model membranes are further investigated through RDFs. The radial distributions of fullerenes with respect to the COM of the membranes are shown in Figure 4.6 for systems containing 10 fullerenes, while they are presented in Figure B.3 for systems containing a single fullerene. It was observed that the interactions of pristine fullerene NPs with the bilayers yield similar profiles regardless of the NP concentration. However, the interaction of Janus fullerenes with the lipid bilayers shows dependency on concentration with additional peak locations. Figure 4.6a and 4.6b reveal that the radial distributions of pristine fullerenes with respect to the regular DOPC and POPC bilayers have similar coordination shells despite the latter being steeper. At high peroxidation levels, i.e., 70% or 100% peroxidation, the interactions of pristine fullerenes with the bilayers result in similar RDF profiles. On the other hand, the interaction of Janus NPs with the model membranes is driven by their aggregation behavior: they more evenly disperse in POPC bilayer and its peroxidized forms than that DOPC (c.f. Figure 4.6c and 4.6d.)

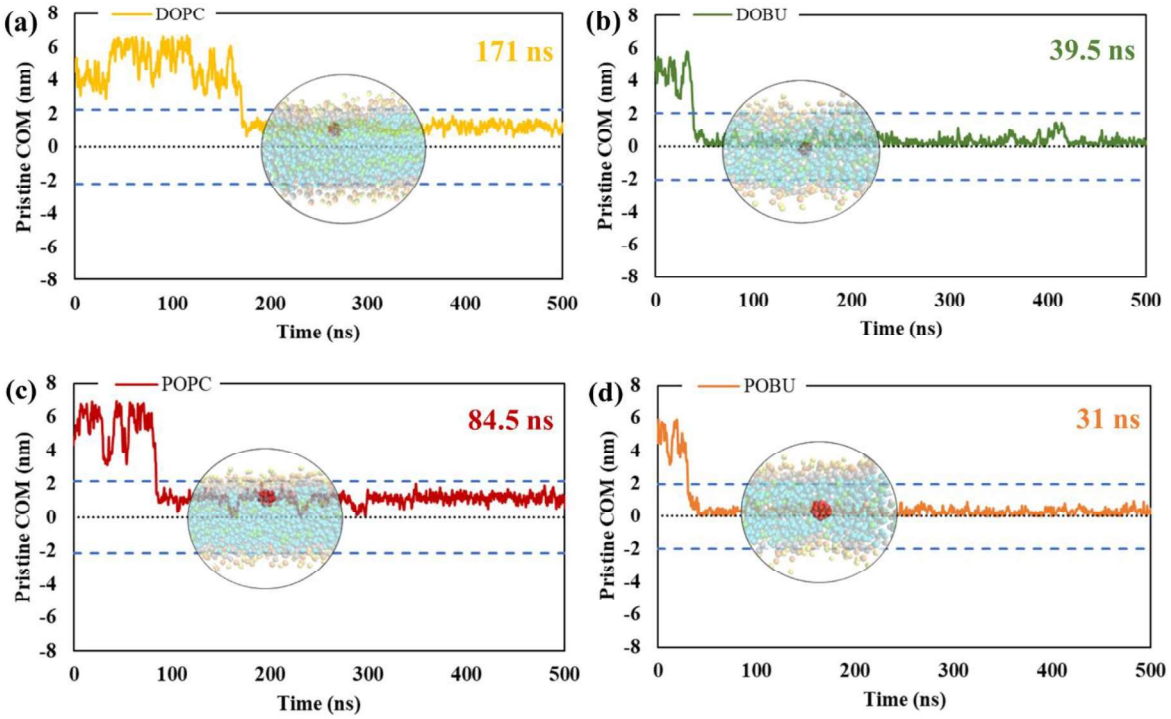

Figure 4.4. The absolute COM distance of pristine fullerene NP from a) DOPC, b) DOBU, c) POPC and d) POBU bilayers, respectively. The two dashed lines in blue denote the bilayer thickness in terms of the distance of PO4 beads between upper and lower leaflet in the corresponding bilayer. The center dashed line in black shows the center of the corresponding bilayer. The times on the upper right of the graphs represent the time fullerene spends in bulk water before entering the corresponding bilayer. The circular pictures demonstrate the average position of fullerene after entering the bilayer (Taken from trajectories at 175 ns, 53 ns, 95 ns, and 44 ns for DOPC, DOBU, POPC and POBU bilayers). Reproduced from Ref. [197] with permission from the Royal Society of Chemistry.

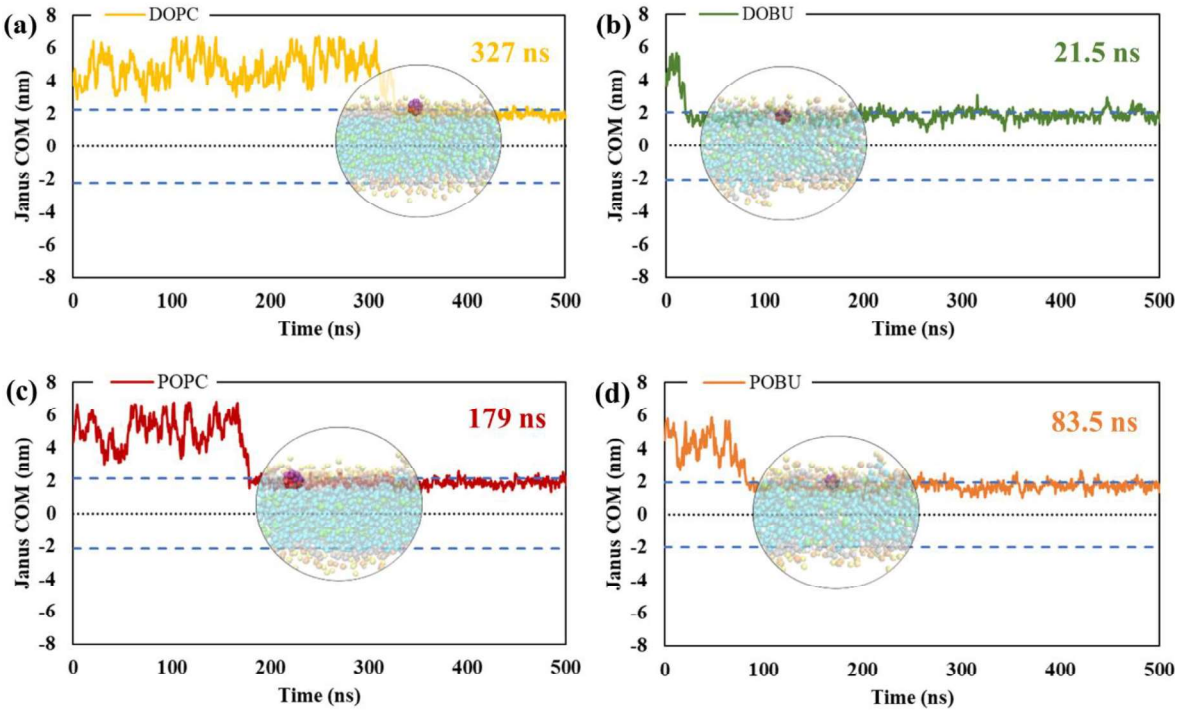

Figure 4.5. The absolute COM distance of Janus fullerene NP from a) DOPC, b) DOBU, c) POPC and d) POBU bilayers, respectively. The two dashed lines in blue denote the bilayer thickness in terms of the distance of PO4 beads between upper and lower leaflet in the corresponding bilayer. The center dashed line in black shows the center of the corresponding bilayer. The times on the upper right of the graphs represent the time fullerene spends in bulk water before entering the corresponding bilayer. The circular pictures demonstrate the average position of fullerene after entering the bilayer (Taken from trajectories at 353 ns, 22 ns, 200 ns, and 105 ns for DOPC, DOBU, POPC and POBU bilayers). Reproduced from Ref. [197] with permission from the Royal Society of Chemistry.

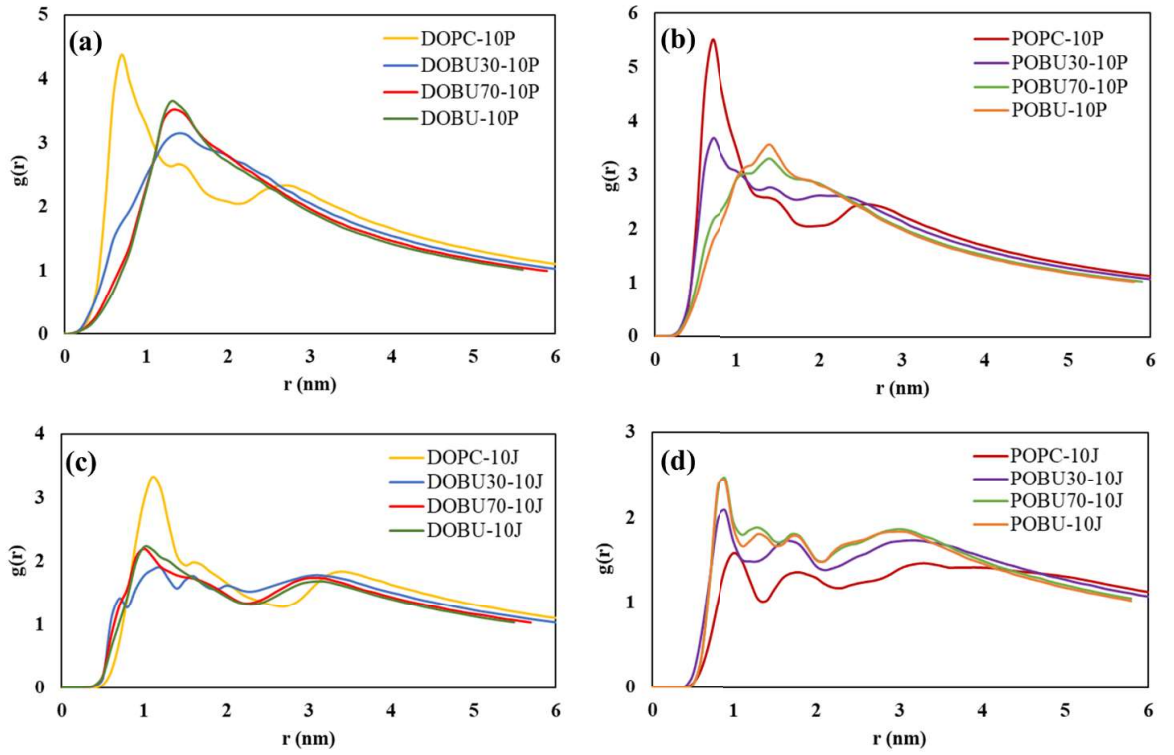

Figure 4.6. Membrane-Fullerene COM radial distribution functions for (a-b) pristine fullerenes, (c-d) Janus fullerenes at a fullerene-to-lipid ratio of 10/512. Reproduced from Ref. [197] with permission from the Royal Society of Chemistry.

The clustering and relative alignment of the fullerene molecules were determined by radial distribution analysis between the COM of the fullerenes. As shown in Figure 4.7, the RDF profiles of pristine fullerenes were found in agreement with previous studies [188,189]. Although the intensity of the peaks varied, the ordering of pristine fullerenes was identified as similar across all membrane types. For instance, in either 30 % peroxidized DOPC or 70% peroxidized POPC, it has been observed that the peak around 1.05 nm has a higher density than that of regular PC membranes due to the aggregation of fullerenes. To support this argument, we showed in Figure 4.8a that pristine fullerenes are internalized by normal PC bilayers as single or in small clusters, while they pass through 30% peroxidized DOPC in clusters of seven. Contrarily, for Janus fullerenes, the first nearest neighbor peak was determined to be high in both regular and peroxidized POPC bilayers. In particular, Janus fullerenes adsorbed on the surface of the POPC bilayer as aggregates of seven to nine molecules (c.f. Figure 4.8b). Nisoh et al. attributed the second nearest neighbor peak at 1.55

nm to the configuration in which a portion of the lipid tail is inserted between two fullerenes. Furthermore, Ding et al. proposed an intermediate peak caused by the peak splitting of the second shell through sharing of two or more atoms. We didn't observe peak splitting for pristine fullerenes but for Janus NPs, we identified an intermediate peak at 1.75 nm between second and third shell. This may be explained by the aggregation behavior of Janus fullerenes which lead to the sharing of second shell.

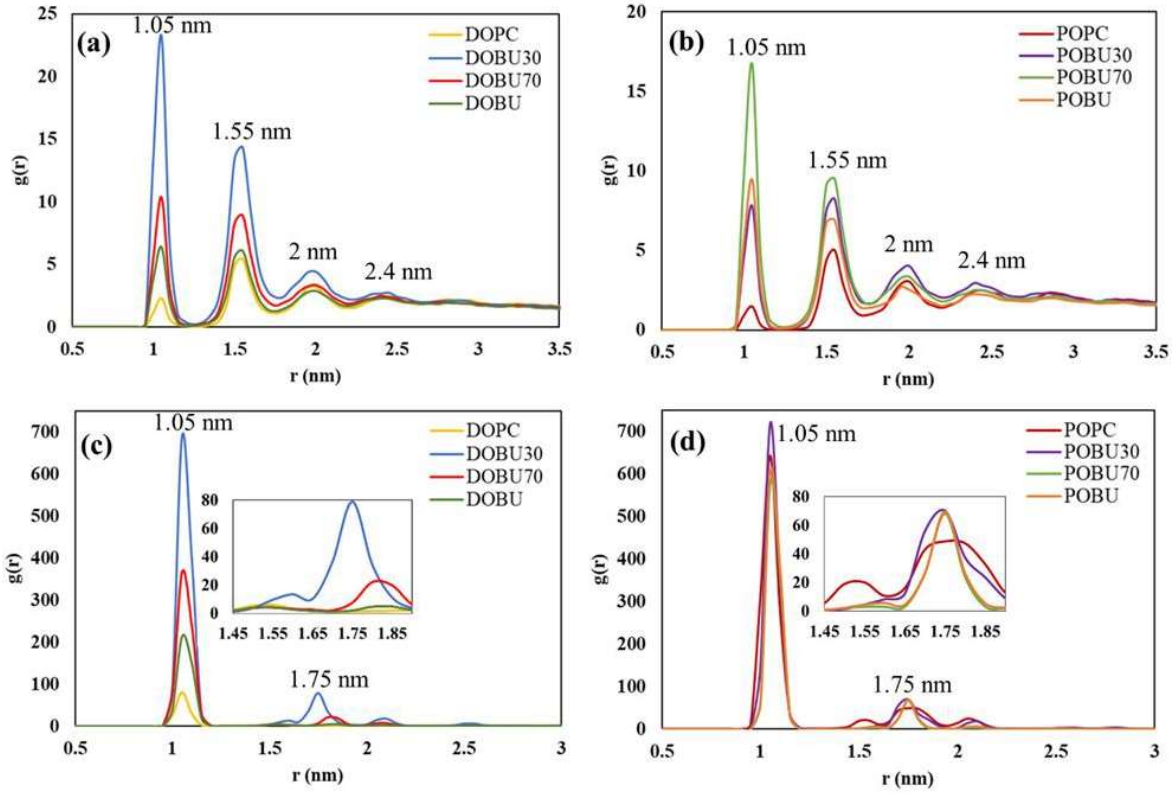

Figure 4.7. Fullerene-Fullerene COM radial distribution functions for (a-b) pristine fullerenes, (c-d) Janus fullerenes (enlarged between 1.45 – 1.90 nm in insets) at fullerene-to-lipid ratio of 10/512. Reproduced from Ref. [197] with permission from the Royal Society of Chemistry.

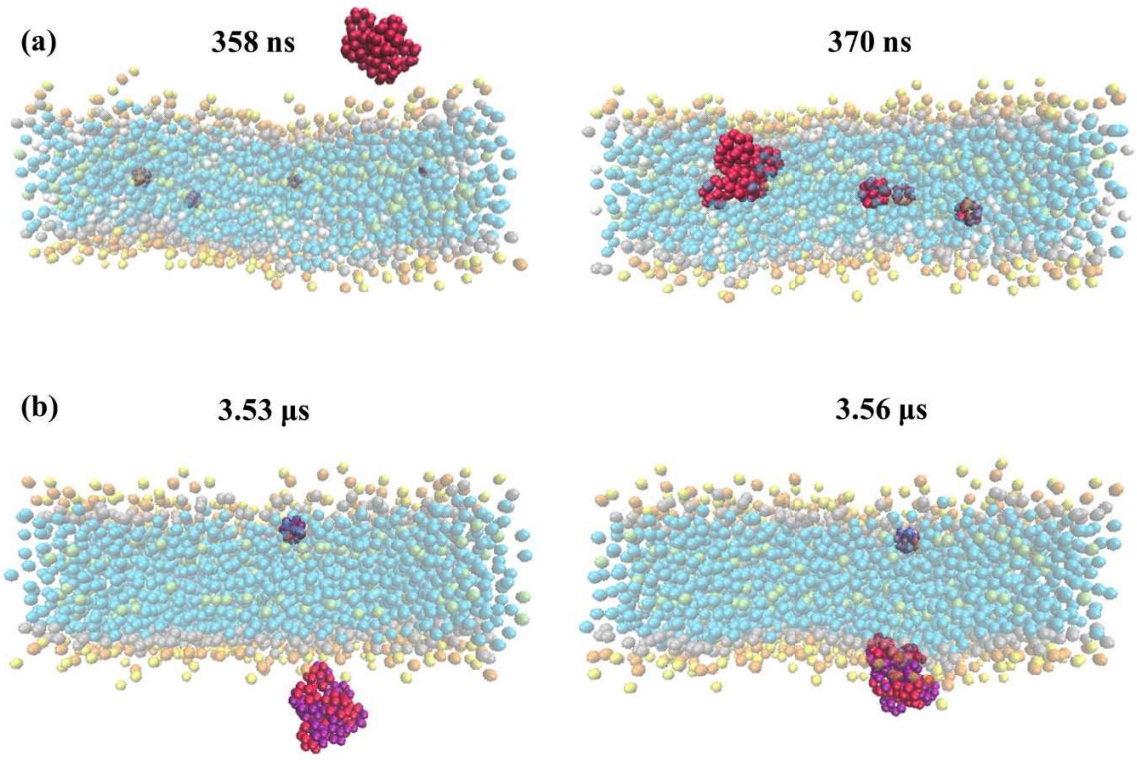

Figure 4.8. The aggregate of a) pristine fullerene molecules interact with DOBU30 bilayer at 358 ns and 370 ns, b) Janus fullerene molecules interact with POPC bilayer at 3.53 µs and 3.56 µs from side view. Reproduced from Ref. [197] with permission from the Royal Society of Chemistry.

In conclusion, we investigated the interactions of fullerenes and their half-polar derivatives with regular and peroxidized PC bilayers by CG simulations. The highlights of this study can be summarized as follows:

- Pristine fullerenes penetrate through the hydrophobic region of the membranes while Janus fullerenes are adsorbed on the lipid headgroups with the polar hemisphere toward the water and the apolar hemisphere toward the interior of the membrane.
- Pristine fullerenes are internalized in monomeric or oligomeric forms but disintegrate upon insertion inside the membranes. Janus fullerenes form larger clusters in water-bilayer interface but do not completely penetrate the bilayer.

- In regular PC bilayers, pristine fullerenes reside near glycerol groups while they concentrate on the center in fully peroxidized PC membranes.
- Fullerene translocation is similar in all peroxidized DOPCs, whereas their distribution differs in peroxidized POPCs. This was explained by the difference in lipid saturation level.
- The residence time of Janus fullerenes in bulk water is longer than that of pristine fullerenes because of the favorable interactions with water molecules.
- Radial distributions of pristine fullerenes with respect to the membrane center is similar in both concentration level while Janus NPs tend to aggregate in high concentration level.
- The diffusion or adsorption of fullerenes does not disrupt membrane integrity and lipid peroxidation is not the likely toxicity mechanism of fullerenes in terms of membrane rupture or damage.

In drug delivery platforms, pristine fullerenes are good candidates for use as nano-carriers, and the saturation and peroxidation levels of lipids, as well as fullerene concentration, are important parameters to control and regulate their performances. In this sense, we believe that our findings will contribute to the understanding of ROS-triggered BBB impairment and create a basis for the development of more complex systems in the future.

4.2. Toxicity Analysis of Nanoparticles by Association Rule Mining

After examining the interactions of fullerenes with membranes and their uptake mechanism, we extended our study and proposed an ML model on the toxicity mechanism of various nanoparticles, including carbon nanoparticles. First, ARM analysis was carried out by combining either single attribute and cell viability or multi attributes and cell viability using 24 hr data which corresponds to 2353 samples. Then, to support the extracted rules and make reliable interpretations, a time-dependent change of lift values was observed. As explained previously, cell viability was classified as high, medium, and low. The associations that resulted in high viability were discussed here while the low viability results are given in Table A.1 and A.2. The significance of a rule is mostly determined by the lift value (the greater the lift value, the higher the positive correlation with high viability), but

the support and confidence should also be taken into account with the corresponding counts. The number of samples satisfying the rule (count) presents evidence about the reliability of that rule. Therefore, if all the samples for a specific rule come from the same article, an asterisk has been added to the counts to alert readers to potential bias.

To clarify the statistical indicators of ARM like support, confidence, lift, and count, we can interpret the use of polystyrene material in association with cell viability. In this example, the antecedent is the material type of 'polystyrene' while the consequent is 'high viability'. There are 2353 samples, 125 of which are polystyrene, in the 24-hour data set, and among the polystyrene samples, 89 show high viability: the support of having high viability with polystyrene is 89/2353 = 0.038. Since 89 out of 125 samples result in high viability, count of high viability is 89 and the confidence of this rule is 89/125 = 0.71. In the data set, 1206 samples belong to the high viability class. The lift is the high viability ratio of the polystyrene material divided by the high viability ratio in the entire data set. Thus, the lift of having high viability with polystyrene material is (89/125)/(1206/2353) = 1.39, indicating that the fraction of having high viability with polystyrene is 1.39 times that in the entire data set. Based on this result, it can be stated that the use of PS as a nanoparticle material type is safe.

4.2.1. Single Variable Association with Cell Viability

Single factor associations with cell viability are presented in Tables 4.2 and 4.3 based on NP-related and cell-related descriptors of toxicity. The predominant factors in determining toxicity appear to be NP material, synthesis method, and exposed cell type. Among the NP material, hydroxyapatite (HAP) shows great potential for being a safe nano-carrier with a lift value of 1.83. Having good biocompatibility and biodegradability HAP exhibits chemical and structural similarity to bone minerals. As a calcium phosphate mineral, they have been extensively used in biomedicine and tissue engineering for bone repair and regeneration owing to their attractive physicochemical properties. Since they can easily bind to bone and interact with cells, they are suitable for use as drug carriers in bone therapy and osteogenesis treatment [288,289]. Similarly, chitosan polymers are biocompatible and biodegradable in addition to their muco-adhesive characteristics. The cationic nature of chitosan allows sustainable interactions with the membrane epithelium and provides

efficient uptake of drugs via mucoadhesion [290,291]. Therefore, it can be stated that biocompatible, and biodegradable NPs promote interactions with the cell membrane and lead to less toxicity.

From Table 4.2, it is also seen that iron oxide NPs have a high lift value of 1.40 with reasonably higher counts than other material types. There are different types of iron oxide in the data set such as iron (III) oxide (Fe_2O_3) or magnetite (Fe_3O_4) and most of the samples yielding high viability belong to the functionalized superparamagnetic iron oxide NPs [292–294]. Besides their magnetic properties, they have attracted attention due to their biocompatibility and biodegradability. On the other hand, iron oxide NPs suffer from aggregation because of the dipole-dipole forces between magnetic particles which are called dipolar coupling. Also, their adsorption of plasma proteins reduces the blood circulation time. Therefore, iron oxide NPs need to be modified with different groups to improve their biomedical usage [294,295].

The shape of the NP has an impact on its toxicity as well. Some NPs like titanium dioxide and silicon dioxide possess polymorphic structures. Titania has a complex shape that can be found in brookite, anatase, or rutile forms [296]. Silica may exist in crystalline forms such as cristobalite, quartz, and tridymite, or in the non-crystalline phase of amorphous form [297]. It was previously reported that amorphous silica nanoparticles do not lead to cytotoxicity, genotoxicity, and morphological transformation on Balb/3T3 mouse fibroblasts cell line [298]. It was also observed that prolonged exposure of amorphous silica to rat skin does not lead to toxicity [299]. Although it is still disputed [300], our findings support that shape disorganization has a positive correlation with cell viability. As the lift values reveal, irregularly shaped nanoparticles are found more beneficial than regularly shaped NPs. This can be explained as the irregularly shaped NPs promote interactions with the cell membrane thanks to their high surface area.

From Table 4.2, the appealing synthesis methods are shown to be reverse microemulsion and ionotropic gelation techniques with high lift values; however, it should be noted that the samples covering these rules are taken from single articles. Nevertheless, these synthesis methods may have potential significance to obtain specific nanoparticle types. For instance, all iron oxide NPs prepared by reverse microemulsion showed non-toxic

behavior [293] and 97 % of chitosan nanoparticles prepared by ionotropic gelation indicated high viability [290]. Although these results are not supported by the other sources in our data set, their potential shouldn't be overlooked.

Table 4.2. Nanoparticle-related single variable and high viability associations. Significant associations were listed in the table based on their ranked lift values. Here, the antecedents are the classes of 'material', 'shape', 'synthesis method', 'coat', 'surface charge', and 'concentration' while the consequent is 'high viability'.

Antecedent	**Support**	**Confidence**	**Lift**	**Count**
Material				
HAP	0.020	0.94	1.83	46
Chitosan	0.014	0.85	1.66	34*
Ceria	0.015	0.81	1.59	35
Eudragit RL	0.012	0.78	1.52	28*
PLGA	0.020	0.74	1.45	46
Iron oxide	0.052	0.72	1.40	122
Polystyrene	0.038	0.71	1.39	90
Shape				
Irregular	0.030	0.72	1.40	71
Synthesis Method				
Reverse Microemulsion	0.017	1.00	1.95	40*
Ionotropic Gelation	0.014	0.97	1.90	34*
Coat				
Silica	0.013	0.73	1.43	30
Carboxyl	0.024	0.73	1.42	57
Surface Charge				
Neutral	0.012	1.00	1.95	29
Concentration				
< 10 μg/ml	0.172	0.72	1.40	406

* Samples are from the same article

Surface functionalization and coating of NPs play important roles in their toxicity. The major functional groups that appear in our data set are citrate, PEG, chitosan, amine (NH_2), and carboxyl groups. Among these groups, silica and carboxyl show high lift values with similar confidence but having carboxyl functionalization results in high viability with more samples. In parallel to this argument, positive, negative, and neutral polystyrene NPs were compared through their cytotoxicity on alveolar macrophages, and it was found that anionic carboxyl modified polystyrene is less toxic than its cationic amine modified counterpart [301]. This was associated with the release of lysosomal enzymes that triggers apoptotic cell death. Similarly, in another study, carboxyl-modified polystyrene NPs changed lysosomal enzyme activity on endothelial cell lines without damaging lysosomal membrane integrity [302].

The interactions between NPs and cellular membranes may also be driven by the surface charge. Cationic NPs have been revealed to easily bind to the cell surface and enter the cell [3,303]; but, they have potentially toxic effects like mitochondrial membrane disruption [304], DNA damage [68,303], and prolongation of G0/G1 phase of the cell cycle [68]. It was reported that the internalization of positively charged gold NPs into the cell takes place faster and in larger amounts but causes more toxic effects [305]. Surface charge was identified as the most important feature of the toxicity of silver NPs by ML techniques [306]. However, we did not observe any prominent toxicity difference between positively and negatively charged NPs irrespective of the material type. Neutral NPs, on the other hand, found a little place in our data set as in the literature. However, this study reveals that neutral nanoparticles (between zeta potentials of ±1 mV in water) have promising potential in drug delivery applications, as all neutral NPs in our dataset exhibited high viability.

Most of the toxicity studies show that NP cytotoxicity is concentration-dependent [307,308]. As presented in Table 4.2, the rule of having high viability with NP concentrations less than 10 μg/ml is highly reliable with 406 counts. 25 % of these samples consist of gold NPs, followed by silver and iron oxides. Therefore, it can be misleading to treat the concentration regardless of the material type. This association will be further discussed in the next section in a material-specific manner.

In addition to the concentration, the diameter of NP has been addressed in determining the efficiency of its cellular uptake and toxic potential. However, we found that the diameter-only does not have any correlation with cell viability. Instead, we encountered a wide variety of cases that prevented us from making a generalization. Therefore, we consider the effect of diameter in the presence of other variables in the next section. The aspect ratio (length over width), on the other hand, is another descriptor of size which show significance with 69% confidence when spherical and cylindrical NPs (nanotubes, rods, and needles) are compared. The aspect ratio was found to be more beneficial between 10 and 100 for the safe design of NPs. It is noteworthy to mention that 74% of these NPs consist of carbon nanotubes of which 65% are MWCNTs.

Table 4.3. Cell-related single variable and high viability associations. Significant associations were listed in the table based on their ranked lift values. Here, the antecedents are the classes of 'cell type' and 'cell morphology' while the consequent is 'high viability'.

Antecedent	**Support**	**Confidence**	**Lift**	**Count**
Cell Type				
MBMC	0.014	0.97	1.90	34*
SIRC	0.010	0.83	1.62	25*
SHSY5Y	0.020	0.78	1.53	47
HCMEC	0.017	0.74	1.44	40*
HUVEC	0.039	0.73	1.43	91
PC12	0.016	0.72	1.40	38
L929	0.018	0.71	1.39	42
Cell Morphology				
Spindle	0.021	0.77	1.50	50
Endothelial	0.042	0.73	1.43	99
Irregular	0.016	0.72	1.40	38

* Samples are from the same article

The cytotoxicity of NPs also varies based on the cell type they are exposed to (Table 4.3). [309] Indeed, previous meta-analysis studies [5,122] demonstrated that cell type is one of the significant descriptors of toxicity. This was confirmed in our cell type association results with the lift values between 1.39-1.90 above 70% confidence. The reason behind the

importance of cell type was mainly attributed to the level and nature of cell association with the NPs, composition differences in cell culture media as well as the degree of NP agglomeration in varying amounts of serum proteins [310]. Moreover, it is seen from Table 4.3 that cell morphology affects the interactions between NPs and the cell membrane. Here, spindle-shaped, and endothelial cell lines are found to be more beneficial in obtaining high cellular viability.

Apart from NP and cell descriptors, the toxicity tests and conditions may have effects on screening toxicity [2]. To test the reliability of the measurements, cell viability was determined by various types of assays. According to the assays used, some experiments showed parallel results [311,312] while some exhibited contradictory outcomes [313]. On the other hand, our results indicate that CCK-8 and MTS assays yield high viability with the lift values of 1.27 and 1.22, respectively above the 60% confidence interval. The common point of both tests is that they rely on the reduction of the tetrazolium salt. However, there may be a correlation between cell type and test type, along with the physicochemical properties of NPs, which could result in different cytotoxic behaviors. Therefore, binary or ternary relationships between these factors and their effects on toxicity are also discussed in the next section.

4.2.2. Multiple Variable Association with Cell Viability

Although the relationships between a single variable and cell viability allow us to draw general conclusions about the importance of the factor itself, these factors may be insufficient to understand the toxic behavior of NPs because these factors are not completely independent of each other. For example, it may not be possible to produce the desired material with every synthesis method or to combine every material with the desired surface group. For this reason, two or more factors are examined together to determine their effects and importance on cytotoxicity. To this end, we first explored material-based associations, taking into account the material type, preparation method, and other properties such as size, shape, surface charge, and PDI. Significant rules are listed in Table 4.4 in the order of their lift values.

Table 4.4. Material-based two factor associations resulting in high viability. Significant associations were listed in the table in the order of lift values with confidence ≥ 70%.

Antecedent	Support	Confidence	Lift	Count
Material & Shape				
HAP, Rod	0.019	1.0	1.95	45
Chitosan, Irregular	0.012	1.0	1.95	28*
PLGA, Sphere	0.018	0.86	1.68	43
Eudragit RL, Sphere	0.012	0.78	1.52	28*
Iron oxide, Sphere	0.052	0.73	1.42	122
Titanium oxide, Sphere	0.017	0.71	1.38	41
Polystyrene, Sphere	0.036	0.70	1.38	84
Material & Diameter				
HAP, (10, 25] nm	0.010	1.0	1.95	24*
Iron oxide, (0, 10] nm	0.017	0.95	1.86	40
Cerium oxide, (10, 25] nm	0.012	0.94	1.82	29
Eudragit RL, (100, 200] nm	0.012	0.78	1.52	28*
Iron oxide, (25, 100] nm	0.011	0.75	1.46	27
Titanium oxide, (10, 25] nm	0.013	0.75	1.46	30
Polystyrene, (25, 100] nm	0.033	0.71	1.38	78
MWCNT, (10, 25] nm	0.017	0.71	1.38	41
Material & PDI				
PLGA, (0, 0.2]	0.010	0.86	1.67	24
Eudragit RL, (0, 0.2]	0.012	0.78	1.52	28*
Polystyrene, [0, 0.2]	0.033	0.75	1.47	77

* Samples are from the same article

From Table 4.4, it is seen that all HAP NPs in rod shape exhibit high viability with 100 % confidence. Chitosan NPs are in favor of irregular geometry whereas other NPs which cause high viability are in a spherical shape. In particular, iron oxide NPs have a sufficient number of samples to support the rule of spherical shape to obtain high viability. When the material and diameter association is analyzed, the appropriate size ranges differ according to the material type. While HAP NPs synthesized between 10-25 nm in size show a high potential to protect cell viability, iron oxide NPs mostly show low toxicity with a diameter

of 10 nm and less. Furthermore, polystyrene NPs with a diameter in the range of 25-100 nm exhibit high viability with the highest counts of samples obeying that rule.

PDI is a measure of heterogeneity in terms of the size of particles. According to literature, PDI values less than 0.2 points out that the particles are uniformly dispersed [314] whereas larger PDI values show the possible agglomeration or aggregation of that particles. In Table 4.3, it is observed that PLGA, Euragit RL, and polystyrene cause fewer toxic effects if they are monodispersed with PDI values of 0.2 and less. The polydispersity of NPs was associated with the adsorption of proteins or other compounds in the cell medium [301] and the resultant agglomeration of NPs considerably reduced the uptake levels and translocation through the tissues. The upper agglomerate size of NPs to be internalized and transfer across the tissue was reported as 250 nm [315].

In Table 4.5, three-factor associations with cell viability are shown. When the association of material and diameter was extended with the incorporation of surface charge, exposure dose, and cell type, we obtained different rules based on statistical significance. In the former, negatively charged NPs, especially iron oxide, and polystyrene, are observed to be more favorable to obtaining low toxicity. Conversely, with the same diameter range of polystyrene (25-100 nm), anionic silver NPs exhibited 50 % more probability of having toxicity (Table A.2). The toxic potential of silver NPs was previously reported by a perturbation based QSAR study conducted on the ecotoxicity and cytotoxicity of metals and metal oxides. However, the association of material, diameter, and dose indicate that silver NPs are not toxic if their concentration is less than 10 μg/ml. Similarly, small gold NPs with 10 nm and less diameter do not show toxicity in the same concentration range of silver. On the other hand, polystyrene in 25-100 nm diameter maintains cell viability at doses up to 100 μg/ml. Furthermore, zinc oxide NPs with 25-100 nm size and concentration ranges of 10-100 μg/ml, were found to have a high negative correlation with cell viability (Table A.2) as reported previously [137,316]. When the material type, diameter, and cell type are associated with the cell viability, the only significant rule which we determined reveals that MWCNTs between 10-25 nm diameter have favorable interactions with human umbilical vein endothelial cells (HUVEC).

Table 4.5. Material-based three factor associations resulting in high viability. Significant associations were listed in the table in the order of lift values with confidence ≥ 70%.

Antecedent	Support	Confidence	Lift	Count
Material, Diameter & Surface Charge				
Iron oxide, (0, 10] nm, Negative	0.013	0.94	1.83	31
Polystyrene, (25, 100] nm, Negative	0.025	0.92	1.80	59
Eudragit RL, (100, 200] nm, Negative	0.012	0.78	1.52	28*
Material, Diameter & Exposure Dose				
Silver, (25, 100] nm, (0, 10) μg/ml	0.012	0.90	1.76	28
Gold, (0, 10] nm, (0, 10) μg/ml	0.016	0.86	1.68	38
Polystyrene, (25, 100] nm, [10, 100] μg/ml	0.027	0.70	1.37	64
Material, Diameter & Cell Type				
MWCNT, (10, 25] nm, HUVEC	0.011	0.75	1.46	27
Material, Coat & Synthesis Method				
HAP, None, Precipitation	0.014	1.0	1.95	33
Chitosan, None, Ionotropic Gelation	0.014	0.97	1.90	34*
Polystyrene, COOH, Commercial	0.017	0.79	1.54	41
Eudragit RL, None, Emulsion–Solvent Evaporation	0.012	0.78	1.52	28*
Titanium oxide, None, Commercial	0.023	0.76	1.49	55

* Samples are from the same article

It has been shown that the toxicity of NPs is related to the hydrophobicity of the coating material and the more the polar surface of the coats the less the possibility of toxicity [6]. We validated this interpretation by observing that hydrophobic polystyrene NPs have less toxicity when modified with polar COOH groups. Additionally, we found that bare HAP NPs prepared by precipitation method show about 2 times more probability of having high viability than that in the data set. Among the metal oxides, we identified that only commercial titanium oxide NPs yield high viability with sufficient counts of samples.

As mentioned earlier, the effects of nanomaterials vary according to the cells to which they are exposed, so the mechanism of cell responses should be well understood. As shown in Table 4.6, specific cell types provide good compatibility with some nanoparticles. For example, the human bone marrow epithelial cell line (SHSY5Y) which is often used as a model in the treatment of neurological diseases such as Parkinson's disease and neurogenesis, maintains its viability in the presence of iron oxide NPs [317,318]. Furthermore, the exposure of MWCNTs to HUVEC which is applied as primary cells in vascular diseases such as atherosclerosis resulted in high viability [319,320].

Material and cell type variables are investigated in conjunction with toxicity assays, as the test methods used may have different effects on the cellular environment. The association of material and test type with the cell viability demonstrates that the CCK-8 assay yields higher viability for HAP NPs with a lift value of 1.95 while MTT assays result in high viability for iron oxide NPs with a high count value of 82. Similarly, the combination of cell types and assays used presents that MTT and CCK-8 assays have a significant correlation with viability. As mentioned before, both tests are based on the reduction of tetrazolium salts to measure metabolically active cells and, previously, it was reported that tetrazolium-based assays result in higher viability when compared to other methods such as LDH release [5]. Chemical constituents of an assay have the potential to be safe or harmful and the response of the cell may even change depending on the interference of assay chemicals with the cell media content. According to the interactions of compounds, the assay may yield misleading results. Indeed, many groups have shown that tetrazolium-based assays in the presence of reducing agents can be misleading by exhibiting lower or higher cell viability [223,321]. Nevertheless, they are widely used assay types and general conclusions can not be drawn based on this outcome.

Table 4.6. Cell- and test- based three factor associations resulting in high viability. Significant associations were listed in the table in the order of lift values with confidence ≥ 70%.

Antecedent	Support	Confidence	Lift	Count
Material & Cell Type				
Iron oxide, SHSY5Y	0.017	1.00	1.95	40
Chitosan, MBMC	0.014	0.97	1.90	34*
Silica, PC12	0.011	0.87	1.69	26*
MWCNT, HUVEC	0.015	0.80	1.56	36
Material & Assay Type				
HAP, CCK-8	0.019	1.00	1.95	45
Chitosan, MTT	0.014	0.85	1.66	34*
MWCNT, MTS	0.012	0.80	1.57	29*
Cerium oxide, MTT	0.011	0.77	1.50	27
Iron oxide, MTT	0.035	0.75	1.47	82
MWCNT, CCK-8	0.011	0.74	1.45	26
Polystyrene, MTT	0.025	0.73	1.42	59
Cell Type & Assay Type				
MBMC, MTT	0.014	0.97	1.90	34*
SIRC, MTT	0.011	0.83	1.62	25*
SHSY5Y, MTT	0.010	0.75	1.46	24
HUVEC, CCK-8	0.029	0.75	1.46	69
HCMEC, MTT	0.017	0.74	1.44	40*
Material, Cell Type & Assay Type				
Chitosan, MBMC, MTT	0.014	0.97	1.90	34*
Silica, PC12, MTT	0.011	0.87	1.69	26*
MWCNT, HUVEC, CCK-8	0.011	0.74	1.45	26

* Samples are from the same article

4.2.3. Long-Term Cell Viability Analysis

In this section, we study the long-term effect of nanoparticles, on cell viability based on material type, preparation method, coating agent, and exposure concentration. We observed the change in lift values with the criterion of maintaining at least 85% cell viability.

Thus, ARM was applied for four-time intervals: viable for more than 24 hr, viable for more than 48 hr, viable for more than 72 hr, and viable for 96 hr. As mentioned before, these criteria are the cumulative combination of time data, i.e., the '24 hr and more' class contains the samples in 24 hr, 48 hours, 72 hours, and 96 hours; '48 hr and more' class includes 48 hr, 72 hr and 96 hr; and so on. The increase in lift values indicates that it is appropriate to use that factor in the long term without creating a toxic effect. Because if the number of viable cells involving that factor does not drop or drop less than the total viable cells with time, the lift value of using that factor increases.

The lift values based on the single factor associations of material, coating agent, preparation method, and exposure concentration with cell viability are presented in Figure 4.9. In 72 hr period, it is shown that cells exposed to HAP, chitosan, and PAMAM dendrimers maintain their viability, however iron oxide NPs cause toxicity. since iron oxide NPs are prone to agglomeration, their blood circulation time is shorter. As a result, they are not suitable to use in the long-term in drug delivery applications, still, their stability and blood circulation halftime can be promoted by surface functionalization [322,323]. Moreover, it is found that the lift values of silver nanoparticles, which are generally toxic, increase on the fourth day. When examining the silver samples in detail, it was found that the samples belonging to the fourth day are rod-shaped and synthesized by electron beam physical vapor deposition (EBPVD) method rather than conventional preparation methods. Therefore, the synthesis method can be considered an important factor to control the toxicity of silver NPs.

Figure 4.9b indicates that the use of the carboxyl functional group provides high cell viability even on the third day. Thus, the carboxyl-modified NPs have high potential in controlled drug delivery in the long term in parallel to our previous findings. Additionally, it is seen that citrate which is mostly used to stabilize gold and silver NPs, appears to be beneficial in two days period but the number of viable samples decreases significantly after the second day. Therefore, it should be noted that citrate coating may maintain cell viability in the short term but can lead to toxicity in the long run. Furthermore, it is observed that the lift values of PEG and chitosan coats rise on the second day. However, there is no PEG or chitosan data in the third and fourth days and to extract a rule, they should be studied further

with more samples. The lift of non-functionalized NPs, on the other hand, was found to be around one implying no correlation with cell viability and therefore is not shown here.

Some synthesis methods including reverse microemulsion, mini-emulsion polymerization, and ionotropic gelation, reveal the potential importance of these methods with high lift values and also give evidence of the heterogeneity of the data set. In the previous section, the material-specific synthesis methods were discussed, however, two important outcomes that are seen in Figure 4.9c are the decrease of lift values in soft templating method and the sudden increase of the lift value of chemical reduction on the fourth day. The former was attributed to the toxic effect of NPs prepared by the soft templating method (usually silica NPs) in cells from the third day. In the latter, the chemical reduction method, which normally exhibits a lift value of around 1 for three days, is identified to be used to prepare star-shaped gold NPs instead of spherical NPs on the fourth day resulting in high viability.

When the effect of concentration of NPs on cell viability is investigated in the long-term, it is observed from Figure 4.9d that NPs which interact with cells at exposure doses less than 10 μg/ml for three days are safer. On the other hand, concentrations higher than 200 μg/ml pose a risk of toxicity as can be seen from the lift values. The lift values of 100-200 μg/ml doses, which are negatively correlated with the cell viability in the first three days, increase on the fourth day. Therefore, it is noteworthy to mention that samples between 100-200 μg/ml emerging on the fourth day as highly viable include star-shaped gold NPs prepared by chemical reduction method and COOH coated silica nanoparticles prepared by the soft templating method.

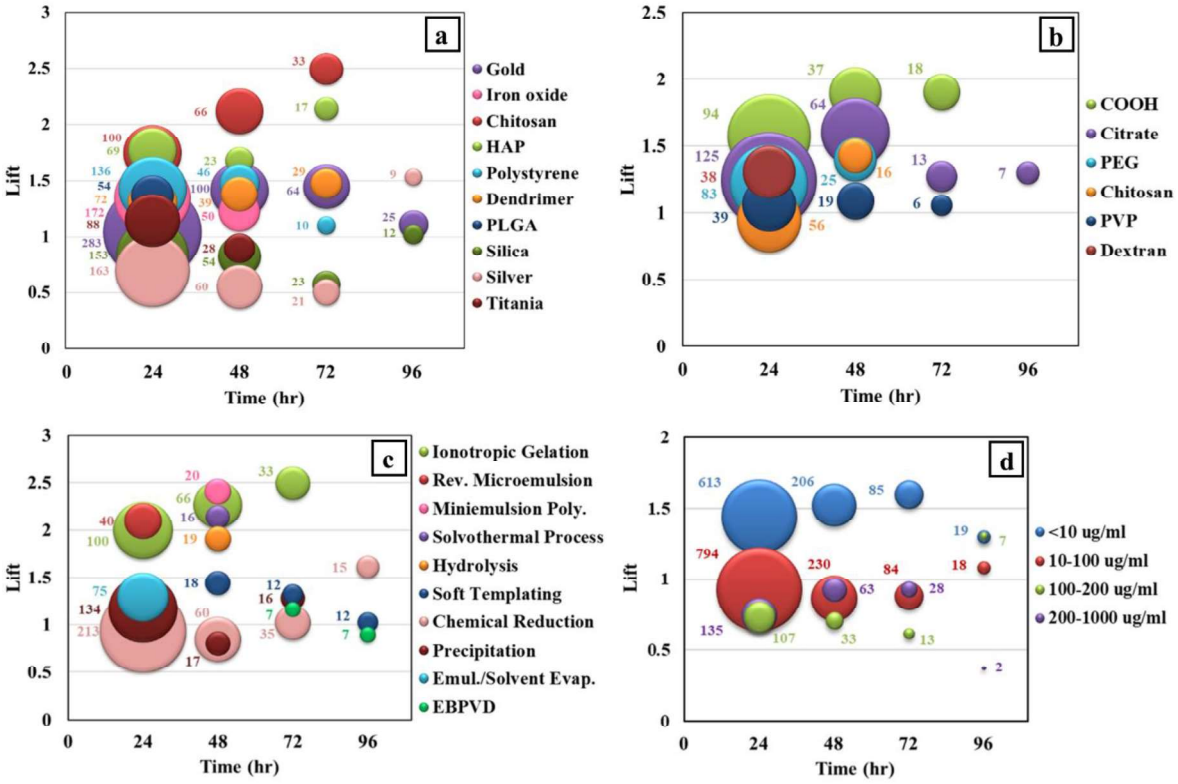

Figure 4.9. The effect of the variables of a) material, b) coating agent, c) preparation method, d) concentration on cell viability with respect to time. Reproduced from Ref. [9] with permission from the Royal Society of Chemistry.

In conclusion, the cytotoxicity of NPs has been investigated by ARM, which is a rule-based ML algorithm, using previously reported in vitro test results of inorganic, organic, and carbon-based NPs. The toxicity endpoint was specified through cell viability while the descriptors were determined as physicochemical properties of materials as well as the cell properties and test conditions. The resultant data set included 4111 samples from 152 articles with 15 qualitative and 10 quantitative attributes. Our results showed that NP toxicity is mainly associated with the core and coating material of the NPs, their synthesis method, and the cell types to which they are exposed. Moreover, the single and combined associations of variables provided easy-to-follow inferences as well as shed light on the hidden relationships between the variables and the cell viability. The conclusions drawn can be summarized as follows:

- Biocompatibility and biodegradability play important roles in NP safety. HAP, chitosan and polystyrene stand out in this sense by yielding high viability in most cases.
- The negative carboxyl group stabilizes the NPs, regulates their interaction with the cell, and provides long-lasting use. In particular, carboxyl-modified polystyrene appear as a safe nano carrier with high count of samples compared to other NPs.
- Cylindrical-shaped NPs with aspect ratios between 10 and 100, like nanotubes, rods, and needles, is advantageous in maintaining cell viability.
- Since it is not possible to prepare the desired NP species with every synthesis method, it is more appropriate to prefer material-specific synthesis methods; for example, precipitation can be used for HAP, reverse microemulsion for iron oxide, and emulsion-solvent evaporation for polymeric NPs (PLGA and Eudragit RL).
- Tetrazolium-based assays like MTT and CCK-8 generally yield higher viability results when compared to color-coded assays like Alamar Blue, and Neutral Red Uptake (NRU).
- In general, NPs that come into contact with cells for one day or less at a concentration below 10 μg/ml do not appear to be toxic.

Consequently, this study shows that based on published experimental findings, NP toxicity can be characterized, and important determinants of toxicity can be identified. As the sample space grows with additional valuable data, more reliable rules can be drawn, and the mechanism of toxicity can be understood more clearly. To achieve this, it is necessary to overcome the limitations caused by the heterogeneity of the data, the lack of standardized testing protocols, and knowledge gaps. Our results will be useful in understanding the underlying causes of the harmful effects of NPs and laying the groundwork for future research so that their safe design can be made.

4.3. Interactions of Carbon Nanotubes with Lipid Bilayers by Atomistic Simulations

In comparison to fullerene NPs, CNTs can carry the drug molecules not only on their surfaces but also inside their tubes and release them to targeted cell regions on demand through surface modification. Moreover, as demonstrated in several studies, CNTs have superior transport properties and can deliver cargo, specifically genes, more efficiently than other NP alternatives [324]. In the previous section, we determined that carboxyl-modified polystyrene NPs are safe for maintaining cell viability, whereas carbon nanoparticles were found to be relatively toxic. Therefore, to improve the performance of carbon nanoparticles and reduce their toxicity, CNTs were functionalized with PS and PSCOOH at atomistic and CG levels.

First, the interactions of pristine and PS functionalized CNTs with the POPC bilayer are investigated in atomistic detail and a model drug, IBU, was loaded to the CNTs to observe their drug release potential. Membrane properties, i.e., APL and bilayer thickness, in the absence and presence of IBU is presented in Table 4.7. The APL and bilayer thickness values of pure POPC were calculated as ~0.65 nm^2 and ~3.9 nm, respectively, in parallel to the experimental ranges of 0.64–0.68 nm^2 and 3.70–3.91 nm [281,282]. With the addition of the NPs, APL values slightly change, however, this variation is less than 2 % in all cases. Similarly, bilayer thickness increases in a negligible manner as is more apparent with PSCOOH-modified CNTs. As reported elsewhere [13,208,216], CNTs penetrate the bilayer passively without showing an adverse effect on membrane structure like pore formation, membrane rupture, or disruption. The uptake mechanism of CNTs is closely related to their length, and it has been previously reported that short nanotubes ($\leq$ 1μm) are internalized from the cell membrane by non-endocytic pathways [209,325]. The passive penetration of the 3 nm CNTs used in our study also confirms this.

Table 4.7. Area per lipid and bilayer thickness values of pure POPC, and with pristine/functionalized CNT models, i.e., pristine carbon nanotube (CNT), polystyrene functionalized carbon nanotube (PSCNT), carboxyl-terminated polystyrene functionalized carbon nanotube (PSCOOHCNT), in the presence and absence of ibuprofen (IBU).

Model	**Area Per Lipid (nm^2)**	**Bilayer Thickness (nm)**
POPC	0.650 ± 0.012	3.88 ± 0.06
POPC – CNT	0.641 ± 0.010	3.97 ± 0.05
POPC – PSCNT	0.654 ± 0.011	3.98 ± 0.05
POPC – PSCOOHCNT	0.646 ± 0.012	4.02 ± 0.06
POPC - CNT – IBU	0.638 ± 0.011	3.99 ± 0.05
POPC - PSCNT – IBU	0.649 ± 0.011	4.01 ± 0.06
POPC - PSCOOHCNT – IBU	0.648 ± 0.010	4.02 ± 0.05

The tilt angle between the long axis vector of CNTs and the membrane normal was calculated throughout the simulation time and presented in Figure 4.10 with the histograms representing the average equilibrium angles. In literature, it has been shown that short CNTs (~2 nm) align parallel to the lipids when embedded within the bilayer [326] while longer CNTs make larger angles with the normal of the bilayer to maximize their interactions with the hydrophobic region of the bilayer [201,219]. Geng et al. determined the tilt angle of 0-15° using CNTs in 1.5 nm inner diameter and 5-15 nm length in DOPC membrane through the cryogenic TEM technique [327]. With a similar sized CNT, Tran et al. calculated the tilt angle of 0-15° range by in situ SAXS measurements and proposed that the addition of CNTs causes local tilting of lipids which results in a bilayer thinning effect [328]. Recently, Sullivan et al. calculated a broader range of tilt angles (0-25°) in equimolar DMPC/DOPC bilayer by developing a geometric model with the apparent CNT height in AFM images [329]. Similar to Sullivan et al., we observed that CNTs were found with a tilt angle of 0°-25° with respect to the membrane normal (c.f. Figure 4.10a). Additionally, we identified that the insertion of CNTs results in a bilayer thickening effect contrary to Tran et al.

Previously, it has been reported that the configurational preferences of CNTs can change based on the functional groups. Vögele et al. stated that modifying CNTs with polar groups like hydroxyl and carboxyl prevent the tilting of nanotubes with respect to the bilayer

normal [219]. In another study, hydroxyl-modified CNTs were shown to orient vertically between lipid headgroups of opposite leaflets when the length of the CNT is less than the bilayer thickness [216]. In our study, PS functionalized CNT was found to prefer near-perpendicular alignment with the lipids with a tilt angle of ~82° (c.f. Figure 4.10b). On the other hand, PSCOOH functionalized nanotube rotated upside down upon insertion into the membrane and tilted with a mean angle about 20° from bilayer normal as shown in Figure 4.10c. Moreover, IBU loading of the nanotubes caused slightly wider angle distributions for both pristine and functionalized CNTs. In the presence of IBU, PS-modified CNT preferred to align almost parallel to the lipids, unlike its unloaded counterpart. The internalization of the IBU-loaded functionalized nanotubes was observed to occur at their non-functionalized rims. Upon insertion into the hydrophobic core of the membrane, both nanotubes rotated upside down and adopted a near-vertical position with about 25 tilting angles. The configurational choices of the CNTs can be understood better by the angle shifts demonstrated in Figure 4.10e and f.

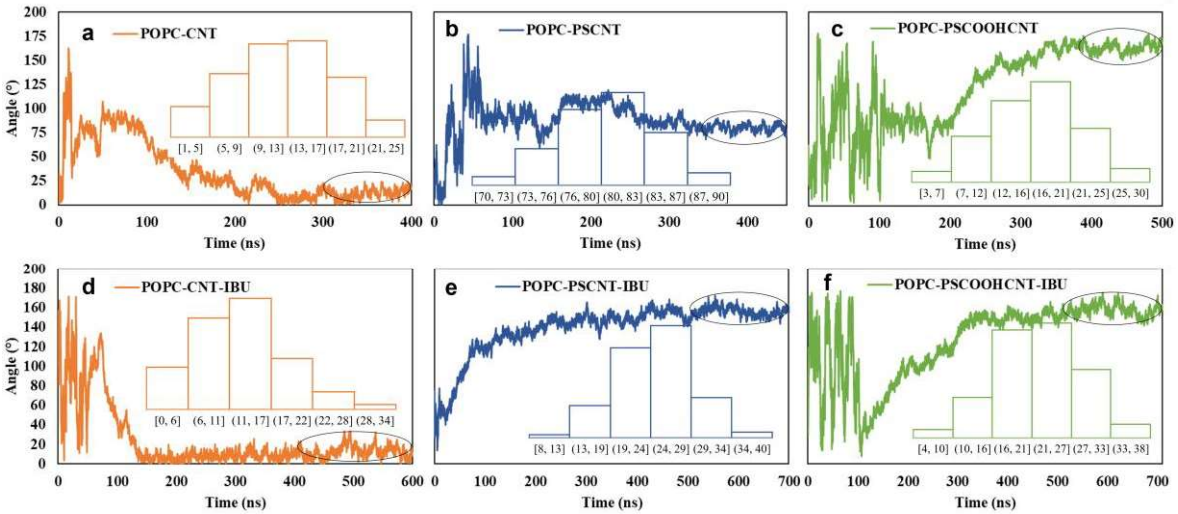

Figure 4.10. The angle distribution between pristine/functionalized CNTs and lipid bilayer normal in the absence (upper panel) and the presence (lower panel) of IBU. The histograms show acute angle distributions after configurational equilibration (from the last 100 ns or 200 ns of the trajectories for no IBU and with IBU, respectively) of the nanoparticles inside the membrane which is encircled. Angles above 90° demonstrate the rotation of the tubes, hence, values were subtracted from 180° while forming the histograms.

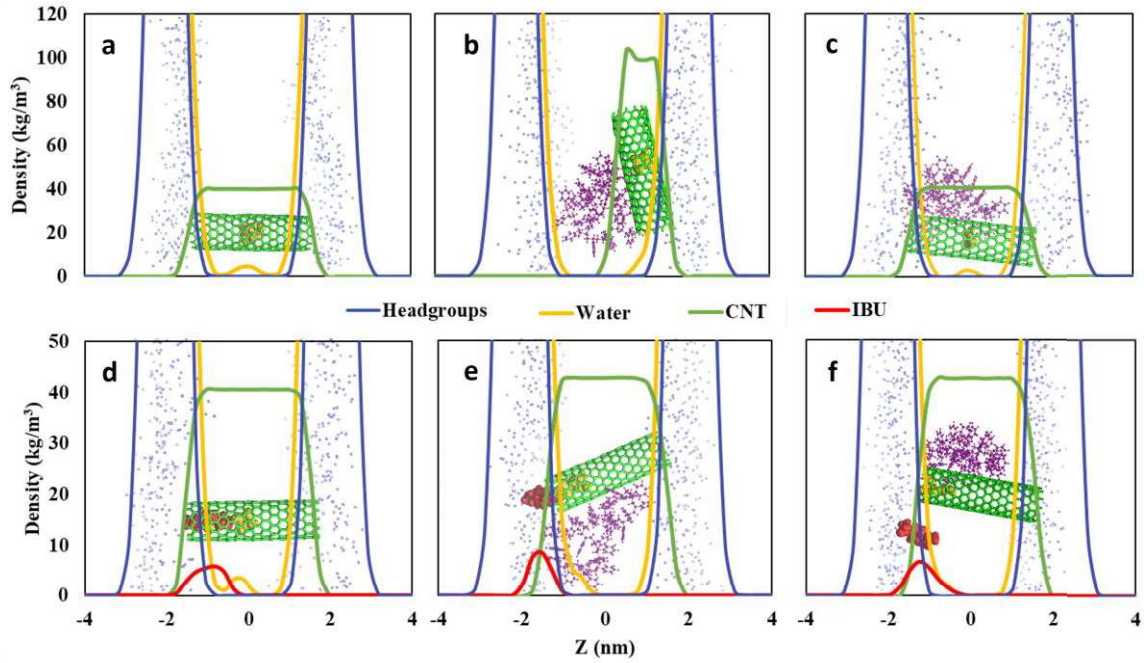

Figure 4.11. The density distributions of the lipid headgroups, water, CNT, and IBU for a) POPC-CNT, b) POPC-PSCNT, c) POPC-PSCOOHCNT, d) POPC-CNT-IBU, e) POPC-PSCNT-IBU, f) POPC-PSCOOHCNT-IBU systems. The illustrations of configurations match the lines in a color-coded manner. Polystyrene functional groups (purple), and water molecules (yellow) between lipid headgroups are not shown in the graphs to avoid confusion.

The translocation behavior of the CNTs is also investigated by density distribution analysis and density profiles of CNTs confirm our findings obtained through angle calculations. From Figure 4.11 it is seen that PS functionalized CNT aligns perpendicular to the bilayer normal at a 1 nm distance away from the bilayer center, while the other CNTs prefer a parallel alignment at the center of the bilayer. Furthermore, the CNTs drag water molecules across the bilayers during their insertion process. The open ends of the CNT allow water molecules to penetrate inside the tube and transport along the bilayer as reported elsewhere [181,202]. It has been discussed that open-ended nanotube may also lead to the penetration of lipid headgroups or lipid tails along the extremity of the bilayer [208]. In this context, closed-ended CNT was identified to give less damage to the structure of the membrane and has a lower free energy barrier to penetrate the phospholipid bilayer [206]. By confirming this argument, we observed in our simulations that lipid bilayers are distorted by the insertion of nanotubes and the inner surface of CNTs is blocked by phospholipids.

However, this distortion is not permanent and does not cause lipids to carry from one leaflet to another. Furthermore, the presence of IBU prevents lipids to penetrate the inner surface of the CNTs.

The hydrophobicity of the CNTs not only affects the distribution of nanotubes within the bilayer but also varies their internalization time. In the absence of IBU, the residence time in the aqueous phase was found to be higher with the functionalized CNTs than with pristine one (c.f. Figure 4.12a). The highest residence time in bulk water was determined ~200 ns with PSCOOH functionalized CNT. Since the carboxyl groups increase the polarity of the nanotube, the interactions with water become more favorable as previously reported [196,197]. From Figure 4.12a it is also shown that pristine and PSCOOH modified CNTs reside almost in the center of the bilayer while PS modified CNT locate in the upper leaflet at about 1 nm distance from the bilayer core to the CNT's COM. In the presence of IBU, on the other hand, the internalization time of functionalized CNTs shorten (c.f. Figure 4.12b). For example, PS functionalized CNT penetrates the bilayer about 2.5 times faster than its no drug-loaded counterpart. This may be explained by the increasing hydrophobic character of the CNTs with IBU loading. Since IBU is an overall hydrophobic drug, it promotes the hydrophobic interactions with the lipid bilayer. Regardless of the functional group, it is also observed that IBU-loaded CNTs prefer to locate in the hydrophobic center of the bilayer.

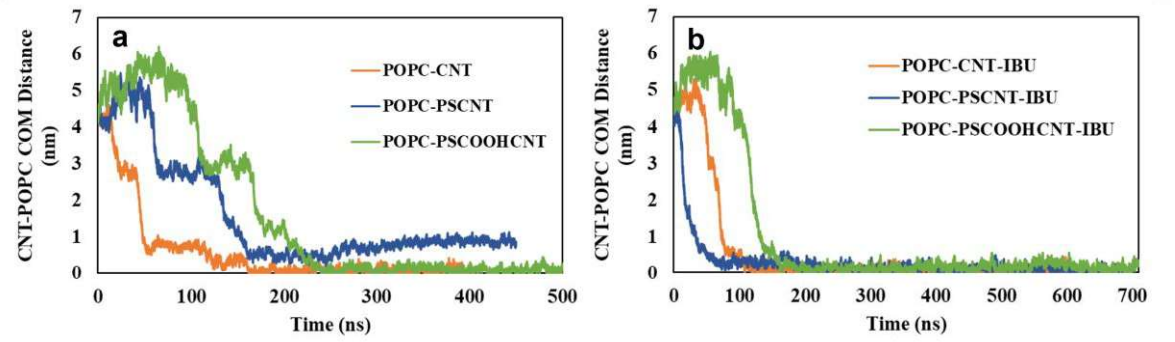

Figure 4.12. The absolute center-of-mass (COM) distance of CNTs from the POPC bilayer center for the pristine and functionalized CNTs a) in the absence of IBU, b) in the presence of IBU.

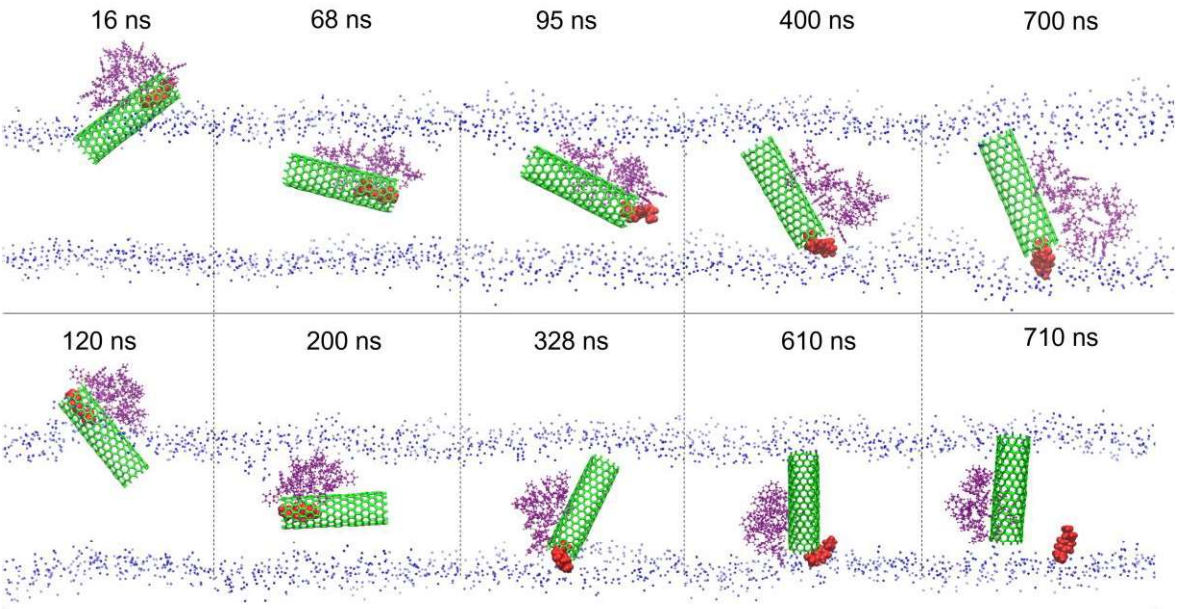

Figure. 4.13. Dynamic evolution of the POPC-PSCNT-IBU system (upper panel), and POPC-PSCOOHCNT-IBU system (lower panel). Water molecules, ions and lipid tails are not shown on the figure for clarity purposes.

Here, IBU, which is a poorly water-soluble drug consisting of a hydrophobic tail and a hydrophilic carboxyl cap, is selected as a model drug since it was previously loaded to polymer functionalized CNTs in experimental studies [330,331]. In the aqueous phase, different chiral forms of IBU molecules are inserted into SWCNTs through their methyl side chains by MD simulations [332]. In this study, the drug release potential of pristine and functionalized CNTs has been investigated by placing a molecule of IBU in the center of the CNTs. In all cases, we observed that IBU remains within the tubes while in water, and IBU-loaded CNTs cross the upper leaflet of the bilayer and then direct the drug to the headgroups of the lower leaflet. For pristine CNT, IBU was still at the lower end of the nanotube after 600 ns simulation time and couldn't be delivered to the bilayer. IBU in PSCNT, on the other hand, partially exited from the nanotube in about 100 ns. However, the hydrophilic cap of IBU couldn't completely save itself from the lower end of the nanotube in which the amide linker is connected until the end of simulation time. Similarly, IBU in PSCOOHCNT was stuck at the lower end of the nanotube from its hydrophilic end but at 610 ns it was completely released. It was observed that the hydrophilic cap of the released drug interacts with the lipid headgroups in the lower leaflet while its hydrophobic tail tends towards the

hydrophobic region of the membrane for the investigated 100 ns. The dynamic evolution of the IBU in functionalized CNTs is demonstrated in Figure 4.13. It should be noted that IBU release could be observed with PSCNT on a longer time scale. Therefore, CG simulations are suggested to further analyze the drug release profiles of PS functionalized CNTs.

There are two main characteristics of polymers: radius of gyration (ROG) and end-to-end (EtE) distances. We calculated ROG and carbon EtE distances of PS functional groups throughout the simulation time and reported the average values taken from equilibrated trajectories in Table 4.8. In the absence of IBU, the ROG values are found between 0.9-1.0 nm for the PS chain with 29 monomers. The addition of IBU increases ROG values by about 15% in PSCNT due to the dispersion of PS on the outer walls of the CNT. Moreover, since IBU is stuck at the lower end of the nanotube, the free end of the PS spreads toward the upper rim of CNT and increases the EtE distance of PS by about 2-fold. COOH modification of PS, on the other hand, does not change the ROG value but decreases the EtE distance to one-third. The increasing polarity of the functional group provides an interactive site with the linker amide group, and the hydrophilic end of IBU strengthens this interaction before its release. As a result, carboxyl groups approach amide linker, reducing EtE distance.

Table 4.8. Radius of gyration (ROG) and carbon end-to-end (EtE) distances of PS functional groups attached to CNTs.

Model	**Radius of Gyration (nm)**	**End-to-End Distance (nm)**	
POPC - PSCNT	0.90 ± 0.02	0.89 ± 0.08	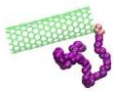
POPC - PSCOOHCNT	0.93 ± 0.01	1.53 ± 0.14	
POPC - PSCNT - IBU	1.03 ± 0.02	2.06 ± 0.13	
POPC - PSCOOHCNT - IBU	0.91 ± 0.01	0.51 ± 0.06	

Consequently, we developed atomistic models of PS and PSCOOH modified SWCNTs and examined their interactions with a POPC lipid bilayer in the presence and absence of the drug, IBU. Our results give the first insights into the polystyrene modification of CNTs in literature by MD modeling and show that polystyrene has a high potential to be used as a functional group for safe and controlled drug delivery. In the next section, we will expand our research by analyzing these systems at a coarse-grained level for longer times and in more realistic environments.

4.4. Validation of Pristine and Functionalized Carbon Nanotube Coarse-Grained Models

Martini2 CG models of CNT were previously developed by different groups [211,219], but recently Martini3 force field has been introduced [265] where the structural and thermodynamic properties of molecules are better represented. Therefore, we adopted the Martini3 small molecule parameterization procedure [264] to obtain more reliable models of pristine and functionalized CNTs. This parameterization relies on the distributions of bonded interactions in atomistic simulations, while non-bonded interactions are tuned to reproduce the free energies of transfer of the target molecules between aqueous and organic phases. The mapping strategy is based on the center-of-geometry (COG) approach, which takes into account the hydrogen atoms in addition to heavy atoms, i.e., carbon, oxygen, and nitrogen. The bonded parameters, i.e., bonds, angles, and dihedrals of CNTs, are derived from atomistic reference simulations and the distributions between AA and CG models are presented in Figure C.3 and C.4.

The non-bonded interactions obtained from atomistic and CG simulations are compared by calculating the free energy values and partition coefficients. We calculated the free energy of transfer of an individual CNT molecule from octanol to water using both atomistic and CG models. Additionally, free energies of transfer of the CNTs between different solvents derived from solubility data were listed with our results in Table 4.9. Here, the computed hydration free energy of -54.9 kJ/mol agrees well with the previous studies measured for C60 by Athawale et al. (−54.1 kJ/mol) [333] and Varanasi et al. (−55.27 kJ/mol) [334] at 300 K. On the other hand, hydration, and solvation-free energies of CNTs have been calculated by MD simulations in literature [335,336] but the values are not

comparable due to different sizes and configurations. However, the transfer free energy of -115.1 kJ/mol shows good agreement with less than 5 % error compared to its atomistic counterpart. Furthermore, the atomistic and CG models are in reasonable agreement with the previously developed models of logP0 with less than 10% deviation.

Table 4.9. Free energies of CNT (6,0) in water and octanol with calculated partition coefficients for all-atom (AA) and coarse-grained (CG) simulations. Reference partition coefficient values were calculated by the proposed models based on chiral vectors in the corresponding articles.

	ΔG_{water} (kJ/mol)	$\Delta G_{octanol}$ (kJ/mol)	$\Delta G_{transfer}$ (kJ/mol)	logP	$logP,^{ref}$
AA	-48.9 ± 0.7	-168.9 ± 0.6	-120.0	21.0	18.7, [337]
CG	-54.9 ± 0.0	-170.0 ± 0.0	-115.1	20.2	19.2 [338]

For PS or PSCOOH functionalized CNTs, the free energy of transfer values are listed in Table 4.10. The negative estimates of free energies are in line with our previous findings and the high negative free energy of CNTs indicates the increased affinity of CNTs for water with functional groups.

Table 4.10. Free energies of transfer of PSCNT and PSCOOHCNT in water and octanol with calculated partition coefficients for all-atom (AA) and coarse-grained (CG) simulations. Here CNT is 1.5 nm in length with (6,0) chirality and the polystyrene chain consists of five monomers.

		$\Delta G_{transfer}$ (kJ/mol)	logP
PSCNT	**AA**	-153.5	26.9
	CG	-144.8	25.4
PSCOOHCNT	**AA**	-155.1	27.2
	CG	-144.2	25.2

To further validate our model, we determined the free energy of transfer of a CNT from water to the interior of a POPC membrane by PMF simulations both at the atomistic and the CG level. We found again a good agreement between AA and CG models (c.f. Figure 4.14). The free energy of the system when CNT is at the center of the bilayer (~-105 kJ/mol for AA and ~-120 kJ/mol for CG), the depth and the location of the free energy minimum, as well as the slope of the PMF lines, are similar in the two presentations. In CG simulations, the position of free energy minimum is at about 0.7 nm with an energy value of ~-125 kJ/mol while in AA simulations it is between ~0.7-0.9 with a slightly higher energy value. Our results show that the MARTINI3 force field is well suited to realistically describe the partitioning of CNT. Furthermore, it overcomes the resolution limits encountered in experiments by providing molecular information close to atomistic level and allows simulations on time scales of tens of microseconds.

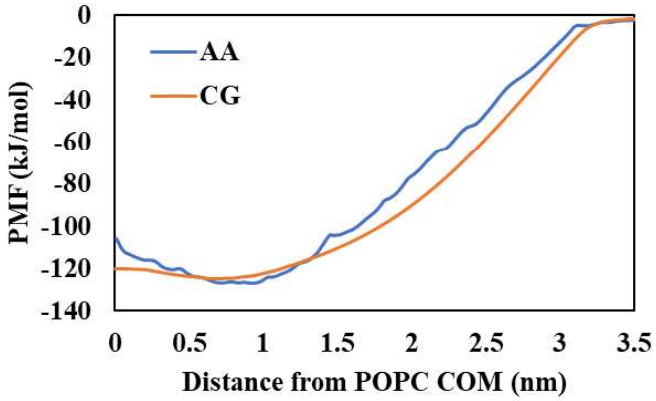

Figure 4.14. PMF change with the distance of the centers of masses of a single CNT (6,0) and a POPC bilayer.

4.5. Interactions of Pristine and Functionalized Carbon Nanotubes with Lipid Bilayers by Coarse-Grained Simulations

The internalization of CNTs into membranes occurs by passive diffusion as previously reported [208,209,216]. For homogeneous bilayers, APL can be calculated by dividing the area of the simulation box in xy direction by half the number of lipids. However, for heterogeneous bilayers which consist of different types of lipids of different sizes (such as PC lipids and cholesterol), Voronoi tessellation is generally used to obtain the projected area

of lipids [273]. Since some of our systems include cholesterol, which is shorter than POPC lipid, APL values were calculated in the latter method and presented in Table 4.11.

The computed APL values for POPC only and POPC with 30% CHOL systems are 0.66 and 0.52 nm^2, respectively and in good agreement with the experimental and computational ranges of ~0.64-0.68 nm^2 for POPC [281,282,339] and ~0.49 nm^2 for POPC/CHOL [284]. Due to the condensing effect of cholesterol, the surface area of a membrane with CHOL is lower [340,341]. Therefore, the APL values are found to be lower for CHOL-included POPC than only POPC as expected. Moreover, the change in APL values in the presence of a single pristine or functionalized CNT is negligible. In the presence of 5 functionalized CNTs, there is a ~2% increase in APL values.

Bilayer thickness of POPC and POPC/CHOL bilayers are computed as 3.85 and 4.04 nm consistent with the experimental and computational values between ~ 3.70 - 3.92 nm [281,282,339] and ~ 4.4 - 4.5 nm, respectively [284,342]. In the presence of a single NP, thickness values do not change whereas the addition of five NPs increases the thickness in all cases. In POPC/CHOL systems, functionalized CNTs with six chains of PS or PSCOOH result in a ~10% increase in thickness due to the compact clustering of CNTs. The clustering of CNTs is illustrated in Figure 4.15. In the presence of five functionalized CNTs, APL and thickness values are found to be very similar with either four or six chains of PS and PSCOOH.

The lipid tail order parameters of POPC and POPC/CHOL are found as ~0.35 and ~0.4, respectively (Table 4.11) as higher than the experimental [342] and atomistic studies. [339] However, these values are in good agreement with the previous Martini models [343,344]. Order parameters don't change much by the addition of NPs in POPC; however, cholesterol increases ordering in both systems. Aggregation of CNTs with four chains of either PS or PSCOOH in the POPC/CHOL bilayer makes the ordering of lipid tails more apparent and compact.

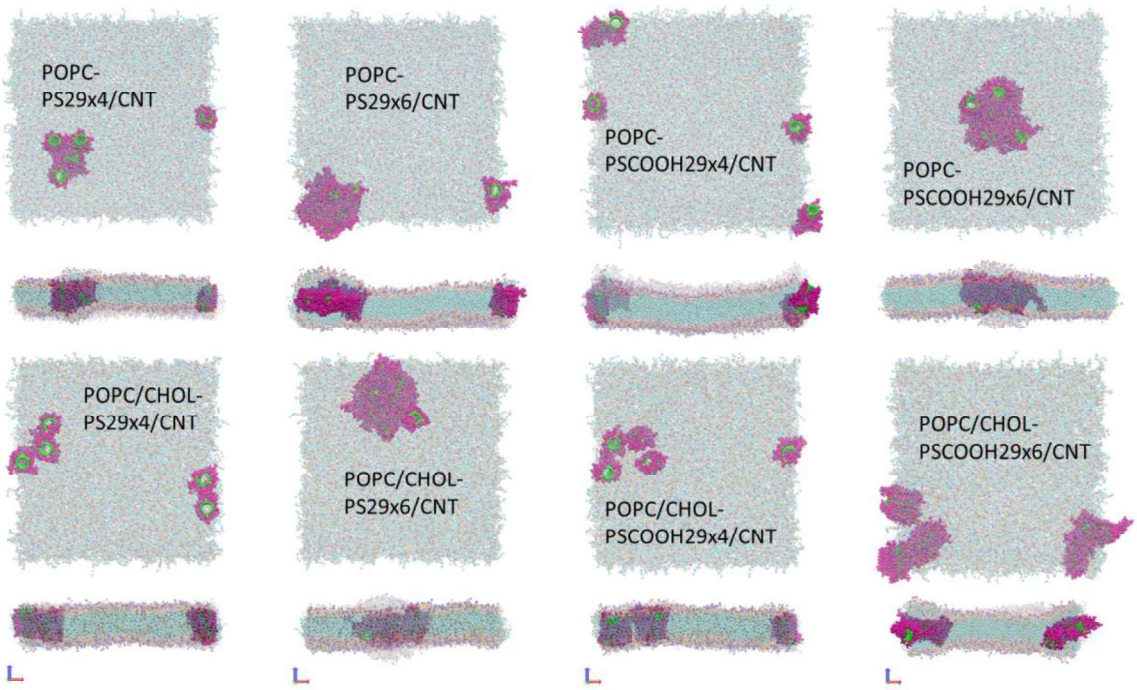

Figure 4.15. Top and side view of configurations taken from the trajectories at 10 μs for POPC (upper panel) and POPC/CHOL (lower panel) systems in the presence of functionalized CNTs at different grafting densities.

The diffusion coefficient estimates in CG simulations are, in general, 2 to 10 times higher than their experimental counterparts. As expected, the lateral diffusion coefficients of PO4 beads in POPC and POPC/CHOL are found as ~72 $\mu m^2/s$ and ~47 $\mu m^2/s$ which are larger than the experimental diffusivity of POPC at 15.3 $\mu m^2/s$ [286]. On the other hand, the diffusion constant of PO4 in POPC is ~1.5 times that of POPC with 30% CHOL, which is consistent with experimental findings [286,345]. It has been observed that POPC/CHOL bilayers are in the liquid disordered phase above 25 °C at all CHOL concentrations and lipid lateral diffusivity constants decrease linearly with increasing CHOL content [345]. Moreover, the presence of a single pristine or functionalized CNT in the POPC bilayer reduces lateral diffusivities by about 10%, while the presence of five functionalized CNTs reduces the diffusivities by about 20%. With five PSCNTs or PSCOOHCNTs in POPC/CHOL bilayers, the diffusion of POPC drops to almost half that in the pure POPC membrane. On the other hand, the lateral diffusion coefficient of ROH beads in the POPC/CHOL bilayer was calculated as ~82 $\mu m^2/s$ and increasing the nanoparticle

concentration decreases the diffusion constants by about 7-15%. Consequently, the addition of five functionalized CNTs reduces the mobility of POPC and CHOL.

Table 4.11. Area per lipid (APL), bilayer thickness, tail order parameter, and lateral diffusion coefficients of POPC and POPC/CHOL bilayers in the presence and absence of pristine and functionalized CNTs. Lateral diffusion coefficients represent the diffusivities of PO4 beads for POPC and ROH beads for CHOL, and standard errors are obtained through regression of MSDs. Order parameters show the average tail order of both chains in POPC. Here NP, PS, and PSCOOH denote nanoparticle, polystyrene, and carboxyl-terminated polystyrene, respectively. The numbers next to 'PS' and 'PSCOOH' show the chain length while the ones after 'x' show the number of chains.

Model	**No of NP**	**APL (nm^2)**	**Bilayer Thickness (nm)**	**Order Parameter**	**Lateral Diffusion Coefficient ($\mu m^2/s$)**	
					PO4	**ROH**
POPC	-	0.661 ± 0.003	3.85 ± 0.01	0.346	71.8 ± 0.04	-
POPC-CNT	1	0.661 ± 0.003	3.86 ± 0.01	0.349	66.1 ± 0.09	-
POPC-PS29CNT	1	0.662 ± 0.003	3.86 ± 0.01	0.349	64.7 ± 0.02	-
POPC-PS48CNT	1	0.663 ± 0.003	3.86 ± 0.01	0.348	65.1 ± 0.04	-
POPC-PS96CNT	1	0.664 ± 0.003	3.86 ± 0.01	0.347	73.7 ± 0.03	-
POPC-PSCOOH29CNT	1	0.662 ± 0.003	3.86 ± 0.01	0.349	69.4 ± 0.05	-
POPC-PSCOOH48CNT	1	0.663 ± 0.003	3.86 ± 0.01	0.348	64.7 ± 0.05	-
POPC-PSCOOH96CNT	1	0.664 ± 0.003	3.86 ± 0.01	0.345	70.0 ± 0.03	-
POPC-PS29x2/CNT	1	0.663 ± 0.003	3.85 ± 0.01	0.348	64.7 ± 0.04	-
POPC-PS29x4/CNT	1	0.664 ± 0.003	3.86 ± 0.01	0.346	66.2 ± 0.08	-
POPC-PS29x6/CNT	1	0.665 ± 0.003	3.87 ± 0.01	0.348	62.2 ± 0.06	-
POPC-PSCOOH29x2/CNT	1	0.663 ± 0.003	3.86 ± 0.01	0.348	67.2 ± 0.03	-
POPC-PSCOOH29x4/CNT	1	0.664 ± 0.003	3.86 ± 0.01	0.348	67.2 ± 0.07	-
POPC-PSCOOH29x6/CNT	1	0.666 ± 0.003	3.87 ± 0.01	0.348	62.5 ± 0.02	-

Table 4.11. Area per lipid (APL), bilayer thickness, tail order parameter, and lateral diffusion coefficients of POPC and POPC/CHOL bilayers in the presence and absence of pristine and functionalized CNTs. Lateral diffusion coefficients represent the diffusivities of PO4 beads for POPC and ROH beads for CHOL, and standard errors are obtained through regression of MSDs. Order parameters show the average tail order of both chains in POPC. Here NP, PS, and PSCOOH denote nanoparticle, polystyrene, and carboxyl-terminated polystyrene, respectively. The numbers next to 'PS' and 'PSCOOH' show the chain length while the ones after 'x' show the number of chains (cont.).

POPC-PS29x4/CNT	5	0.674 ± 0.004	3.91 ± 0.02	0.346	58.2 ± 0.05	-
POPC-PS29x6/CNT	5	0.674 ± 0.003	3.98 ± 0.02	0.334	54.6 ± 0.02	-
POPC-PSCOOH29x4/CNT	5	0.676 ± 0.004	3.89 ± 0.02	0.345	55.9 ± 0.03	-
POPC-PSCOOH29x6/CNT	5	0.676 ± 0.003	3.97 ± 0.02	0.338	56.0 ± 0.09	-
POPC/CHOL	-	0.523 ± 0.004	4.04 ± 0.02	0.399	46.6 ± 0.04	81.9 ± 0.06
POPC/CHOL-PS29x4/CNT	1	0.527 ± 0.004	4.05 ± 0.02	0.401	43.2 ± 0.05	85.5 ± 0.08
POPC/CHOL-PS29x6/CNT	1	0.528 ± 0.004	4.05 ± 0.02	0.402	43.4 ± 0.05	81.2 ± 0.05
POPC/CHOL-PSCOOH29x4/CNT	1	0.527 ± 0.004	4.05 ± 0.02	0.403	46.9 ± 0.03	83.7 ± 0.06
POPC/CHOL-PSCOOH29x6/CNT	1	0.528 ± 0.004	4.02 ± 0.02	0.401	47.0 ± 0.02	80.9 ± 0.04
POPC/CHOL-PS29x4/CNT	5	0.543 ± 0.005	4.06 ± 0.02	0.407	41.7 ± 0.02	73.2 ± 0.02
POPC/CHOL-PS29x6/CNT	5	0.538 ± 0.006	4.22 ± 0.02	0.387	39.4 ± 0.02	76.0 ± 0.07
POPC/CHOL-PSCOOH29x4/CNT	5	0.544 ± 0.005	4.08 ± 0.02	0.409	39.9 ± 0.05	69.2 ± 0.10
POPC/CHOL-PSCOOH29x6/CNT	5	0.539 ± 0.006	4.24 ± 0.02	0.372	42.9 ± 0.04	72.1 ± 0.04

Throughout the simulations, it is observed that CHOL molecules penetrate the inner region of the bilayer, then migrate to the other leaflet or return to the same leaflet. In Table 4.12, the successful CHOL flip-flop events identified in the last 2 μs of trajectories are listed.

The flip-flop rates of CHOL do not change in the presence of a single nanoparticle but decrease by about 6-12% with the addition of five NPs. Since clustering of CNTs inside the bilayer restricts the rotation and translocation of CHOL, the drop of trans-bilayer motion of CHOL is more pronounced in the presence of CNTs with 6 PS or PSCOOH chains. Previous studies have revealed that CHOL flip-flop rates occur on a sub-millisecond timescale and depend on the temperature, bilayer order, lipid saturation level, and CHOL concentration [346–348]. For instance, decreasing the temperature from 310 K to 290 has increased lipid tail ordering and drop the flip-flop rate to one-tenth [348]. Flip-flop rates have been found faster in poly-unsaturated DAPC lipid bilayers than in more saturated DPPC and POPC bilayers [346]. Moreover, it has been determined that increasing the concentration of CHOL from 20 to 40 % decreases the flip-flop rate in DPPC by orders of magnitude [349]. The CHOL flip-flop rates calculated in our study are found smaller than their counterparts in the literature. However, it should be noted that the temperature of the systems, calculation methods, and simulation types, i.e., atomistic or CG, plays an important role in obtaining different results.

Table 4.12. Cholesterol flip-flop rates in POPC/CHOL bilayers. Values are based on the last 2 μs of trajectories.

Model	**No of NP**	**No of Successful Flip-Flops**	**Cholesterol Flip-Flop Rate (μs^{-1})**
POPC/CHOL	-	13978	11.4
POPC/CHOL-PS29x4/CNT	1	13842	11.3
POPC/CHOL-PS29x6/CNT	1	13781	11.2
POPC/CHOL-PSCOOH29x4/CNT	1	13781	11.2
POPC/CHOL-PSCOOH29x6/CNT	1	13719	11.2
POPC/CHOL-PS29x4/CNT	5	13128	10.7
POPC/CHOL-PS29x6/CNT	5	12662	10.3
POPC/CHOL-PSCOOH29x4/CNT	5	13033	10.6
POPC/CHOL-PSCOOH29x6/CNT	5	12292	10.0

The angle distributions between the long axis vector of CNT and bilayer normal are shown in Figure 4.16 based on different PS or PSCOOH chain lengths and grafting density. As mentioned in the previous section, it has been reported that short CNTs (D_i = 1.5 nm)

have tilt angles between 0°-15° in the DOPC bilayer through cryogenic TEM analysis [327] and in situ SAXS calculations [328]. Using CNTs of similar size, Sullivan et al. calculated a larger tilt angle (0°-25°) by scanning AFM images across the equimolar DMPC/DOPC membrane [329]. These findings are supported here where the pristine CNT makes mostly less than 20° angle with POPC. (c.f. Figure C.7) Furthermore, short CNTs with ~2 nm in length are confirmed to orient parallel to lipid molecules when embedded in a phospholipid bilayer [326]. By modifying CNTs with 29 monomers of PS or PSCOOH, we obtain similar tilt angle distributions (mostly below 25°). Upon grafting of the 48 or 96 monomer PS chain, wider angle distributions are observed with similar intensities. Differently, a tilt angle of about 80° is found with 96 monomers of PSCOOH attached to a CNT. Since the PSCOOH chain covers both the interior and exterior regions of CNT in this configuration, lipids cannot diffuse into the nanotube, and CNT prefers to be near-perpendicular to the bilayer normal, unlike the ones that allow the diffusion of lipids inside the nanotube.

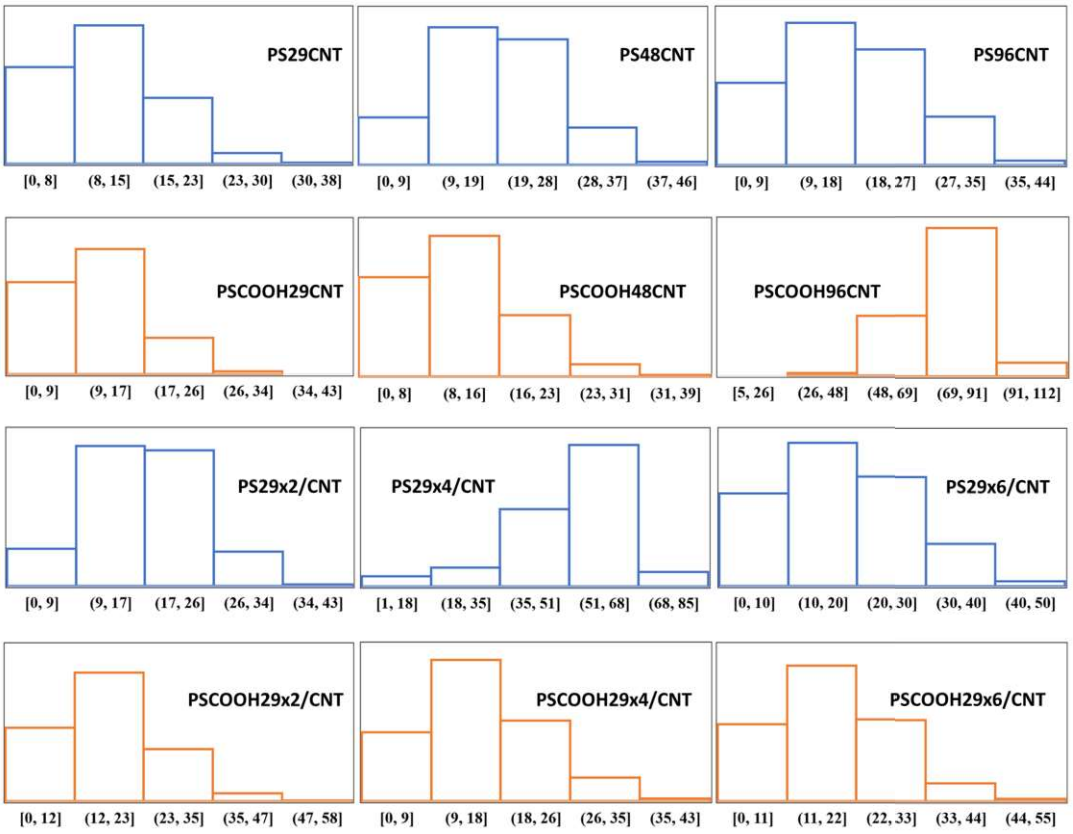

Figure 4.16. Distribution of angles (°) between CNT long axis and POPC bilayer normal at different chain lengths and grafting densities of PS or PSCOOH. Data is taken from the last 2 μs trajectories of single functionalized CNTs in POPC membrane.

Functionalization of CNTs with different groups may change their configurations and polar functional groups can inhibit tilting [219]. It has been shown that hydroxyl modified CNTs tend to be vertical in the bilayer center when the length of the CNT is shorter than the bilayer thickness [216]. However, by varying the grafting density of PSCOOH at the end of CNTs, we didn't observe a hindrance effect. But wider tilt angle distributions were observed mostly at ~10°-20° range. This may be attributed to the amphiphilic nature of the PSCOOH model. When CNTs are functionalized with four chains of PS, the nanotube tilts about 60° with respect to the POPC normal due to PS blockage. Therefore, the occupation of CNTs with either PS or PSCOOH results in an increase in tilting angle with the bilayer normal.

The distribution of the NP models inside POPC and POPC/CHOL membranes were analyzed through density profiles. No significant change in the bilayer properties was observed in the presence of a single pristine/functionalized CNT. The density distribution of lipids (i.e., PO4 or ROH beads), CNTs, water, and ion molecules with five NP systems are demonstrated in Figure 4.17. The introduction of PSCNT or PSCOOHCNT into the bilayers results in a decrease in the intensity of PO4 and/or ROH density peaks both in POPC and POPC/CHOL bilayers. This effect is more significant with CNTs with six PSCOOH chains in POPC/CHOL bilayer (c.f. Figure 4.17j). The density peaks of CNTs in the POPC/CHOL are lower and broader than those in the POPC bilayer. As shown in Figure 4.17g and i), CNTs with four chains of PS or PSCOOOH yield similar CNT density profiles in the POPC-CHOL membrane. Likewise, CNTs with six chains of PS or PSCOOOH have similar CNT density profiles (c.f. Figure 4.17h and j). Therefore, it may be said that the number of polystyrene chains is the determining factor in the configuration that CNT will take. CHOL is also observed to translocate through interior regions of the bilayer confirming our previous findings (c.f. Figure 4.17f and j).

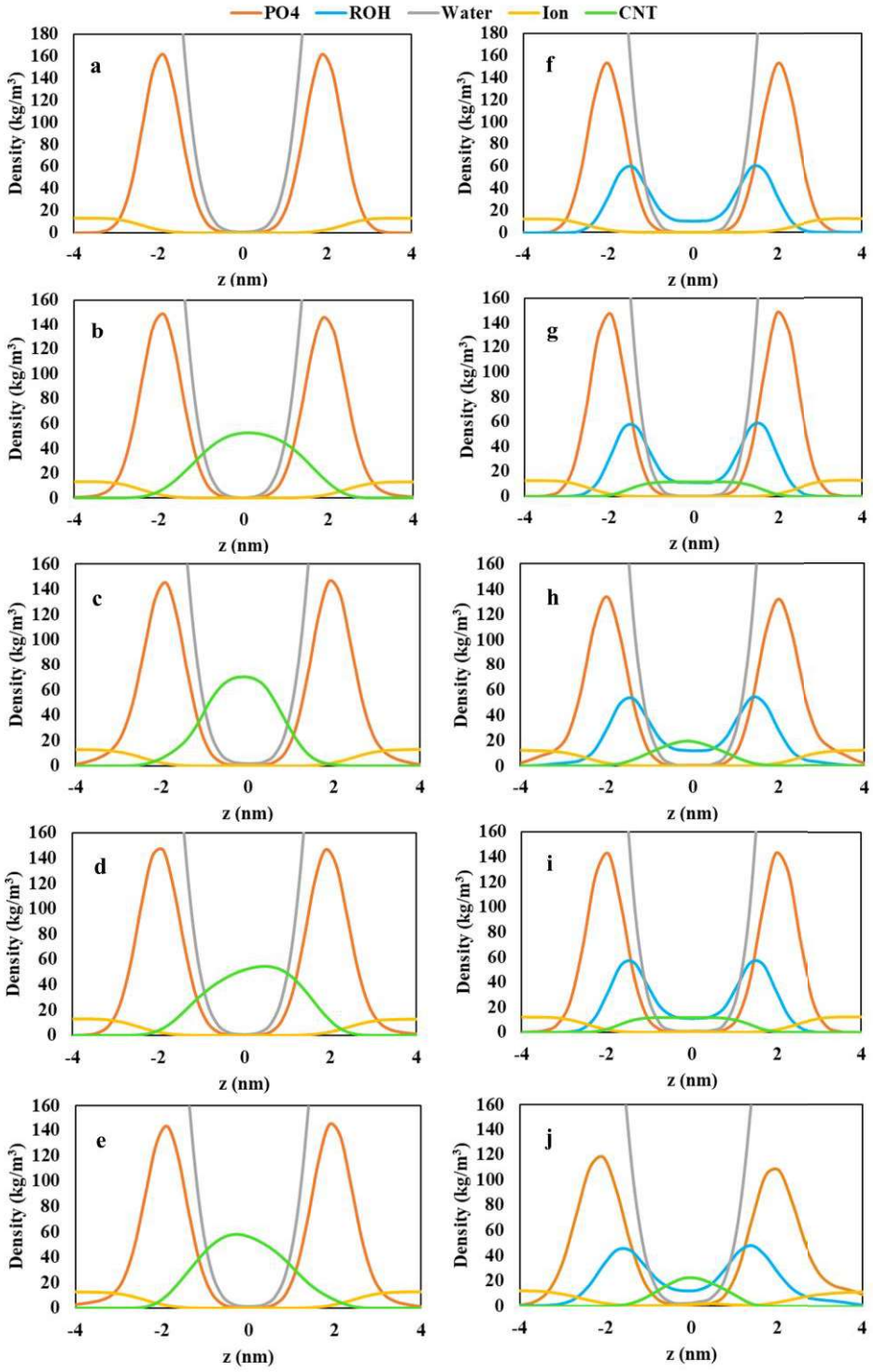

Figure 4.17. Density distributions of lipid phosphate (PO4) and hydroxyl (ROH) groups, and water, ion, and CNT molecules in the presence of five functionalized CNTs for a) POPC, b) POPC-PS29x4/CNT, c) POPC-PS29x6/CNT, d) POPC- PSCOOH29x4/CNT, e) POPC- PSCOOH29x6/CNT, f) POPC/CHOL, g) POPC/CHOL-PS29x4/CNT, h) POPC/CHOL-PS29x6/CNT, i) POPC/CHOL- PSCOOH29x4/CNT, j) POPC/CHOL-PSCOOH29x6/CNT.

As we observed in atomistic simulations in the previous section, water molecules are transported into the bilayer during the internalization of CNTs into the membrane. The open-ended structure of the CNT allows water molecules to enter the tube and be dragged along the bilayer in agreement with the literature [181,202]. In the POPC bilayer, water transport is observed with both PSCNT and PSCOOHCNT, however, not only water molecules but also ions are transported into the membrane by CNTs with six chains of PS or PSCOOH (c.f. Figure C.8c and e). On the other hand, in POPC/CHOL membrane, waters and ions are observed to be present inside the bilayer only for PSCOOH functionalized CNTs (c.f. Figure C.8i and j). Contrarily, in the equilibrated trajectories of AA simulations or CG simulations with single NPs, ions are not found in the bilayer. Therefore, we can draw this conclusion: as the grafting density of PSCOOH or the concentration of functionalized CNTs increases, dragged ions become prone to stay inside the bilayer. As mentioned before, it has been reported that open-ended CNTs may cause the penetration of lipid headgroups or lipid tails across the bilayer [208]. Moreover, the free energy barrier that must be overcome to penetrate the bilayer has been found higher for open ended nanotubes because of the larger distortions in the lipid bilayer than that for the capped CNTs [206]. Capped CNTs are out of the scope of this study, however, both in the POPC and POPC/CHOL membranes, CNTs with six chains of PS or PSCOOH are observed to be blocked by POPC lipids (c.f. Figure C.8(c,e,h,j)). Still, the encapsulation of a drug can inhibit the lipid blockage of nanotubes as shown in the previous section.

As previously discussed, not only the insertion mechanism but also the insertion time into the bilayers depend on the functional groups. However, we couldn't find a correlation between PS chain length or grafting density with the internalization time of CNTs. Instead, the residence time spent in bulk water show variability (c.f. Figure C.9 and C.10). Among single CNTs in POPC systems, the longest residence time in bulk water is found for CNTs which are functionalized with 96 monomers of PS or PSCOOH as ~132 and ~110 ns, respectively. In the presence of five functionalized CNTs, on the other hand, the longest internalization time into the POPC is recorded with six chains of PS as ~220 ns, while the internalization time into the POPC/CHOL membrane is ~258 ns with six chains of PSCOOH functional group. This is explained by the increasing hydrophilicity of the nanotube with carboxylated functional groups [196,197].

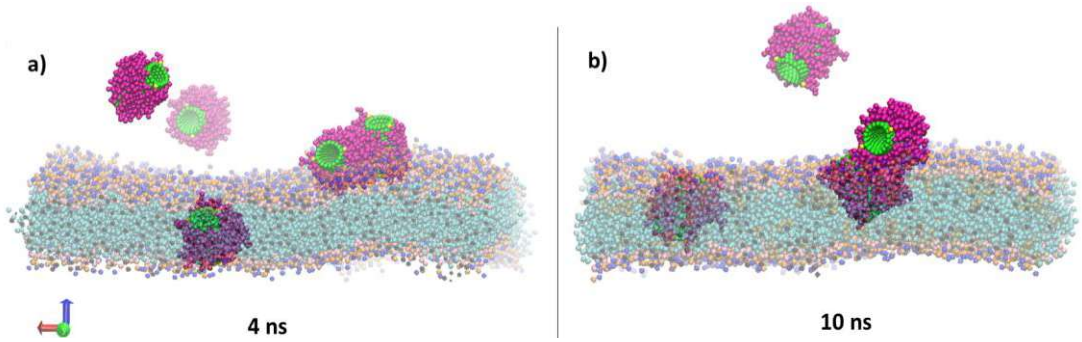

Figure 4.18. Internalization of PS29x4/CNT through a) POPC, b) POPC/CHOL membranes.

PS and PSCOOH functionalized CNTs penetrate the membranes individually or by making clusters of two (c.f. Figure 4.18). Once they are internalized, they form clusters of two or three and all CNTs which are functionalized with six polymer chains form clusters of five at the end of the 10 μs simulation time (c.f. Figure 4.15). In the POPC-CHOL system, CNTs which are modified by four chains of PS or PSCOOH align near parallel with the bilayer normal while the others have mixed (with 6 chains of PS) or near perpendicular (with six chains of PSCOOH) alignment as shown in Figure 4.19.

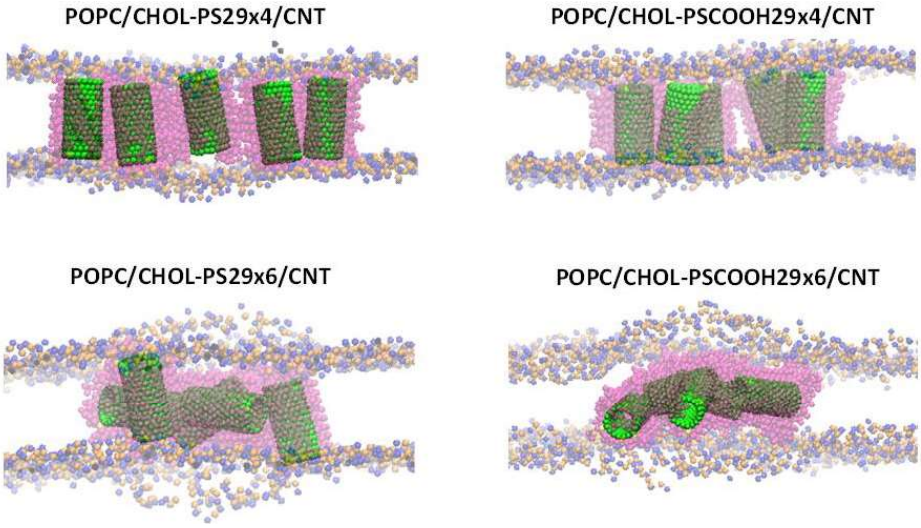

Figure 4.19. Clustering of functionalized CNTs inside POPC/CHOL membrane. The snapshots are taken from the last frame of 10 μs simulation time. Here CNT is green while PS and PSCOOH are in purple. For clarity, only headgroups of POPC (NC3 is in blue, PO4 in orange) is shown on the figure.

The radius of gyration (ROG) and carbon end-to-end (EtE) distance are two important structural descriptors of a polymer. ROG and EtE distances of PS or PSCOOH chains that are covalently linked to single CNTs are plotted in Figure 4.20 with changing polystyrene chain lengths. For both hydrogen and carboxyl-terminated polystyrene, ROG increases as chain length increases, confirming the previous findings in the literature [268]. EtE distances, on the other hand, increase with the increasing number of monomers in PS; while it is almost the same in PSCOOH with 29 and 48 monomers but decreases with 96 monomers. This EtE distance reduction in PSCOOH with 96 monomers can be attributed to the open carboxyl end of the PSCOOH passing inside the CNT and approaching the polar junction group.

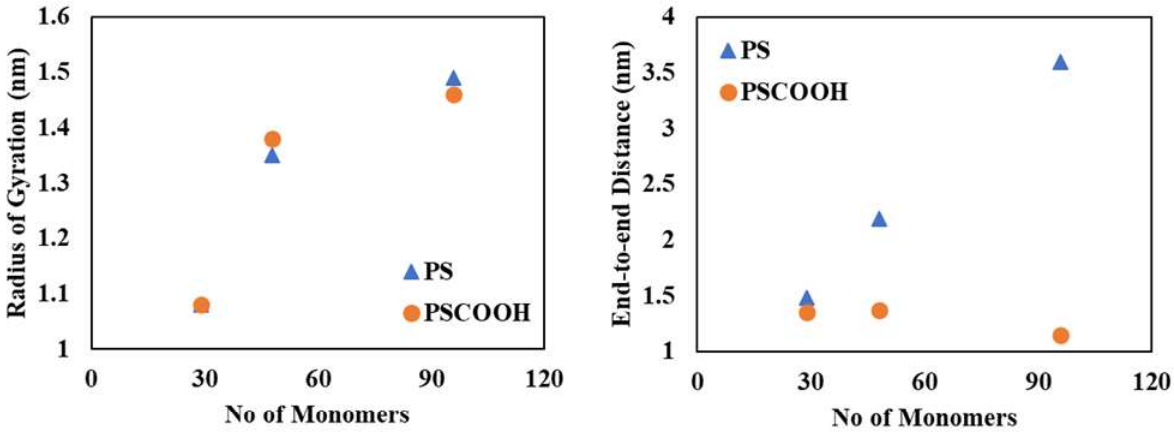

Figure 4.20. The average radius of gyration and end-to-end distances of PS and PSCOOH which are connected to a CNT with 29, 48, and 96 monomers. Data is taken from the last 2 μs trajectories of single functionalized CNTs in POPC membrane.

In conclusion, Martini3 CG models of pristine and polystyrene functionalized CNTs were developed in agreement with their structural and thermodynamic properties. The developed models at different chain lengths and grafting densities of PS or PSCOOH were investigated in terms of their translocation behavior through POPC and POPC/CHOL membranes. The highlights of this study are summarized as in the following:

- At the studied concentrations, CNTs passively diffuse into the membranes and alter structural and elastic properties of membranes but cause no permanent physical damage to the membrane integrity.
- Due to the condensing effect of cholesterol, the properties of lipid bilayers change, i.e., area-per-lipid and lateral diffusion constants decrease, whereas the bilayer thickness and tail order parameters increase.
- At increasing CNT concentrations, flip-flop rates of cholesterol are reduced because of the diminished OH density in the core region of the membrane.
- The tilt angles between CNTs and the bilayer normal are affected by the inclusion of either lipids or polystyrene chains into the CNT as well as by the polarity of polystyrene chains.

Consequently, PS or PSCOOH-modified CNTs have the potential to be used as delivery agents in drug delivery platforms. Hence, CNT concentration, polystyrene chain length, and polystyrene grafting density are the important parameters to consider in the design of safe and controlled drug delivery. In the future, our results may be evaluated further by forming a basis for the development of more complex systems, especially in the presence of drug molecules.

5. CONCLUSION

5.1. Conclusions

This thesis aims to understand the toxicity and cellular uptake of NPs through Machine Learning and Molecular Dynamics methods. First, the toxicity mechanism of fullerenes and their polar derivatives was investigated through their interactions with the model cell membranes using MD simulations. CG simulation results revealed that the translocation behavior and internalization time of fullerenes through the membrane depend on the level of peroxidation of lipids and the degree of polarity of fullerenes. While the distribution of fullerenes in the bilayer is mainly explained by the degree of peroxidation and saturation of the lipid acyl chains, it was determined that hydrophobic interactions govern their penetration through the membrane. It was also observed that the possible toxicity mechanism of fullerenes may not be lipid peroxidation in terms of membrane integrity disruption. Upon these findings, to further understand the toxicity mechanism of NPs, the cytotoxicity of various inorganic, organic, and carbon-based NPs was investigated under the variables of physicochemical characteristics of NPs, cell properties, and test conditions. Meta-heuristic mining of association rules performed on a comprehensive data set consisting of 4111 samples has revealed the hidden relationships of variables with the toxicity descriptor of cell viability. In this context, biocompatible and biodegradable NPs such as hydroxyapatite, chitosan, and polystyrene were found to be suitable for use in drug delivery systems without causing toxic effects and modification of NPs with the carboxyl group (especially polystyrene) was found to be advantageous in terms of maintaining cell viability in the long term. Since compared to fullerenes, CNTs can carry the drug molecules not only on their surfaces but also inside their tubes and release them in targeted cells on demand through surface functionalization, in this study, CNTs were functionalized with PS and PSCOOH at atomistic and CG levels. Atomistic simulations showed that carboxyl-terminated PS functionalization allows the drug to be completely released into the lower leaflet of the bilayer without imposing damage to the membrane. According to the CG results, it was found that increasing CNT concentration alters structural and elastic properties of the bilayers without causing permanent membrane damage and decreases cholesterol flip-flop rates. Furthermore, the equilibrium configuration of the CNTs and tilting angles within the

membrane were identified to depend on the chain length and grafting density of PS as well as the hydrophilic character gained by the carboxyl group. Therefore, to eliminate the blockage of nanotubes by lipids or PS chains which may pose a risk in the drug delivery process the chain length and grafting density of PS were suggested to be optimized. In conclusion, our study provides insights into the translocation of pristine and functionalized carbon nanoparticles across cell membranes and their potential to be used as nanocarriers. These findings reveal important information and relationships in molecular resolution that may contribute to the design of experimental drug delivery systems in the future.

5.2. Recommendations

Considering the results of the present study, the following recommendations can be made in future studies.

- The interactions of carbon NPs with cell membranes can be investigated using more complex lipid membrane systems reflecting the plasma membrane.
- The distribution of NPs can be studied in the presence of membrane proteins.
- Asymmetric membrane models can be developed.
- The effect of size of NPs, i.e., diameter, length, can be studied with the developed models.
- To obtain the force field parameters, automated CG modeler (like a python script) can be developed based on the size and chirality of CNTs.
- Drug release performance of NPs can be evaluated through changing the type and concentration of drugs.

REFERENCES

1. Nakamura, H. and S. Watano, “Direct Permeation of Nanoparticles across Cell Membrane: A Review”, *KONA Powder and Particle Journal*, Vol. 2018, No. 35, pp. 49–65, 2018.

2. Kumar, V., Sharma, N. and S.S. Maitra, “In vitro and in vivo toxicity assessment of nanoparticles”, *International Nano Letters*, Vol. 7, No. 4, pp. 243–256, 2017.

3. Sukhanova, A., Bozrova, S., Sokolov, P., Berestovoy, M., Karaulov, A. and I. Nabiev, “Dependence of Nanoparticle Toxicity on Their Physical and Chemical Properties”, *Nanoscale Research Letters*, Vol. 13, 2018.

4. Oh, E., Liu, R., Nel, A., Gemill, K.B., Bilal, M., Cohen, Y. and I.L. Medintz, “Meta-analysis of cellular toxicity for cadmium-containing quantum dots”, *Nature Nanotechnology*, Vol. 11, No. 5, pp. 479–486, 2016.

5. Labouta, H.I., Asgarian, N., Rinker, K. and D. T. Cramb, “Meta-Analysis of Nanoparticle Cytotoxicity via Data-Mining the Literature”, *ACS Nano*, Vol. 13, No. 2, pp. 1583–1594, 2019.

6. Concu, R., Kleandrova, V.V., Speck-Planche, A. and M.N.D.S. Cordeiro, “Probing the toxicity of nanoparticles: a unified in silico machine learning model based on perturbation theory”, *Nanotoxicology*, Vol. 11, No. 7, pp. 891–906, 2017.

7. Jones, D.E., Ghandehari, H. and J.C. Facelli, “A review of the applications of data mining and machine learning for the prediction of biomedical properties of nanoparticles”, *Computer Methods and Programs in Biomedicine*, Vol. 132, pp. 93–103, 2016.

8. Liu, R., France, B., George, S., Rallo, R., Zhang, H., Xia, T., Nel, A. E., Bradley, K. and Y. Cohen, “Association rule mining of cellular responses induced by metal and metal oxide nanoparticles”, *Analyst*, Vol. 139, No. 5, pp. 943–953, 2014.

9. Gul, G., Yildirim, R. and N. Ileri-Ercan, “Cytotoxicity analysis of nanoparticles by association rule mining”, *Environmental Science: Nano*, Vol. 8, No. 4, pp. 937–949, 2021.

10. Heikkilä, E., Martinez-Seara, H., Gurtovenko, A.A., Vattulainen, I. and J. Akola, “Atomistic simulations of anionic Au144(SR)60 nanoparticles interacting with asymmetric model lipid membranes”, *Biochimica et Biophysica Acta - Biomembranes*, Vol. 1838, No. 11, pp. 2852–2860, 2014.

11. Zolghadr, A.R. and S.S. Moosavi, “Interactions of neutral gold nanoparticles with DPPC and POPC lipid bilayers: Simulation and experiment”, *RSC Advances*, Vol. 9, No. 9, pp. 5197–5205, 2019.

12. Bedrov, D., Smith, G.D., Davande, H. and W. Li, “Passive transport of C60 fullerenes through a lipid membrane: A molecular dynamics simulation study”, *The Journal of Physical Chemistry B*, Vol. 112, No. 7, pp. 2078–2084, 2008.

13. Kraszewski, S., Picaud, F., Elhechmi, I., Gharbi, T. and C. Ramseyer, “How long a functionalized carbon nanotube can passively penetrate a lipid membrane”, *Carbon*, Vol. 50, No. 14, pp. 5301–5308, 2012.

14. Bradley, R. and R. Radhakrishnan, “Coarse-grained models for protein-cell membrane interactions”, *Polymers (Basel)*, Vol. 5, No. 3, pp. 890–936, 2013.

15. Ingólfsson, H.I., Lopez, C.A., Uusitalo, J.J., de Jong, D.H., Gopal, S.M., Periole, X. and S.J. Marrink, “The power of coarse graining in biomolecular simulations”, *Wiley Interdisciplinary Reviews: Computational Molecular Science*, Vol. 4, No. 3, pp. 225–248, 2014.

16. Alessandri, R., Grünewald, F. and S.J. Marrink, “The Martini Model in Materials Science”, *Advanced Materials*, Vol. 33, No. 24, pp. 1–25, 2021.

17. Popov, V.N., “Carbon nanotubes: Properties and application”, *Materials Science and Engineering: R: Reports*, Vol. 43, No. 3, pp. 61–102, 2004.

18. Liu, Z., Robinson, J.T., Tabakman, S.M., Yang, K. and H. Dai, “Carbon materials for drug delivery & cancer therapy”, *Materials Today*, Vol. 14, No. 7–8, pp. 316–323, 2011.

19. Colvin, V.L., “The potential environmental impact of engineered nanomaterials”, *Nature Biotechnology*, Vol. 22, No. 6, pp. 760–760, 2004.

20. Kraemer, Â.B., Parfitt, G.M., Acosta, D. da S., Bruch, G.E., Cordeiro, M.F., Marins, L.F., Ventura-Lima, J., Monserrat, J.M. and D.M., Barros, “Fullerene (C60) particle size implications in neurotoxicity following infusion into the hippocampi of Wistar rats”, *Toxicology and Applied Pharmacology*, Vol. 338, pp. 197–203, 2018.

21. Lacerda, L., Raffa, S., Prato, M., Bianco, A. and K. Kostarelos, “Cell-penetrating CNTs for delivery of therapeutics”, *Nanotoday*, Vol. 2, No. 6, pp. 38–43, 2007.

22. Sayes, C.M., Fortner, J.D., Guo, W., Lyon, D., Boyd, A.M., Ausman, K.D., Tao, Y.J., Sitharaman, B., Wilson, L.J., Hughes, J.B., West, J.L. and V.L. Colvin, “The differential cytotoxicity of water-soluble fullerenes”, *Nano Letters*, Vol. 4, No. 10, pp. 1881–1887, 2004.

23. Trpkovic, A., Todorovic-Markovic, B. and V. Trajkovic, “Toxicity of pristine versus functionalized fullerenes: Mechanisms of cell damage and the role of oxidative stress”, *Archives of Toxicology*, Vol. 86, No. 12, pp. 1809–1827, 2012.

24. Kamat, J.P., Devasagayam, T.P.A., Priyadarsini, K.I. and H. Mohan, “Reactive oxygen species mediated membrane damage induced by fullerene derivatives and its possible biological implications”, *Toxicology*, Vol. 155, No. 1–3, pp. 55–61, 2000.

25. Oberdörster, E., “Manufactured nanomaterials (fullerenes, C60) induce oxidative stress in the brain of juvenile largemouth bass”, *Environmental Health Perspectives*, Vol. 112, No. 10, pp. 1058–1062, 2004.

26. Sayes, C.M., Gobin, A.M., Ausman, K.D., Mendez, J., West, J.L. and V. L. Colvin, “Nano-C60 cytotoxicity is due to lipid peroxidation”, *Biomaterials*, Vol. 26, No. 36, pp. 7587–7595, 2005.

27. Wang, I.C., Tai, L.A., Lee, D.D., Kanakamma, P.P., Shen, C.K.F., Luh, T.Y., Cheng, C.H. and K.C. Hwang, “C60 and water-soluble fullerene derivatives as antioxidants against radical-initiated lipid peroxidation”, *Journal of Medicinal Chemistry*, Vol. 42, No. 22, pp. 4614–4620, 1999.

28. Chen, R.J., Bangsaruntip, S., Drouvalakis, K.A., Wong Shi Kam, N., Shim, M., Li, Y., Kim, W., Utz, P.J. and H. Dai, “Noncovalent functionalization of carbon nanotubes for highly specific electronic biosensors”, *Proceedings of the National Academy of Sciences of the United States of America*, Vol. 100, No. 9, pp. 4984–4989, 2003.

29. Hirsch, A. and O. Vostrowsky, “Functionalization of carbon nanotubes”, *Topics in Current Chemistry*, Vol. 245, pp. 193–237, 2005.

30. Costa, P.M., Bourgognon, M., Wang, J.T.W. and K.T. Al-Jamal, “Functionalized carbon nanotubes: From intracellular uptake and cell-related toxicity to systemic brain delivery”, *Journal of Controlled Release*, Vol. 241, pp. 200–219, 2016.

31. Liu, Z., Cai, W., He, L., Nakayama, N., Chen, K., Sun, X., Chen, X. and H. Dai, “In vivo biodistribution and highly efficient tumour targeting of carbon nanotubes in mice”, *Nature Nanotechnology*, Vol. 2, No. 1, pp. 47–52, 2007.

32. Liu, Z., Davis, C., Cai, W., He, L., Chen, X. and H. Dai, “Circulation and long-term fate of functionalized, biocompatible single-walled carbon nanotubes in mice probed by Raman spectroscopy”, *Proceedings of the National Academy of Sciences of the United States of America*, Vol. 105, No. 5, pp. 1410–1415, 2008.

33. Prencipe, G., Tabakman, S.M., Welsher, K., Liu, Z., Goodwin, A.P., Zhang, L., Henry, J. and H. Dai, “PEG branched polymer for functionalization of nanomaterials with ultralong blood circulation”, *Journal of the American Chemical Society*, Vol. 131, No. 13, pp. 4783–4787, 2009.

34. Ham, H.T., Koo, C.M., Kim, S.O., Choi, S. and I.J. Chung, “Chemical Modification of Carbon Nanotubes and Preparation of Polystyrene/Carbon Nanotubes Composites”, *Macromolecular Research*, Vol. 12, No. 4, pp. 384–390, 2004.

35. Li, H., Cheng, F., Duft, A.M. and A. Adronov, “Functionalization of single-walled carbon nanotubes with well-defined polystyrene by ‘click’ coupling”, *Journal of the American Chemical Society*, Vol. 127, No. 41, pp. 14518–14524, 2005.

36. Chadwick, R.C., Khan, U., Coleman, J.N. and A. Adronov, “Polymer grafting to single-walled carbon nanotubes: Effect of chain length on solubility, graft density and mechanical properties of macroscopic structures”, *Small*, Vol. 9, No. 4, pp. 552–560, 2013.

37. Fragneaud, B., Masenelli-Varlot, K., Gonzalez-Montiel, A., Terrones, M. and J.Y. Cavaillé, “Mechanical behavior of polystyrene grafted carbon nanotubes/polystyrene nanocomposites", *Composites Science and Technology*, Vol. 68, No. 15–16, pp. 3265–3271, 2019.

38. Tabet, L., Bussy, C., Setyan, A., Simon-Deckers, A., Rossi, M.J., Boczkowski, J. and S. Lanone, “Coating carbon nanotubes with a polystyrene-based polymer protects against pulmonary toxicity”, *Particle and Fibre Toxicology*, Vol. 8, pp. 1–13, 2011.

39. “Membrane”, https://www.britannica.com/science/membrane-biology, accessed on August 2, 2022.

40. Singer, S.J. and G.L. Nicolson, “The fluid mosaic model of the structure of cell membranes”, *Science*, Vol. 175, No. 4023, pp. 720–731, 1972.

41. Cooper, G.M., *Structure of the Plasma Membrane*, Second Edition, The Cell: A Molecular Approach, Sunderland, MA, 2000.

42. "Eukaryotic Cells - The Plasma Membrane and the Cytoplasm", https://bio.libretexts.org/Bookshelves/Introductory_and_General_Biology/Book%3A_General_Biology_%28Boundless%29/04%3A_Cell_Structure/4.07%3A_Eukaryotic_Cells_-_The_Plasma_Membrane_and_the_Cytoplasm, accessed on August 2, 2022.

43. Andersen, O.S. and R.E. Koeppe, "Bilayer thickness and membrane protein function: An energetic perspective", *Annual Review of Biophysics and Biomolecular Structure*, Vol. 36, pp. 107–130, 2007.

44. "Lipid Molecules - Phospholipids", https://bio.libretexts.org/Bookshelves/Introductory_and_General_Biology/Book%3A_General_Biology_%28Boundless%29/03%3A_Biological_Macromolecules/3.05%3A_Lipid_Molecules_-_Phospholipids, accessed on August 2, 2022.

45. Eberhard, W.G. and W.T. Wcislo, "Plenty of room at the bottom?", *American Scientist*, Vol. 100, No. 3, pp. 226–233, 2012.

46. Taniguchi, N., "On the Basic Concept of Nanotechnology", paper presented at the *Proceedings of the International Conference on Production Engineering*, Tokyo, 1974.

47. Roco, M.C., "The long view of nanotechnology development: The National Nanotechnology Initiative at 10 years", *Journal of Nanoparticle Research*, Vol. 13, No. 2, pp. 427–445, 2011.

48. Schaming, D. and H. Remita, "Nanotechnology: from the ancient time to nowadays", *Foundations of Chemistry*, Vol. 17, No. 3, pp. 187–205, 2015.

49. Bayda, S., Adeel, M., Tuccinardi, T., Cordani, M. and F. Rizzolio, "The history of nanoscience and nanotechnology: From chemical-physical applications to nanomedicine", *Molecules*, Vol. 25, No. 1, pp. 1–15, 2020.

50. Tewari, D., “Nanotechnology Market By Type: Global Opportunity Analysis and Industry Forecast, 2021–2030”, https://www.alliedmarketresearch.com/nanotechnology-market, accessed on July 20, 2022.

51. Emergen Research, “Nanotechnology Market, By Type, By End-use, and By Region Forecast to 2030”, 2022, https://www.emergenresearch.com/industry-report/nanotechnology-market, accessed on July 20, 2022.

52. Talebian, S., Rodrigues, T., Das Neves, J., Sarmento, B., Langer, R. and J. Conde, “Facts and Figures on Materials Science and Nanotechnology Progress and Investment”, *ACS Nano*, Vol. 15, No. 10, pp. 15940–15952, 2021.

53. Emergen Research, “Smart Nanomaterials Market Types, By Application, By End-Use, and By Region”, 2021, https://www.emergenresearch.com/industry-report/smart-nanomaterials-market, accessed on July 20, 2022.

54. Research and Markets, “Nanomaterials - Global Market Trajectory & Analytics,” 2022, https://www.researchandmarkets.com/reports/344105/nanomaterials_global_market_trajectory_and, accessed on July 20, 2022.

55. Chen, R., Qiao, J., Bai, R., Zhao, Y. and C. Chen, “Intelligent testing strategy and analytical techniques for the safety assessment of nanomaterials”, *Analytical and Bioanalytical Chemistry*, Vol. 410, No. 24, pp. 6051–6066, 2018.

56. ECHA, “Report on the current status of regulatory applicability of non-animal approaches under the REACH, CLP and Biocidal Products regulations”, 2017.

57. ECHA, “The Use of Alternatives to Testing on Animals for the REACH Regulation”, Vol. 117, 2020.

58. Foroozandeh, P. and A.A. Aziz, “Insight into Cellular Uptake and Intracellular Trafficking of Nanoparticles”, *Nanoscale Research Letters*, Vol. 13, No. 339, 2018.

59. Qu, Z.G., He, X.C., Lin, M., Sha, B.Y., Shi, X.H., Lu, T.J. and F. Xu, “Advances in the understanding of nanomaterial-biomembrane interactions and their mathematical and numerical modeling”, *Nanomedicine*, Vol. 8, No. 6, pp. 995–1011, 2013.

60. Singh, R.K., Knowles, J.C. and H.W. Kim, “Advances in nanoparticle development for improved therapeutics delivery: nanoscale topographical aspect”, *Journal of Tissue Engineering*, Vol. 10, 2019.

61. Pan, Y., Neuss, S., Leifert, A., Fischler, M., Wen, F., Simon, U., Schmid, G., Brandau, W. and W. Jahnen-Dechent, “Size-dependent cytotoxicity of gold nanoparticles”, *Small*, Vol. 3, No. 11, pp. 1941–1949, 2007.

62. Rejman, J., Oberle, V., Zuhorn, I.S. and D. Hoekstra, “Size-dependent internalization of particles via the pathways of clathrin-and caveolae-mediated endocytosis”, *Biochemical Journal*, Vol. 377, No. 1, pp. 159–169, 2004.

63. Panariti, A., Miserocchi, G. and I. Rivolta, “The effect of nanoparticle uptake on cellular behavior: Disrupting or enabling functions?”, *Nanotechnology, Science and Applications*, Vol. 5, No. 1, pp. 87–100, 2012.

64. Chithrani, B.D. and W.C.W. Chan, “Elucidating the mechanism of cellular uptake and removal of protein-coated gold nanoparticles of different sizes and shapes”, *Nano Letters*, Vol. 7, No. 6, pp. 1542–1550, 2007.

65. Wang, S.H., Lee, C.W., Chiou, A. and P.K. Wei, “Size-dependent endocytosis of gold nanoparticles studied by three-dimensional mapping of plasmonic scattering images”, *Journal of Nanobiotechnology*, Vol. 8, pp. 1–13, 2010.

66. Chithrani, B.D., Ghazani, A.A. and W.C.W. Chan, “Determining the size and shape dependence of gold nanoparticle uptake into mammalian cells”, *Nano Letters*, Vol. 6, No. 4, pp. 662–668, 2006.

67. Zhao, X., Ng, S., Heng, B. C., Guo, J., Ma, L., Tan, T.T.Y., Ng, K.W. and S.C.J. Loo, "Cytotoxicity of hydroxyapatite nanoparticles is shape and cell dependent", *Archives of Toxicology*, Vol. 87, No. 6, pp. 1037–1052, 2013.

68. Liu, Y., Li, W., Lao, F., Liu, Y., Wang, L., Bai, R., Zhao, Y. and C. Chen, "Intracellular dynamics of cationic and anionic polystyrene nanoparticles without direct interaction with mitotic spindle and chromosomes", *Biomaterials*, Vol. 32, No. 32, pp. 8291–8303, 2011.

69. Dausend, J., Musyanovych, A., Dass, M., Walther, P., Schrezenmeier, H., Landfester, K. and V. Mailänder, "Uptake mechanism of oppositely charged fluorescent nanoparticles in Hela cells", *Macromolecular Bioscience*, Vol. 8, No. 12, pp. 1135–1143, 2008.

70. Qiu, Y., Liu, Y., Wang, L., Xu, L., Bai, R., Ji, Y., Wu, X., Zhao, Y., Li, Y. and C. Chen, "Surface chemistry and aspect ratio mediated cellular uptake of Au nanorods", *Biomaterials*, Vol. 31, No. 30, pp. 7606–7619, 2010.

71. Jiang, X., Dausend, J., Hafner, M., Musyanovych, A., Röcker, C., Landfester, K., Mailänder, V. and G. Ulrich Nienhaus, "Specific effects of surface amines on polystyrene nanoparticles in their interactions with mesenchymal stem cells", *Biomacromolecules*, Vol. 11, No. 3, pp. 748–753, 2010.

72. Tao, W., Zeng, X., Wu, J., Zhu, X., Yu, X., Zhang, X., Zhang, J., Liu, G. and L. Mei, "Polydopamine-based surface modification of novel nanoparticle-aptamer bioconjugates for in vivo breast cancer targeting and enhanced therapeutic effects", *Theranostics*, Vol. 6, No. 4, pp. 470–484, 2016.

73. Dai, H., "Carbon nanotubes: Opportunities and challenges", *Surface Science*, Vol. 500, No. 1–3, pp. 218–241, 2002.

74. Johnston, H.J., Hutchison, G.R., Christensen, F.M., Aschberger, K. and V. Stone, "The biological mechanisms and physicochemical characteristics responsible for driving fullerene toxicity", *Toxicological Sciences*, Vol. 114, No. 2, pp. 162–182, 2009.

75. Pantarotto, D., Briand, J.P., Prato, M. and A. Bianco, "Translocation of bioactive peptides across cell membranes by carbon nanotubes", *Chemical Communications*, Vol. 4, No. 1, pp. 16–17, 2004.

76. Pantarotto, D., Singh, R., McCarthy, D., Erhardt, M., Briand, J.P., Prato, M., Kostarelos, K. and A. Bianco, "Functionalized carbon nanotubes for plasmid DNA gene delivery", *Angewandte Chemie International Edition*, Vol. 43, No. 39, pp. 5242–5246, 2004.

77. Kam, N.W.S., Jessop, T.C., Wender, P.A. and H. Dai, "Nanotube molecular transporters: Internalization of carbon nanotube-protein conjugates into mammalian cells", *Journal of the American Chemical Society*, Vol. 126, No. 22, pp. 6850–6851, 2004.

78. Zhang, X., Meng, L., Lu, Q., Fei, Z. and P.J. Dyson, "Targeted delivery and controlled release of doxorubicin to cancer cells using modified single wall carbon nanotubes", *Biomaterials*, Vol. 30, No. 30, pp. 6041–6047, 2009.

79. Aschberger, K., Johnston, H.J., Stone, V., Aitken, R.J., Tran, C.L., Hankin, S.M., Peters, S.A.K. and F.M. Christensen, "Review of fullerene toxicity and exposure - Appraisal of a human health risk assessment, based on open literature", *Regulatory Toxicology and Pharmacology*, Vol. 58, No. 3, pp. 455–473, 2010.

80. Porter, A.E., Muller, K., Skepper, J., Midgley, P. and M. Welland, "Uptake of C60 by human monocyte macrophages, its localization and implications for toxicity: Studied by high resolution electron microscopy and electron tomography", *Acta Biomaterialia*, Vol. 2, No. 4, pp. 409–419, 2006.

81. Su, Y., Xu, J. ying, Shen, P., Li, J., Wang, L., Li, Q., Li, W., Xu, G. tong, Fan, C. and Q. Huang, "Cellular uptake and cytotoxic evaluation of fullerenol in different cell lines", *Toxicology*, Vol. 269, No. 2–3, pp. 155–159, 2010.

82. Jia, G., Wang, H., Yan, L., Wang, X., Pei, R., Yan, T., Zhao, Y. and X. Guo, "Cytotoxicity of carbon nanomaterials: Single-wall nanotube, multi-wall nanotube, and fullerene", *Environmental Science & Technology*, Vol. 39, No. 5, pp. 1378–1383, 2005.

83. Fiorito, S., Serafino, A., Andreola, F. and P. Bernier, "Effects of fullerenes and single-wall carbon nanotubes on murine and human macrophages", *Carbon*, Vol. 44, No. 6, pp. 1100–1105, 2006.

84. Markovic, Z. and V. Trajkovic, "Biomedical potential of the reactive oxygen species generation and quenching by fullerenes (C60)", *Biomaterials*, Vol. 29, No. 26, pp. 3561–3573, 2008.

85. Tsai, M.C., Chen, Y.H. and L.Y. Chiang, "Polyhydroxylated C60, fullerenol, a novel free-radical trapper, prevented hydrogen peroxide- and cumene hydroperoxide-elicited changes in rat hippocampus in-vitro", *Journal of Pharmacy and Pharmacology*, Vol. 49, No. 4, pp. 438–445, 1997.

86. Yin, J.J., Lao, F., Fu, P.P., Wamer, W.G., Zhao, Y., Wang, P.C., Qiu, Y., Sun, B., Xing, G., Dong, J., Liang, X.J. and C. Chen, "The scavenging of reactive oxygen species and the potential for cell protection by functionalized fullerene materials", *Biomaterials*, Vol. 30, No. 4, pp. 611–621, 2009.

87. Dugan, L.L., Gabrielsen, J.K., Yu, S.P., Lin, T.S. and D.W. Choi, "Buckminsterfullerenol free radical scavengers reduce excitotoxic and apoptotic death of cultured cortical neurons", *Neurobiology of Disease*, Vol. 3, No. 2, pp. 129–135, 1996.

88. Andrievsky, G.V., Bruskov, V.I., Tykhomyrov, A.A. and S.V. Gudkov, "Peculiarities of the antioxidant and radioprotective effects of hydrated C60 fullerene nanostuctures in vitro and in vivo", *Free Radical Biology and Medicine*, Vol. 47, No. 6, pp. 786–793, 2009.

89. "What is Graphene?", https://www.sciencealert.com/graphene, accessed on August 6, 2022.

90. Fujita, K., Fukuda, M., Endoh, S., Maru, J., Kato, H., Nakamura, A., Shinohara, N., Uchino, K. and K. Honda, “Size effects of single-walled carbon nanotubes on in vivo and in vitro pulmonary toxicity”, *Inhalation Toxicology*, Vol. 27, No. 4, pp. 207–223, 2015.

91. Sweeney, S., Grandolfo, D., Ruenraroengsak, P. and T.D. Tetley, “Functional consequences for primary human alveolar macrophages following treatment with long, but not short, multiwalled carbon nanotubes”, *International Journal of Nanomedicine*, Vol. 10, pp. 3115–3129, 2015.

92. Yamashita, K., Yoshioka, Y., Higashisaka, K., Morishita, Y., Yoshida, T., Fujimura, M., Kayamuro, H., Nabeshi, H., Yamashita, T., Nagano, K., Abe, Y., Kamada, H., Kawai, Y., Mayumi, T., Yoshikawa, T., Itoh, N., Tsunoda, S.I. and Y. Tsutsumi, “Carbon nanotubes elicit DNA damage and inflammatory response relative to their size and shape”, *Inflammation*, Vol. 33, No. 4, pp. 276–280, 2010.

93. Nagai, H., Okazaki, Y., Chew, S.H., Misawa, N., Yamashita, Y., Akatsuka, S., Ishihara, T., Yamashita, K., Yoshikawa, Y., Yasui, H., Jiang, L., Ohara, H., Takahashi, T., Ichihara, G., Kostarelos, K., Miyata, Y., Shinohara, H. and S. Toyokuni, “Diameter and rigidity of multiwalled carbon nanotubes are critical factors in mesothelial injury and carcinogenesis”, *Proceedings of the National Academy of Sciences of the United States of America*, Vol. 108, No. 49, 2011.

94. Fenoglio, I., Aldieri, E., Gazzano, E., Cesano, F., Colonna, M., Scarano, D., Mazzucco, G., Attanasio, A., Yakoub, Y., Lison, D. and B. Fubini, “Thickness of multiwalled carbon nanotubes affects their lung toxicity”, *Chemical Research in Toxicology*, Vol. 25, No. 1, pp. 74–82, 2012.

95. Sohaebuddin, S.K., Thevenot, P.T., Baker, D., Eaton, J.W. and L. Tang, “Nanomaterial cytotoxicity is composition, size, and cell type dependent”, *Particle and Fibre Toxicology,* Vol. 7, No. 22, 2010.

96. Jiang, Y., Zhang, H., Wang, Y., Chen, M., Ye, S., Hou, Z. and L. Ren, "Modulation of Apoptotic Pathways of Macrophages by Surface-Functionalized Multi-Walled Carbon Nanotubes," *PLoS One*, Vol. 8, No. 6, pp. 1–15, 2013.

97. Zhu, L., Schrand, A.M., Voevodin, A.A., Chang, D.W., Dai, L. and S.M. Hussain, "Assessment of human lung macrophages after exposure to multi-walled carbon nanotubes part II. DNA damage", *Nanoscience and Nanotechnology Letters*, Vol. 3, No. 1, pp. 94–98, 2011.

98. Sweeney, S., Hu, S., Ruenraroengsak, P., Chen, S., Gow, A., Schwander, S., Zhang, J., Chung, K.F., Ryan, M.P., Porter, A.E., Shaffer, M.S. and T.D. Tetley, "Carboxylation of multiwalled carbon nanotubes reduces their toxicity in primary human alveolar macrophages", *Environmental Science: Nano*, Vol. 3, No. 6, pp. 1340–1350, 2016.

99. Bhirde, A.A., Patel, S., Sousa, A.A., Patel, V., Molinolo, A.A., Ji, Y., Leapman, R.D., Gutkind, J.S. and J.F. Rusling, "Distribution and Clearance of PEG-Single-Walled Carbon Nanotube Cancer Drug Delivery Vehicles in Mice", *Nanomedicine*, Vol. 5, No. 10, pp. 1535–1546, 2010.

100. Krajcik, R., Jung, A., Hirsch, A., Neuhuber, W. and O. Zolk, "Functionalization of carbon nanotubes enables non-covalent binding and intracellular delivery of small interfering RNA for efficient knock-down of genes", *Biochemical and Biophysical Research Communications*, Vol. 369, No. 2, pp. 595–602, 2008.

101. Singh, A.V., Rosenkranz, D., Ansari, M.H.D., Singh, R., Kanase, A., Singh, S.P., Johnston, B., Tentschert, J., Laux, P. and A. Luch, "Artificial Intelligence and Machine Learning Empower Advanced Biomedical Material Design to Toxicity Prediction", *Advanced Intelligent Systems*, Vol. 2, No. 2000084, 2020.

102. Furxhi, I., Murphy, F., Mullins, M., Arvanitis, A. and C.A. Poland, "Nanotoxicology data for in silico tools: a literature review", *Nanotoxicology*, Vol. 14, No. 5, pp. 612–637, 2020.

103. Hu, X., Cook, S., Wang, P. and H. min Hwang, “In vitro evaluation of cytotoxicity of engineered metal oxide nanoparticles”, *Science of The Total Environment*, Vol. 407, No. 8, pp. 3070–3072, 2009.

104. Sayes, C. and I. Ivanov, “Comparative Study of Predictive Computational Models for Nanoparticle-Induced Cytotoxicity”, *Risk Analysis*, Vol. 30, No. 11, pp. 1723–1734, 2010.

105. Liu, R., Rallo, R., George, S., Ji, Z., Nair, S., Nel, A.E. and Y. Cohen, “Classification NanoSAR development for cytotoxicity of metal oxide nanoparticles”, *Small*, Vol. 7, No. 8, pp. 1118–1126, 2011.

106. Puzyn, T., Rasulev, B., Gajewicz, A., Hu, X., Dasari, T.P., Michalkova, A., Hwang, H.M., Toropov, A., Leszczynska, D. and J. Leszczynski, “Using nano-QSAR to predict the cytotoxicity of metal oxide nanoparticles”, *Nature Nanotechnology*, Vol. 6, No. 3, pp. 175–178, 2011.

107. Pan, Y., Li, T., Cheng, J., Telesca, D., Zink, J.I. and J. Jiang, “Nano-QSAR modeling for predicting the cytotoxicity of metal oxide nanoparticles using novel descriptors”, *RSC Advances*, Vol. 6, No. 31, pp. 25766–25775, 2016.

108. Toropov, A.A., Toropova, A.P., Benfenati, E., Gini, G., Puzyn, T., Leszczynska, D. and J. Leszczynski, “Novel application of the CORAL software to model cytotoxicity of metal oxide nanoparticles to bacteria Escherichia coli”, *Chemosphere*, Vol. 89, No. 9, pp. 1098–1102, 2012.

109. Kar, S., Gajewicz, A, Puzyn, T., Roy, K. and J. Leszczynski, “Periodic table-based descriptors to encode cytotoxicity profile of metal oxide nanoparticles: A mechanistic QSTR approach”, *Ecotoxicology and Environmental Safety*, Vol. 107, pp. 162–169, 2014.

110. Sizochenko, N., Rasulev, B., Gajewicz, A., Kuz'Min, V., Puzyn, T. and J. Leszczynski, "From basic physics to mechanisms of toxicity: The 'liquid drop' approach applied to develop predictive classification models for toxicity of metal oxide nanoparticles", *Nanoscale*, Vol. 6, No. 22, pp. 13986–13993, 2014.

111. Singh, K.P. and S. Gupta, "Nano-QSAR modeling for predicting biological activity of diverse nanomaterials", *RSC Advances*, Vol. 4, No. 26, pp. 13215–13230, 2014.

112. Gajewicz, A., Cronin, M.T.D., Rasulev, B., Leszczynski, J. and T. Puzyn, "Novel approach for efficient predictions properties of large pool of nanomaterials based on limited set of species: Nano-read-across", *Nanotechnology*, Vol. 26, No. 1, 2015.

113. Pathakoti, K., Huang, M.J., Watts, J.D., He, X. and H.M. Hwang, "Using experimental data of Escherichia coli to develop a QSAR model for predicting the photo-induced cytotoxicity of metal oxide nanoparticles", *Journal of Photochemistry and Photobiology B: Biology*, Vol. 130, pp. 234–240, 2014.

114. "CORAL-QSAR/QSPR", http://www.insilico.eu/CORAL, accessed on July 24, 2022.

115. Toropova, A.P., Toropov, A.A., Rallo, R., Leszczynska, D. and J. Leszczynski, "Optimal descriptor as a translator of eclectic data into prediction of cytotoxicity for metal oxide nanoparticles under different conditions", *Ecotoxicology and Environmental Safety*, Vol. 112, pp. 39–45, 2015.

116. Choi, J.S., Trinh, T.X., Yoon, T.H., Kim, J. and H.G. Byun, "Quasi-QSAR for predicting the cell viability of human lung and skin cells exposed to different metal oxide nanomaterials", *Chemosphere*, Vol. 217, pp. 243–249, 2019.

117. Cao, J., Pan, Y., Jiang, Y., Qi, R., Yuan, B., Jia, Z., Jiang, J. and Q. Wang, "Computer-aided nanotoxicology: risk assessment of metal oxide nanoparticlesvianano-QSAR", *Green Chemistry*, Vol. 22, No. 11, pp. 3512–3521, 2020.

118. Trinh, T.X., Choi, J.S., Jeon, H., Byun, H.G., Yoon, T.H. and J. Kim, "Quasi-SMILES-Based Nano-Quantitative Structure-Activity Relationship Model to Predict the Cytotoxicity of Multiwalled Carbon Nanotubes to Human Lung Cells", *Chemical Research in Toxicology*, Vol. 31, No. 3, pp. 183–190, 2018.

119. Leone, C., Bertuzzi, E.E., Toropova, A.P., Toropov, A.A. and E. Benfenati, "CORAL: Predictive models for cytotoxicity of functionalized nanozeolites based on quasi-SMILES", *Chemosphere*, Vol. 210, pp. 52–56, 2018.

120. Manganelli, S., Leone, C., Toropov, A.A., Toropova, A.P. and E. Benfenati, "QSAR model for predicting cell viability of human embryonic kidney cells exposed to SiO2 nanoparticles", *Chemosphere*, Vol. 144, pp. 995–1001, 2016.

121. Cassano, A., Robinson, R.L.M., Palczewska, A., Puzyn, T., Gajewicz, A., Tran, L., Manganelli, S. and M.T.D. Cronin, "Comparing the CORAL and random forest approaches for modelling the in vitro cytotoxicity of silica nanomaterials", *Alternatives to Laboratory Animals*, Vol. 44, No. 6, pp. 533–556, 2016.

122. Horev-Azaria, L., Kirkpatrick, C.J., Korenstein, R., Marche, P.N., Maimon, O., Ponti, J., Romano, R., Rossi, F., Golla-Schindler, U., Sommer, D., Uboldi, C., Unger, R. E. and C. Villiers, "Predictive toxicology of cobalt nanoparticles and ions: Comparative in vitro study of different cellular models using methods of knowledge discovery from data", *Toxicological Sciences*, Vol. 122, No. 2, pp. 489–501, 2011.

123. Zhang, H., Ji, Z., Xia, T., Meng, H., Low-Kam, C., Liu, R., Pokhrel, S., Lin, S., Wang, X., Liao, Y. P., Wang, M., Li, L., Rallo, R., Damoiseaux, R., Telesca, D., Mädler, L., Cohen, Y., Zink, J. I. and A.E. Nel, "Use of metal oxide nanoparticle band gap to develop a predictive paradigm for oxidative stress and acute pulmonary inflammation", *ACS Nano*, Vol. 6, No. 5, pp. 4349–4368, 2012.

124. Liu, R., Zhang, H. Y., Ji, Z. X., Rallo, R., Xia, T., Chang, C. H., Nel, A. and Y. Cohen, "Development of structure-activity relationship for metal oxide nanoparticles", *Nanoscale*, Vol. 5, No. 12, pp. 5644–5653, 2013.

125. Liu, R., Rallo, R., Weissleder, R., Tassa, C., Shaw, S. and Y. Cohen, “Nano-SAR development for bioactivity of nanoparticles with considerations of decision boundaries”, *Small*, Vol. 9, No. 9–10, pp. 1842–1852, 2013.

126. Winkler, D.A., Burden, F.R., Yan, B., Weissleder, R., Tassa, C., Shaw, S. and V.C. Epa, “Modelling and predicting the biological effects of nanomaterials”, *SAR and QSAR in Environmental Research*, Vol. 25, No. 2, pp. 161–172, 2014.

127. Gernand, J.M. and E.A. Casman, “A meta-analysis of carbon nanotube pulmonary toxicity studies-how physical dimensions and impurities affect the toxicity of carbon nanotubes”, *Risk Analysis*, Vol. 34, No. 3, pp. 583–597, 2014.

128. Fourches, D., Pu, D., Li, L., Zhou, H., Mu, Q., Su, G., Yan, B. and A. Tropsha, “Computer-aided design of carbon nanotubes with the desired bioactivity and safety profiles”, *Nanotoxicology*, Vol. 10, No. 3, pp. 374–383, 2016.

129. Gajewicz, A., Schaeublin, N., Rasulev, B., Hussain, S., Leszczynska, D., Puzyn, T. and J. Leszczynski, “Towards understanding mechanisms governing cytotoxicity of metal oxides nanoparticles: Hints from nano-QSAR studies”, *Nanotoxicology*, Vol. 9, No. 3, pp. 313–325, 2015.

130. Gajewicz, A., “Development of valuable predictive read-across models based on ‘real-life’ (sparse) nanotoxicity data”, *Environmental Science: Nano*, Vol. 4, No. 6, pp. 1389–1403, 2017.

131. Gajewicz, A., Jagiello, K., Cronin, M.T.D., Leszczynski, J. and T. Puzyn, “Addressing a bottle neck for regulation of nanomaterials: quantitative read-across (Nano-QRA) algorithm for cases when only limited data is available”, *Environmental Science: Nano*, Vol. 4, No. 2, pp. 346–358, 2017.

132. Smirnov, B.V., “Processes involving clusters and small particles in a buffer gas”, *Physics-Uspekhi*, Vol. 54, No. 7, pp. 691–721, 2011.

133. Sizochenko, N., Rasulev, B., Gajewicz, A., Mokshyna, E., Kuz'min, V. E., Leszczynski, J. and T. Puzyn, "Causal inference methods to assist in mechanistic interpretation of classification nano-SAR models", *RSC Advances*, Vol. 5, No. 95, pp. 77739–77745, 2015.

134. Kuz'min, V.E., Ognichenko, L.N., Sizochenko, N., Chapkin, V.A., Stelmakh, S. I., Shyrykalova, A.O. and J. Leszczynski, "Combining Features of Metal Oxide Nanoparticles", *International Journal of Quantitative Structure-Property Relationships*, Vol. 4, No. 1, pp. 28–40, 2018.

135. Luan, F., Kleandrova, V.V., González-Díaz, H., Ruso, J.M., Melo, A., Speck-Planche, A. and M.N.D.S. Cordeiro, "Computer-aided nanotoxicology: Assessing cytotoxicity of nanoparticles under diverse experimental conditions by using a novel QSTR-perturbation approach", *Nanoscale*, Vol. 6, No. 18, pp. 10623–10630, 2014.

136. Kleandrova, V.V., Luan, F., González-Díaz, H., Ruso, J.M., Speck-Planche, A. and M.N.D.S. Cordeiro, "Computational tool for risk assessment of nanomaterials: Novel QSTR-perturbation model for simultaneous prediction of ecotoxicity and cytotoxicity of uncoated and coated nanoparticles under multiple experimental conditions", *Environmental Science & Technology*, Vol. 48, No. 24, pp. 14686–14694, 2014.

137. Halder, A.K., Melo, A. and M.N.D.S. Cordeiro, "A unified in silico model based on perturbation theory for assessing the genotoxicity of metal oxide nanoparticles", *Chemosphere*, Vol. 244, 2020.

138. Bilal, M., Oh, E., Liu, R., Breger, J.C., Medintz, I.L. and Y. Cohen, "Bayesian Network Resource for Meta-Analysis: Cellular Toxicity of Quantum Dots", *Small*, Vol. 15, No. 34, pp. 1–12, 2019.

139. Ban, Z., Zhou, Q., Sun, A., Mu, L. and X. Hu, "Screening Priority Factors Determining and Predicting the Reproductive Toxicity of Various Nanoparticles", *Environmental Science & Technology*, Vol. 52, No. 17, pp. 9666–9676, 2018.

140. Liu, X., Tang, K., Harper, S., Harper, B., Steevens, J.A. and R. Xu, "Predictive modeling of nanomaterial exposure effects in biological systems", *International Journal of Nanomedicine*, Vol. 8, No. SUPPL. 1, pp. 31–43, 2013.

141. Jones, D.E., Ghandehari, H. and J.C. Facelli, "Predicting cytotoxicity of PAMAM dendrimers using molecular descriptors", *Beilstein Journal of Nanotechnology*, Vol. 6, No. 1, pp. 1886–1896, 2015.

142. "S2NANO", http://portal.s2nano.org/, accessed on July 24, 2022.

143. Ha, M.K., Trinh, T.X., Choi, J.S., Maulina, D., Byun, H.G. and T.H. Yoon, "Toxicity Classification of Oxide Nanomaterials: Effects of Data Gap Filling and PChem Score-based Screening Approaches", *Scientific Reports*, Vol. 8, No. 1, pp. 1–11, 2018.

144. Choi, J.S., Ha, M.K., Trinh, T.X., Yoon, T.H. and H.G. Byun, "Towards a generalized toxicity prediction model for oxide nanomaterials using integrated data from different sources", *Scientific Reports*, Vol. 8, No. 1, pp. 1–10, 2018.

145. Papadiamantis, A.G., Jänes, J., Voyiatzis, E., Sikk, L., Burk, J., Burk, P., Tsoumanis, A., Ha, M.K., Yoon, T.H., Valsami-Jones, E., Lynch, I., Melagraki, G., Tämm, K. and A. Afantitis, "Predicting cytotoxicity of metal oxide nanoparticles using isalos analytics platform", *Nanomaterials*, Vol. 10, No. 10, pp. 1–19, 2020.

146. "NanoDESK", http://sudoenanodesk.net/, accessed on July 24, 2022.

147. "eNanoMapper", http://www.enanomapper.net/data, accessed on July 24, 2022.

148. "NANoREG", https://nanoreg.eu/, accessed on July 24, 2022.

149. Ambure, P., Ballesteros, A., Huertas, F., Camilleri, P., Barigye, S.J. and R. Gozalbes, "Development of Generalized QSAR Models for Predicting Cytotoxicity and Genotoxicity of Metal Oxides Nanoparticles", *International Journal of Quantitative Structure-Property Relationships*, Vol. 5, No. 4, pp. 83–100, 2020.

150. Papa, E., Doucet, J.P. and A. Doucet-Panaye, “Linear and non-linear modelling of the cytotoxicity of TiO2 and ZnO nanoparticles by empirical descriptors”, *SAR and QSAR in Environmental Research*, Vol. 26, No. 7–9, pp. 647–665, 2015.

151. Le, T. C., Yin, H., Chen, R., Chen, Y., Zhao, L., Casey, P. S., Chen, C. and D.A. Winkler, “An Experimental and Computational Approach to the Development of ZnO Nanoparticles that are Safe by Design”, *Small*, Vol. 12, No. 26, pp. 3568–3577, 2016.

152. Mu, Y., Wu, F., Zhao, Q., Ji, R., Qie, Y., Zhou, Y., Hu, Y., Pang, C., Hristozov, D., Giesy, J. P. and B. Xing, “Predicting toxic potencies of metal oxide nanoparticles by means of nano-QSARs”, *Nanotoxicology*, Vol. 10, No. 9, pp. 1207–1214, 2016.

153. Oksel, C., Winkler, D.A., Ma, C.Y., Wilkins, T. and X.Z. Wang, “Accurate and interpretable nanoSAR models from genetic programming-based decision tree construction approaches”, *Nanotoxicology*, Vol. 10, No. 7, pp. 1001–1012, 2016.

154. Fjodorova, N., Novic, M., Gajewicz, A. and B. Rasulev, “The way to cover prediction for cytotoxicity for all existing nano-sized metal oxides by using neural network method”, *Nanotoxicology*, Vol. 11, No. 4, pp. 475–483, 2017.

155. Shin, H.K., Kim, K.Y., Park, J.W. and K.T. No, “Use of metal/metal oxide spherical cluster and hydroxyl metal coordination complex for descriptor calculation in development of nanoparticle cytotoxicity classification model”, *SAR and QSAR in Environmental Research*, Vol. 28, No. 11, pp. 875–888, 2017.

156. Mikolajczyk, A., Sizochenko, N., Mulkiewicz, E., Malankowska, A., Nischk, M., Jurczak, P., Hirano, S., Nowaczyk, G., Zaleska-Medynska, A., Leszczynski, J., Gajewicz, A. and T. Puzyn, “Evaluating the toxicity of TiO2-based nanoparticles to Chinese hamster ovary cells and Escherichia coli: A complementary experimental and computational approach”, *Beilstein Journal of Nanotechnology*, Vol. 8, No. 1, pp. 2171–2180, 2017.

157. Marvin, H.J.P., Bouzembrak, Y., Janssen, E.M., van der Zande, M., Murphy, F., Sheehan, B., Mullins, M. and H. Bouwmeester, "Application of Bayesian networks for hazard ranking of nanomaterials to support human health risk assessment", *Nanotoxicology*, Vol. 11, No. 1, pp. 123–133, 2017.

158. Basant, N. and S. Gupta, "Multi-target QSTR modeling for simultaneous prediction of multiple toxicity endpoints of nano-metal oxides", *Nanotoxicology*, Vol. 11, No. 3, pp. 339–350, 2017.

159. Mikolajczyk, A., Gajewicz, A., Mulkiewicz, E., Rasulev, B., Marchelek, M., Diak, M., Hirano, S., Zaleska-Medynska, A. and T. Puzyn, "Nano-QSAR modeling for ecosafe design of heterogeneous TiO2-based nano-photocatalysts", *Environmental Science: Nano*, Vol. 5, No. 5, pp. 1150–1160, 2018.

160. Cheng, Y.H., Riviere, J.E., Monteiro-Riviere, N.A. and Z. Lin, "Probabilistic risk assessment of gold nanoparticles after intravenous administration by integrating in vitro and in vivo toxicity with physiologically based pharmacokinetic modeling", *Nanotoxicology*, Vol. 12, No. 5, pp. 453–469, 2018.

161. Furxhi, I., Murphy, F., Poland, C.A., Sheehan, B., Mullins, M. and P. Mantecca, "Application of Bayesian networks in determining nanoparticle-induced cellular outcomes using transcriptomics", *Nanotoxicology*, Vol. 13, No. 6, pp. 827–848, 2019.

162. Forest, V., Hochepied, J.F., Leclerc, L., Trouvé, A., Abdelkebir, K., Sarry, G., Augusto, V. and J. Pourchez, "Towards an alternative to nano-QSAR for nanoparticle toxicity ranking in case of small datasets", *Journal of Nanoparticle Research*, Vol. 21, No. 5, 2019.

163. Kotzabasaki, M.I., Sotiropoulos, I. and H. Sarimveis, "QSAR modeling of the toxicity classification of superparamagnetic iron oxide nanoparticles (SPIONs) in stem-cell monitoring applications: An integrated study from data curation to model development", *RSC Advances*, Vol. 10, No. 9, pp. 5385–5391, 2020.

164. Furxhi, I. and F. Murphy, “Predicting in vitro neurotoxicity induced by nanoparticles using machine learning”, *International Journal of Molecular Sciences*, Vol. 21, No. 15, pp. 1–21, 2020.

165. Huang, Y., Li, X., Xu, S., Zheng, H., Zhang, L., Chen, J., Hong, H., Kusko, R. and R. Li, “Quantitative structure–activity relationship models for predicting inflammatory potential of metal oxide nanoparticles”, *Environmental Health Perspectives*, Vol. 128, No. 6, pp. 1–13, 2020.

166. Kar, S., Pathakoti, K., Tchounwou, P.B., Leszczynska, D. and J. Leszczynski, “Evaluating the cytotoxicity of a large pool of metal oxide nanoparticles to Escherichia coli: Mechanistic understanding through In Vitro and In Silico studies”, *Chemosphere*, Vol. 264, No. 128428, 2021.

167. Ma, Y., Wang, J., Wu, J., Tong, C. and T. Zhang, “Meta-analysis of cellular toxicity for graphene via data-mining the literature and machine learning”, *Science of The Total Environment*, Vol. 793, No. 148532, 2021.

168. Liu, L., Zhang, Z., Cao, L., Xiong, Z., Tang, Y. and Y. Pan, “Cytotoxicity of phytosynthesized silver nanoparticles: A meta-analysis by machine learning algorithms”, *Sustainable Chemistry and Pharmacy*, Vol. 21, No. 100425, 2021.

169. Kad, A., Pundir, A., Arya, S.K., Puri, S. and M. Khatri, “Meta-analysis of in-vitro cytotoxicity evaluation studies of zinc oxide nanoparticles: Paving way for safer innovations”, *Toxicology in Vitro*, Vol. 83, No. 105418, 2022.

170. Furxhi, I., Murphy, F., Mullins, M., Arvanitis, A. and C.A. Poland, “Practices and trends of machine learning application in nanotoxicology”, *Nanomaterials*, Vol. 10, No. 1, pp. 1–32, 2020.

171. Ingólfsson, H.I., Melo, M.N., Van Eerden, F.J., Arnarez, C., Lopez, C.A., Wassenaar, T.A., Periole, X., De Vries, A.H., Tieleman, D.P. and S.J. Marrink, "Lipid organization of the plasma membrane", *Journal of the American Chemical Society*, Vol. 136, No. 41, pp. 14554–14559, 2014.

172. Ingólfsson, H.I., Carpenter, T.S., Bhatia, H., Bremer, P.T., Marrink, S.J. and F.C. Lightstone, "Computational Lipidomics of the Neuronal Plasma Membrane", *Biophysical Journal*, Vol. 113, No. 10, pp. 2271–2280, 2017.

173. Koldsø, H., Reddy, T., Fowler, P.W., Duncan, A.L. and M.S.P. Sansom, "Membrane Compartmentalization Reducing the Mobility of Lipids and Proteins within a Model Plasma Membrane", *The Journal of Physical Chemistry B*, Vol. 120, No. 34, pp. 8873–8881, 2016.

174. Thallmair, S., Ingólfsson, H.I. and S.J. Marrink, "Cholesterol Flip-Flop Impacts Domain Registration in Plasma Membrane Models", *The Journal of Physical Chemistry Letters*, Vol. 9, No. 18, pp. 5527–5533, 2018.

175. Girifalco, L.A., "Molecular properties of C60 in the gas and solid phases", *The Journal of Physical Chemistry*, Vol. 96, No. 2, pp. 858–861, 1992.

176. Monticelli, L., "On atomistic and coarse-grained models for C 60 fullerene", *Journal of Chemical Theory and Computation*, Vol. 8, No. 4, pp. 1370–1378, 2012.

177. Qiao, R., Roberts, A.P., Mount, A.S., Klaine, S.J. and P.C. Ke, "Translocation of C60 and its derivatives across a lipid bilayer", *Nano Letters*, Vol. 7, No. 3, pp. 614–619, 2007.

178. Monticelli, L., Salonen, E., Ke, P.C. and I. Vattulainen, "Effects of carbon nanoparticles on lipid membranes: A molecular simulation perspective", *Soft Matter*, Vol. 5, No. 22, pp. 4433–4445, 2009.

179. Li, W., Davande, H., Bedrov, D. and G.D. Smith, “A molecular dynamics simulation study of C60 fullerenes inside a dimyristoylphosphatidylcholine lipid bilayer”, *The Journal of Physical Chemistry B*, Vol. 111, No. 16, pp. 4067–4072, 2007.

180. Wong-Ekkabut, J., Baoukina, S., Triampo, W., Tang, I.M., Tieleman, D.P. and L. Monticelli, “Computer simulation study of fullerene translocation through lipid membranes”, *Nature Nanotechnology*, Vol. 3, No. 6, pp. 363–368, 2008.

181. Wallace, E.J. and M.S.P. Sansom, “Blocking of carbon nanotube based nanoinjectors by lipids: A simulation study”, *Nano Letters*, Vol. 8, No. 9, pp. 2751–2756, 2008.

182. D’Rozario, R.S.G., Wee, C.L., Jayne Wallace, E. and M.S.P. Sansom, “The interaction of C60 and its derivatives with a lipid bilayer via molecular dynamics simulations”, *Nanotechnology*, Vol. 20, No. 11, 2009.

183. Chang, R. and J. Lee, “Dynamics of C60 molecules in biological membranes: Computer simulation studies”, *Bulletin of the Korean Chemical Society*, Vol. 31, No. 11, pp. 3195–3200, 2010.

184. Zhang, S., Mu, Y., Zhang, J.Z.H. and W. Xu, “Effect of self-assembly of fullerene nano-particles on lipid membrane”, *PLoS One*, Vol. 8, No. 10, pp. 29–32, 2013.

185. Barnoud, J., Rossi, G. and L. Monticelli, “Lipid membranes as solvents for carbon nanoparticles”, *Physical Review Letters*, Vol. 112, No. 6, 2014.

186. Xie, L. qiang, Liu, Y. zhi, Xi, Z. hong, Li, H. yi, Liang, S. de and K. li Zhu, “Computer simulations of the interaction of fullerene clusters with lipid membranes”, *Molecular Simulation*, Vol. 43, No. 18, pp. 1532–1538, 2017.

187. Nisoh, N., Karttunen, M., Monticelli, L. and J. Wong-Ekkabut, “Lipid monolayer disruption caused by aggregated carbon nanoparticles”, *RSC Advances*, Vol. 5, No. 15, pp. 11676–11685, 2015.

188. Nalakarn, P., Boonnoy, P., Nisoh, N., Karttunen, M. and J. Wong-ekkabut, “Dependence of fullerene aggregation on lipid saturation due to a balance between entropy and enthalpy”, *Scientific Reports*, Vol. 9, No. 1, pp. 1–11, 2019.

189. Nisoh, N., Jarerattanachat, V., Karttunen, M. and J. Wong-ekkabut, “Formation of aggregates, icosahedral structures and percolation clusters of fullerenes in lipids bilayers: The key role of lipid saturation”, *Biochimica et Biophysica Acta - Biomembranes*, Vol. 1862, No. 183328, 2020.

190. Kraszewski, S., Tarek, M. and C. Ramseyer, “Uptake and translocation mechanisms of cationic amino derivatives functionalized on pristine C60 by lipid membranes: A molecular dynamics simulation study”, *ACS Nano*, Vol. 5, No. 11, pp. 8571–8578, 2011.

191. Bozdaganyan, M.E., Orekhov, P.S., Shaytan, A.K. and K.V. Shaitan, “Comparative computational study of interaction of C60-fullerene and tris-malonyl-C60-fullerene isomers with lipid bilayer: Relation to their antioxidant effect”, *PLoS One*, Vol. 9, No. 7, 2014.

192. Mohammadyani, D., Modarress, H., To, A.C. and A. Amani, “Interactions of Fullerene (C60) and its Hydroxyl Derivatives with Lipid Bilayer: A Coarse-Grained Molecular Dynamics Simulation”, *Brazilian Journal of Physics*, Vol. 44, No. 1, pp. 1–7, 2014.

193. Nakamura, H., Nozaki, Y., Koizumi, Y. and S. Watano, “Effect of number of hydroxyl groups of fullerenol C60(OH)n on its interaction with cell membrane”, *Journal of the Taiwan Institute of Chemical Engineers*, Vol. 90, pp. 18–24, 2018.

194. Sun, D., Lin, X. and N. Gu, “Cholesterol affects C60 translocation across lipid bilayers”, *Soft Matter*, Vol. 10, No. 13, pp. 2160–2168, 2014.

195. Alves, E.D., Colherinhas, G. and S.A. Mendanha, “Assessing the DOPC-cholesterol interactions and their influence on fullerene C60 partitioning in lipid bilayers”, *Journal of Molecular Liquids*, Vol. 315, p. 113698, 2020.

196. Sridhar, A., Srikanth, B., Kumar, A. and A.K. Dasmahapatra, “Coarse-grain molecular dynamics study of fullerene transport across a cell membrane”, *The Journal of Chemical Physics*, Vol. 143, No. 2, 2015.

197. Gul, G. and N. Ileri-Ercan, “Fullerene translocation through peroxidized lipid membranes”, *RSC Advances*, Vol. 11, No. 13, pp. 7575–7586, 2021.

198. Gupta, R. and B. Rai, “Molecular dynamics simulation study of translocation of fullerene C60 through skin bilayer: effect of concentration on barrier properties”, *Nanoscale*, Vol. 9, No. 12, pp. 4114–4127, 2017.

199. Sastre, J., Mannelli, I. and R. Reigada, “Effects of fullerene on lipid bilayers displaying different liquid ordering: a coarse-grained molecular dynamics study”, *Biochimica et Biophysica Acta - General Subjects*, Vol. 1861, No. 11, pp. 2872–2882, 2017.

200. Devane, R., Jusufi, A., Shinoda, W., Chiu, C.C., Nielsen, S.O., Moore, P.B. and M.L. Klein, “Parametrization and application of a coarse grained force field for benzene/fullerene interactions with lipids”, *The Journal of Physical Chemistry B*, Vol. 114, No. 49, pp. 16364–16372, 2010.

201. Lopez, C.F., Nielsen, S.O., Moore, P.B. and M.L. Klein, “Understanding nature’s design for a nanosyringe”, *Proceedings of the National Academy of Sciences of the United States of America*, Vol. 101, No. 13, pp. 4431–4434, 2004.

202. Lopez, C.F., Nielsen, S.O., Ensing, B., Moore, P.B. and M.L. Klein, “Structure and dynamics of model pore insertion into a membrane”, *Biophysical Journal*, Vol. 88, No. 5, pp. 3083–3094, 2005.

203. Gan, Y. and Z. Chen, “Molecular dynamics simulation of the size effect of carbon nanotubes on the bulk modulus of a lipid bilayer”, *MCB Molecular and Cellular Biomechanics*, Vol. 3, No. 3, pp. 89–94, 2006.

204. Shi, X., Kong, Y. and H. Gao, “Coarse grained molecular dynamics and theoretical studies of carbon nanotubes entering cell membrane”, *Acta Mechanica Sinica*, Vol. 24, No. 2, pp. 161–169, 2008.

205. Capaldi, F.M. and V.K. Gangupomu, “Interactions of carbon nanotube with lipid bilayer membranes”, *Journal of Nanomaterials*, Vol. 2011, No. 830436, 2011.

206. Raczyński, P., Górny, K., Pabiszczak, M. and Z. Gburski, “Nanoindentation of biomembrane by carbon nanotubes - MD simulation”, *Computational Materials Science*, Vol. 70, pp. 13–18, 2013.

207. Raczyński, P., Górny, K., Raczyńska, V., Pabiszczak, M., Dendzik, Z. and Z. Gburski, “On the impact of nanotube diameter on biomembrane indentation – Computer simulations study”, *Biochimica et Biophysica Acta - Biomembranes*, Vol. 1860, No. 2, pp. 310–318, 2018.

208. Kraszewski, S., Bianco, A., Tarek, M. and C. Ramseyer, “Insertion of short amino-functionalized single-walled carbon nanotubes into phospholipid bilayer occurs by passive diffusion”, *PLoS One*, Vol. 7, No. 7, pp. 1–11, 2012.

209. Kraszewski, S., Picaud, F., Elhechmi, I., Gharbi, T. and C. Ramseyer, “How long a functionalized carbon nanotube can passively penetrate a lipid membrane”, *Carbon*, Vol. 50, No. 14, pp. 5301–5308, 2012.

210. Lacerda, L., Ali-Boucetta, H., Kraszewski, S., Tarek, M., Prato, M., Ramseyer, C., Kostarelos, K. and A. Bianco, “How do functionalized carbon nanotubes land on, bind to and pierce through model and plasma membranes”, *Nanoscale*, Vol. 5, No. 21, pp. 10242–10250, 2013.

211. Baoukina, S., Monticelli, L. and D.P. Tieleman, “Interaction of pristine and functionalized carbon nanotubes with lipid membranes”, *The Journal of Physical Chemistry B*, Vol. 117, No. 40, pp. 12113–12123, 2013.

212. Lee, H., “Interparticle dispersion, membrane curvature, and penetration induced by single-walled carbon nanotubes wrapped with lipids and PEGylated lipids”, *The Journal of Physical Chemistry B*, Vol. 117, No. 5, pp. 1337–1344, 2013.

213. Lee, H., “Dispersion and bilayer interaction of single-walled carbon nanotubes modulated by covalent and noncovalent PEGylation”, *Molecular Simulation*, Vol. 41, No. 15, pp. 1254–1263, 2015.

214. Choi, M.K., Kim, H., Lee, B.H., Kim, T., Rho, J., Kim, M.K. and K. Kim, “Understanding carbon nanotube channel formation in the lipid membrane”, *Nanotechnology*, Vol. 29, No. 11, p. 115702, 2018.

215. Shen, C., Zou, G., Guo, W. and H. Gao, “Lipid coating and end functionalization govern the formation and stability of transmembrane carbon nanotube porins”, *Carbon*, Vol. 164, pp. 391–397, 2020.

216. Gao, Y., Mao, D., Wu, J., Wang, X., Wang, Z., Zhou, G., Chen, L., Chen, J. and S. Zeng, “Carbon nanotubes translocation through a lipid membrane and transporting small hydrophobic and hydrophilic molecules”, *Applied Sciences*, Vol. 9, No. 20, 2019.

217. Parthasarathi, R., Tummala, N.R. and A. Striolo, “Embedded single-walled carbon nanotubes locally perturb dopc phospholipid bilayers”, *The Journal of Physical Chemistry B*, Vol. 116, No. 42, pp. 12769–12782, 2012.

218. Lelimousin, M. and M.S.P. Sansom, “Membrane perturbation by carbon nanotube insertion: Pathways to internalization”, *Small*, Vol. 9, No. 21, pp. 3639–3646, 2013.

219. Vögele, M., Köfinger, J. and G. Hummer, “Molecular dynamics simulations of carbon nanotube porins in lipid bilayers”, *Faraday Discussions*, Vol. 209, pp. 341–358, 2018.

220. Rohatgi, A., “WebPlotDigitizer”, https://automeris.io/WebPlotDigitizer/, accessed on October 5, 2020.

221. Rivera-Gil, P., Jimenez De Aberasturi, D., Wulf, V., Pelaz, B., Del Pino, P., Zhao, Y., De La Fuente, J.M., Ruiz De Larramendi, I., Rojo, T., Liang, X.J. and W.J. Parak, "The challenge to relate the physicochemical properties of colloidal nanoparticles to their cytotoxicity", *Accounts of Chemical Research*, Vol. 46, No. 3, pp. 743–749, 2013.

222. Ramírez-Gallego, S., García, S., Mouriño-Talín, H., Martínez-Rego, D., Bolón-Canedo, V., Alonso-Betanzos, A., Benítez, J.M. and F. Herrera, "Data discretization: Taxonomy and big data challenge", *Wiley Interdisciplinary Reviews: Data Mining and Knowledge Discovery*, Vol. 6, No. 1, pp. 5–21, 2016.

223. Scarcello, E., Lambremont, A., Vanbever, R., Jacques, P.J. and D. Lison, "Mind your assays: Misleading cytotoxicity with the WST-1 assay in the presence of manganese", *PLoS One*, Vol. 15, No. 4, pp. 1–14, 2020.

224. Brandelli, A., "The interaction of nanostructured antimicrobials with biological systems: Cellular uptake, trafficking and potential toxicity", *Food Science and Human Wellness*, Vol. 9, No. 1, pp. 8–20, 2020.

225. Agrawal, R. and R. Srikant, "Fast Algorithms for Mining Association Rules", paper presented at the *Proceedings of the 20th International Conference on Very Large Data Bases*, San Jose, pp. 487-499, 1994.

226. Raschka, S., "MLxtend: Providing machine learning and data science utilities and extensions to Python's scientific computing stack", *Journal of Open Source Software*, Vol. 3, No. 24, p. 638, 2018.

227. van Rossum, G., "Python tutorial, May 1995," *Centrum voor Wiskunde& Informatica (CWI) Report*, No. CS-R9526, pp. 1–65, 1995.

228. Karplus, M. and J.A. McCammon, "Molecular Dynamics Simulations of Biomolecules", *Nature Structural Biology*, Vol. 9, No. 9, pp. 646–652, 2002.

229. Brooks, B.R., Bruccoleri, R.E., Olafson, B.D., States, D.J., Swaminathan, S. and M. Karplus, “CHARMM: A program for macromolecular energy, minimization, and dynamics calculations”, *Journal of Computational Chemistry*, Vol. 4, No. 2, pp. 187–217, 1983.

230. MacKerell, A.D., Bashford, D., Bellott, M., Dunbrack, R.L., Evanseck, J.D., Field, M.J., Fischer, S., Gao, J., Guo, H., Ha, S., Joseph-McCarthy, D., Kuchnir, L., Kuczera, K., Lau, F. T. K., Mattos, C., Michnick, S., Ngo, T., Nguyen, D. T., Prodhom, B. and M. Karplus, “All-atom empirical potential for molecular modeling and dynamics studies of proteins”, *The Journal of Physical Chemistry B*, Vol. 102, No. 18, pp. 3586–3616, 1998.

231. Marrink, S.J., De Vries, A.H. and A.E. Mark, “Coarse Grained Model for Semiquantitative Lipid Simulations”, *The Journal of Physical Chemistry B*, Vol. 108, No. 2, pp. 750–760, 2004.

232. Marrink, S.J., Risselada, H.J., Yefimov, S., Tieleman, D.P. and A.H. De Vries, “The MARTINI force field: Coarse grained model for biomolecular simulations”, *The Journal of Physical Chemistry B*, Vol. 111, No. 27, pp. 7812–7824, 2007.

233. Berendsen, H.J.C., van der Spoel, D. and R. van Drunen, “GROMACS: A message-passing parallel molecular dynamics implementation”, *Computer Physics Communications*, Vol. 91, No. 1–3, pp. 43–56, 1995.

234. Humphrey, W., Dalke, A. and K. Schulten, “VMD: Visual Molecular Dynamics”, *Journal of Molecular Graphics*, Vol. 14, pp. 33–38, 1996.

235. Wassenaar, T.A., Ingólfsson, H.I., Böckmann, R.A., Tieleman, D.P. and S.J. Marrink, “Computational lipidomics with insane: A versatile tool for generating custom membranes for molecular simulations”, *Journal of Chemical Theory and Computation*, Vol. 11, No. 5, pp. 2144–2155, 2015.

236. Guo, Y., Baulin, V.A. and F. Thalmann, “Peroxidised phospholipid bilayers: Insight from coarse-grained molecular dynamics simulations”, *Soft Matter*, Vol. 12, No. 1, pp. 263–271, 2015.

237. Berendsen, H.J.C., Postma, J.P.M., Van Gunsteren, W.F., Dinola, A. and J.R. Haak, “Molecular dynamics with coupling to an external bath”, *The Journal of Chemical Physics*, Vol. 81, No. 8, pp. 3684–3690, 1984.

238. Bussi, G., Donadio, D. and M. Parrinello, “Canonical sampling through velocity rescaling”, *The Journal of Chemical Physics*, Vol. 126, No. 1, 2007.

239. Parrinello, M. and A. Rahman, “Polymorphic transitions in single crystals: A new molecular dynamics method”, *Journal of Applied Physics*, Vol. 52, No. 12, pp. 7182–7190, 1981.

240. De Jong, D.H., Baoukina, S., Ingólfsson, H.I. and S.J. Marrink, “Martini straight: Boosting performance using a shorter cutoff and GPUs”, *Computer Physics Communications*, Vol. 199, pp. 1–7, 2016.

241. Van Der Spoel, D. and P.J. Van Maaren, “The Origin of Layer Structure Artifacts in Simulations of Liquid Water”, *Journal of Chemical Theory and Computation*, Vol. 2, pp. 1–11, 2006.

242. Tironi, I.G., Sperb, R., Smith, P.E. and W.F. Van Gunsteren, “A generalized reaction field method for molecular dynamics simulations”, *The Journal of Chemical Physics*, Vol. 102, No. 13, pp. 5451–5459, 1995.

243. Torrie, G.M. and J.P. Valleau, “Nonphysical Sampling Distributions in Monte Carlo Free-Energy Estimation: Umbrella Sampling”, *Journal of Computational Physics*, Vol. 23, pp. 187–199, 1977.

244. Kumar, S., Rosenberg, J.M., Bouzida, D., Swendsen, R.H. and P.A. Kollman, “THE weighted histogram analysis method for free-energy calculations on biomolecules. I. The method”, *Journal of Computational Chemistry*, Vol. 13, No. 8, pp. 1011–1021, 1992.

245. Hub, J.S., De Groot, B.L. and D. Van Der Spoel, “G-whams-a free Weighted Histogram Analysis implementation including robust error and autocorrelation estimates”, *Journal of Chemical Theory and Computation*, Vol. 6, No. 12, pp. 3713–3720, 2010.

246. Choi, Y.K., Kern, N.R., Kim, S., Kanhaiya, K., Afshar, Y., Jeon, S.H., Jo, S., Brooks, B.R., Lee, J., Tadmor, E.B., Heinz, H. and W. Im, “CHARMM-GUI Nanomaterial Modeler for Modeling and Simulation of Nanomaterial Systems”, *Journal of Chemical Theory and Computation*, Vol. 18, No. 1, pp. 479-493, 2022.

247. Kim, S., Lee, J., Jo, S., Brooks, C.L., Lee, H.S. and W. Im, “CHARMM-GUI ligand reader and modeler for CHARMM force field generation of small molecules”, *Journal of Computational Chemistry*, Vol. 38, No. 21, pp. 1879–1886, 2017.

248. Choi, Y.K., Park, S.J., Park, S., Kim, S., Kern, N.R., Lee, J. and W. Im, “CHARMM-GUI Polymer Builder for Modeling and Simulation of Synthetic Polymers”, *Journal of Chemical Theory and Computation*, Vol. 17, No. 4, pp. 2431–2443, 2021.

249. Jo, S., Kim, T. and W. Im, “Automated builder and database of protein/membrane complexes for molecular dynamics simulations”, *PLoS One*, Vol. 2, No. 9, 2007.

250. Wu, E.L., Cheng, X., Jo, S., Rui, H., Song, K.C., Dávila-Contreras, E.M., Qi, Y., Lee, J., Monje-Galvan, V., Venable, R.M., Klauda, J.B. and W. Im, “CHARMM-GUI membrane builder toward realistic biological membrane simulations”, *Journal of Computational Chemistry*, Vol. 35, No. 27, pp. 1997–2004, 2014.

251. Lee, J., Cheng, X., Swails, J.M., Yeom, M.S., Eastman, P.K., Lemkul, J.A., Wei, S., Buckner, J., Jeong, J.C., Qi, Y., Jo, S., Pande, V.S., Case, D.A., Brooks, C.L., MacKerell, A.D., Klauda, J.B. and W. Im, "CHARMM-GUI Input Generator for NAMD, GROMACS, AMBER, OpenMM, and CHARMM/OpenMM Simulations Using the CHARMM36 Additive Force Field", *Journal of Chemical Theory and Computation*, Vol. 12, No. 1, pp. 405–413, 2016.

252. Jo, S., Kim, T., Iyer, V.G. and W. Im, "CHARMM-GUI: A Web-Based Graphical User Interface for CHARMM", *Journal of Computational Chemistry*, Vol. 29, No. 11, pp. 1859–1865, 2008.

253. Czerw, R., Guo, Z., Ajayan, P.M., Sun, Y.P. and D.L. Carroll, "Organization of Polymers onto Carbon Nanotubes: A Route to Nanoscale Assembly", *Nano Letters*, Vol. 1, No. 8, pp. 423–427, 2001.

254. Huang, H.M., Liu, I.C., Chang, C.Y.U., Tsai, H.C., Hsu, C.H. and R.C.C. Tsiang, "Preparing a polystyrene-functionalized multiple-walled carbon nanotubes via covalently linking acyl chloride functionalities with living polystyryllithium", *Journal of Polymer Science Part A: Polymer Chemistry*, Vol. 42, No. 22, pp. 5802–5810, 2004.

255. Yang, Y., Xie, X., Wu, J. and Y.W. Mai, "Synthesis and Self-Assembly of Polystyrene-Grafted Multiwalled Carbon Nanotubes with a Hairy-Rod Nanostructure", *Journal of Polymer Science Part A: Polymer Chemistry*, Vol. 44, pp. 3869–3881, 2006.

256. Huang, J. and A.D. Mackerell, "CHARMM36 all-atom additive protein force field: Validation based on comparison to NMR data", *Journal of Computational Chemistry*, Vol. 34, No. 25, pp. 2135–2145, 2013.

257. Huang, J., Rauscher, S., Nawrocki, G., Ran, T., Feig, M., De Groot, B.L., Grubmüller, H. and A.D. MacKerell Jr., "CHARMM36m: An Improved Force Field for Folded and Intrinsically Disordered Proteins", *Nature Methods*, Vol. 14, No. 1, pp. 71–73, 2017.

258. Klauda, J.B., Venable, R.M., Freites, J.A., O'Connor, J.W., Tobias, D.J., Mondragon-Ramirez, C., Vorobyov, I., MacKerell, A.D. and R.W. Pastor, "Update of the CHARMM All-Atom Additive Force Field for Lipids: Validation on Six Lipid Types", *The Journal of Physical Chemistry B*, Vol. 114, No. 23, pp. 7830–7843, 2010.

259. Vanommeslaeghe, K., Hatcher, E., Acharya, C., Kundu, S., Zhong, S., Shim, J., Darian, E., Guvench, O., Lopes, P., Vorobyov, I. and A.D. MacKerell Jr., "CHARMM General Force Field (CGenFF): A force field for drug-like molecules compatible with the CHARMM all-atom additive biological force fields", *Journal of Computational Chemistry*, Vol. 31, No. 4, pp. 671–690, 2010.

260. Pramanik, C., Gissinger, J.R., Kumar, S. and H. Heinz, "Carbon Nanotube Dispersion in Solvents and Polymer Solutions: Mechanisms, Assembly, and Preferences", *ACS Nano*, Vol. 11, No. 12, pp. 12805–12816, 2017.

261. "CGENFF", https://cgenff.umaryland.edu/, accessed on September 15, 2021.

262. Darden, T., York, D. and L. Pedersen, "Particle mesh Ewald: An N·log(N) method for Ewald sums in large systems", *The Journal of Chemical Physics*, Vol. 98, No. 12, pp. 10089–10092, 1993.

263. Hess, B., Bekker, H., Berendsen, H.J.C. and J.G.E.M. Fraaije, "LINCS: A Linear Constraint Solver for molecular simulations", *Journal of Computational Chemistry*, Vol. 18, No. 12, pp. 1463–1472, 1997.

264. Alessandri, R., Barnoud, J., Gertsen, A.S., Patmanidis, I., Vries, A.H. de, Souza, P.C.T. and S.J. Marrink, "Martini 3 Coarse-Grained Force Field: Small Molecules", *Advanced Theory and Simulations*, Vol. 5, No. 1, pp. 1–48, 2021.

265. Souza, P.C.T., Alessandri, R., Barnoud, J., Thallmair, S., Faustino, I., Grünewald, F., Patmanidis, I., Abdizadeh, H., Bruininks, B.M.H., Wassenaar, T.A., Kroon, P.C., Melcr, J., Nieto, V., Corradi, V., Khan, H.M., Domański, J., Javanainen, M., Martinez-Seara, H., Reuter, N. … and S.J. Marrink, "Martini 3: a general purpose force field for coarse-grained molecular dynamics", *Nature Methods*, Vol. 18, No. 4, pp. 382–388, 2021.

266. "CGBuilder", https://jbarnoud.github.io/cgbuilder/, accessed on September 17, 2021.

267. Grünewald, F., Alessandri, R., Kroon, P.C., Monticelli, L., Souza, P.C.T. and S.J. Marrink, "Polyply; a python suite for facilitating simulations of macromolecules and nanomaterials", *Nature Communications*, Vol. 13, No. 1, pp. 1–12, 2022.

268. Rossi, G., Monticelli, L., Puisto, S.R., Vattulainen, I. and T. Ala-Nissila, "Coarse-graining polymers with the MARTINI force-field: Polystyrene as a benchmark case", *Soft Matter*, Vol. 7, No. 2, pp. 698–708, 2011.

269. Bennett, C.H., "Efficient estimation of free energy differences from Monte Carlo data", *Journal of Computational Physics*, Vol. 22, No. 2, pp. 245–268, 1976.

270. Leach, A.R., *Molecular Modelling Principles and Applications*, Second Edition, Prentice Hall, 2001.

271. Bannan, C.C., Calabró, G., Kyu, D.Y. and D.L. Mobley, "Calculating Partition Coefficients of Small Molecules in Octanol/Water and Cyclohexane/Water", *Journal of Chemical Theory and Computation*, Vol. 12, No. 8, pp. 4015–4024, 2016.

272. Beutler, T.C., Mark, A.E., van Schaik, R.C., Gerber, P.R. and W.F. Van Gunsteren, "Avoiding Singularities and Numerical Instabilities in Free Energy Calculations Based on Molecular Simulations", *Chemical Physics Letters*, Vol. 222, pp. 529–539, 1994.

273. Buchoux, S., "FATSLiM: A fast and robust software to analyze MD simulations of membranes", *Bioinformatics*, Vol. 33, No. 1, pp. 133–134, 2017.

274. “Order Parameter”, http://www.cgmartini.nl/index.php/tools2/other-tools, accessed on April 6, 2021.

275. Ileri Ercan, N., “Understanding Interactions of Curcumin with Lipid Bilayers: A Coarse-Grained Molecular Dynamics Study”, *Journal of Chemical Information and Modeling*, Vol. 59, pp. 4413–4426, 2019.

276. “MATLAB”, The MathWorks Inc, Natick, Massachusetts, 2018.

277. Smith, P. and C.D. Lorenz, “LiPyphilic: A Python Toolkit for the Analysis of Lipid Membrane Simulations”, *Journal of Chemical Theory and Computation*, Vol. 17, No. 9, pp. 5907–5919, 2021.

278. Kučerka, N., Nagle, J.F., Sachs, J.N., Feller, S.E., Pencer, J., Jackson, A. and J. Katsaras, “Lipid bilayer structure determined by the simultaneous analysis of neutron and X-ray scattering data”, *Biophysical Journal*, Vol. 95, No. 5, pp. 2356–2367, 2008.

279. Pan, J., Tristram-Nagle, S., Kučerka, N. and J.F. Nagle, “Temperature dependence of structure, bending rigidity, and bilayer interactions of dioleoylphosphatidylcholine bilayers”, *Biophysical Journal*, Vol. 94, No. 1, pp. 117–124, 2008.

280. Tristram-Nagle, S., Petrache, H.I. and J.F. Nagle, “Structure and interactions of fully hydrated dioleoylphosphatidylcholine bilayers”, *Biophysical Journal*, Vol. 75, No. 2, pp. 917–925, 1998.

281. Kučerka, N., Tristram-Nagle, S. and J.F. Nagle, “Structure of fully hydrated fluid phase lipid bilayers with monounsaturated chains”, *The Journal of Membrane Biology*, Vol. 208, No. 3, pp. 193–202, 2006.

282. Kučerka, N., Nieh, M.P. and J. Katsaras, “Fluid phase lipid areas and bilayer thicknesses of commonly used phosphatidylcholines as a function of temperature”, *Biochimica et Biophysica Acta - Biomembranes*, Vol. 1808, No. 11, pp. 2761–2771, 2011.

283. Pluhackova, K., Kirsch, S.A., Han, J., Sun, L., Jiang, Z., Unruh, T. and R.A. Böckmann, “A Critical Comparison of Biomembrane Force Fields: Structure and Dynamics of Model DMPC, POPC, and POPE Bilayers”, *The Journal of Physical Chemistry B*, Vol. 120, No. 16, pp. 3888–3903, 2016.

284. Shahane, G., Ding, W., Palaiokostas, M. and M. Orsi, “Physical properties of model biological lipid bilayers: insights from all-atom molecular dynamics simulations”, *Journal of Molecular Modeling*, Vol. 25, No. 3, pp. 1–13, 2019.

285. Weber, G., Charitat, T., Baptista, M.S., Uchoa, A.F., Pavani, C., Junqueira, H.C., Guo, Y., Baulin, V.A., Itri, R., Marques, C.M. and A.P. Schroder, “Lipid oxidation induces structural changes in biomimetic membranes”, *Soft Matter*, Vol. 10, No. 24, pp. 4241–4247, 2014.

286. Filippov, A., Orädd, G. and G. Lindblom, “Influence of cholesterol and water content on phospholipid lateral diffusion in bilayers”, *Langmuir*, Vol. 19, No. 16, pp. 6397–6400, 2003.

287. Hsieh, F.Y., Zhilenkov, A.V., Voronov, I.I., Khakina, E.A., Mischenko, D.V., Troshin, P.A. and S.H. Hsu, “Water-Soluble Fullerene Derivatives as Brain Medicine: Surface Chemistry Determines if They Are Neuroprotective and Antitumor”, *ACS Applied Materials & Interfaces*, Vol. 9, No. 13, pp. 11482–11492, 2017.

288. Chen, L., Mccrate, J.M., Lee, J.C.M. and H. Li, “The role of surface charge on the uptake and biocompatibility of hydroxyapatite nanoparticles with osteoblast cells”, *Nanotechnology*, Vol. 22, No. 10, 2011.

289. Yang, X., Li, Y., Liu, X., Zhang, R. and Q. Feng, “In vitro uptake of hydroxyapatite nanoparticles and their effect on osteogenic differentiation of human mesenchymal stem cells”, *Stem Cells International*, Vol. 2018, 2018.

290. Omar Zaki, S.S., Katas, H. and Z.A. Hamid, “Lineage-related and particle size-dependent cytotoxicity of chitosan nanoparticles on mouse bone marrow-derived hematopoietic stem and progenitor cells”, *Food and Chemical Toxicology*, Vol. 85, pp. 31–44, 2015.

291. Mohammed, M.A., Syeda, J.T.M., Wasan, K.M. and E.K. Wasan, “An overview of chitosan nanoparticles and its application in non-parenteral drug delivery”, *Pharmaceutics*, Vol. 9, No. 4, 2017.

292. Krais, A., Wortmann, L., Hermanns, L., Feliu, N., Vahter, M., Stucky, S., Mathur, S. and B. Fadeel, “Targeted uptake of folic acid-functionalized iron oxide nanoparticles by ovarian cancer cells in the presence but not in the absence of serum”, *Nanomedicine*, Vol. 10, No. 7, pp. 1421–1431, 2014.

293. Costa, C., Brandão, F., Bessa, M. J., Costa, S., Valdiglesias, V., Kiliç, G., Fernández-Bertólez, N., Quaresma, P., Pereira, E., Pásaro, E., Laffon, B. and J.P. Teixeira, “In vitro cytotoxicity of superparamagnetic iron oxide nanoparticles on neuronal and glial cells. Evaluation of nanoparticle interference with viability tests”, *Journal of Applied Toxicology*, Vol. 36, No. 3, pp. 361–372, 2016.

294. Feng, Q., Liu, Y., Huang, J., Chen, K., Huang, J. and K. Xiao, “Uptake, distribution, clearance, and toxicity of iron oxide nanoparticles with different sizes and coatings”, *Scientific Reports*, Vol. 8, No. 1, pp. 1–13, 2018.

295. Seabra, A.B., Pelegrino, M.T. and P.S. Haddad, *Antimicrobial Applications of Superparamagnetic Iron Oxide Nanoparticles: Perspectives and Challenges*, Elsevier Inc., 2017.

296. Kobayashi, M., Osada, M., Kato, H. and M. Kakihana, “Design of crystal structures, morphologies and functionalities of titanium oxide using water-soluble complexes and molecular control agents”, *Polymer Journal*, Vol. 47, No. 2, pp. 78–83, 2015.

297. Dapiaggi, M., Pagliari, L., Pavese, A., Sciascia, L., Merli, M. and F. Francescon, "The formation of silica high temperature polymorphs from quartz: Influence of grain size and mineralising agents", *Journal of the European Ceramic Society*, Vol. 35, No. 16, pp. 4547–4555, 2015.

298. Uboldi, C., Giudetti, G., Broggi, F., Gilliland, D., Ponti, J. and F. Rossi, "Amorphous silica nanoparticles do not induce cytotoxicity, cell transformation or genotoxicity in Balb/3T3 mouse fibroblasts", *Mutation Research/Genetic Toxicology and Environmental Mutagenesis*, Vol. 745, No. 1–2, pp. 11–20, 2012.

299. Ryu, H.J., Seong, N.W., So, B.J., Seo, H.S., Kim, J.H., Hong, J.S., Park, M.K., Kim, M.S., Kim, Y.R., Cho, K.B., Seo, M.Y., Kim, M.K., Maeng, E.H. and S.W. Son, "Evaluation of silica nanoparticle toxicity after topical exposure for 90 days", *International Journal of Nanomedicine*, Vol. 9, pp. 127–136, 2014.

300. Lee, G.H., Kim, Y.S., Kwon, E., Yun, J.W. and B.C. Kang, "Toxicologic evaluation for amorphous silica nanoparticles: Genotoxic and non-genotoxic tumor-promoting potential", *Pharmaceutics*, Vol. 12, No. 9, pp. 1–17, 2020.

301. Ruenraroengsak, P. and T.D. Tetley, "Differential bioreactivity of neutral, cationic and anionic polystyrene nanoparticles with cells from the human alveolar compartment: Robust response of alveolar type 1 epithelial cells", *Particle and Fibre Toxicology*, Vol. 12, No. 1, pp. 1–20, 2015.

302. Fröhlich, E., Meindl, C., Roblegg, E., Ebner, B., Absenger, M. and T.R. Pieber, "Action of polystyrene nanoparticles of different sizes on lysosomal function and integrity", *Particle and Fibre Toxicology*, Vol. 9, pp. 1–13, 2012.

303. Huang, Y.W., Cambre, M. and H.J. Lee, "The Toxicity of Nanoparticles Depends on Multiple Molecular and Physicochemical Mechanisms", *International Journal of Molecular Sciences*, Vol. 18, No. 12, 2017.

304. Bhattacharjee, S., de Haan, L.H.J., Evers, N.M., Jiang, X., Marcelis, A.T.M., Zuilhof, H., Rietjens, I.M.C.M. and G.M. Alink, "Role of surface charge and oxidative stress in cytotoxicity of organic monolayer-coated silicon nanoparticles towards macrophage NR8383 cells", *Particle and Fibre Toxicology*, Vol. 7, p. 25, 2010.

305. Hühn, D., Kantner, K., Geidel, C., Brandholt, S., De Cock, I., Soenen, S.J.H., Riveragil, P., Montenegro, J.M., Braeckmans, K., Müllen, K., Nienhaus, G.U., Klapper, M. and W.J. Parak, "Polymer-coated nanoparticles interacting with proteins and cells: Focusing on the sign of the net charge", *ACS Nano*, Vol. 7, No. 4, pp. 3253–3263, 2013.

306. Findlay, M.R., Freitas, D.N., Mobed-Miremadi, M. and K.E. Wheeler, "Machine learning provides predictive analysis into silver nanoparticle protein corona formation from physicochemical properties", *Environmental Science: Nano*, Vol. 5, No. 1, pp. 64–71, 2018.

307. Rischitor, G., Parracino, M., La Spina, R., Urbán, P., Ojea-Jiménez, I., Bellido, E., Valsesia, A., Gioria, S., Capomaccio, R., Kinsner-Ovaskainen, A., Gilliland, D., Rossi, F. and P. Colpo, "Quantification of the cellular dose and characterization of nanoparticle transport during in vitro testing", *Particle and Fibre Toxicology*, Vol. 13, No. 1, pp. 1–16, 2016.

308. Teeguarden, J.G., Hinderliter, P.M., Orr, G., Thrall, B.D. and J.G. Pounds, "Particokinetics in vitro: Dosimetry considerations for in vitro nanoparticle toxicity assessments", *Toxicological Sciences*, Vol. 95, No. 2, pp. 300–312, 2007.

309. Sohaebuddin, S.K., Thevenot, P.T., Baker, D., Eaton, J.W. and L. Tang, "Nanomaterial cytotoxicity is composition, size, and cell type dependent", *Particle and Fibre Toxicology*, Vol. 7, pp. 1–17, 2010.

310. Manshian, B.B., Soenen, S.J., Al-Ali, A., Brown, A., Hondow, N., Wills, J., Jenkins, G.J.S. and S.H. Doak, "Cell type-dependent changes in cdse/ZnS quantum dot uptake and toxic endpoints", *Toxicological Sciences*, Vol. 144, No. 2, pp. 246–258, 2015.

311. Zeng, Y., Kurokawa, Y., Win-Shwe, T. T., Zeng, Q., Hirano, S., Zhang, Z. and H. Sone, “Effects of PAMAM dendrimers with various surface functional groups and multiple generations on cytotoxicity and neuronal differentiation using human neural progenitor cells”, *The Journal of Toxicological Sciences*, Vol. 41, No. 3, pp. 351–370, 2016.

312. Ashtami, J., Anju, S. and P.V. Mohanan, “Conformity of dextran-coated fullerene C70 with L929 fibroblast cells”, *Colloids and Surfaces B: Biointerfaces*, Vol. 184, No. 110530, 2019.

313. Mannerström, M., Zou, J., Toimela, T., Pyykkö, I. and T. Heinonen, “The applicability of conventional cytotoxicity assays to predict safety/toxicity of mesoporous silica nanoparticles, silver and gold nanoparticles and multi-walled carbon nanotubes”, *Toxicology in Vitro*, Vol. 37, pp. 113–120, 2016.

314. de Lima, R., do Espirito Santo Pereira, A., Porto, R.M. and L.F. Fraceto, “Evaluation of Cyto- and Genotoxicity of Poly(lactide-co-glycolide) Nanoparticles”, *Journal of Polymers and the Environment*, Vol. 19, No. 1, pp. 196–202, 2011.

315. Bruinink, A., Wang, J. and P. Wick, “Effect of particle agglomeration in nanotoxicology”, *Archives of Toxicology*, Vol. 89, No. 5, pp. 659–675, 2015.

316. Karlsson, H.L., Cronholm, P., Gustafsson, J. and L. Möller, “Copper oxide nanoparticles are highly toxic: A comparison between metal oxide nanoparticles and carbon nanotubes”, *Chemical Research in Toxicology*, Vol. 21, No. 9, pp. 1726–1732, 2008.

317. Valdiglesias, V., Costa, C., Kiliç, G., Costa, S., Pásaro, E., Laffon, B. and J.P. Teixeira, “Neuronal cytotoxicity and genotoxicity induced by zinc oxide nanoparticles”, *Environment International*, Vol. 55, pp. 92–100, 2013.

318. Ferraro, S.A., Domingo, M.G., Etcheverrito, A., Olmedo, D.G. and D.R. Tasat, "Neurotoxicity mediated by oxidative stress caused by titanium dioxide nanoparticles in human neuroblastoma (SH-SY5Y) cells", *Journal of Trace Elements in Medicine and Biology*, Vol. 57, No. 126413, 2020.

319. Long, J., Xiao, Y., Liu, L. and Y. Cao, "The adverse vascular effects of multi-walled carbon nanotubes (MWCNTs) to human vein endothelial cells (HUVECs) in vitro: Role of length of MWCNTs", *Journal of Nanobiotechnology*, Vol. 15, No. 1, pp. 1–13, 2017.

320. Zhao, X., Chang, S., Long, J., Li, J., Li, X. and Y. Cao, "The toxicity of multi-walled carbon nanotubes (MWCNTs) to human endothelial cells: The influence of diameters of MWCNTs", *Food and Chemical Toxicology*, Vol. 126, pp. 169–177, 2019.

321. Fischer, J., Prosenc, M.H., Wolff, M., Hort, N., Willumeit, R. and F. Feyerabend, "Interference of magnesium corrosion with tetrazolium-based cytotoxicity assays", *Acta Biomaterialia*, Vol. 6, No. 5, pp. 1813–1823, 2010.

322. Santiago-Rodríguez, L., Lafontaine, M.M., Castro, C., Méndez-Vega, J., Latorre-Esteves, M., Juan, E.J., Mora, E., Torres-Lugo, M. and C. Rinaldi, "Synthesis, stability, cellular uptake, and blood circulation time of carboxymethyl-inulin coated magnetic nanoparticles", *Journal of Materials Chemistry B*, Vol. 1, No. 22, pp. 2807–2817, 2013.

323. Wang, Q., Shen, M., Zhao, T., Xu, Y., Lin, J., Duan, Y. and H. Gu, "Low toxicity and long circulation time of Polyampholyte-coated magnetic nanoparticles for blood pool contrast agents", *Scientific Reports*, Vol. 5, pp. 1–8, 2015.

324. Zare, H., Ahmadi, S., Ghasemi, A., Ghanbari, M., Rabiee, N., Bagherzadeh, M., Karimi, M., Webster, T.J., Hamblin, M.R. and E. Mostafavi, "Carbon nanotubes: Smart drug/gene delivery carriers", *International Journal of Nanomedicine*, Vol. 16, pp. 1681–1706, 2021.

325. Raffa, V., Ciofani, G., Nitodas, S., Karachalios, T., D'Alessandro, D., Masini, M. and A. Cuschieri, "Can the properties of carbon nanotubes influence their internalization by living cells?", *Carbon*, Vol. 46, No. 12, pp. 1600–1610, 2008.

326. Höfinger, S., Melle-Franco, M., Gallo, T., Cantelli, A., Calvaresi, M., Gomes, J. A.N.F. and F. Zerbetto, "A computational analysis of the insertion of carbon nanotubes into cellular membranes", *Biomaterials*, Vol. 32, No. 29, pp. 7079–7085, 2011.

327. Geng, J., Kim, K., Zhang, J., Escalada, A., Tunuguntla, R., Comolli, L.R., Allen, F.I., Shnyrova, A.V., Cho, K.R., Munoz, D., Wang, Y.M., Grigoropoulos, C.P., Ajo-Franklin, C.M., Frolov, V.A. and A. Noy, "Stochastic transport through carbon nanotubes in lipid bilayers and live cell membranes", *Nature*, Vol. 514, No. 7524, pp. 612–615, 2014.

328. Tran, I.C., Tunuguntla, R.H., Kim, K., Lee, J.R.I., Willey, T.M., Weiss, T.M., Noy, A. and T. Van Buuren, "Structure of carbon nanotube porins in lipid bilayers: An in situ small-angle X-ray scattering (SAXS) study", *Nano Letters*, Vol. 16, No. 7, pp. 4019–4024, 2016.

329. Sullivan, K., Zhang, Y., Lopez, J., Lowe, M. and A. Noy, "Carbon nanotube porin diffusion in mixed composition supported lipid bilayers", *Scientific Reports*, Vol. 10, No. 1, pp. 1–8, 2020.

330. Li, Y., Xu, W., Zhang, W. and L. Gao, "Folate functionalized carbon nanotubes for delivery and controlled release of ibuprofen", *Journal of Functional Materials*, Vol. 46, No. 13, pp. 13070–13073, 2015.

331. Habibizadeh, M., Rostamizadeh, K., Dalali, N. and A. Ramazani, "Preparation and characterization of PEGylated multiwall carbon nanotubes as covalently conjugated and non-covalent drug carrier: A comparative study", *Materials Science and Engineering: C*, Vol. 74, pp. 1–9, 2017.

332. Farhadian, N., “Investigating the Ibuprofen Chiral Forms Interactions with Single Wall Carbon Nanotube”, *International Journal of NanoScience and Nanotechnology*, Vol. 9, No. 3, pp. 127–138, 2013.

333. Athawale, M.V., Jamadagni, S.N. and S. Garde, “How hydrophobic hydration responds to solute size and attractions: Theory and simulations”, *The Journal of Chemical Physics*, Vol. 131, No. 11, 2009.

334. Varanasi, S.R., Guskova, O.A., John, A. and J.U. Sommer, “Water around fullerene shape amphiphiles: A molecular dynamics simulation study of hydrophobic hydration”, *The Journal of Chemical Physics*, Vol. 142, No. 22, 2015.

335. Chaban, V.V. and E.E. Fileti, “Free energy of solvation of carbon nanotubes in pyridinium-based ionic liquids”, *Physical Chemistry Chemical Physics*, Vol. 18, No. 30, pp. 20357–20362, 2016.

336. Fileti, E. and V.V. Chaban, “Solubility origin at the nanoscale: Enthalpic and entropic contributions in polar and nonpolar environments”, *Physical Chemistry Chemical Physics*, Vol. 19, No. 5, pp. 3903–3910, 2017.

337. Toropov, A.A., Leszczynska, D. and J. Leszczynski, “Predicting water solubility and octanol water partition coefficient for carbon nanotubes based on the chiral vector”, *Computational Biology and Chemistry*, Vol. 31, No. 2, pp. 127–128, 2007.

338. Torrens, F. and G. Castellano, “(Co-)solvent selection for single-wall carbon nanotubes: Best solvents, acids, superacids and guest–host inclusion complexes”, *Nanoscale*, Vol. 3, No. 6, pp. 2494–2510, 2011.

339. Plesnar, E., Subczynski, W.K. and M. Pasenkiewicz-Gierula, “Saturation with cholesterol increases vertical order and smoothes the surface of the phosphatidylcholine bilayer: A molecular simulation study”, *Biochimica et Biophysica Acta - Biomembranes*, Vol. 1818, No. 3, pp. 520–529, 2012.

340. Falck, E., Patra, M., Karttunen, M., Hyvönen, M.T. and I. Vattulainen, “Response to comment by Almeida et al.: Free area theories for lipid bilayers - Predictive or not?”, *Biophysical Journal*, Vol. 89, No. 1, pp. 745–752, 2005.

341. Róg, T., Pasenkiewicz-Gierula, M., Vattulainen, I. and M. Karttunen, “Ordering effects of cholesterol and its analogues”, *Biochimica et Biophysica Acta - Biomembranes*, Vol. 1788, No. 1, pp. 97–121, 2009.

342. Olsen, B.N., Bielska, A.A., Lee, T., Daily, M.D., Covey, D.F., Schlesinger, P.H., Baker, N.A. and D.S. Ory, “The structural basis of cholesterol accessibility in membranes”, *Biophysical Journal*, Vol. 105, No. 8, pp. 1838–1847, 2013.

343. Melo, M.N., Ingólfsson, H.I. and S.J. Marrink, “Parameters for Martini sterols and hopanoids based on a virtual-site description”, *The Journal of Chemical Physics*, Vol. 143, No. 24, 2015.

344. Arnarez, C., Uusitalo, J.J., Masman, M.F., Ingólfsson, H.I., De Jong, D.H., Melo, M.N., Periole, X., De Vries, A.H. and S.J. Marrink, “Dry martini, a coarse-grained force field for lipid membrane simulations with implicit solvent”, *Journal of Chemical Theory and Computation*, Vol. 11, No. 1, pp. 260–275, 2015.

345. Filippov, A., Orädd, G. and G. Lindblom, “The effect of cholesterol on the lateral diffusion of phospholipids in oriented bilayers”, *Biophysical Journal*, Vol. 84, No. 5, pp. 3079–3086, 2003.

346. Jo, S., Rui, H., Lim, J.B., Klauda, J.B. and W. Im, “Cholesterol flip-flop: Insights from free energy simulation studies”, *The Journal of Physical Chemistry B*, Vol. 114, No. 42, pp. 13342–13348, 2010.

347. Bennett, W.F.D. and D.P. Tieleman, “Molecular simulation of rapid translocation of cholesterol, diacylglycerol, and ceramide in model raft and nonraft membranes”, *Journal of Lipid Research*, Vol. 53, No. 3, pp. 421–429, 2012.

348. Gu, R.X., Baoukina, S. and D.P. Tieleman, “Cholesterol Flip-Flop in Heterogeneous Membranes”, *Journal of Chemical Theory and Computation*, Vol. 15, No. 3, pp. 2064–2070, 2019.

349. Bennett, W.F.D, MacCallum, J.L. and P. Tieleman, “Thermodynamic analysis of the effect of cholesterol on dipalmitoylphosphatidylcholine lipid membranes”, *Journal of the American Chemical Society*, Vol. 131, No. 5, pp. 1972–1978, 2009.

APPENDIX A: ADDITIONAL ARM RESULTS

Table A.1. Single factor associations resulting in low viability (≤ 50%). The associations were listed based on their ranked lift values (above 1).

Antecedent	Support	Confidence	Lift	Count
Material				
Solid-Lipid	0.014	0.54	2.97	33
Zinc oxide	0.020	0.41	2.27	46
Silver	0.025	0.27	1.47	59
Silica	0.024	0.25	1.36	56
Gold	0.033	0.19	1.06	77
Coat				
CTAB	0.011	0.61	3.36	27
Chitosan	0.014	0.34	1.86	33
None	0.124	0.20	1.09	293
Synthesis Method				
Sol-Gel Method	0.014	0.23	1.24	32
Commercial	0.097	0.22	1.19	229
Shape				
Rod	0.016	0.24	1.32	39
Sphere	0.140	0.19	1.02	330
Surface Charge				
Positive	0.043	0.24	1.34	102
Concentration				
(200, 1000] μg/ml	0.037	0.40	2.21	88
(100, 200] μg/ml	0.020	0.24	1.29	46
PDI				
(0.2, 0.4]	0.016	0.26	1.40	37
Cell Type				
HaCat	0.016	0.45	2.48	39
HepG2	0.015	0.19	1.04	36

Table A.1. Single factor associations resulting in low viability (≤ 50%). The associations were listed based on their ranked lift values (above 1) (cont.).

Cell Morphology				
Keratinocyte	0.017	0.44	2.41	40
Macrophage	0.015	0.20	1.11	36
Fibroblast	0.034	0.19	1.04	80
Assay Type				
Alamar Blue	0.022	0.36	1.95	52
MTT	0.093	0.19	1.05	220

Table A.2. Combined factor associations resulting in low viability (≤ 50%). The associations were listed based on their ranked lift values (above 1).

Antecedent	**Support**	**Confidence**	**Lift**	**Count**
Material & Shape				
Solid-Lipid, Sphere	0.014	0.54	2.97	33
Zinc oxide, Sphere	0.015	0.41	2.26	35
Silver, Shape = Sphere	0.023	0.32	1.73	54
Silica, Shape = Sphere	0.024	0.25	1.36	56
Material & Diameter				
Zinc oxide, (25, 100] nm	0.014	0.44	2.44	33
Silver, (25, 100] nm	0.016	0.26	1.43	39
Material & PDI				
Solid-Lipid, [0, 0.2]	0.014	0.54	2.97	33
Material & Test				
Zinc oxide, MTT	0.012	0.44	2.40	28
Gold, MTT	0.023	0.21	1.17	54
Cell Type & Test				
HepG2, MTT	0.010	0.21	1.16	24
Material, Coat & Synthesis Method				
Silica, None, Commercial	0.014	0.43	2.34	32
Zinc oxide, None, Commercial	0.019	0.42	2.28	44
Silver, None, Commercial	0.014	0.30	1.66	34

Table A.2. Combined factor associations resulting in low viability (≤ 50%). The associations were listed based on their ranked lift values (above 1) (cont.).

Material, Diameter & Surface Charge				
Silver, (25, 100] nm, Negative	0.015	0.27	1.50	36
Material, Diameter & Dose				
Zinc oxide, (25, 100] nm, [10, 100] μg/ml	0.013	0.57	3.10	30

APPENDIX B: SUPPORTING INFORMATION ON FULLERENE SYSTEMS

Table B.1. List of the simulated systems. Here P denotes pristine fullerenes while J denotes janus fullerenes. Third column represents the regular PC number (either DOPC or POPC) while fourth column shows the oxidized number of lipids (either DOBU or POBU) according to the membrane model. Salt concentration is determined as 0.15 M and ion numbers are calculated based on the simulated box volumes. The total simulation time including equilibration exceeds 400 μs.

Membrane	No of Molecules						Simulation Time (μs)	No
	Fullerene	DOPC/ POPC	DOBU/ POBU	Water	Na^+	Cl^-		
DOPC	no	512	-	12312	204	204	10	1
	1P	512	-	12312	204	204	10	2
	1J	512	-	12312	204	204	10	3
	10P	512	-	12312	204	204	10	4
	10J	512	-	12312	204	204	10	5
DOBU30	no	358	154	12312	208	208	10	6
	1P	358	154	12312	208	208	10	7
	1J	358	154	12312	208	208	10	8
	10P	358	154	12312	208	208	10	9
	10J	358	154	12312	208	208	10	10
DOBU70	no	154	358	12312	210	210	10	11
	1P	154	358	12312	210	210	10	12
	1J	154	358	12312	210	210	10	13
	10P	154	358	12312	210	210	10	14
	10J	154	358	12312	210	210	10	15
DOBU	no	-	512	12312	212	212	10	16
	1P	-	512	12312	212	212	10	17
	1J	-	512	12312	212	212	10	18
	10P	-	512	12312	212	212	10	19
	10J	-	512	12312	212	212	10	20

Table B.1. List of the simulated systems. Here P denotes pristine fullerenes while J denotes janus fullerenes. Third column represents the regular PC number (either DOPC or POPC) while fourth column shows the oxidized number of lipids (either DOBU or POBU) according to the membrane model. Salt concentration is determined as 0.15 M and ion numbers are calculated based on the simulated box volumes. The total simulation time including equilibration exceeds 400 μs (cont.).

POPC	no	512	-	12312	200	200	10	21
	1P	512	-	12312	200	200	10	22
	1J	512	-	12312	200	200	10	23
	10P	512	-	12312	200	200	10	24
	10J	512	-	12312	200	200	10	25
POBU30	no	358	154	12312	201	201	10	26
	1P	358	154	12312	201	201	10	27
	1J	358	154	12312	201	201	10	28
	10P	358	154	12312	201	201	10	29
	10J	358	154	12312	201	201	10	30
POBU70	no	154	358	12312	202	202	10	31
	1P	154	358	12312	202	202	10	32
	1J	154	358	12312	202	202	10	33
	10P	154	358	12312	202	202	10	34
	10J	154	358	12312	202	202	10	35
POBU	no	-	512	12312	204	204	10	36
	1P	-	512	12312	204	204	10	37
	1J	-	512	12312	204	204	10	38
	10P	-	512	12312	204	204	10	39
	10J	-	512	12312	204	204	10	40

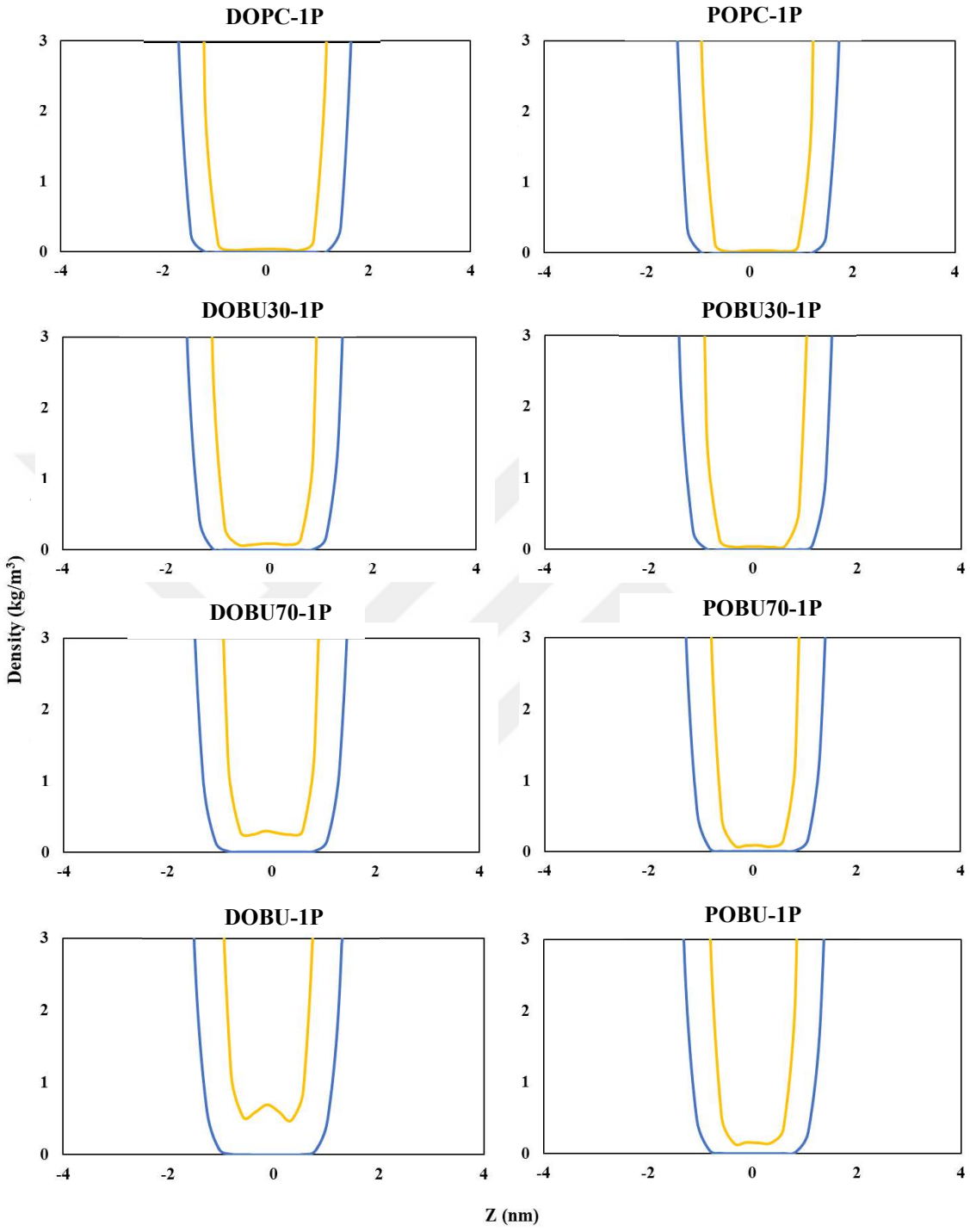

Figure B.1. Density distribution profiles of water (yellow) and ion (blue) molecules for DOPC and POPC and their peroxidized forms at pristine fullerene to lipid ratio of F/L =10/512.

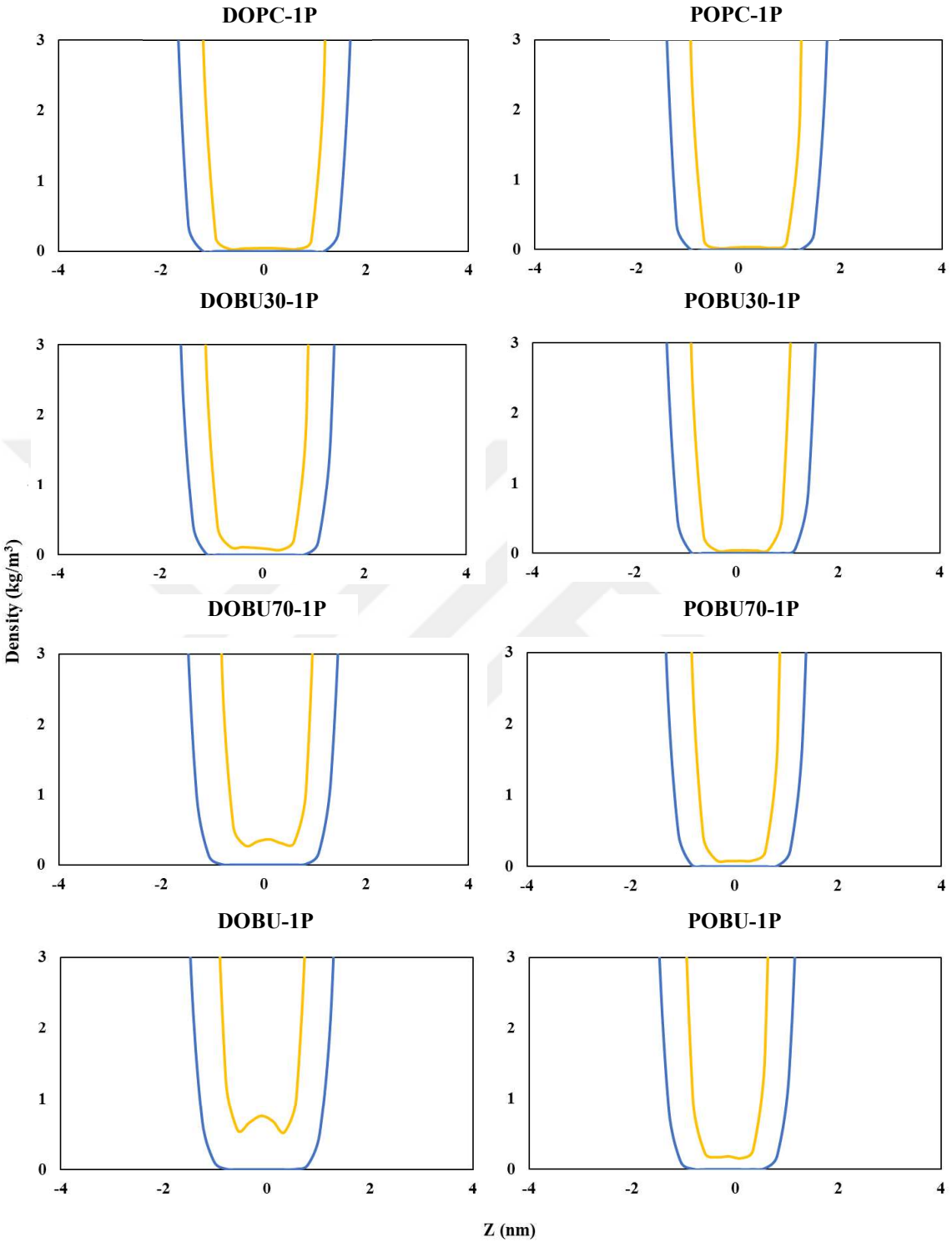

Figure B.2. Density distribution profiles of water (yellow) and ion (blue) molecules for DOPC and POPC and their peroxidized forms at Janus fullerene to lipid ratio of F/L =10/512.

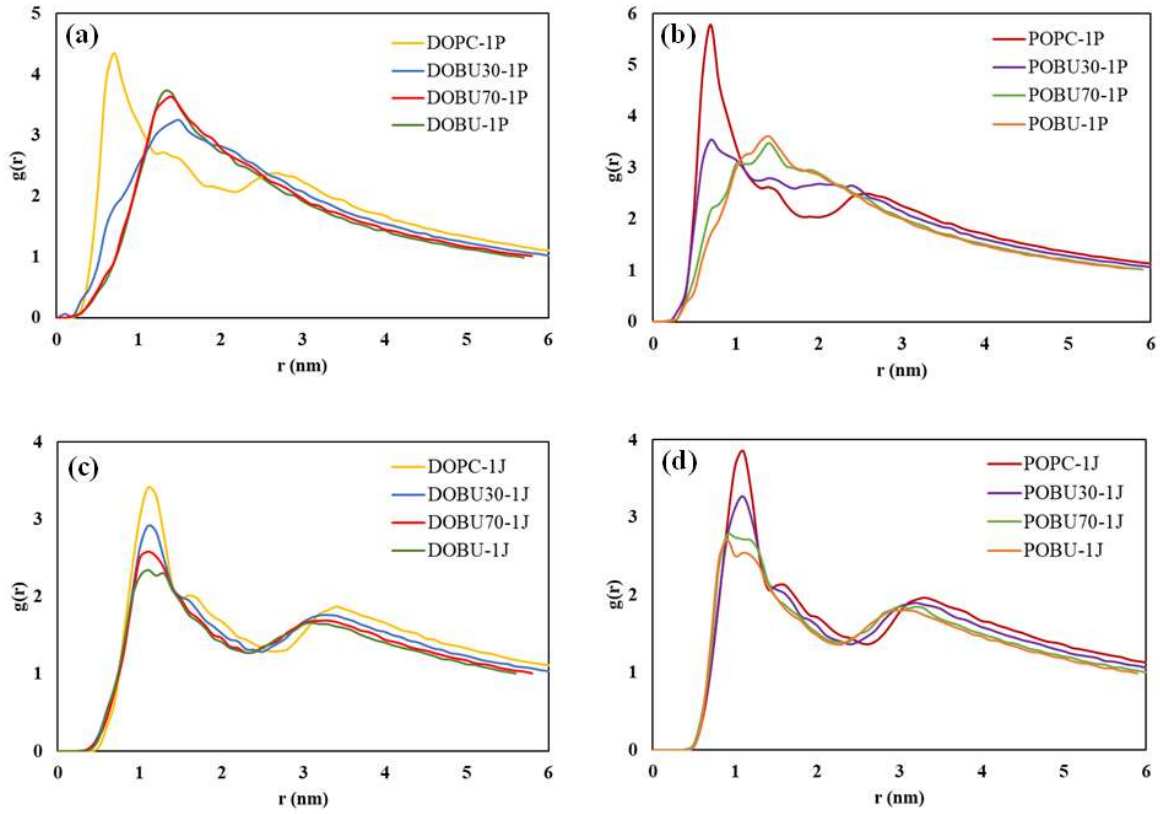

Figure B.3. Membrane-Fullerene COM radial distribution functions for (a-b) pristine fullerenes, (c-d) janus fullerenes at fullerene-to-lipid ratio of 1/512.

APPENDIX C: SUPPORTING INFORMATION ON CARBON NANOTUBE SYSTEMS

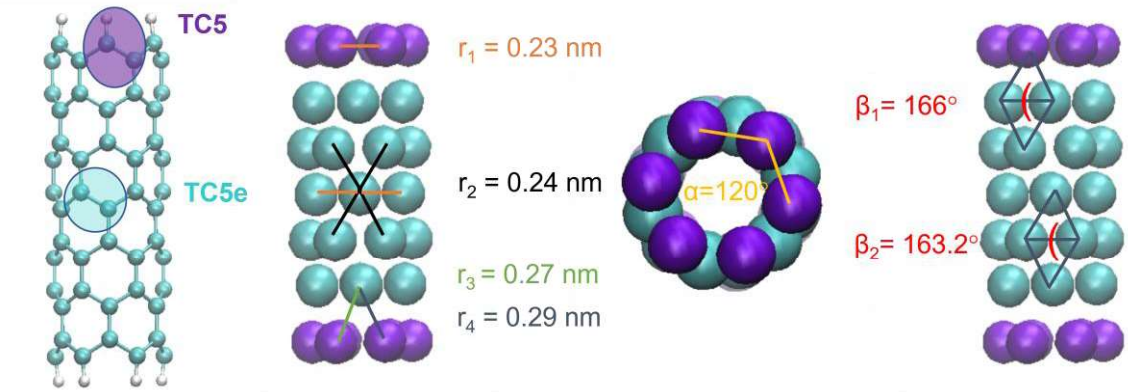

Figure C.1. CNT (6,0) mapping from all-atom to CG MARTINI model with bond lengths, angles and improper dihedrals described with color coding. Force constants of 50000 kJ mol^{-1} was used to capture equilibrium bond lengths while 350 kJ mol^{-1} rad^{-2} was used for angles, and dihedrals.

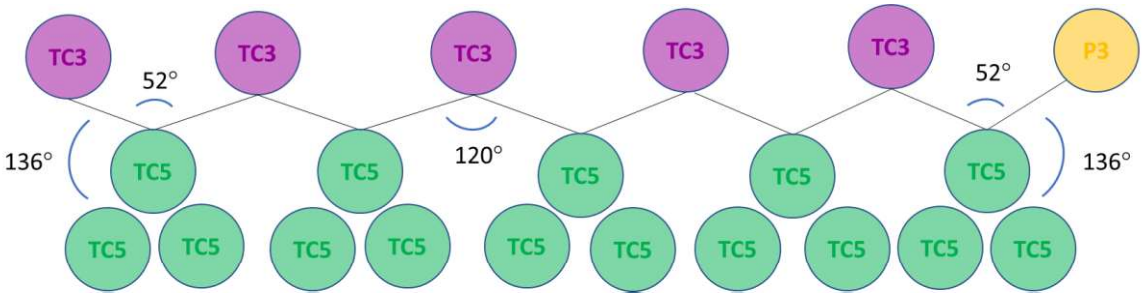

Figure C.2. Bonded parameters of carboxyl-terminated polystyrene chain where P represents the carboxyl group. All bonds are taken as 0.27 nm while constraints (between ring beads) are 0.29 nm. Here purple, green and yellow represent the TC3 bead, TC5 bead, and P3 bead, respectively.

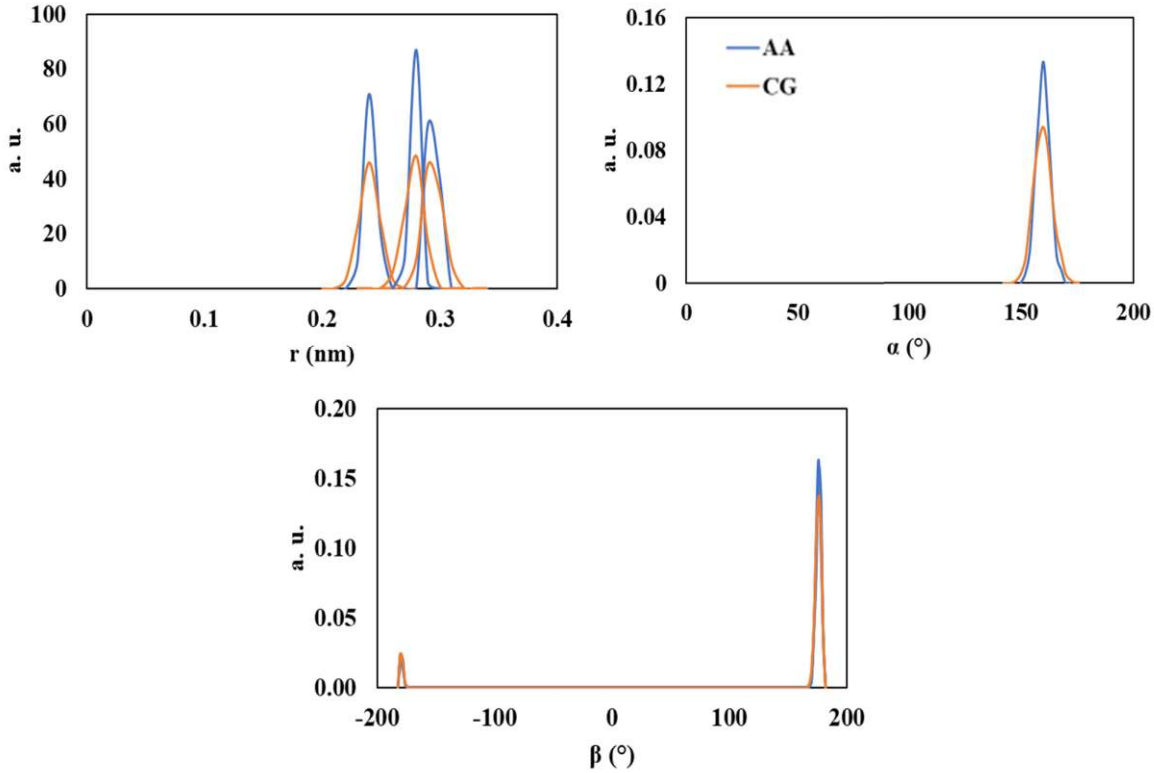

Figure C.3. Bond (r), angle (α) and improper dihedral (β) distributions of CNT obtained from AA and CG simulations. Force constants used in CG simulations are 50000 kJ mol^{-1}, 1500 kJ mol^{-1} rad^{-2} and 1000 kJ mol^{-1} rad^{-2} for bonds, angles, and dihedrals, respectively.

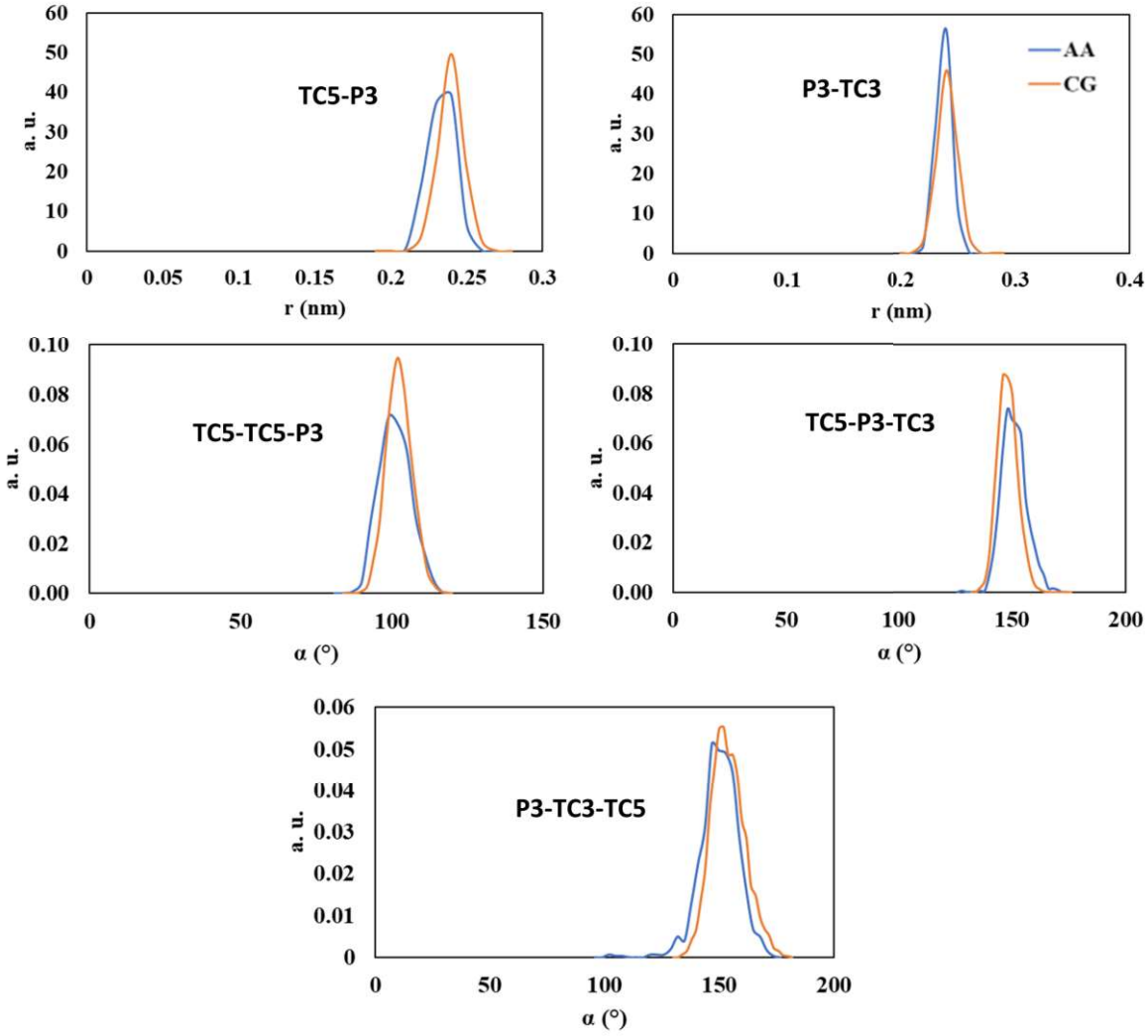

Figure C.4**.** Bond (r), and angle (α) distributions between CNT, linker and PS obtained from AA and CG simulations.

CG bond force constants are 50000 kJ mol^{-1} while angle force constants are listed below.

Martini Bead Type	**Force Constant (kJ mol^{-1} rad^{-2})**
TC5-TC5-P3	50
TC5-P3-TC3	1500
P3-TC3-TC5	750

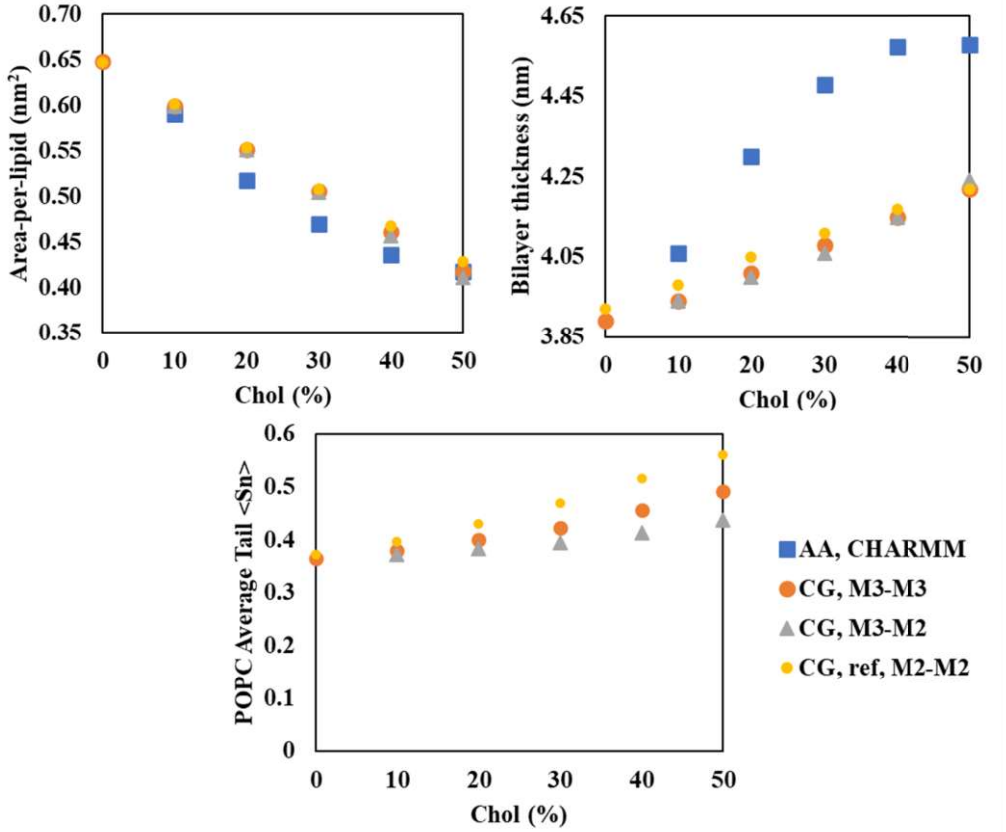

Figure C.5. Fully hydrated POPC bilayers were simulated with 0–50 mol % of the cholesterol. Each AA and CG simulation had 128 and 336 lipids, 7680 AA, and 5054 CG waters and were simulated for 50 ns and 1 μs at 300 K, respectively; the last halves were used for the analysis. Area-per-lipid values are calculated by dividing the box area into the number of lipids in one leaflet. Bilayer thickness represents the distance between POPC's P atoms or PO4 beads in the upper and lower leaflet and the POPC average order parameter is found by averaging all bonds from both tails. M3 and M2 stand for Martini3 and Martini2 force fields for POPC and Cholesterol, respectively. M2 reference is taken from Melo et al. [344]

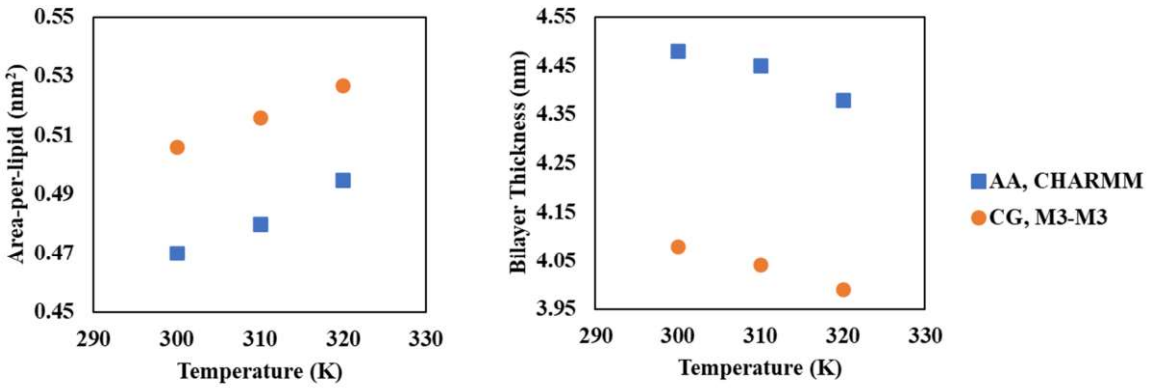

Figure C.6. Membrane properties of POPC with 30 % cholesterol with respect to the temperature.

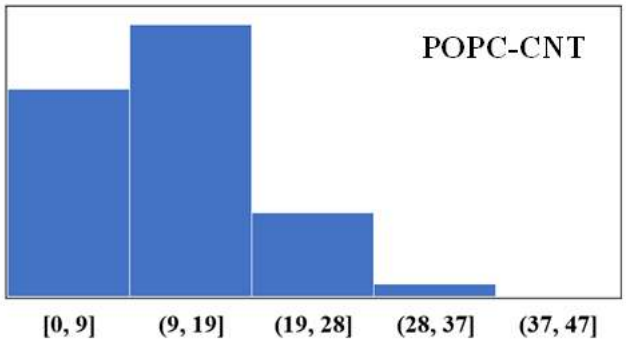

Figure C.7. Distribution of angles (°) between pristine CNT long axis and POPC bilayer normal. Data is taken from the last 2 μs trajectories.

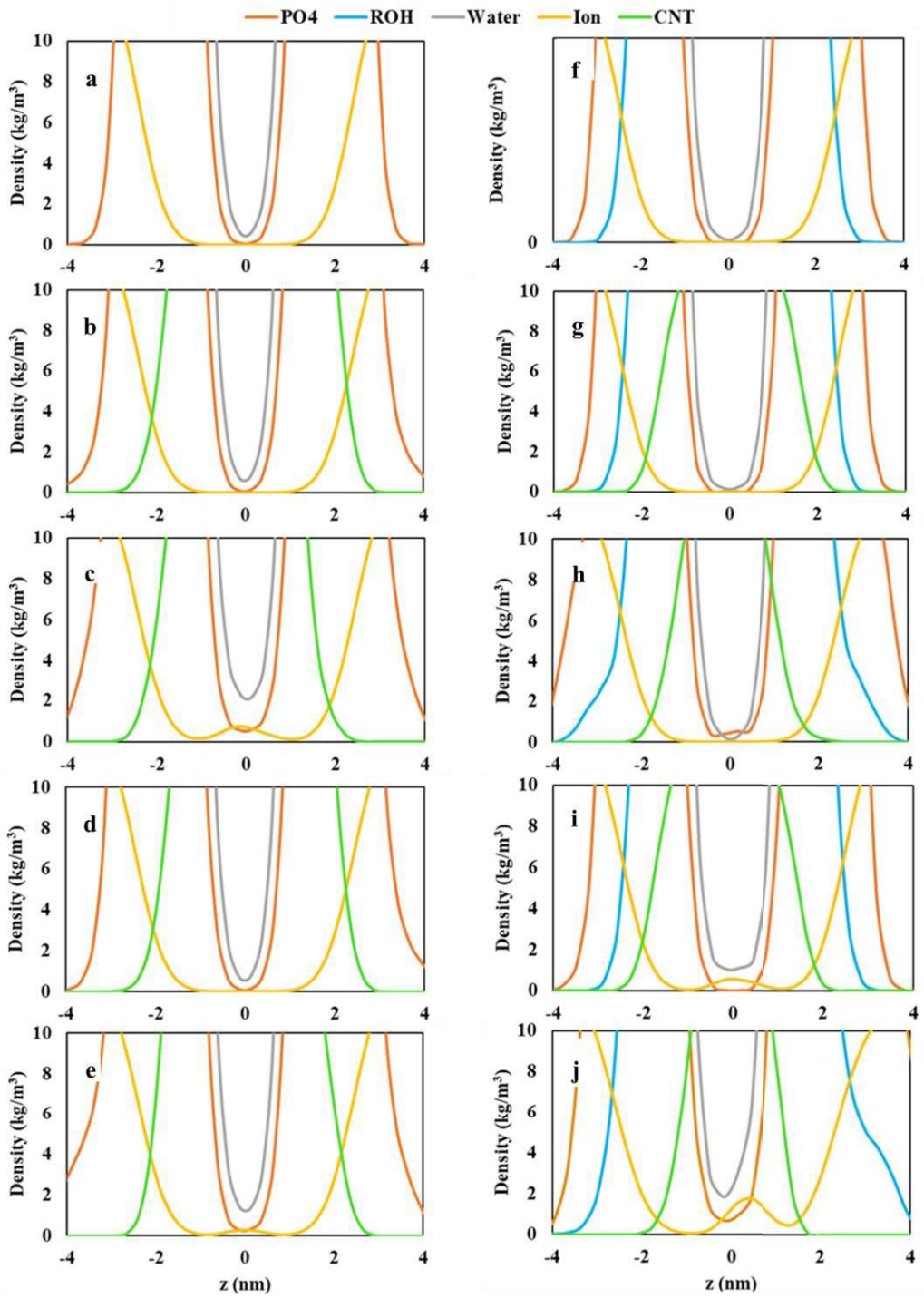

Figure C.8. Density distributions of lipid phosphate (PO4) and hydroxyl (ROH) groups, and water, ion, and CNT molecules in the presence of 5 functionalized CNTs for a) POPC, b) POPC-PS29CNTx4, c) POPC-PS29CNTx6, d) POPC- PSCOOH29CNTx4, e) POPC- PSCOOH29CNTx6, f) POPC/CHOL, g) POPC/CHOL-PS29CNTx4, h) POPC/CHOL-PS29CNTx6, i) POPC/CHOL- PSCOOH29CNTx4, j) POPC/CHOL-PSCOOH29CNTx6.

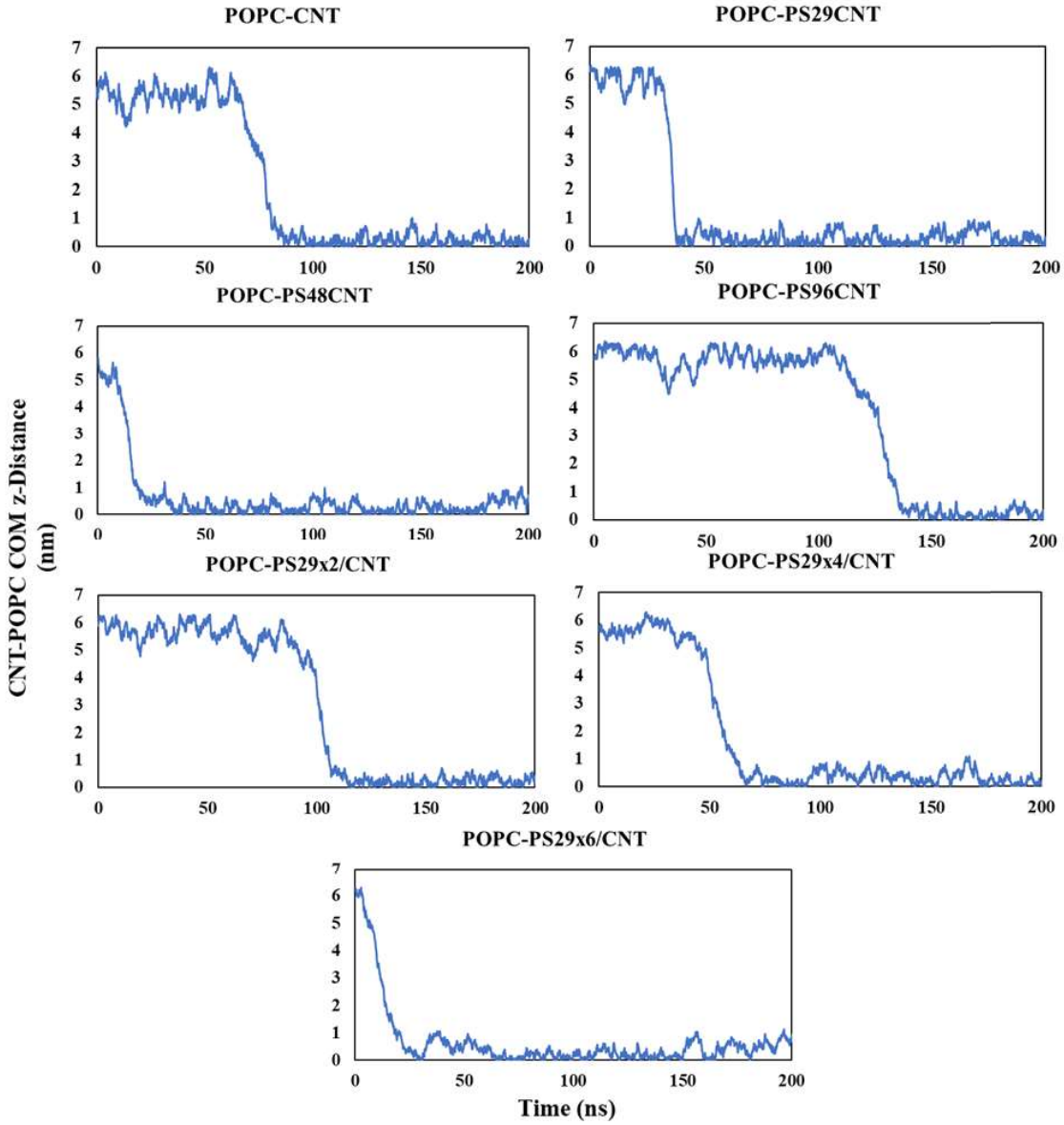

Figure C.9. The absolute center-of-mass (COM) distance of CNT (18,0) from the POPC bilayer in the z-direction for pristine and polystyrene (PS) functionalized CNT systems at 29, 48, and 96 monomers of PS and 29 monomers of PS with 2, 4 or 6 chains. Data represents the first 200 ns of trajectories.

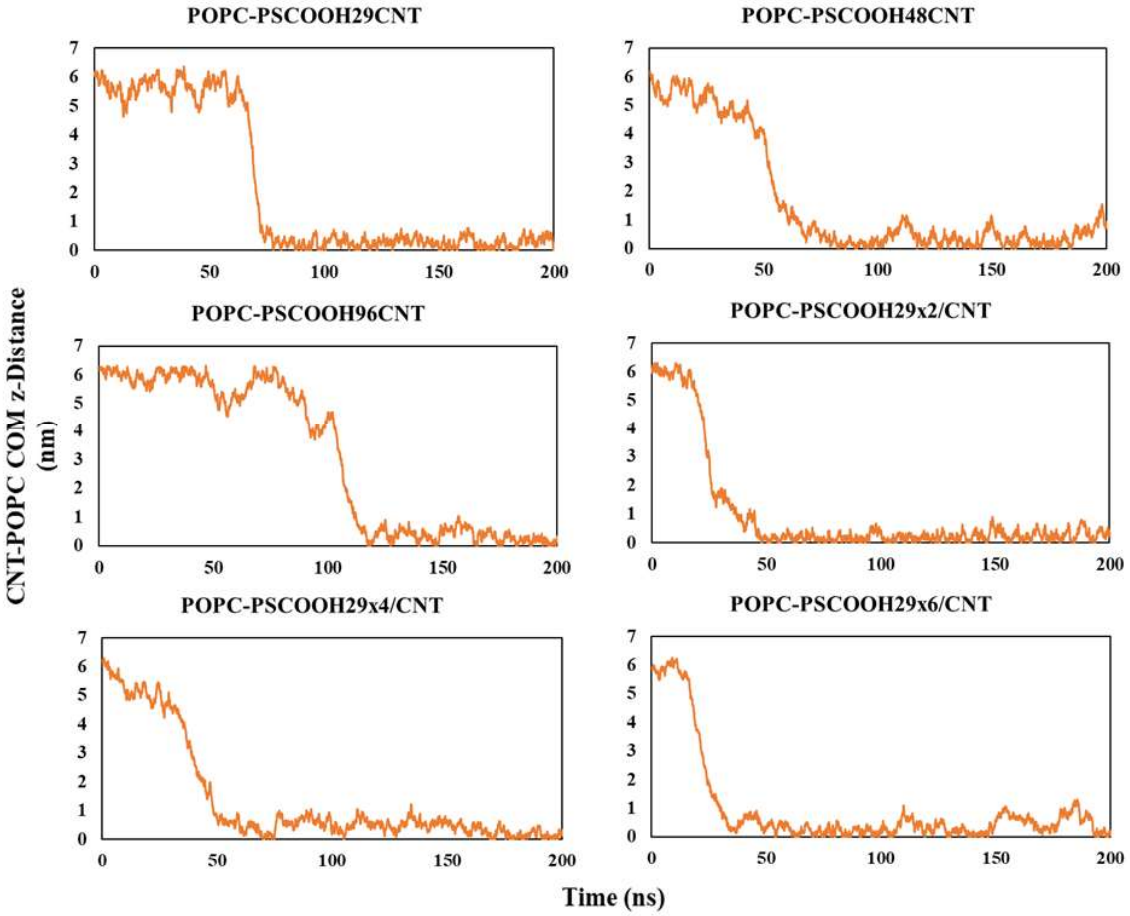

Figure C.10. The absolute center-of-mass (COM) distance of CNT (18,0) from the POPC bilayer in the z-direction for carboxyl-terminated polystyrene (PSCOOH) functionalized CNT systems at 29, 48, and 96 monomers of PSCOOH and 29 monomers of PSCOOH with 2, 4 or 6 chains. Data represents the first 200 ns of trajectories.